Cranfield University

School of Applied Sciences

PhD Thesis

Academic year 2011-2012

H. E. Coules

Characterising the effects of high-pressure rolling on residual stress in structural steel welds

This thesis is submitted in fulfilment of the requirements for the degree of Doctor of Philosophy.

Supervisor: Dr P. Colegrove

Date of presentation: 12th September 2012

Abstract

The large residual stresses which occur in welded objects are an unavoidable consequence of the non-uniform cycle of thermal strain inherent in most welding processes. Furthermore, the particular distributions of residual stress which are characteristic of welding can adversely influence several material and structural failure mechanisms, including fatigue fracture, elastic fracture and buckling. This thesis describes an experimental investigation into the use of localised high-pressure rolling of the weld seam for the purpose of residual stress reduction in steel welds.

In preliminary experiments, it is demonstrated that the transient stresses which occur in an object while part of it is welded or rolled, can be inferred from strain measurements taken during the process. Furthermore, such measurements can be used to estimate the resulting residual stresses. Good agreement is observed between residual stress distributions found using this method and determined using neutron diffraction. The effect of rolling on residual stress in structural steel welds is then investigated using both of these measurement techniques. Rolling is shown to greatly reduce tensile residual stress at the weld seam, even introducing compressive stress when a greater rolling force is used. However, this is only the case when rolling is applied post-weld: by contrast, methods involving rolling prior to or during welding do not improve the residual stress distribution. It is proposed, on the basis of transient stress measurements, that this is because the deformation which occurs in a weld during cooling greatly exceeds its yield strain, and so any effect of high-temperature deformation on residual stress is subsequently erased.

Other effects of rolling on the properties of a weld have also been studied. Using mechanical tests and microstructural analysis it is shown that while post-weld rolling causes work-hardening of structural steel welds, rolling the weld at high temperature results in refinement of the weld microstructure, also hardening it. The effect of roller geometry on residual stress and fatigue life of rolled specimens has been investigated: the induced residual stress distribution is relatively insensitive to the roller's cross-sectional profile, while the fatigue life is shown to be reduced by post-weld rolling.

The implications of these findings for the practical implementation of weld rolling, along with many other applied aspects of the process are discussed. While rolling is undoubtedly a useful and highly effective tool for residual stress mitigation in welds, its secondary effects should always be carefully considered.

Acknowledgements

Finally, this thesis owes a great deal to Katie Hore who, acting in various capacities as cook, girlfriend, secretary, research chemist and zoo-keeper, contributed enormously to its completion.

Declaration

Many of the chapters in this thesis are largely based on articles which have been, or are intended to be, published elsewhere. A list of these is given below. For each of these, the candidate (H. E. Coules) contributed principally to all aspects of the work described therein.

- H. E. Coules, P. Colegrove, L. D. Cozzolino and S. W. Wen. High-pressure rolling of low-carbon steel weld seams, Part 1: Effects on mechanical properties and microstructure. *Science and Technology of Welding and Joining,* 2012*. Accepted, in press.*
- H. E. Coules, P. Colegrove, L. D. Cozzolino, S. W. Wen and J. F. Kelleher. High-pressure rolling of low-carbon steel weld seams, Part 2: Roller geometry and residual stress. *Science and Technology of Welding and Joining,* 2012*. Accepted, in press.*
- H. E. Coules. Contemporary approaches to reducing weld-induced residual stress. *Materials Science and Technology*, 2012*. Accepted, in press.*
- H. E. Coules, L. D. Cozzolino, P. Colegrove, S. Ganguly, S. W. Wen and T. Pirling. Residual strain measurement for arc welding and localised high-pressure rolling using resistance strain gauges and neutron diffraction. *Journal of Strain Analysis for Engineering Design*, 2012*. Accepted, in press.*
- H. E. Coules, L. D. Cozzolino, P. Colegrove, S. Ganguly, S. W. Wen and T. Pirling. Neutron diffraction analysis of complete residual stress tensors in conventional and rolled gas metal arc welds. *Experimental Mechanics*, 2012*. Accepted, in press.*
- H. E. Coules, P. Colegrove, L. D. Cozzolino, S. W. Wen, S. Ganguly and T. Pirling. Effect of high pressure rolling on weld-induced residual stresses. *Science and Technology of Welding and Joining*, 17(5): 394-401, 2012.
- H. E. Coules, P. Colegrove, L. D. Cozzolino and S. W. Wen. Experimental measurement of biaxial thermal stress fields caused by arc welding. *Journal of Materials Processing Technology*, 212(4): 962-968, 2012.
- H. E. Coules, L. D. Cozzolino, P. Colegrove and S. W. Wen. Measurement and modelling of the transient thermal-mechanical strain field during GMA welding. *Proceedings of the IWOTE '11: International Workshop on Thermal Forming and Welding Distortion*, F. Vollertsen (ed.), 267-278, 2011
- H. E. Coules, L. D. Cozzolino, P. Colegrove and S. W. Wen. The effect of pre-weld rolling on distortion and residual stress in fusion welded steel plate*. Materials Science Forum*, 681: 486-491, 2011.

Additionally, while the work described in Chapters 9 and 10 is the candidate's own, some of the results presented in these chapters have also been included in the following articles:

- P. Colegrove, H. E. Coules, J. Fairman, F. Martina, T. Kashoob and H. Mamash. Microstructure and residual stress improvement in wire and arc additively manufactured parts through high-pressure rolling. *Submitted to: Journal of Materials Processing Technology, 2012.*
- L. D. Cozzolino, H. E. Coules, P. Colegrove and S. W. Wen. Modelling distortion reduction on pre- and post-weld rolled gas metal arc welded plates. *Proceedings of the IWOTE '11: International Workshop on Thermal Forming and Welding Distortion*, F. Vollertsen (ed.), 169-179, 2011

This thesis is submitted on the conditions contained in the Regulations, and has not been submitted for any other academic or professional award. All of the work described was carried out as part of the course of study at Cranfield University and not previously or subsequently.

Candidate (H. E. Coules):   *Date:*

Supervisor (P. Colegrove):   *Date:*

Contents

Chapter 1: Introduction

Background

In the absence of any external force, many objects still contain a residual stress field. When the distribution of plastic strain within an object is not completely homogeneous, the physical incompatibility between different regions of material causes such stresses to arise. While the residual stress field must be fully self-equilibrating (i.e. non-divergent), it is superimposed on any applied stresses, and consequently can affect material failure *via* several mechanisms [1].

The welding of metals typically requires localised heating and cooling of the material at the join. The constrained plastic deformation which results from this produces a characteristic distribution of residual stress which has particularly adverse mechanical effects. In a linear weld, a residual stress state with a large tensile component aligned close to the longitudinal direction of the weld typically arises in and directly adjacent to the weld seam [2]. The presence of a tensile residual stress in the weld region, whose mechanical properties may already be compromised by imperfect microstructure and geometric stress concentrations, increases vulnerability to fracture-based material failure. Furthermore, residual stress is associated with physical distortion of the welded object. In thin-walled structures, for example, the residual stresses which result from welding can cause buckling of the welded structure and associated manufacturing problems.

While many methods for residual stress reduction in welds have been investigated, few have seen widespread industrial implementation. This is mainly due to the costs and technical difficulties associated with their practical application. However high-pressure rolling is one such process which has been largely overlooked, with only a single experimental study in recent years focussing on this method [3]. Rolling has the potential advantages of being easy to control and conducive to automation while requiring no consumable materials, and having a large and repeatable effect on the residual stress distribution. On the other hand it is an immature technology, and would be difficult to apply to complex structures.

All of the work described in this thesis was carried out as part of a project entitled "Static and dynamic rolling to reduce residual stress and distortion", jointly funded by the UK Engineering and Physical Sciences Research Council (EPSRC) and Tata Steel UK Ltd., the aim of which was to investigate weld seam rolling. This involved two research students at Cranfield: Luis Daniel Cozzolino and myself. While the project incorporated both experimental and modelling aspects, my focus was on experimental work – a fact which is reflected in the content of this thesis.

Research objectives

The basic objectives of this research were to increase the scientific understanding of high-pressure rolling of weld seams for residual stress control, and to better enable its practical implementation. Consequently, it was necessary to investigate several different aspects of this process:

- *Rolling methods*: What rolling arrangements are most effective for controlling residual stress in a weld? For instance should rolling take place before, during or after the welding operation, and what roller geometries have the most beneficial effect?
- *Mechanisms of residual stress control*: The development of the stress field in an object as it is welded is known to be complex. How do different rolling techniques interact with this, and how can the outcome of this interaction be optimised for low residual stress?
- *Effects on weld material*: What effects does rolling have on the material properties and microstructure of steel welds?
- *Application*: Can rolling be usefully applied to more complex weld geometries and residual stress states? What techniques could be used to make rolling easier to implement?

Thesis outline

The majority of chapters in this thesis are based on published articles. A citation of the relevant paper is given at the start of each chapter, and a complete list of articles is provided with the declaration by the candidate.

Chapters 3-6 discuss residual stress in welds, its formation, and the use of high-pressure rolling for its mitigation. The first experimental chapter (Chapter 3) deals with measurement of the developing stress field which occurs during welding, and introduces techniques used in subsequent chapters for investigating stress development during weld rolling. In Chapter 4, this work is extended to the measurement of residual stresses, and the effect of rolling is studied using this technique and neutron diffraction. Chapter 5 contains the results of the main investigation into weld seam rolling methods: neutron diffraction and the techniques introduced in Chapter 3 are used to examine the effects of several different forms of rolling on residual stress in welds and the associated mechanism of residual stress formation. In Chapter 6, an experimental method extending the capability of neutron diffraction residual stress measurement is applied to rolled weld specimens, confirming and generalising some of the findings of the previous chapter.

In Chapter 7, the effects of rolling on the material properties and microstructure of structural steel welds are investigated, and following on from this the effects of

different roller geometries were studied in Chapter 8. Chapters 9 and 10 discuss specialised rolling techniques: Chapter 9 focusses on the possibility of residual stress reduction *via* localised rolling of the parent metal before it is welded, while Chapter 10 is on the application of rolling during an additive manufacturing process. Finally, a general discussion of the findings of the preceding chapters is given in Chapter 11.

List of symbols and abbreviations

All symbols and abbreviations are defined where they first appear in each chapter. Below is a partial list of commonly-used symbols in this thesis.

Symbol	Description
a	Acceleration OR lattice parameter OR plate length (in longitudinal direction)
a_0	Stress-free lattice parameter
$\boldsymbol{A}$	Matrix of direction cosines
b	Plate width (in transverse direction)
c	Width of central region of tensile residual stress in a welded plate
d	Lattice spacing
d_0	Stress-free lattice spacing
D	Flexural rigidity
E	Young's modulus
g	Gravitational acceleration
k	Curvature
l	Direction cosine resulting from rotation about the x axis
m	Direction cosine resulting from rotation about the y axis *or* Mass
n	Direction cosine resulting from rotation about the z axis
N_x	Externally-applied force (in x direction)
P	Vertical applied force
R_1	Force per unit width (tensile)
R_2	Force per unit width (compressive)
$\boldsymbol{R}$	Rotation matrix
t	Plate thickness (dimension in z direction)
T	Work done by external forces
U	Internal elastic bending energy
w	Out-of-plane deflection of plate surface
x	Direction parallel to weld/roller path
y	Direction transverse to weld/roller path
z	Direction normal to plate/substrate surface
δ	Standard uncertainty
ε	Strain
ε_{lmn}	Strain in arbitrary direction defined by rotation cosines lmn
$\boldsymbol{\varepsilon}$	Strain tensor
$\boldsymbol{\varepsilon_e}$	Elastic component of the strain tensor
$\boldsymbol{\varepsilon_p}$	Plastic component of the strain tensor
$\boldsymbol{\varepsilon_t}$	Thermal dilation component of the total strain tensor
θ	(Neutron) Scattering angle
κ	Condition number
λ	(Neutron) Wavelength
ν	Poisson ratio
σ	Stress
σ_{cr}	Critical buckling stress
σ_{vm}	von Mises stress
$\boldsymbol{\sigma}$	Stress tensor
τ	Shear stress
$_{11}$	Suffix denotes direction of first axis of arbitrary Cartesian coordinate system
$_{22}$	Suffix denotes direction of second axis of arbitrary Cartesian coordinate system

Symbol	Description
$_{33}$	Suffix denotes direction of third axis of arbitrary Cartesian coordinate system
xx	Suffix denotes normal stress/strain in x direction
yy	Suffix denotes normal stress/strain in y direction
zz	Suffix denotes normal stress/strain in z direction
xy	Suffix denotes shear in x-y plane
yz	Suffix denotes shear in y-z plane
xz	Suffix denotes shear in x-z plane

Abbreviation	Description
DIC	Digital Image Correlation
FE(M)	Finite Element (Method)
FBG	Fibre Bragg Grating
GMAW	Gas-Metal Arc Weld/ Gas-Metal Arc Welding
GMT	Global Mechanical Tensioning
GTAW	Gas-Tungsten Arc Weld/ Gas-Tungsten Arc Welding
HAZ	Heat-Affected Zone
PWHT	Post-Weld Heat Treatment
UTS	Ultimate Tensile Strength
WAAM	Wire and Arc Additive Manufacturing

Chapter 2: Literature review

This chapter is an edited version of the following article:

> H. E. Coules. Contemporary approaches to reducing weld-induced residual stress. *Materials Science and Technology*, 2012. *Accepted, in press.*

Abstract

Self-equilibrating residual stresses may occur in materials in the absence of external loading due to internal strain inhomogeneity. While favourable distributions of residual stress can bestow an object with the appearance of superior material properties, most welding processes leave behind residual stresses in particularly unfavourable patterns, causing a greater susceptibility to fracture-based failure mechanisms and unintended deformation. Currently, heat treatment is the primary means of removing these stresses, but since the formation of residual stress is dependent upon many material and process factors, there are several other viable mechanisms (using thermal, mechanical or phase transformation effects) by which it may be modified. It is only now, using relevant advances in numerical and experimental methods, that these techniques are being fully explored. This chapter gives a brief introduction to weld-induced residual stresses and reviews the current state-of-the-art with regard to their reduction. Emphasis is placed on the recent development of unconventional techniques, and the mechanisms by which they act.

Introduction

Residual stress

Macro-scale residual stresses, which equilibrate internally over a component or assembly, are ubiquitous in everyday life. They allow tempered glass to resist fracture by inhibiting the propagation of cracks at the material's surface. They keep common fasteners such as nails and screws from slipping free by exerting a contact force at the interface of the different components. They even act within our own bodies to brace our arteries against the pressure of our blood[1]. However, adverse distributions of residual stress in engineering components (specifically, high tensile stresses in areas prone to fracture or fatigue), can lead to unexpected or premature failure [1]. The

---

[1] Mammalian arteries have been shown to contain circumferential residual stresses which are compressive at the inner arterial wall, and tensile at the outer wall. This is believed to make the total distribution of stress in the artery more uniform when the vessel is internally pressurised *in vivo* [256].

formation and relaxation of residual stresses during manufacturing processes also causes unwanted and problematic deformation which can be costly to correct. The large amount of non-uniform heat input inherent in most forms of welding generates characteristic distributions of residual stress which tend to have particularly adverse mechanical effects. This makes welding a frequent cause of residual stress problems in engineering practice.

Broadly, residual stresses can be categorised into three groups based on scale [4]. Type I stresses, which exist in the macro- scale, are most frequently of concern to engineers [5]. In polycrystalline materials, inter-granular scale Type II stresses are generated by mechanical incompatibility between adjacent crystallites [6]. Type III stresses, on the inter-atomic scale, result from crystallographic defects [5, 7, 8]. With the greatest immediate implications for engineering design, only Type I stresses resulting from welding process will be discussed here.

Formation of residual stresses during welding

Due to their widespread occurrence and notorious effects, weld-induced stresses are the prototypical example of detrimental residual stress in structural materials. The formation of residual stresses during welding is a consequence of the fact that different parts of a welded object experience different cycles of thermal expansion and contraction. The resulting thermal stress causes a non-uniform distribution of irreversible material deformation, and some of this deformation remains after the material has cooled, resulting in an internal and completely self-equilibrating stress field.

Residual stress formation during welding is illustrated schematically in Figure 1. Most forms of welding require a large amount of localised heat input at the joint interface to achieve material bonding, which occurs by mixing in a liquid or partially-melted state, or by solid-phase diffusion[2] [9]. Inevitably this elevated temperature causes thermal dilation of material, accompanied by a gradual decrease in yield strength and eventually, in the case in fusion welding, melting. By contrast, material remote from the weld seam remains at a relatively low temperature throughout (see Section B-B in Figure 1). The heated material at the interface then begins to cool, and any liquid metal solidifies. The material then cools and contracts as a solid, but is mechanically constrained by the surrounding cold material (Section C-C). This results in a characteristic distribution of residual stress, with very large tensile stresses in the

---

[2] Welding processes which involve complete melting of some part of the material are known under the umbrella term of 'fusion welding'. This encompasses most common welding methods, but excludes solid-state processes such as linear friction welding and diffusion bonding.

region of the joint (where material is prevented from contracting as much as it otherwise would) which are balanced by compressive stresses elsewhere [7, 10, 11].
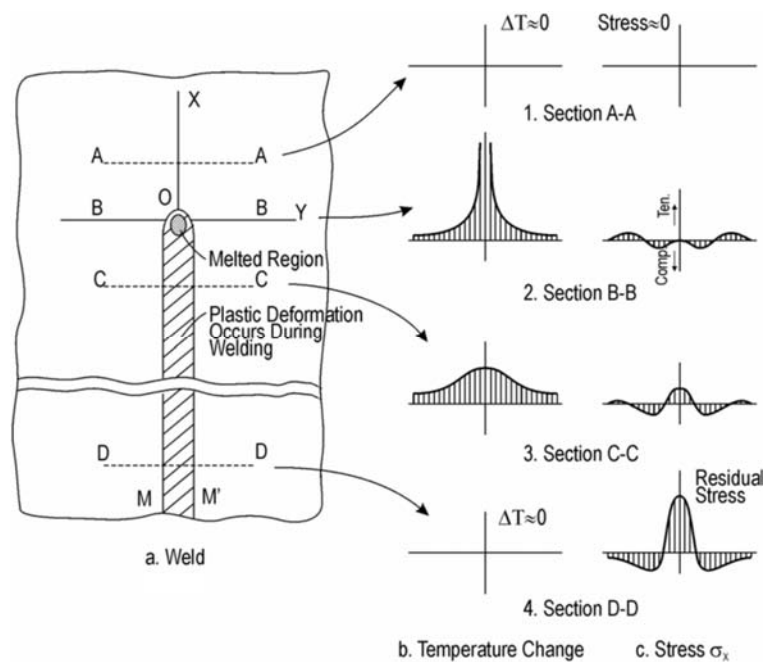
Figure 1: Process of residual stress formation in a weld [2]: a. schematic of the weld line, b. temperature distribution across transverse sections, c. distribution of (longitudinal) stress across transverse sections. Note how significant tensile stress forms at the weld as it cools.

The exact magnitude and orientation of the resultant residual stresses depends on the direction of the greatest thermal gradients encountered as the material cools, and on the mechanical constraint applied to the cooling weld metal. A simple example is shown in Figure 2a: in a mechanically-unconstrained linear weld, the largest thermal gradient typically occurs across the transverse direction. Material can therefore contract freely in this direction since the contraction is approximately uniform along the length of the weld. Correspondingly, in the out-of-plane direction the weld metal is unconstrained, and therefore free to contract. However in the *longitudinal* direction, contraction is impeded by the surrounding cold material. Consequently, the largest tensile component of residual stress in a weld of this type is almost always oriented in the longitudinal direction. In other situations, for example for welds in thicker material and on objects of greater complexity other residual stress distributions may arise, but they are always determined by the pattern of thermal contraction and mechanical constraint[3]. Figure 2b shows an example of a more heavily-constrained weld. In this case, the more rigid mechanical boundary conditions imposed on the contracting weld metal mean that large tensile residual stresses may arise in the transverse direction, as well as the longitudinal.

---

[3] The distributions of residual stress found in other types of weld geometry are discussed by Leggatt [11].

a.

b.
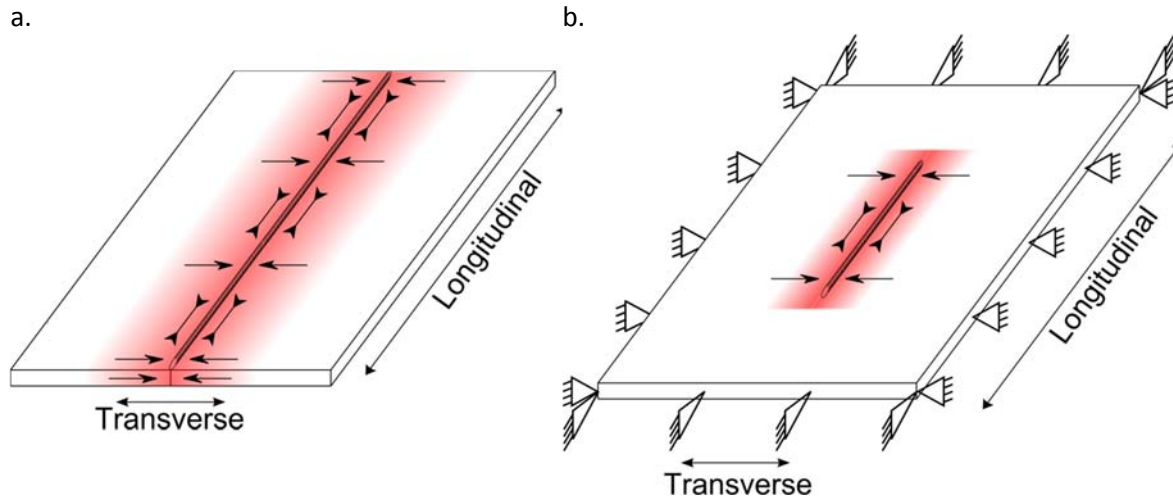
Figure 2: Thermal contraction of material during cooling of linear weld: a. unconstrained butt weld, b. bead-on-plate or repair weld, where the surrounding material or structure provides mechanical constraint.

The peak tensile residual stress observed at the centre of a fusion weld can approach the yield strength of the unaffected parent material, or even exceed it wherever there is hardening of the weld material due to compositional or microstructural change [11, 12]. However, the actual magnitude depends on the thermal field and the properties of the material, specifically its strain-temperature and yield stress-temperature relationships [13]. For example, in aluminium alloy welds the development of tensile stresses at the weld interface is normally limited by the low elevated-temperature yield stress and low post-weld hardness compared with the parent metal (see Figure 3), resulting in a characteristic 'M-shaped' tensile stress profile [14, 15]. However, in fusion welds the total size of the tensile region is typically larger than the extent of the melted zone (Figure 3), corresponding instead to the extent of plastic deformation induced by thermal stress. Consequently, welding with a greater heat input generally results in a wider tensile region [12, 16].
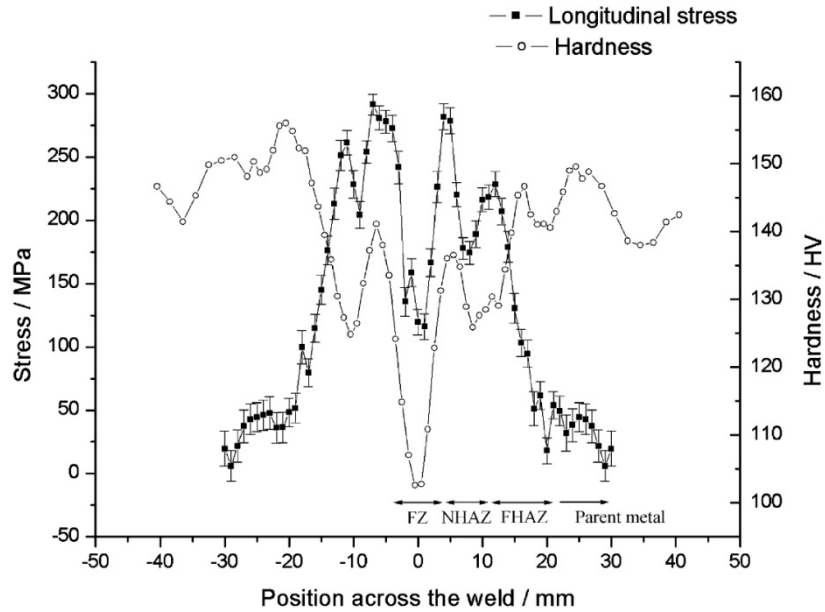
Figure 3: Comparison of longitudinal residual stress (measured using neutron diffraction) and hardness in a gas metal arc weld in 2024 aluminium alloy. Widths of the weld fusion zone (FZ), near heat-affected zone (NHAZ), far heat-affected zone (FHAZ) are indicated. The magnitude of the residual stress in the weld is limited by the variation in yield strength brought about by the thermal effects of welding [17].

While simple in concept, residual stress formation in welds is quite difficult to predict quantitatively. The main problem is that since the process includes coupled thermal and mechanical components, the number of input variables involved is large [18]. A list of factors affecting residual stress would include: the geometry of the welded object, its thermal history, its (temperature-dependent) material properties, its phase transformations and metallurgical phenomena, and its mechanical boundary conditions. Over the last forty years, researchers have used numerical models of increasing complexity to study the process. Today, the use of the finite element method is dominant and modelling of welding residual stresses can be considered a relatively mature field, which finds substantial industrial application [19]. An example finite element mesh for a welded object is shown in Figure 4.
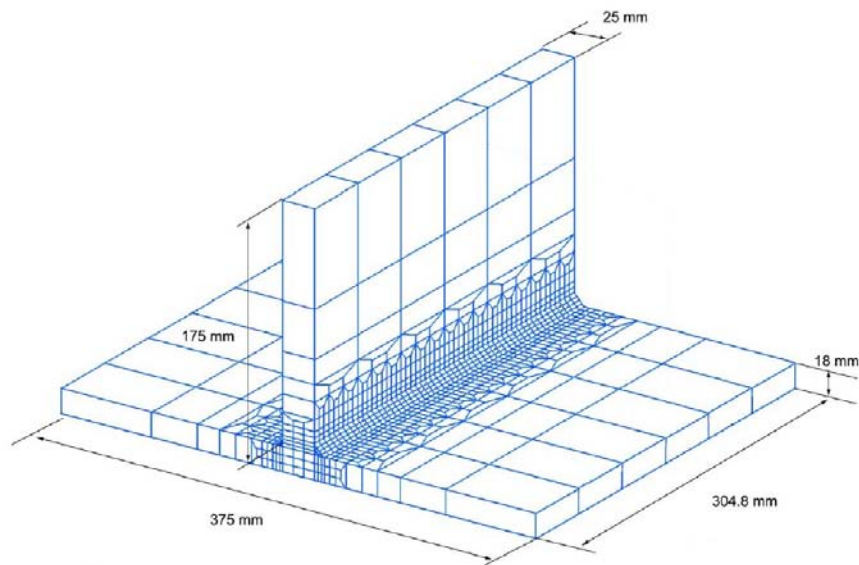
Figure 4: Finite element mesh for modelling of residual stress formation in a welded T-joint [20]. Note that the mesh density is much greater around the weld seam, where large temperature and deformation gradients are expected.

Despite recent advances in computing power, in most practical cases it is necessary to take advantage of the fact that the coupling between some of the different physical processes involved is quite weak (see Figure 5), by solving these different parts of the problem separately [19, 21]. For example, in an arc weld the heat generation due to material plasticity and viscoelasticity is usually small compared with the thermal energy transferred by the arc, i.e. the mechanical process only weakly affects the thermal one. However, the thermal field has a large mechanical effect via thermal dilation, so most models calculate the complete temperature history first, ignoring internal heat generation, and then use this to determine mechanical effects. By extending this concept and using judicious consideration of the coupling between different physical processes, it is also possible to consider mechanical and material changes at different length scales and throughout consecutive manufacturing processes: recent examples of this have been discussed by Hattel [22]. Introductions to contemporary weld modelling methods are given by Michaleris [21], Lindgren [19, 23] and Goldak and Akhlaghi [24], while further discussion of the formation of residual stress during welding can be found in the textbooks by Masubuchi [25] and Radaj [26], and an introductory article by Nitschke-Pagel and Wohlfahrt [27].
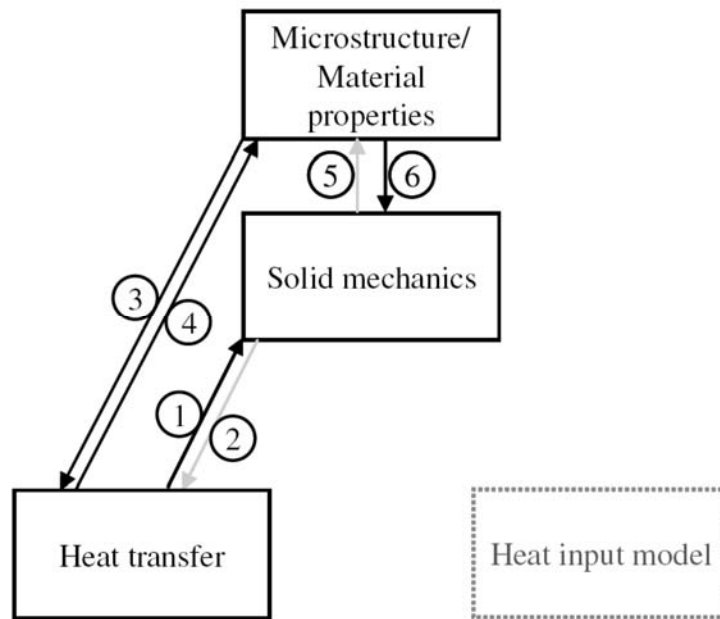
Figure 5: Coupling between the different physical processes involved in thermo-mechanical modelling of a weld. Strong couplings are indicated by black arrows, while weaker couplings are grey. 1. thermal expansion causes deformation, 2. heat generation due to irreversible deformation changes temperature, 3. latent heat and material thermal properties affect heat transfer, 4. temperature affects microstructure, 5. deformation affects microstructure, 6. mechanical properties depend on microstructure [19].

Effects of welding residual stresses

Of the many mechanisms which can lead to material failure, most are affected by the presence of residual stress. A thorough review of this subject has recently been provided by Withers [4], but a few of the most important effects of welding-related stresses are outlined below.

Fracture and fatigue

Residual stress is known to affect both the static fracture and fatigue properties of welded joints. In general, the superposition of a residual stress field with one due to external loading modifies the stress intensity at crack tips and hence the crack driving force [28, 29, 30, 31]. Indeed, in the prediction of weld fatigue lifetimes, it is commonly assumed that the large tensile stresses which may be present in the weld region dominate over the effect of the mean stress applied during the loading cycle [32]. However, while residual stresses affect fully elastic fracture and high-cycle fatigue significantly, they have much less influence over ductile failure because they are rapidly accommodated by plastic deformation [33, 34, 35]. Several researchers have recently suggested that residual stress may also have a noticeable effect on ductile tearing resistance [31, 36], but currently the mechanism for this is unclear.

Fatigue cracks often initiate at an object's surface, and they require tensile stresses to propagate. Therefore, near-surface tensile residual stresses tend to accelerate fatigue

cracking, while compressive stresses hinder it [37]. Consequently, many fatigue-life improvement methods such as shot peening and autofrettage rely on creating compressive residual stresses in areas most at risk. Of course, since residual stresses must be self-equilibrating, corresponding tensile stresses must also exist somewhere. In the example of shot peening, compressive stresses are only induced in a thin surface layer (typically < 1 mm) [38], while the corresponding tensile stresses form further into the material. Welding, by contrast, tends to result in large tensile residual stresses throughout the weld thickness, which equilibrate with opposing stresses situated further away from the joint [39]. As a result of this, both methods which induce compressive surface stresses and methods which reduce stresses through the entire weld thickness may be used to improve fatigue life of welds.

As well as causing residual stresses, welding also causes microstructural change and geometric stress concentrations [40, 41, 42]. Both of these factors can also affect fatigue, which complicates the study of welding residual stresses with respect to fatigue life [43, 44]. Furthermore, residual stress distributions can themselves be changed by in-service loading conditions, generally by yielding during the first loading cycle [37, 45].

Stress corrosion cracking

Stress-corrosion cracking (SCC) is a form of environmentally-assisted material failure which occurs when the combined effect of chemical and mechanical driving forces causes gradual crack propagation throughout the affected material [46]. Since both chemical and mechanical factors are involved, only materials exposed to particular corrosive environments while under mechanical stress are susceptible to SCC. The residual stresses left behind by welding are often sufficient to initiate SCC in areas where it would not otherwise occur due to the lack of a sufficient mechanical driving force [47]. Furthermore, welding can also cause geometric stress concentrations and increased metallurgical susceptibility to corrosion [48], so SCC frequently initiates at welded joints. This causes serious problems in applications (such as gas pipelines and nuclear reactor components) where welded parts are used in a corrosive environment [49, 50], often necessitating costly inspection programmes to prevent this 'insidious' form of failure.

Distortion

By definition, the residual stress field within an object is internally self-equilibrating. For a stress distribution to exist in the absence of any externally-applied force or temperature differential, there must be an internal incompatibility in strain[4] [51, 52].

---

[4] This incompatibility is variously referred to by researchers as 'eigenstrain', 'inherent strain' and 'misfit strain'.

Therefore, when residual stress is added or relaxed during any manufacturing process, there must also be a corresponding inhomogeneous deformation. Residual stresses due to welding, for example, are associated with strains which when accumulated along the length of a weld seam, can often cause visible warping of a welded object. This distortion is by far the most evident and frequently the most problematic effect of residual stress. Small residual strains due to plastic deformation at the weld seam cause different modes of distortion, originally categorised by Masubuchi [25], depending on the weld and object geometry. In addition to shrinkage and bending-type distortion modes, welds in thin-walled structures often produce residual stresses large enough to cause buckling, which can complicate distortion analysis and prediction [53].

The implications of welding distortion for manufacturing (aside from those related to other effects of residual stress) are of great practical concern [54, 55], and have led to the development of a host of techniques specifically to prevent distortion, without aiming to remediate the underlying residual stress. These include bending-back of distorted weldments, presetting [56], control of mechanical constraint [57, 58, 59], control of weld sequencing [54, 60, 61], and flame straightening. An example of the effects of varying mechanical constraint is shown in Figure 6, and such methods of distortion control are discussed further by Conrardy and Dull [62] and Masubuchi [25].

a.   b.
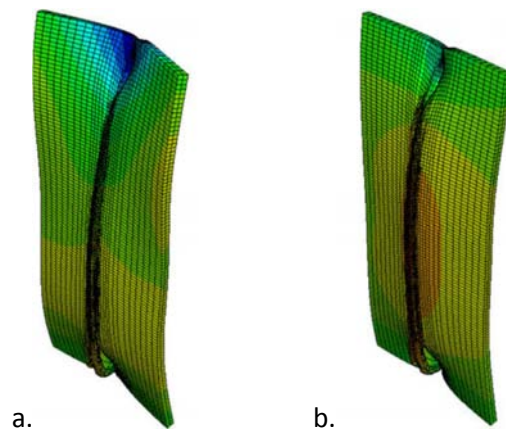
Figure 6: Predicted distortion of a dual-phase steel overlap weld with clamping released a. immediately after welding, b. once the weld has cooled to room temperature. Out-of-plane displacements magnified 50x [63].

Measurement

Techniques for measuring residual stress have been recently discussed by Rossini et al. [64] and Withers et al. [65], but briefly, three fundamental strategies exist:

1. Measuring the change in strain as residual stresses are relaxed by removal or cutting of material.
2. Measuring the inter-atomic spacing and comparing this to the spacing in an unstressed reference specimen.

3. Measuring the change in another physical phenomenon with which stress interacts.

Practical implementations of the first option include the hole-drilling method, in which stresses are back-calculated from strain measurements made near a small hole as it is drilled [66, 67], and the contour method [68], where accurate measurement of the profile of a cut face is used to reconstruct a map of the residual stresses before cutting. Of course, all such 'relaxation' methods are at least partially destructive to the sample; such techniques are the subject of a recent review by Schajer [69]. The second option is possible because the inter-atomic spacing in a crystalline material changes in response to applied stress – a fact which is reflected in the elastic strain response of the bulk material. Therefore, by using x-ray or neutron diffraction to measure the crystal lattice-spacing, strain can be measured non-destructively in (polycrystalline) metals and ceramics, and from this the stress state can be calculated. For the final method, it is possible to use changes in the sonic and magnetic properties of some materials to measure stress. For example, the configuration of magnetic domains in ferromagnetic materials is sensitive to stress, and so residual stresses can be inferred from (calibrated) measurements of magnetic Barkhausen noise [70]. However, the effect of residual stress on these properties is not well understood and is often relatively weak in comparison to the effect of other factors (eg. microstructure), so these techniques are normally used only for comparative measurements [1].

To measure residual stresses produced by welding, diffraction using neutrons or high-energy synchrotron x-rays is currently favoured by researchers. These methods have been developed to a point of practical and quantifiable accuracy, and can be used at a range of spatial resolutions conducive to the study of engineering structures. Furthermore, usable quantities of neutron or synchrotron radiation can penetrate deeply (in the order of tens of mm) into most common metals, and can therefore be used for measurement at locations which cannot be probed by other means (see Figure 7). Unfortunately, these methods can only be performed at a small number of neutron and synchrotron facilities, and are therefore not suitable for common use in industry. Neutron techniques are discussed by Krawitz [71] and Withers [4], and synchrotron diffraction by Reimers et al. [72]. Diffraction of lower-energy x-rays (produced using conventional x-ray tubes [73]) is more widely used due to its accessibility and relative accuracy. However, a major drawback is that the penetration depth of this radiation is low, and so only stresses close to the surface of the material (conventionally, within a few tens of microns) may be measured.
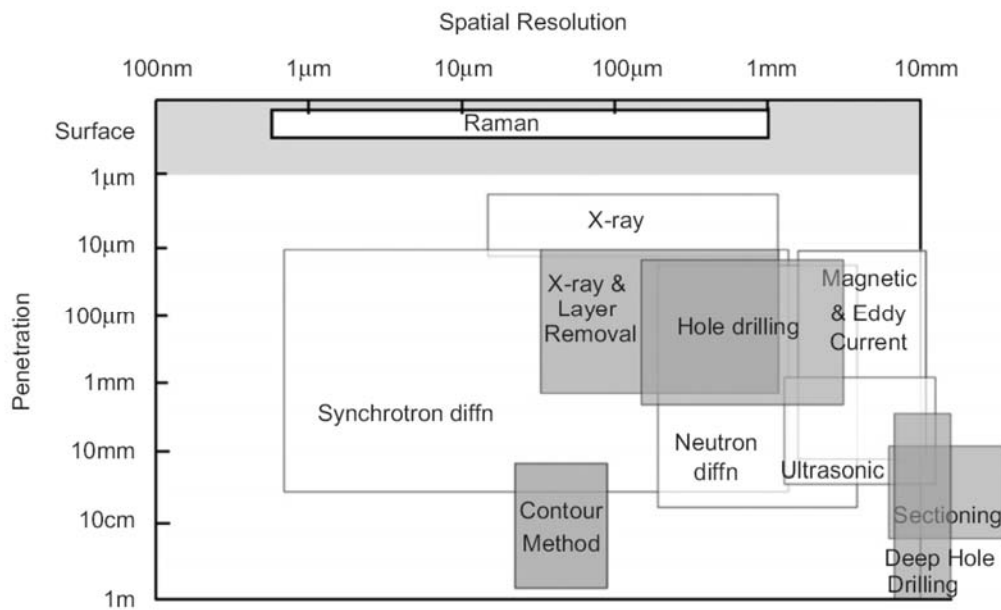
Figure 7: Approximate capabilities, in terms of spatial resolution and penetration depth, of different residual measurement techniques [65].

Reduction of welding residual stresses

Overview

A wide variety of techniques are available for the reduction or modification of residual stress distributions in bulk materials. Some of these, such as annealing and peening processes have been adapted or optimised for use on welded joints. However, there also exist welding-specific methods such as in-process cooling and Global Mechanical Tensioning (GMT), which are designed to work against the particular thermal strain mechanism of residual stress formation which exists in welding, or against the particular distributions of residual stress which welding produces. These methods have received increased attention over the past two decades, as researchers seek cheaper and more effective alternatives to long-standing techniques.

To cause a change in the residual stress state in an object, a permanent plastic deformation must be introduced, or the occurrence during welding of such a deformation must be influenced. This can be done by using an externally-applied mechanical force, by the application or modification of a thermal field, or by inducing a solid-state phase transformation. It is therefore possible to categorise residual stress modification strategies into three broad groups based on these three mechanisms of action. Here, welding residual stress mitigation methods have been further categorised into 'conventional' techniques, which currently see widespread application, and 'advanced' techniques which are mainly at the experimental stage of development and not commonly encountered outside of research. Additional reviews of the application of stress engineering techniques to welding can be found in works by Radaj [26], Feng

et al. [74], Withers [1], Williams and Steuwer [75], and Altenkirch [76], while a helpful guide to early work on the topic from the USSR is provided by Pavlovsky and Masubuchi [77].

Conventional thermal techniques

Post-weld heat treatment
Stress-relief annealing involves heating an object uniformly, normally to several hundred degrees above ambient temperature, to allow residual stresses to relax automatically. Application of this procedure to welded joints, which is known as Post-Weld Heat Treatment (PWHT), is a very commonly accepted method of residual stress relief and has been shown to be effective for this purpose under a wide range of circumstances [78, 79, 80, 81, 82]. Primarily, the reduction in yield strength at high temperature causes the material to yield locally under its own internal stresses, however it is also believed that in many cases additional deformation can be caused by creep and recrystallisation [83, 84, 85]. After the stress has been relaxed, gradual and uniform cooling is used to prevent subsequent stress formation. Depending on the material, sufficient stress-relief may take place at below the temperature required for any change in microstructure, but typically diffusional processes or even gross recrystallisation will also occur [1, 26]. Often this is a welcome side-effect; in carbon-manganese steel weld zones containing brittle phases (particularly martensite) generated during rapid cooling of the weld metal, tempering which occurs during PWHT can act to restore fracture toughness.

Though it is effective at reducing residual stress in most bulk metals, PWHT is not universally applicable. For example, PWHT is not normally applied to precipitation-hardening alloys due to the risk of over-aging the parent metal[5]: temperature-controlled diffusion acts to coarsen the precipitate distribution, reducing the precipitate's effectiveness at impeding dislocation movement. Likewise, in dissimilar-material welds, mismatch between different thermal expansion coefficients can cause PWHT to be ineffective, or even detrimental [86, 22]. The application of PWHT can also cause a form of brittle failure known as stress-relief cracking or reheat cracking, in which thermally-induced embrittlement leads to cracking as high-temperature yielding or inter-granular creep occurs [87]. Finally, the process becomes both expensive and time-consuming when large components are involved.

Control of heat input during welding
The energy input per unit length of weld made obviously has a pronounced effect on the distribution of temperature in the material [88]. This can in turn affect both the

---

[5] The weld itself and the surrounding heat-affected zone will typically be over-aged anyway after the welding thermal cycle.

weld microstructure and the formation of residual stresses. Unfortunately, the need for a sufficient temperature at the joint interface to allow material bonding puts a practical limit on the amount by which heat input can be reduced. The heat input is further constrained by factors relating to the welding process itself: in laser welding for example, reducing the heat input will eventually cause transition of the process from keyhole to conduction mode[6]. Therefore, control of welding heat input can never completely prevent residual stresses from forming, but it can reduce the width over which plastic strain (and hence tensile residual stress) occurs [12, 16].

Uniform preheating of the weld region is widely employed to reduce the large thermal gradient necessary to enable fusion at the weld interface, which is the cause of three common problems: 'hot cracking' (thermal fracture which can occur during the welding of brittle materials), the formation of brittle martensite due to rapid cooling of the weld material, and residual stress. Preheating the weld region may also be used to dry the surface of the material, which is sometimes necessary to prevent hydrogen embrittlement - a common symptom of excessive hydrogen absorption in high-strength steel welds [89]. However, due to the decreased yield strength of the parent material at elevated temperature, preheating can also allow increased plastic deformation, having a detrimental effect on residual stress [90]. Therefore, though it may reduce residual stresses in some material/thermal cycle combinations, preheat cannot be considered a universally effective method of residual stress control.

Conventional mechanical techniques

Peening
Peening describes a set of dynamic processes which use impact or the propagation of shock waves to cause deformation. The object of applying peening to a surface is to create an inherent strain which results in a compressive state of residual stress there. This compressive state of stress is equilibrated by tensile stresses deeper within the bulk of the material. While hammer and shot-peening of welds have long been practiced, similar treatments such as needle, ultrasonic and laser shock peening are becoming more widespread [91, 92]. As in many other applications, peening is used to improve the fatigue life of welded joints, since the compressive residual stresses which it introduces inhibit fatigue crack propagation from the material's surface [93, 94, 95]. Impact indentations can also smooth imperfections in the shape of the weld toe (see Figure 8), reducing stress concentrations and hence further increasing fatigue life [96].

---

[6] There are normally considered to be two distinct modes of laser welding. In keyhole mode, continual vaporisation opens a 'keyhole' in the material, which allows a very deep and thin weld cross-section. In conduction mode, material vaporisation is insufficient to sustain a keyhole, resulting in a wide and shallow weld [257].

Figure 8: Ultrasonic peening being applied to a steel weld toe [92].

Due to their impactive nature, and the need for stresses to equilibrate over the thickness of the peened object, peening processes typically produce a compressive stress distribution only to a limited depth of penetration [38, 92, 97]. Since residual stress due to welding usually exists throughout the thickness of the joined material, peening cannot normally be said to remove welding residual stresses but rather to superimpose an additional, protective residual stress distribution. Consequently, peening does not protect against crack propagation from internal defects, and residual stress which exists deeper in the material may still cause distortion of the welded object.

Vibratory stress relief

The difficulty and cost involved in applying PWHT, especially to large assemblies and castings, led to the development of Vibratory Stress Relief (VSR) during the Second World War [98]. In this method, the welded object is simply vibrated strongly using motorised or electromagnetic equipment. Despite many years of research, there is still disagreement over the fundamental mechanism by which this acts to reduce stresses, or indeed whether it has any significant effect at all [99, 100]. It has been proposed that VSR provides a driving force for dislocation movement at the intra-granular level [101], or even that it initiates a martensitic transformation in steels [102]. However currently the most widespread view is that under some conditions, VSR may cause local plastic deformation in the regions of material which, due to the presence of residual stress, are already close to their yield point. This theory explains both the gradual nature (i.e. occurring over many vibration cycles) of observed strain changes, and the apparent presence of a critical vibration amplitude, under which no stress relief will occur [103, 104, 105]. One implication of this idea is that cyclic plasticity occurs during the process, which might negatively impact the subsequent fatigue lifetime of any treated component. Despite recent advances in residual stress

measurement techniques there is still a lack of published data on the topic of VSR, and so its efficacy and theoretical basis remain controversial.

Advanced thermal techniques

Localised cooling

By manipulating the distribution of temperature in a component as it is welded, localised cooling aims to modify or generally reduce the final pattern of residual stress. The earliest experiments were carried out in the 1960s in support of NASA's Saturn programme [106]. Although several cooling arrangements have been suggested, most modern experimenters have used an intense heat sink trailing the welding heat source to create a characteristic valley-shaped temperature distribution[7] [107, 108, 109, 110, 111], shown in Figure 9. An example of a cooling device designed to achieve this is shown in Figure 10. Guan et al. [112] originally proposed that this can prevent the formation of a single wide region of tensile residual stress at the weld line, instead creating a more complex distribution of stress consisting of several local maxima and minima. The mechanism of thermal strain by which this comes about was subsequently explained by van der Aa et al. [110] and Richards et al. [111], using numerical modelling.
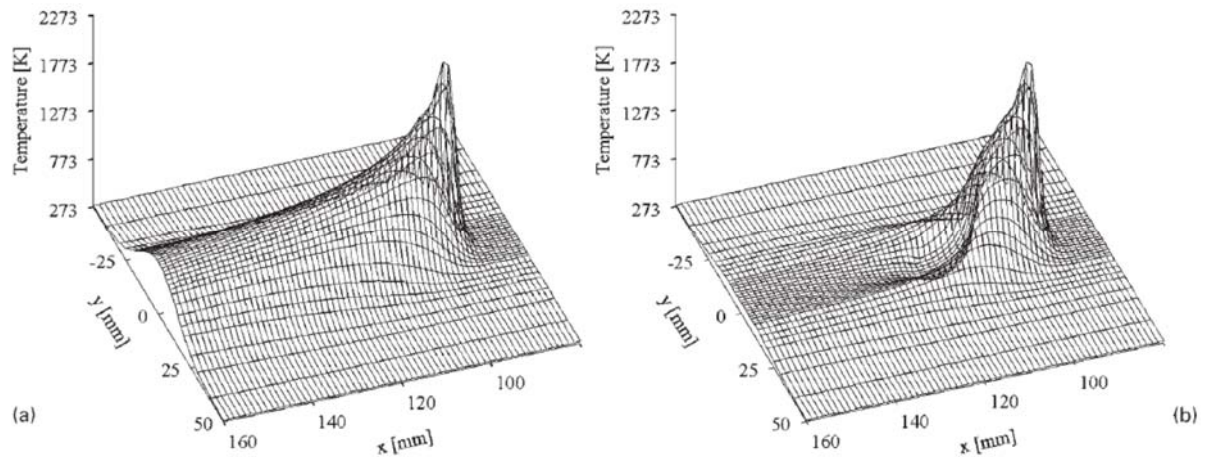
Figure 9: Simulated temperature distributions in thin aluminium alloy sheet: a. conventional arc welding, and b. arc welding with a trailing heat sink [110]. The arc is located at x = 100 mm and is moving in the negative x-direction.

---

[7] Following the convention of Guan et al. [258], this process is alternatively referred to as Low Stress No Distortion (LSND) welding.
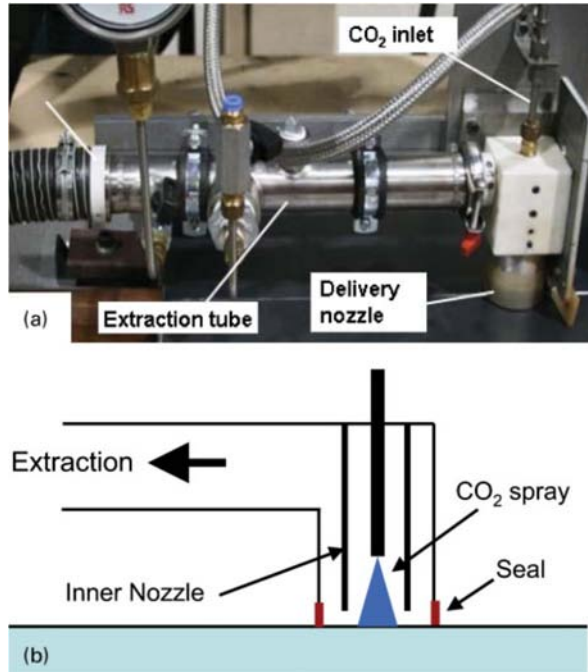
Figure 10: Nozzle arrangement for cryogenic cooling of the weld seam during welding, allowing continuous delivery and extraction of CO_2 spray [111].

Efforts to model the process agree that relief of residual stress is greatest with a very localised and intense cooling source, positioned as close behind the welding heat source as possible (see Figure 11) [110, 113, 114, 111]. Various researchers have used different cooling media: solid CO_2 'snow' [115, 116, 117] and argon-atomised water [108] have featured in recent studies. Liquid nitrogen has also been suggested as a suitable coolant [111, 118], however it does not appear to have been tested experimentally in any study to date. Further reviews of available literature on in-process cooling are given by Bagshaw et al. [119], van der Aa [117] and Richards [120].
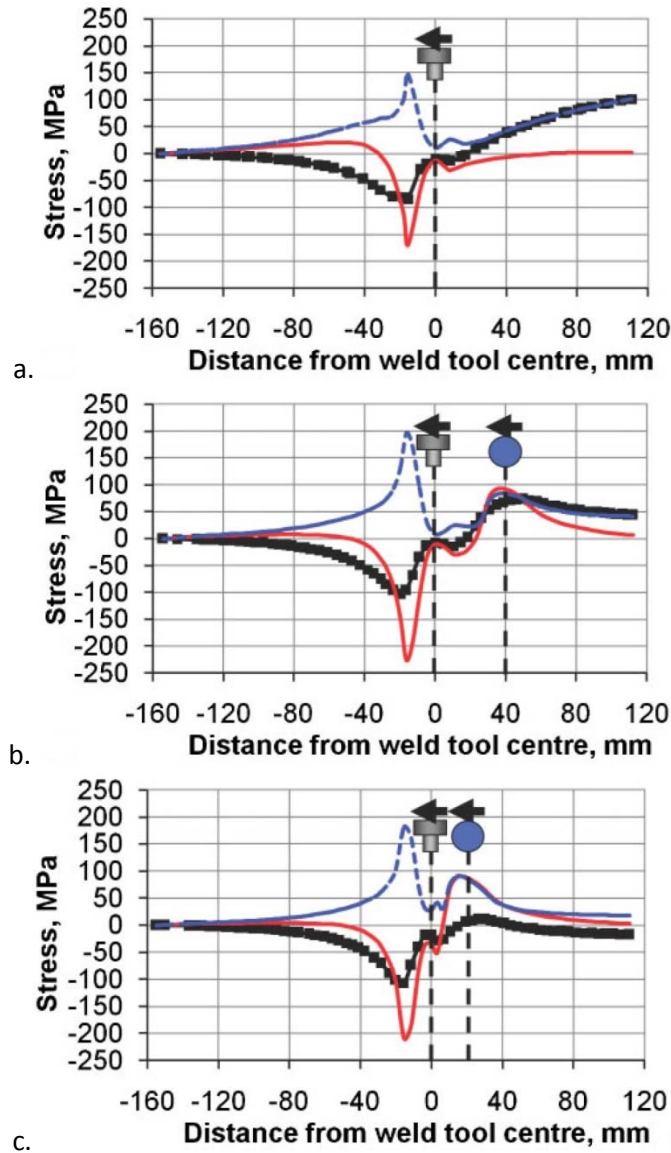
Figure 11: Effect of cooling source position on stress development during friction stir welding of aluminium alloy with localised cooling: a. no cooling, b. trailing the welding tool by 40 mm, c. trailing by 20 mm. The black line with squares represents the longitudinal component of stress, the solid red line is the transverse component, and the dashed blue line is the von Mises stress [111].

Localised heating

As with localised cooling, a number of schemes of in-process heating have been investigated, with the intention of modifying the stress distribution in the vicinity of the welding heat source [121, 122]. Most researchers describe how the process creates a tensile stress in the longitudinal direction during welding[8] [123, 124, 125]. The presence of a tensile stress during welding, and its subsequent removal due to temperature equilibration, has a similar effect to GMT (see section on GMT below); reducing the longitudinal strain misfit between the weld material and the parent

---

[8] For this reason, localised heating methods are often alternatively described as 'thermal tensioning' by some authors.

metal. An alternative mechanism was first investigated by Greene and Holzbaur, who pioneered this form of stress-relieving during the latter part of the Second World War [126]. They used localised heating adjacent to the weld after it had been completed to overstress the weld material - yielding it, and removing the tensile residual stress (Figure 12c).

In practice, thermal tensioning can be carried out either by creating a transverse thermal gradient simultaneously along the entire length of the weld ('steady-state thermal tensioning', Figure 12a), or by using moving heat sources to create a stressed region around the welding tool only ('transient thermal tensioning', Figure 12b) [127]. For transient tensioning, a suitably intense heat source is required, and various researchers have investigated the use of flame heaters [123, 125, 127], laser spots [114, 121], and induction heaters [128] for this purpose. Of course, in all cases the mechanism by which the stress state in the weld is changed (via thermal dilation of part of the material), is fundamentally the same. Reporting of the level of residual stress reduction achievable using this method has been quite mixed, however, ranging from 21-32% [123] to 74% [129] in experimental studies.
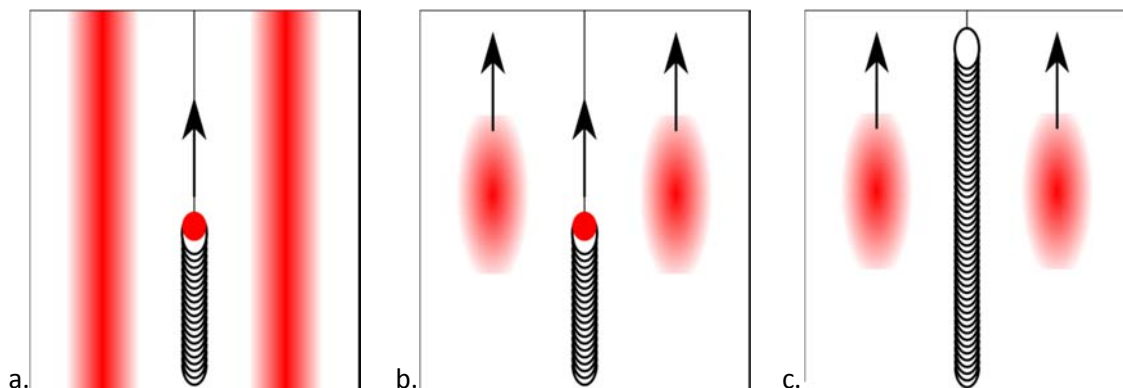
Figure 12: Localised heating methods: a. steady-state thermal tensioning, b. transient thermal tensioning, c. post-weld thermal overloading. The welding arc (red circle) and additional heated regions (diffuse red areas) are shown.

Advanced mechanical techniques

Rolling

Through the application of a large compressive force to the material's surface, localised high-pressure rolling of welded joints causes yielding of metal in the weld region, relieving the large residual stresses which exist here [130, 131, 3, 132]. In most systems, this is achieved using a single narrow roller applied directly to the weld line, with the material backed by a rigid surface. However, rolling the weld seam between a pair of rollers has also been described [130, 133, 134, 135, 136]. An obvious limitation of the process, therefore, is that both sides of the weld must be accessible so that the underside of the weld may be supported during rolling.

Both rolling *in situ* (i.e. during welding), and post-weld have been studied. Recent experimental and modelling studies indicate that post-weld rolling gives a far greater reduction in the residual stress field [3, 132, 137], however the reason for this is not currently clear. An example of the residual stress reduction caused by application of post-weld rolling to a friction stir weld is shown in Figure 13. The temperature of the rolled material does however determine both the amount of plastic deformation that is possible for a given roller load [76, 136], and the material microstructural response to the process [138, 139, 140, 141]. A future application of *in situ* rolling may therefore be to improve weld microstructure by hot deformation. It has been suggested that tandem systems for *in situ* rolling, where the first roller produces a large deformation at high temperature and the second work-hardens the material when it is cooler, may be advantageous. While this method was investigated by researchers working in the USSR, it has not been attempted in any recent work [139, 140].
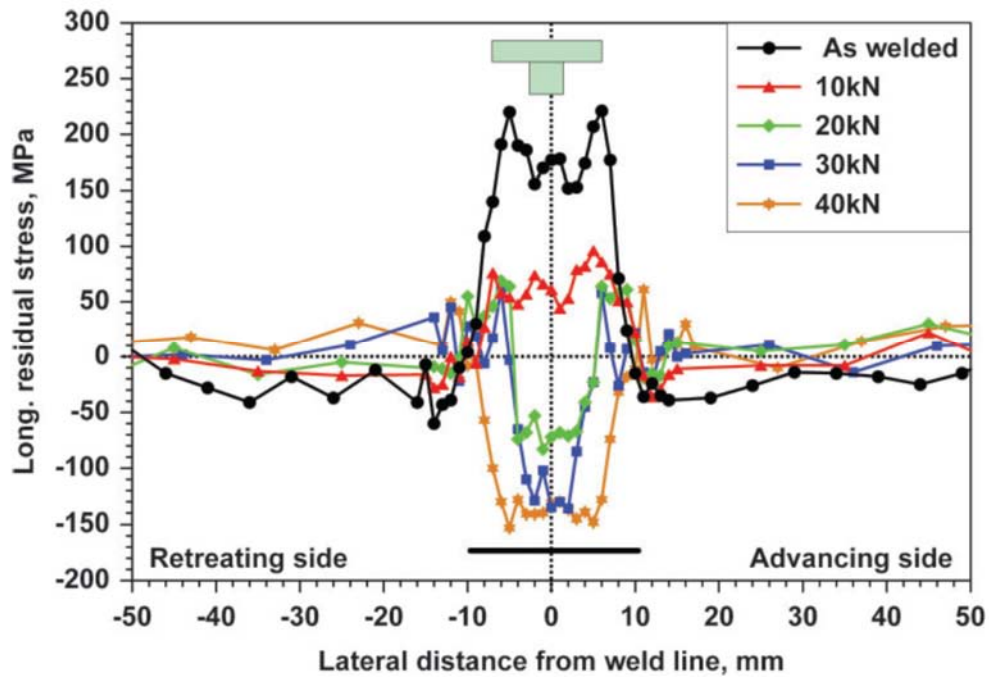
Figure 13: Synchrotron x-ray measurements of the longitudinal residual stress distribution resulting from post-weld rolling of friction stir welds at different levels of roller force [3]. The widths of the FSW tool (above plot) and roller (below plot) are shown.

Global mechanical tensioning

Global Mechanical Tensioning (GMT), shown in Figure 14a, involves stretching material in the direction of the weld line to cause a longitudinal tensile stress throughout it during welding [142, 143]. The mechanism by which this reduces the residual stress is summarised by Richards et al. [14, 120]. Essentially, the magnitude of the tensile longitudinal stress which can exist at the weld is always limited by the yield strength of the weld material. By tensioning the surrounding material to an appreciable fraction of

this, the mismatch in strain between these two regions can be reduced or even reversed. When the tensioning is released after welding, this results in a corresponding reduction in residual stress.

Depending on the longitudinal tensioning load used, GMT can greatly reduce residual stresses at the weld line, or even introduce compressive stresses in this region [144, 145, 146, 147], see Figure 14b. For welds in 2000-series aluminium alloy, the magnitude of tensioning stress that must be applied during welding to reduce the longitudinal residual stress to approximately zero, has been reported as 25-40% of the room temperature yield stress of the parent material [145, 147]. GMT therefore requires expensive tensioning equipment to apply this large force. Additionally, since the force needs to be applied in the same direction as the weld line, application to complex welds would be very difficult. Consequently, the applicability of GMT to practical industrial processes has not yet been demonstrated [144].

Figure 14: a. Equipment for GMT, b. longitudinal residual stress in three aluminium alloy friction stir welds with GMT at different levels of tensioning (synchrotron x-ray diffraction measurements). The magnitude of the applied stress is given as a percentage of the room-temperature yield stress of the parent material [145].

Weld material transformations

Transformations between different solid material phases are often accompanied by significant deformation. Consequently, transfor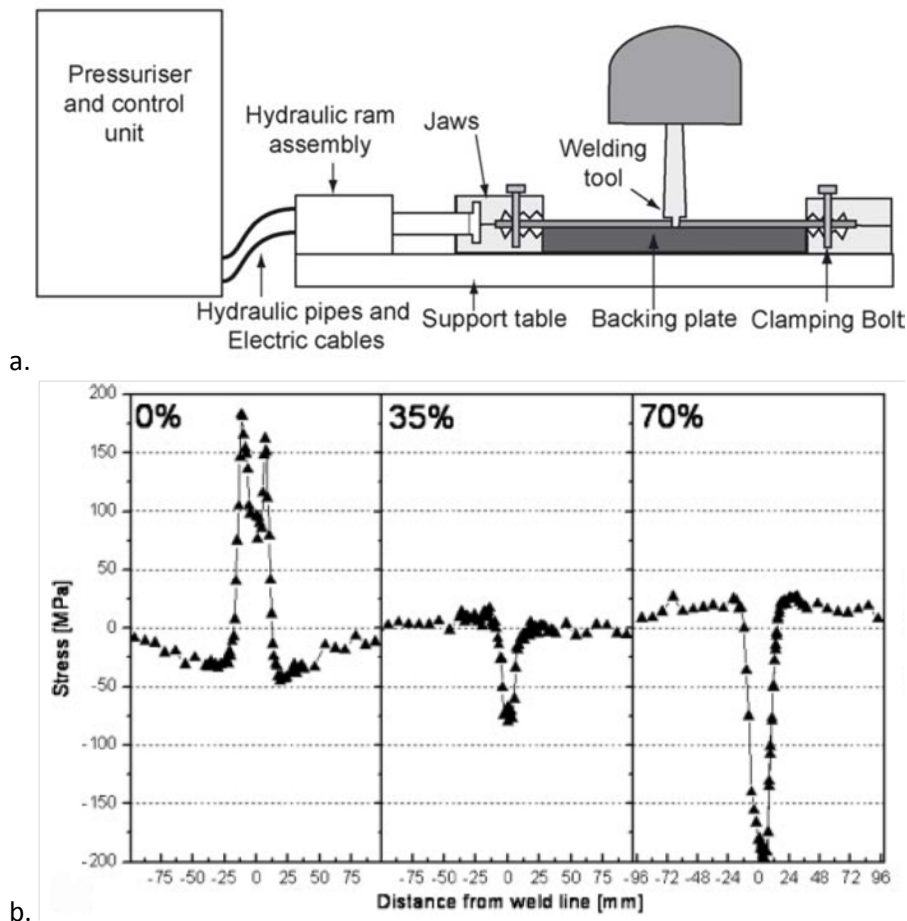mations encountered during the welding thermal cycle can significantly affect the formation of residual stress [148, 149]. A discussion of the stress/microstructure relationship in the context of welding is given by Bhadeshia [150].The effect was investigated in the 1970s by Satoh [151] and Jones and Alberry [152], who measured the stress induced in constrained steel specimens as a thermal cycle was applied. Of particular interest are the austenite → martensite and austenite → bainite transformations; these displacive transformations, which (in carbon steels) often occur during the cooling of the weld metal, are associated with a dilational strain that can be used to counteract the thermal contraction which causes tensile residual stress[9].

To prevent the accumulation of tensile residual stresses, the material of the weld must be carefully chosen so that it undergoes a transformation at the correct point in the thermal cycle. It is generally taken that the transformation should occur at a temperature low enough to preclude subsequent build-up of stress, but should be complete by the time the metal cools to room temperature[10] [153, 154]. Figure 15 shows schematically the effect of different phase transformations on the build-up of stress in uniaxially-constrained steel specimens as they are cooled from 1000°C. The austenite → ferrite transformation (a) takes place a too high a temperature to have a great effect on the residual stress: thermal contraction continues after the transformation, and the tensile stress resulting from this saturates at the yield strength of the material. On the other hand, lines (b) and (c) show the effect of bainitic or martensitic transformations taking place at a lower temperature. In both cases, while the transformation is complete by the time the material has cooled to room temperature, varying the transformation temperature affects how much thermal contraction can occur subsequent to transformation.

---

[9] During both the martensitic and bainitic transformations the shear component of lattice deformation is far greater than the dilational component (approximately 0.25 versus 0.03)[259]. During the formation of bainite, it has been shown that in addition to the relaxation of tensile stresses by dilational lattice deformation, there is also preferential growth of the new phase in crystallographic orientations which accommodate the applied stress [156, 260, 233]. This allows the shear component to influence the stress state too, however the extent to which this may be deliberately controlled is not currently known.

[10] Although an incomplete martensitic transformation is not necessarily detrimental to the residual stress state, large amounts of untransformed austenite could seriously reduce the material's mechanical properties [261].
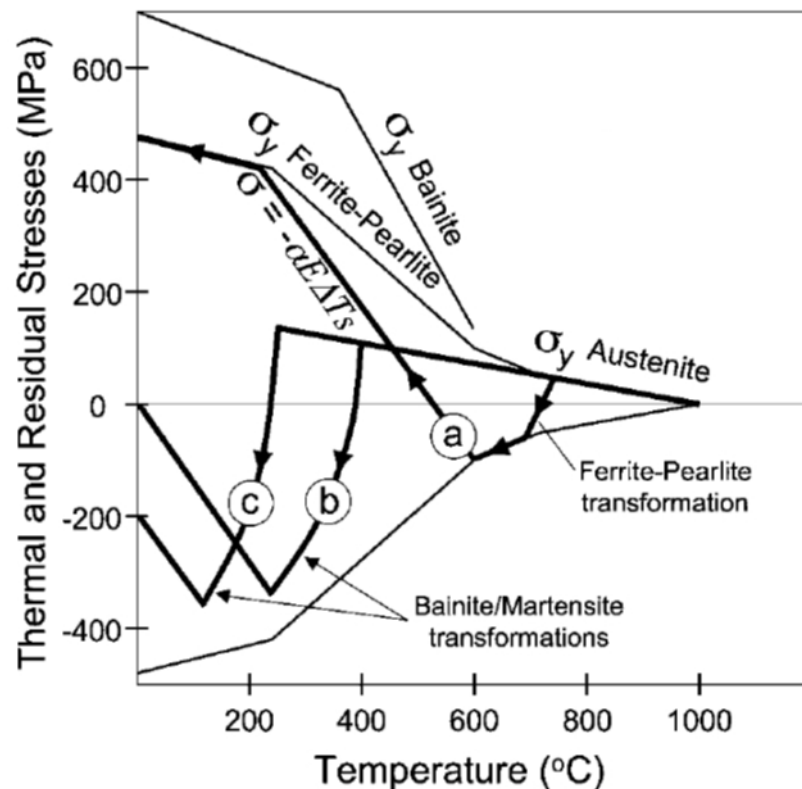
Figure 15: Thermal stress development during the cooling of axially-constrained specimens of different steels: a. is ferritic-pearlitic, whereas b. and c. exhibit bainitic or martensitic transformations ([47], after [27]).

 Since the majority of common welding processes involve the addition of filler material at the joint interface, there is an opportunity to take advantage of transformation effects at the interface only, without changing the material used for the rest of the welded structure. Recently, there has been a concerted effort to design weld filler metals which reduce residual stress while maintaining acceptable mechanical properties. Most researchers have concentrated on the martensitic transformation, using additional carbon and/or a combination of nickel and chromium (in quantities up to about 15 wt.% each) to reduce the temperature at which martensite begins to form [155, 156, 157]. Unfortunately, the increased carbon content and presence of brittle martensite can give low-transformation-temperature weld material reduced impact toughness [154]. Therefore, while the effectiveness of this approach for reducing residual stresses has been demonstrated in several studies [154, 156], further research is needed to simultaneously achieve excellent mechanical properties. A final important limitation of low transformation temperature materials is that they can undergo significant transformation strain when reheated, the effects of which would have to be carefully considered if such materials were ever to be used in elevated-temperature service.

27

Discussion

Mechanisms of stress reduction

The fundamental physical phenomena (such as thermal transport, solid mechanics and phase transformation) which underpin the formation of welding residual stress are individually well-understood. The complex interaction of these processes during welding is difficult to observe and predict, but at the same time means that there are number of possibilities available for residual stress reduction. Consequently, it has been seen here that thermal, mechanical and phase transformation mechanisms can be used to affect the residual stress state in a welded joint. However, in the case of most materials none of these mechanisms are fully independent of the mechanical properties: thermal methods can change the proportion of metastable phases present, cold deformation causes strain hardening [3], and methods based on filler metal transformations normally require a change in both the phase fraction and material composition away from their 'ideal' values (see Table 1). It is therefore likely that as research into residual stress reduction progresses, there will be continued specialisation of these different methods towards different material applications. For example, mechanical deformation is well-suited for use on low carbon steels since these do not strain-harden excessively. Localised cooling methods, by contrast, could cause unwanted formation of brittle martensite in some steels, and are therefore more suited to materials where this problem does not occur, such as Al-Cu alloy [117].

Table 1: Simplified overview of the metallurgical side-effects of welding residual stress reduction processes.

Class of process	Material parameters changed	Physical strengthening mechanisms most affected
Thermal	• Phase fraction • Microstructure	• Precipitation hardening • Transformation hardening
Mechanical	• Dislocation density	• Strain hardening
Phase transformation	• Chemical composition • Phase fraction • Microstructure	• Transformation hardening

Current state of the art

Ideally, designers of welded assemblies would have techniques at their disposal which could reduce the residual stress field effectively to zero, or induce any state of stress deemed beneficial (for example, to impart increased fatigue resistance), while being both cost-effective and versatile. Much of the progress which has been made towards this in recent years can be attributed, at least in part, to advances in both numerical and experimental methods - especially the use of neutron and synchrotron diffraction

for residual stress measurement [32]. However, accurate quantitative analysis of residual stress in welded objects remains a non-trivial problem. This means that generating 'feedback' for the design process of any stress-reduction technique is time-consuming and costly.

There is also no perfect way of introducing the inherent strain required to change the residual stress state. It is evident that some of the methods discussed above, especially those based on manipulation of the thermal field, are difficult to control. Most are also difficult to apply to stresses deep within the material, and can also have potentially detrimental effects on material properties. To compound this issue, stress is not a simple scalar quantity, but a tensor with six independent components varying over three spatial dimensions [158]. Therefore, imposing a desired residual stress in a particular direction or location may result in an undesirable one elsewhere.

Industrial awareness of welding residual stress has always been high. This can be attributed to the very visible nature of the distortion caused, and the occasional spectacular failures which occur when residual stress issues go unresolved. Residual stress relief is allowed for, and sometimes required, by most relevant national and international standards. However, this is almost universally in the form of PWHT, which remains by far the most accepted method. Other methods such as flame and induction heating are often used where PWHT is impractical [55], however all of the 'advanced' methods discussed here are still mainly at the experimental stage of development.

Prospect for future research

Arguably, the most successful fundamental studies into residual stress reduction mechanisms take a reductionist approach, using the simplest geometric cases so that the underlying processes can be more easily revealed. This is especially important when one considers that for even relatively simple cases the distribution of material properties, and the thermal and residual stress fields, may be quite complex. However in the practical application of these concepts, even more complex situations are common. For example, in multi-pass welds and additive manufacture, further thermal cycling during the subsequent deposition of additional weld metal causes secondary metallurgical transformations, and affects the residual stress in previous layers [26, 80, 159]. Driven by the practical need for stress-reduction techniques in industry, it is likely that a great deal of prospective research will focus on applying stress-reduction methods to these more complex cases.

Several of the techniques mentioned above are relatively new, and therefore the limits of their application are not well mapped. For example, the limit of material ductility at which post-weld rolling may be successfully applied is not currently known, and the

effects of rapid weld metal quenching during localised cooling (which, of course, vary greatly depending on the material used [117]) have not been fully explored. For these processes to be applied practically, there is a need for such limitations to be more fully understood.

Until relatively recently, experimental studies of welding residual stress and stress reduction methods have been confined to 'post-mortem' stress analysis, i.e. determining the residual stress state after a process has finished. Consequently, modelling has been the main source of information on the evolution of strain during the process itself. However, as neutron and synchrotron diffraction instruments continue to develop, there has been increasing interest in the use of diffraction techniques to study welding residual stress formation *in situ*. So far, the focus has been on observing the phase transformations which occur during weld metal cooling [156, 160, 161]. However, it is likely that in the near future, simultaneous *in situ* measurements of phase fraction and strain/stress will be important in understanding the interplay between microstructural evolution and residual stress.

Concluding remarks

Residual stress due to welding is an ongoing problem in engineering which affects multiple material and structural failure mechanisms. The current development of residual stress reduction technologies is driven by the high cost and inherent limitations of conventional processes such as post-weld heat treatment, and has been aided by continual advances in measurement methods and computer modelling capability. Since stress formation during welding is affected by thermal, mechanical and material factors, there has been a proliferation of different approaches to the problem based on these different physical mechanisms. Some techniques (notably the mechanical methods – rolling and global mechanical tensioning) have been proven capable of comprehensively changing the distribution of stress in a weld, but all come with their own practical limitations. Consequently, it is likely that a greater degree of specialisation will occur as these processes develop, since each is more suited to particular materials and applications.

Using the processes described above, some very encouraging results in terms of the residual stress distribution have been achieved in recent years. It is now necessary to consolidate such results with research into the accompanying material properties and microstructure, to show that these new stress reduction techniques can be safely applied to structural welds outside of the laboratory.

Chapter 3: Measurement of the biaxial thermal stress field during arc welding

The majority of this chapter is taken from the following article:

> H. E. Coules, P. Colegrove, L. D. Cozzolino and S. W. Wen. Experimental measurement of biaxial thermal stress fields caused by arc welding. *Journal of Materials Processing Technology*, 212(4): 962-968, 2012.

Abstract

The strain field within thin steel plates during gas metal arc welding has been studied using resistance strain gauges and digital image correlation, allowing the initial formation of stresses around the weld seam to be observed. Major features of the transient stress field have been identified, and are explained with reference to the underlying thermal and mechanical processes. A comparison of stresses occurring during bead-on-plate and butt welding shows they are very similar. The assumptions and limitations associated with determination of the stress state are addressed, and the application of such methods to the problem of reducing welding residual stresses is discussed.

Introduction

Nearly all welding processes induce significant residual stresses due to constrained expansion and contraction of material under the influence of a non-uniform thermal field. The highest stresses occur in the region around the joint interface, where the highest temperatures (and temperature gradients) are experienced. Here, both the loading due to thermal expansion and contraction, and the softening of material due to elevated temperature during the welding thermal cycle are most pronounced. These central stresses are generally highly tensile in the longitudinal direction of the weld, and are counterbalanced by compressive stresses further away from it [2].

A variety of experimental methods including neutron diffraction, x-ray diffraction and mechanical strain-relaxation techniques are frequently used to study welding residual stresses [65], however most of what is known about the transient stress and strain fields, which occur during the welding process, comes from Finite Element (FE) modelling rather than direct measurement. Since FE models typically need to simulate the entire thermal-mechanical history of the process to arrive at accurate values of residual stress, even early models of welding such as those by Ueda and Yamakawa [162] and Muraki et al. [163], were also used to investigate transient stresses.

Recently, modelling of transient stresses has been used to aid the development of residual stress reduction techniques in studies such as those by Richards et al. [111] and Wen et al. [132]. This is especially applicable to techniques which act *in situ* (as the weld is carried out) to impede the initial formation of residual stresses; these include quench-cooling [117], global mechanical tensioning [14] and rolling [3]. The ability to take experimental measurements of the transient stress field would greatly aid the development of these methods, allow verification of modelling efforts, and give further insight into the development of welding residual stresses.

Measurement of transient welding strains

Metal foil strain gauges are used extensively in most areas of experimental mechanics, and have been previously employed to measure welding-induced strains. Early experiments by Pattee [164] and Papazoglou and Masubuchi [165] proved the concept of *in situ* strain measurement during welding, however produced mixed results in terms of the strain field. Subsequent studies by Jonsson and Josefson [166], Tekriwal and Mazumder [167] and Chidiac and Mirza [168] showed agreement between *in situ* strain measurements and modelling results. More recent experiments have focused on the use of alternative measurement techniques which avoid some of the limitations of resistance strain gauges, such as their limited operating temperature range, lengthy installation process, and impracticality for full-field measurement. Suárez et al. [169] and Richter-Trummer et al. [170] successfully applied Fibre Bragg Grating (FBG) sensors to measure welding transient strains, while De Strycker et al. [171] demonstrated the feasibility of using Digital Image Correlation (DIC). Recently, initial experiments using *in situ* neutron diffraction strain measurement during welding have also been undertaken by Woo et al. [172] and Gharghouri et al. [173]. While the above studies have been successful in measuring transient strains due to welding, none have so far addressed the practical considerations associated with calculation of the corresponding stresses. For example, a linear equivalence between strain and stress cannot be assumed for areas which undergo plastic deformation during welding (i.e. those areas where large residual strains form), and this prevents stresses in these regions from being calculated, limiting the technique. Also, the stress field may be significantly multiaxial, requiring several simultaneous strain measurements and simplifying assumptions. The aim of this work is to demonstrate experimental measurement of the transient stresses remote from the weld line during Gas Metal Arc Welding (GMAW), while taking these considerations into account.

Experimental

Strain gauge measurements

Four bead-on-plate welds and four butt welds were carried out using 3mm-thick S355JR+AR mild steel plates prepared in the layout shown in Figure 16a. The basic

32

properties of the plate material are given in Appendix D. Single-pass GMAW was used, and the welding parameters (shown in Table 1) were designed so as to produce full penetration, defect-free welds in both the butt and bead-on-plate specimens. After welding the specimens were allowed to cool for 600 seconds, after which time the temperature had approximately equilibrated, before being released from the clamping device. Temperature and strain measurements were taken throughout the welding and cooling processes at a rate of 2 Hz.
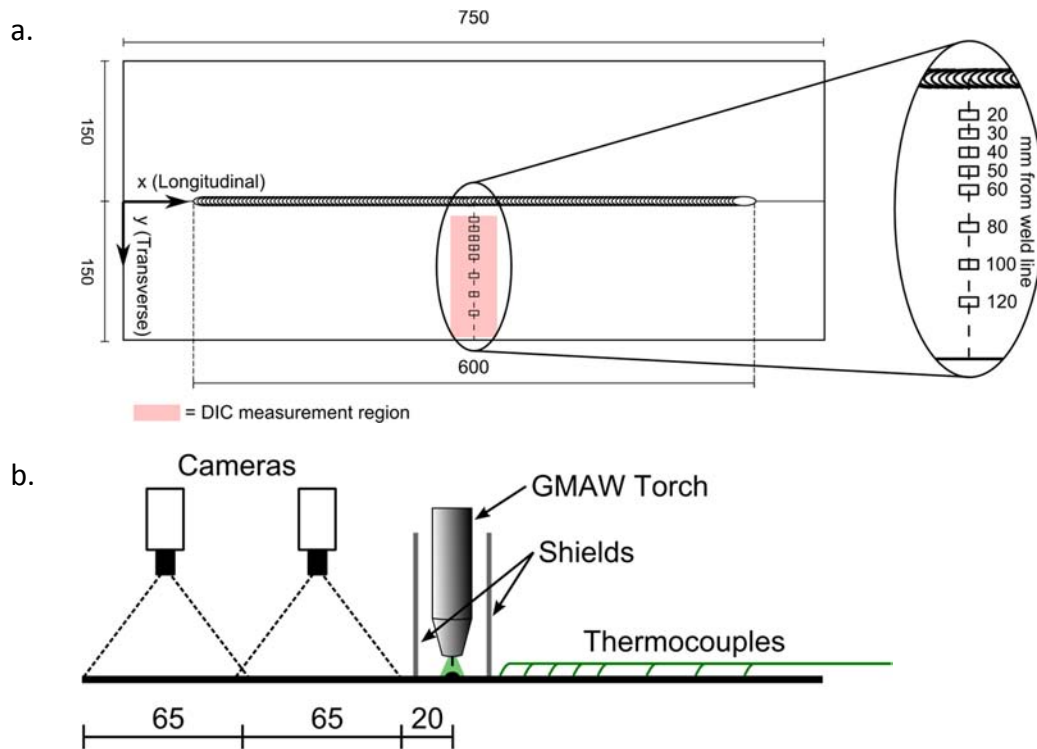
Figure 16: (a.) Specimen layout for welding experiments (a butt weld is shown; bead-on-plate welds each used a single 300 x 750 mm plate). (b.) Measurement setup for digital image correlation, showing a view down the weld line (dimensions in mm).

Table 2: Welding parameters used for the welds in 3mm-thick S355 steel. The same conditions were used for both the bead-on-plate and butt welds

Process	GMAW (pulsed)
Power supply	Fronius TransPuls Synergic 5000
Contact tip to work distance	13 mm
Filler wire	1 mm dia. EN440:G3Si1
Wire feed speed	173 mm s^{-1}
Torch speed	10.8 mm s^{-1}
Current (mean)	235 A
Voltage (mean)	29.3 V
Gas composition	20% CO_2, 2% O_2, balance Ar
Gas flow rate	200 ml s^{-1}

A vacuum clamping system was used to secure the specimens. This applied a constant low-vacuum pressure (<5 kPa) to the underside of the plates, keeping them completely flat for the duration of the experiments, and ensuring that there were no local stress concentrations. The specimen geometry and clamping conditions were intended to produce results which both represented the most general case of a linear weld in thin material, and which could be analysed easily. By preventing any bending of the

34

specimen throughout the test, and using the assumption that it contains a purely biaxial state of stress, strain data from only one face of the plate was used to calculate the stress field.

Strain gauge measurements were taken using gauges arranged in a line running from the central weld line to the edge of the plate (see Figure 16a). Strain measurements were only taken from one side of the specimen since the state of stress was assumed to be symmetrical about the weld line. At 20 and 30 mm from the weld line, Ni-Cr foil gauges (Micro Measurements WK-series) were used for their ability to measure at the elevated temperatures experienced here, which preliminary measurements had shown to peak at approximately 200°C. General-purpose constantan foil gauges (Micro Measurements CEA and L2A-series) were employed elsewhere. All strain gauges had a measurement grid length of 3.05 or 3.18 mm, and individual quarter-bridge circuits were used for each gauge.

To fully characterise the biaxial state of strain, it was necessary to use strain rosettes, measuring strain in three directions at each measurement point. However, since the number of channels available for strain measurement was limited to 16, rosettes could not be used at all the measurement points simultaneously. Consequently, two specimens (one butt weld and one bead-on-plate) used rosettes at 20 and 30 mm, and longitudinally-aligned uniaxial gauges elsewhere. Another two used rosettes at 40, 50, 60 and 80 mm and uniaxial gauges elsewhere, while the remaining specimens used uniaxial gauges in all locations.

K-type thermocouples were capacitance-discharge welded to the specimens, to measure the temperature variations at the gauge locations 20, 30, 40, and 50 mm from the weld line. Further from the weld line, the maximum temperatures encountered were determined to be too low to affect the strain measurement greatly. Both the strain gauges and thermocouples were protected from the radiated heat and electronic interference generated by the welding arc using glass fibre and aluminium foil shielding. As found in a previous study by Davoud [174], careful shielding of the instrumentation was necessary to achieve accurate measurements in the presence of the GMAW arc.

Digital Image Correlation

In addition to the measurements using strain gauges, transient strain measurement was carried out using DIC in a separate experiment. Specimens, clamping fixtures and welding parameters identical to those employed in the strain gauge measurements were used. Part of each specimen was coloured white using a temperature-resistant powder coating, and black speckles of graphite were applied to this area using an aerosol, to provide an easily-discernable image for the DIC cameras.

Two digital cameras (Correlated Solutions LIMESS, 1.4 megapixels) were used to capture the images used for DIC at a rate of 1 Hz throughout welding and cooling. They were positioned so as to capture separate areas of the plate surface, and were aligned perpendicular to it (see Figure 16). Between the two cameras, an area of 50 x 130 mm was covered by the DIC measurements. Metal shields were used to protect the measurement area from the welding arc. Images taken by the cameras were analysed using computer software (Correlated Solutions Vic2D) to generate a map of the biaxial state of strain. In this analysis, the measurement region was assumed to remain completely plane, a condition which was approximated (as in the strain gauge measurements) by the use of vacuum clamping.

Due to the low strain resolution of DIC, relatively poor precision was expected in the data. Therefore, strains calculated by the DIC software were subsequently averaged over areas of 300 mm^2 (50 mm in the longitudinal direction by 6 mm in the transverse direction), to give strain results representative of the strain gauge locations shown in Figure 16a.

Calculation of the stress field

The apparent state of strain (ε) at any point on the specimen is composed of the sum of strain due to temperature dilation of the material (ε_t), strain due to elastic deformation (ε_e), and strain from any plastic deformation ε_p [165].

Equation 1

$$\varepsilon = \varepsilon_t + \varepsilon_e + \varepsilon_p$$

For calculation of the stress tensor, it is necessary to isolate ε_e. The strain gauges used in this study were matched to the coefficient of thermal expansion of the specimen material, so that only $\varepsilon_e + \varepsilon_p$ was measured. Temperature data from the thermocouples was used to compensate for the effects of temperature on the gauges themselves, in accordance with the manufacturer's instructions [175]. By contrast, the results of the DIC analysis contained all three strain components, so to find $\varepsilon_e + \varepsilon_p$ an approximation of ε_t was made using the product of temperature and the material's coefficient of thermal expansion (assumed constant 1.217 x 10^{-5} K^{-1} for the temperature range of interest) and subtracted from the total strain.

Hooke's law was used to calculate the biaxial state of stress from the measured strain state at each strain rosette location, assuming plane stress conditions at the plate upper surface:

Equation 2

$$\begin{bmatrix} \sigma_{xx} \\ \sigma_{yy} \\ \tau_{xy} \end{bmatrix} = \begin{bmatrix} \dfrac{E}{1-v^2} & \dfrac{vE}{1-v^2} & 0 \\ \dfrac{vE}{1-v^2} & \dfrac{E}{1-v^2} & 0 \\ 0 & 0 & \dfrac{E}{2(1+v)} \end{bmatrix} \begin{bmatrix} \varepsilon_{xx} \\ \varepsilon_{yy} \\ 2\varepsilon_{xy} \end{bmatrix}$$

Where E and v are the Young's modulus and Poisson ratio of the material (202 GPa and 0.30 respectively), and σ_{xx}, ε_{xx} etc. represent the stress and strain components for the coordinate directions given in Figure 16a. This assumes that the material is both isotropic and linearly elastic at the measurement points, and that it does not undergo any plastic deformation during the welding process, i.e. that the plastic strain ε_p in Equation 1 is equal to zero throughout. The absence of plastic deformation at the gauge locations was verified by calculating the von Mises equivalent stress [176]:

Equation 3

$$\sigma_{vm} = (\sigma_{xx}^2 + \sigma_{yy}^2 - \sigma_{xx}\sigma_{yy} + 3\tau_{xy}^2)^{\frac{1}{2}}$$

and checking that this remained below the yield stress of the material throughout the experiment.

The use of Hooke's law here also assumes that the plate can be treated as a flat membrane bearing only in-plane stresses, a condition which was approximated by the use of vacuum clamping in the experiments. Lastly, it assumes that the specimens contained no residual stresses at the start of the measurements. Initial residual stress levels were not evaluated in this investigation, however typical values of in-plane residual stress in this type of hot-rolled material used are low, being around ±10 MPa in the direction of rolling during manufacture [177].

Results

Plots of the longitudinal, transverse and von Mises components of stress in the specimens during welding, calculated from strain gauge data, are shown in Figure 17. Due to the limited number of strain rosettes per specimen, strain measurements from two bead-on-plate specimens and two butt weld specimens were used to calculate these stress fields. Since the stress measurements only extend from 20 mm to 80 mm from the weld line, the development of the tensile peak in longitudinal residual stress is not shown, only the stresses remote from the weld.

Nature of the transient stress field

For stress in the longitudinal direction (Figure 17a and b), a small compressive 'bow-wave' is observed ahead of the arc, since rapidly expanding material around the arc causes compression of the cooler material ahead of it. As the arc passes (at zero seconds), this rapid expansion at the weld line causes tensile stresses away from the central region. However, soon after the arc passes, material along the weld line rapidly cools and contracts relative to the rest of the plate. This causes a large tensile stress to develop at the weld line (not shown), while significant compressive stresses can be seen to form in the rest of the plate. The development of stress in the transverse direction (Figure 17c and d) follows an equivalent but broadly opposite pattern, due to the Poisson effect. The stresses measured in this direction were smaller than the longitudinal stresses, though still a significant fraction of the yield stress of the material. After completion of the weld, strain measurement continued as the specimen cooled (see Figure 18); the calculated values of stress after cooling indicate the residual stresses induced by the welding process.

It is interesting to note how the von Mises equivalent stress (Figure 17e and f), initially increases and then dips just in front of the welding arc. This is because the weld pool cannot support any stress, and therefore the material around relaxes. As the weld pool solidifies and the material cools, the evolution of stress continues. At no point during the measurements did the calculated von Mises stress exceed the nominal yield stress of the material at any of the measurement locations, indicating that no plastic deformation took place there, and hence that the assumption of linear elasticity at these points was sound. Since the closest gauge was 20 mm from the weld line, it can be inferred that for these welds all of the plastic deformation induced by the welding process occurred within 20 mm of the weld centreline.

In Figure 17e and Figure 17f, the nominal yield stress of the material is shown as a constant of 355 MPa. In reality, the yield stress varies with temperature, however for this type of steel the effect is relatively small over the temperature range (20 - 200°C) encountered at the measurement points [178]. Additionally, tensile testing of the material revealed that that its actual room-temperature yield strength was 490 MPa; far higher than the specified minimum value (see also Appendix D).
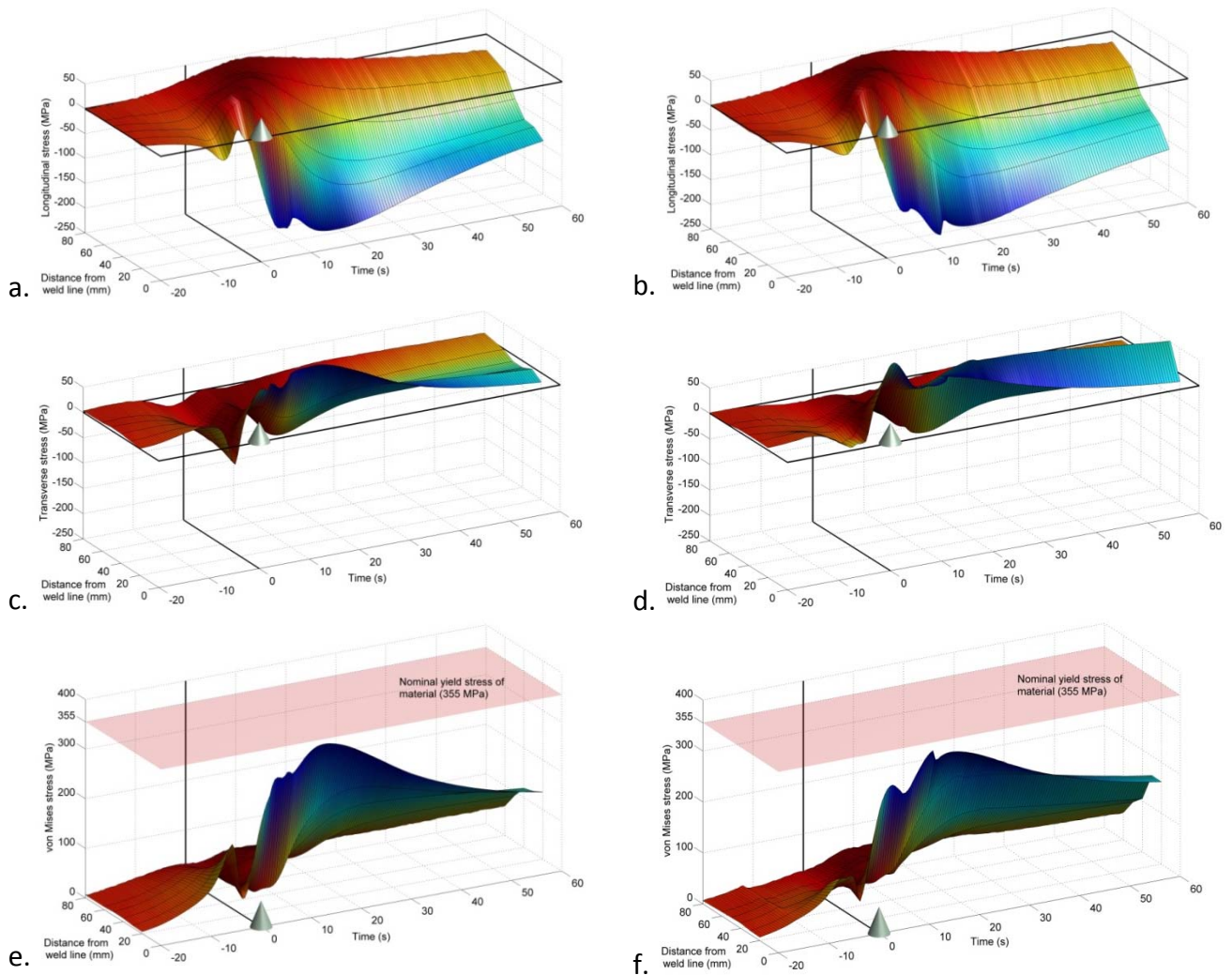
Figure 17: Components of the time-dependent biaxial stress field in thin plate GMA welds. The longitudinal component of stress for bead-on-plate (a.) and butt (b.) welding, transverse component for bead-on-plate (c.) and butt (d.) welding, and von Mises equivalent stress for bead-on-plate (e.) and butt welding (f.) are shown. The cone in the foreground of each image represents the location of the welding arc, and the moment at which the arc passes the measurement line has been defined as zero seconds.

Effect of bead-on-plate vs. butt weld geometry

Transient stresses observed during bead-on-plate (Figure 17a, c and e) and butt welding (Figure 17b, d and f) are very similar. This is especially true for the longitudinal stress (Figure 17a and b), which is practically identical for both cases. In the transverse direction, bead-on-plate welding (Figure 17c) shows a larger compressive region ahead of the weld pool (approximately -5 sec). It therefore seems likely that in butt welding, the plates being initially unconnected along the weld line allows the joint to expand more freely in the transverse direction ahead of the arc, but does not significantly affect the longitudinal direction.

Strain gauge measurement uncertainty

To assess the repeatability of the strain gauge measurements, measured strains for the four nominally identical bead-on-plate specimens are shown in Figure 18. The strain

plots are very similar, especially during welding (-28 to +28 seconds). However, cooling results in a range of measured residual strains: the standard deviation of the longitudinal residual strain values at +600 seconds is 108 $\mu\varepsilon$ at 20 mm from the weld line, and 60 $\mu\varepsilon$ at 30 mm. The accuracy of the strain measurement setup was estimated by calculating the linear sum of the uncertainties in bridge circuit accuracy, bridge non-linearity, gauge factor thermal drift evaluation, and strain gauge transverse sensitivity (uniaxial gauges only), giving an overall uncertainty of ±3.9%. Consequently, it is likely that the observed sample-to-sample variation in residual strain is caused primarily by variation in the actual strain field due, for example, to small differences in clamping force and plate alignment. The high transverse gradient in residual stress which is expected to occur close to the weld line magnifies this effect for the measurements at 20 mm. However, it should be noted that additional potential sources of measurement error exist which have not been evaluated here. These include thermal drift in gauge lead-wire resistance, angular misalignment of gauges, imperfect thermal and mechanical coupling between the gauges and specimens, out-of-plane movement of the specimen surface, and specimen material anisotropy. Time-dependent gauge resistance drift was also assumed to be negligible due to the short duration of the experiments.
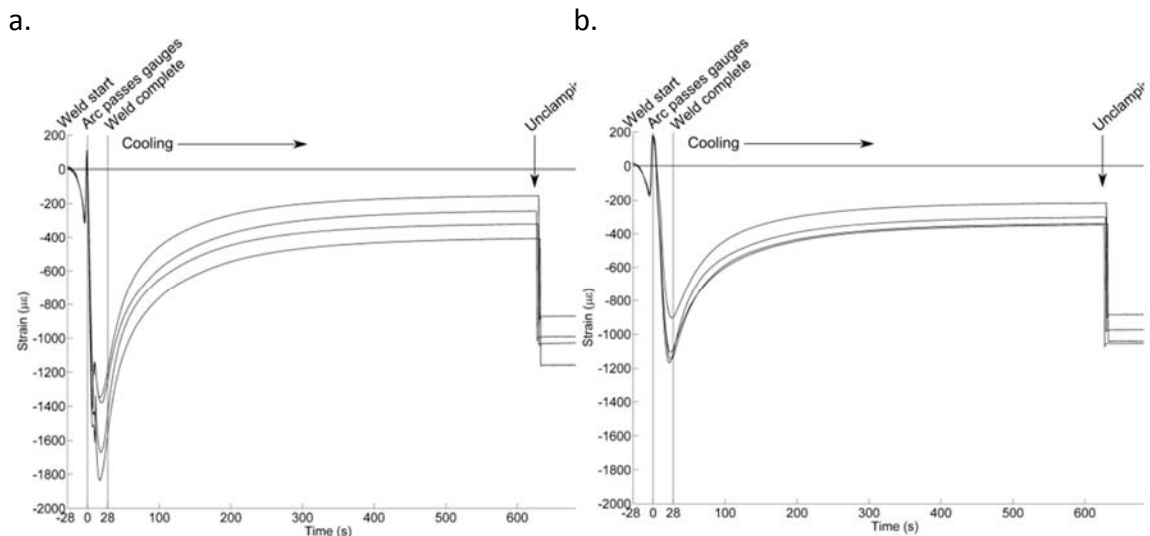
Figure 18: Non-thermal strain component ($\varepsilon_e + \varepsilon_p$) in the longitudinal direction, measured at (a) 20 mm and (b) 30 mm from the weld line for four identical bead-on-plate welds.

Digital image correlation

Figure 19 shows transient strain in the longitudinal and transverse directions at two locations on separate but identical bead-on-plate specimens using strain gauges and DIC. Noticeable scatter is seen in the DIC measurements due to the limited strain resolution of this method; but nevertheless the general trend is clear. Good agreement is observed between the strain gauge measurements and the DIC for the longitudinal strain direction, however there is significant deviation in the transverse direction,

especially at the closest distance from the weld line (20 mm). The cause of this discrepancy could not be determined with certainty, but is possibly due to slight out-of plane movement of the specimen. It should also be noted that DIC can be very sensitive to vibration and changes in light level, both of which may be associated with arc welding. Consequently, only 25% of the specimens welded yielded image sets which could be analysed to produce uninterrupted strain traces over the entire duration of the experiment.

a.

b.

c.

d.
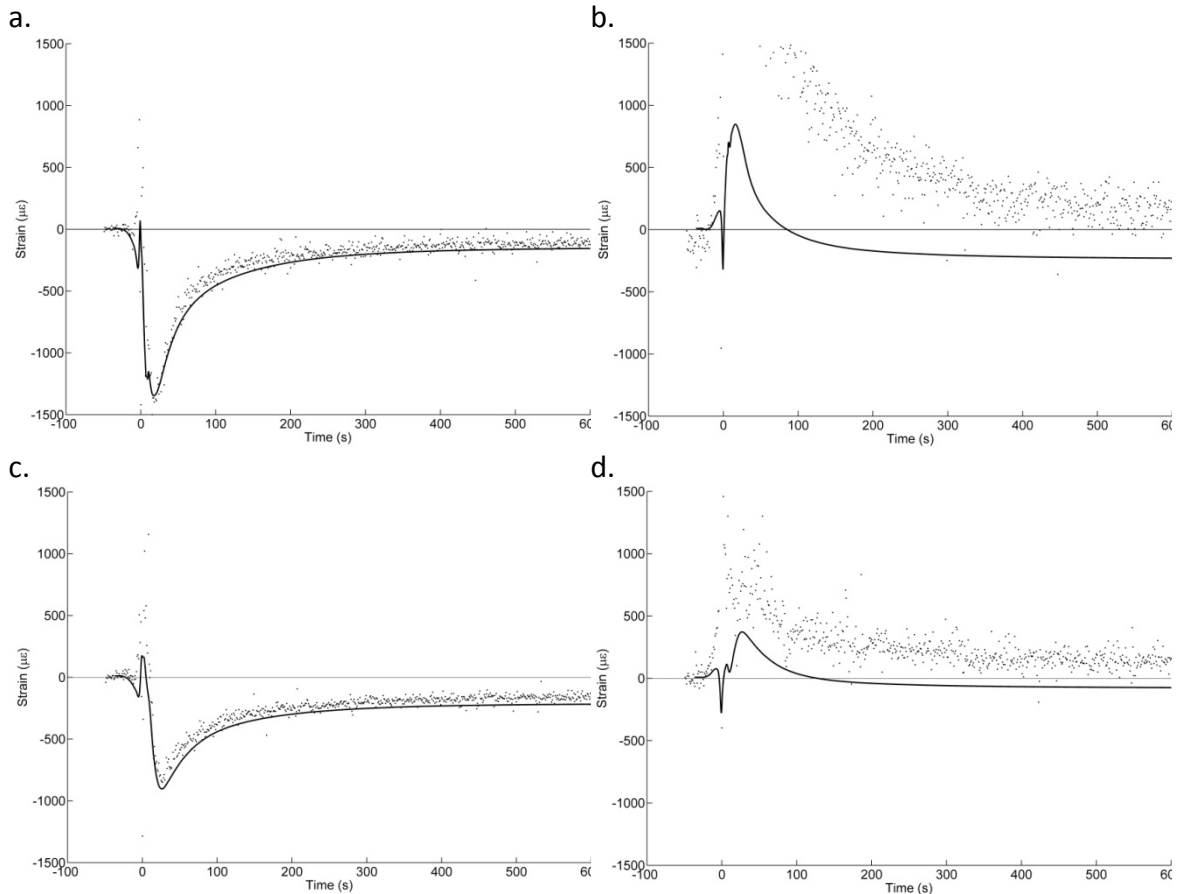
Figure 19: Comparison of transient strains measured using strain gauges (solid lines) and digital image correlation (points). (a) Longitudinal strain at 20 mm, (b) transverse strain at 20 mm, (c) longitudinal strain at 30 mm, (d) transverse strain at 30 mm. Strain components due to thermal dilation have been removed.

Discussion

The calculation of transient stresses remote from the weld line gives a better insight into the effect of the welding than strain measurement alone. However, it relies upon the ability to measure several directional strain components, since (as can be seen from Figure 17) the stress distribution during welding and subsequent cooling is far from uniaxial, especially close to the weld line. In these experiments, this was aided by a greatly simplified specimen geometry and mechanical boundary conditions. Evaluation of the transient stresses also requires verification that material at the measurement points remains in the fully elastic regime.

Although no previous experimental measurements of transient stress due to welding have been found in literature, the stresses presented here can be compared with previous modelling results. Comparing the experimental transient stresses with those from FE models by Richards et al. [14] and Shanghvi and Michaleris [179], and the analytical model by Al-Huniti et al. [180], general qualitative agreement is observed. It is also well known from modelling results that any plastic strain caused by welding tends to be highly localised around the weld region [181], and indeed this fact is commonly exploited to simplify the prediction of welding distortion [20]. This is compatible with the observation here that plastic strain did not appear to occur at 20 mm from the weld line or at any of the measurement locations further away. Finally, the individual transient strain components measured in this study (such as those presented in Figure 18) bear good qualitative comparison with those observed for equivalent cases in previous experimental efforts (such as are mentioned in the introduction).

While both metal foil strain gauges and DIC are viable methods of measuring welding-induced thermal strains, strain gauges have been seen here to possess better precision and robustness, the latter being of special importance during arc welding. For the calculation of transient stresses, strain gauges also have the advantage that when self-temperature-compensating types are used, the magnitude of the correction for thermal effects is small. DIC strain results, meanwhile, must be subsequently compensated for thermal dilation. This correction can be large for material heated by the welding process, which magnifies the effect of uncertainty in the temperature measurements corresponding to the strain measurement region. However, it is likely that with greater technical consideration to image capture methods and correlation techniques, such as employed by De Strycker et al. [171], DIC could be used routinely for this type of measurement.

Although "far-field" stress measurement (to a minimum distance of 20 mm from the weld line) has been demonstrated here, in general inferring the stress state close to the fusion zone during arc welding remains problematic for three reasons. Firstly, the measurement environment becomes increasingly harsh (due to high temperature, electromagnetic noise and arc radiation) with decreasing distance to the weld, which causes problems with most contact and non-contact methods. Secondly, the strain gradient becomes large, requiring a relatively high measurement resolution. Finally, plastic deformation of material around the weld makes it essentially impossible to relate measured strain values to stress. This is unfortunate, since it is the weld line region which is of greatest practical significance; bearing the greatest (and most troublesome) transient and residual stresses. Nevertheless, stresses measured further from the weld line can be used to observe the general development of the stress field

relatively well, and results such as those presented here can also be used to validate numerical models which include the weld line region. Alternatively, using the inherent strain approach developed by Ueda et al. [182], appropriate assumptions regarding the symmetry of the system and the conditions necessary for stress equilibrium could be used to calculate stresses at the weld line. Some contemporary examples using this type of inverse analysis are provided by Korsunsky [158].

The development of welding parameters to achieve low residual stress, and of specialised stress reduction techniques usually relies on the study of residual stresses only. However, an emphasis on investigating transient stresses, *via* experimental methods such as described here or by numerical modelling, gives an additional perspective on how residual stresses may be reduced. For example, it can be seen from Figure 17 that the stress distribution is still developing at 60 seconds after the arc pass, as the temperature distribution in the plate equilibrates. This suggests that mechanical treatments which act by plastic deformation of the weld metal (such as peening and rolling) are unlikely to be particularly effective if applied to the area directly behind the weld pool, since material here will continue to yield during the cooling process, erasing any effect on the final stress. Naturally, transient stress measurements could also benefit the study of other stress-related phenomena which occur during welding, such as solidification cracking and in-process distortion.

The close comparison observed between the transient stress fields for butt and bead-on-plate welding is readily accounted for when the conditions of mechanical restraint provided by each case are considered. Longitudinal stresses are very similar, since there is little difference in longitudinal restraint. Transverse stresses during the approach of the welding arc cannot be sustained during butt welding to the same extent as for bead-on-plate, since the plates are initially unattached. This implies that during butt welding, these stresses are accommodated by transverse movement of the plates ahead of the welding arc. However, since the transient stresses in the two cases are so similar it is likely that, in general, results concerning stress in thin plate butt welding will also apply to the bead-on-plate case, and *vice versa*.

Conclusions

1. The transient strain field caused by GMA welding of steel plate specimens can be measured using resistance strain gauges. Qualitatively very similar results taken from identical specimens show that the use of such gauges in this application is repeatable.
2. The thermally-induced transient stress field in areas remote from the weld line, which undergo purely elastic deformation during welding, can be calculated using Hooke's law. Closer to the weld line, plastic deformation prevents the use of this method. In these experiments, the von Mises yield criterion was used to

check where it could be applied, and it was shown that in this case, all plastic deformation was confined to within 20 mm of the weld centreline.

3. Major features in the development of the stress field were clearly observed from experimental measurements. This may be useful for the development of residual stress reduction techniques and for the study of welding phenomena which are affected by the transient thermal stress.

4. For GMA welding of thin mild steel plate, little difference in the longitudinal stress field in surrounding material is observed whether the weld is carried out at a butt joint interface or on single solid piece of material (bead-on-plate configuration). Those differences which do exist are almost exclusively in the transverse direction, and are due to the difference in initial transverse restraint at the weld line.

5. Although less precise than resistance strain gauges, Digital Image Correlation (DIC) can also be used to monitor strain development during welding.

Chapter 4: Measurement of residual elastic strain and stress in welded and rolled specimens

The majority of this chapter is taken from the following article:

Abstract

Neutron diffraction and foil resistance strain gauges have been used to study the state of residual stress introduced by localised high-pressure rolling of structural steel plates, and compare it to that caused by gas metal arc welding. Rolling creates a region in which the residual stress state is highly compressive in the rolling direction. Furthermore, this region is sharply-defined, making it potentially very suitable for cancelling out the tensile residual stresses caused by welding. It is also demonstrated that non-destructive strain measurements made during the welding and rolling processes can be used to indicate residual elastic strain and stress, and that this method shows good agreement with conventional neutron diffraction measurements. Determination of residual stresses in this way requires consideration of the effect of curvature on the values of strain measured at the surface of the object.

Introduction

Localised rolling of the weld region, to produce the in-plane elongation necessary to relieve tensile residual stresses in the longitudinal direction of the weld, is one method to reduce the detrimental residual stresses created by welding. While rolling may be applied either during the welding process (*in situ* rolling) or thereafter (post-weld rolling), only post-weld rolling has been shown to be effective at reducing longitudinal residual stress [3, 132]. During *in situ* rolling, the subsequent yielding of weld metal as thermal contraction occurs means that the strain induced by the roller at high temperature has no effect on the residual stress state (see Chapter 5).

The extent to which rolling can induce compressive residual stresses along the roller path (and tensile stresses beside it) has been the focus of several modelling studies [183, 184], but has not been extensively studied experimentally. The accuracy with which residual stress distributions may be controlled by rolling is also an important factor: welding produces large gradients in longitudinal residual stress, and therefore a

process capable of producing similarly large gradients is required to counteract this. If the stress distribution that can be introduced by rolling is less sharply-defined than that which results from welding, then the two will never completely cancel out. The transient stresses which occur during rolling are also of practical significance: since they may be larger than the final residual stress, they are the critical factor for the initiation of in-process cracking during the rolling of less ductile materials.

Residual stresses in welded components can be measured using a wide variety of methods [7]. Neutron diffraction and synchrotron X-ray diffraction are often used for research, but are too expensive and impractical for most commercial purposes, since they can only be carried out at dedicated facilities [71, 65]. Diffraction using lower-energy laboratory X-rays is more convenient but it also requires expensive and specialised equipment. Methods based on measuring strain changes due to relaxation of residual stresses, such as sectioning [185], hole drilling [67], and the contour method [68] are widely used but are often time-consuming, and by their nature must be destructive to some degree [69]. Furthermore, such 'relaxation' methods are not normally able to measure more than three directional components of the stress tensor, or the variation in residual stress over three dimensions.

It was shown in the previous chapter of that just as strains due to destructive relaxation of residual stresses can be measured, so can the (equal and opposite) strains that are associated with their initial formation. This implies that the residual stresses added by an operation such as welding can be found using the strain differences measured between the beginning and the end of the process. Strain development during welding has been previously measured using metal foil resistance strain gauges [165, 166, 167], fibre Bragg grating sensors [170, 169] and digital image correlation [171]. However, the final (i.e. residual) values of strain measured in this way have never been compared to reliable residual stress measurements. Although the accurate calculation of stress from strain requires that the material be in a purely elastic state throughout the process, during welding this is usually the case for all but a small region around the weld bead [25]. In this work, residual elastic strains and stresses due to Gas Metal Arc (GMA) welding and localised high-pressure rolling have been determined using this method and compared with neutron diffraction measurements.

Experimental

Overview

Two processes were investigated: GMA welding and localised high pressure rolling. These were applied to thin plate specimens of S355 structural steel, shown in Figure 20. Strain measurements were taken from the surface of each specimen as it was

welded or rolled, using metal foil resistance strain gauges. At the end of the process the specimen was released from its restraint, allowing it to buckle. The resulting distorted specimen was then scanned using a laser coordinate measurement device. Surface profiles measured in this way were used for two purposes: firstly to allow the residual distortions of different specimens to be compared, and secondly to compensate the final strain gauge readings (from the unconstrained, distorted plates) for the effect of bending on the measured strain. Neutron diffraction measurement of residual elastic strain in the (still unconstrained) specimens was carried out. Finally, residual stresses were calculated from the diffraction and strain gauge measurements, and the residual strains and stresses found by these two methods were compared.

Strain gauge measurements

Welded specimens

A more comprehensive explanation of the measurements carried out on the welded specimens is given in the previous chapter. Single-pass, full-penetration GMA welding was carried out on rectangular thin plate samples of 3mm-thick S355 mild steel[11], which were instrumented with thermocouples and foil resistance strain gauges (see Figure 20a). Four butt welds and four bead-on-plate welds were produced using the same overall geometry, under identical conditions. The plate specimens were held completely flat using a vacuum clamping system as they were welded, and were released 600 seconds after completion of the weld. Throughout the welding process, and during the subsequent cooling, temperature and strain measurements were taken at the upper surfaces of these specimens. To measure the full biaxial state of strain, rosette gauges (incorporating three strain gauges measuring in different directions) were used. Although the number of channels available for strain data collection was limited, by combining strain data from two identical samples it was possible to find the biaxial state of strain at six points across the plate, and strain in the longitudinal direction only at a further two (100 and 120 mm from the weld line, see Figure 20a), for both the bead-on-plate and butt welds. This allowed characterisation of part of the transient biaxial thermal stress field induced by the welding process, further details of which are given in the previous chapter. Eight K-type thermocouples placed 50 mm adjacent to the strain measurement locations in the longitudinal direction were used to compensate the strain gauges for temperature effects, and check that none of the strain gauges exceeded their rated temperature during welding. Elevated-temperature Ni-Cr strain gauges (Micro Measurements WK-series) were used at 20 and 30 mm from the weld line, while general-purpose constantan gauges (Micro Measurements CEA

---

[11] Preliminary uniaxial tensile tests (see Appendix D) were used to determine that the material had a yield strength of approximately 490 MPa and ultimate tensile strength of 555 MPa in the direction of mill rolling.

and L2A-series) were used elsewhere. In all cases, the strain gauge's measurement area was approximately 3.2 x 2.0 mm.

Since strain measurement was continued after welding and throughout the cooling period of the specimens, the residual stresses at the instrumented locations caused by the weld could be evaluated using the final measured strains. Since it assumes that the sample material remains perfectly elastic throughout the welding and cooling processes, this method of residual stress calculation was limited to areas of the specimen which did not undergo yielding [186]. The absence of plasticity at the gauge locations was verified by checking that the biaxial stress state calculated from the strain measurements did not exceed the von Mises yield criterion at any time during the process.
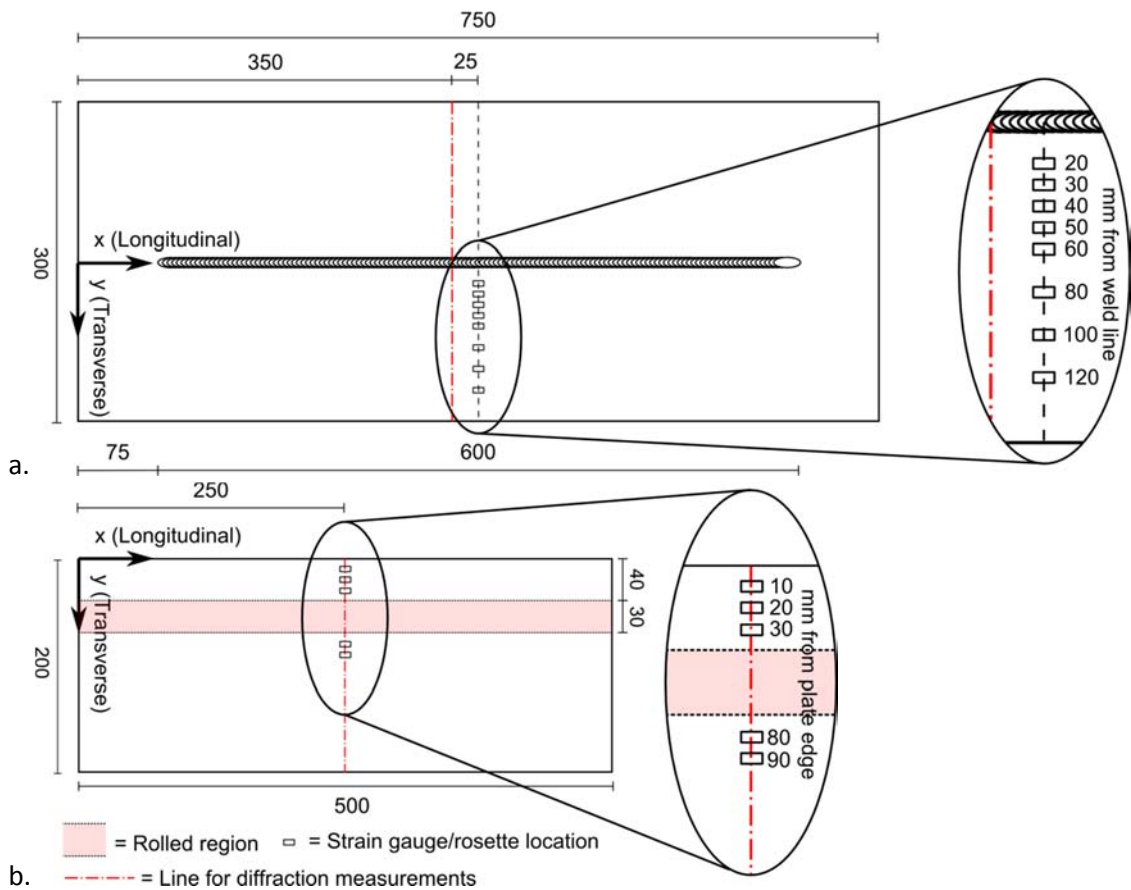

Figure 20: Strain measurement locations on (a.) welded and (b.) rolled specimens, which were 3 mm and 4 mm in thickness respectively.

Localised rolling

Rolling of three 4mm-thick S355 steel specimens[12] was carried out using a hydraulic rolling machine described in Appendix A. A flat roller, 30 mm in axial width and 100 mm in diameter, was applied to the plates during a single pass of rolling at a velocity of 8.33 mm s^{-1}, in the region highlighted in Figure 20b. A constant roller force of 50, 100 and 200 kN was used for each of the three samples respectively, and the specimens were constrained during rolling using the same vacuum clamping system as was used for the welded specimens. Strain measurements were taken using single gauges measuring in the longitudinal direction only, at five locations around the roller path (see Figure 20b). Since only one direction of strain was measured at each point, calculation of the corresponding stress is not presented here, since that would require the assumption that the stress field was purely uniaxial. After rolling, a micrometer was used to measure the plate thickness at three equally-spaced points along the roller path, and the average thickness reduction was calculated by comparing these data to equivalent measurements taken prior to rolling.

Residual distortion

Total level of distortion

On release from the clamping system, all of the plate specimens buckled immediately under their internal stresses, assuming an upwardly-curved shape (see Figure 21a). Laser coordinate scanning (Figure 21b) of the upper surfaces of all samples was performed to quantify this distortion. Interpolation of the raw coordinate data was used to fit a rectangular grid of 10 x 10 mm elements, resulting in a regular surface representing the sample's upper face (Figure 21c). This was done using the biharmonic spline interpolation method described by Sandwell [187], as implemented in MATLAB R2009b® software (The MathWorks inc., Natick, USA). The mean out-of plane displacement of all nodes of this surface was used to summarise the total level of distortion occurring in a sample.

---

[12] Uniaxial tensile tests were used to determine that upper yield strength if the original 4mm-thick material was approximately 475 MPa, and its ultimate tensile strength was approximately 535 MPa in the direction of mill rolling (see Appendix D).
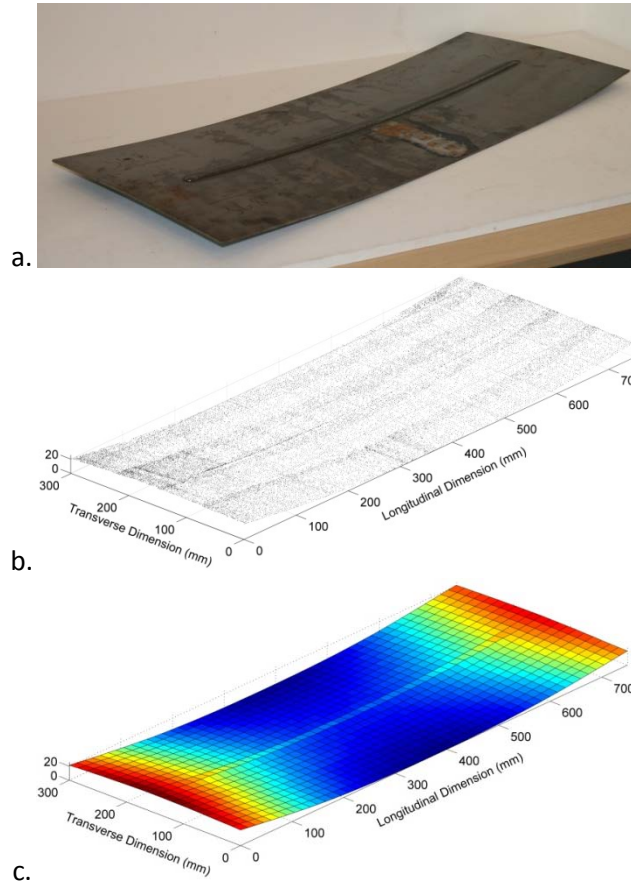
Figure 21: Measurement of out-of-plane distortion: (a.) as-welded specimen, (b.) raw coordinate data from laser scanning, (c.) fitted measurement grid.

Compensation of final strain gauge measurements for the effect of bending

Directly after welding, and while the specimen was still held flat by the clamping system, it was assumed (since the specimens were thin) that the strain measured by each strain gauge was representative of the strain throughout the plate thickness. However, after unclamping, the plates buckled under their internal stress, creating a biaxial curvature at the strain gauge locations. In this situation, a strain gradient exists through the plate's thickness, and strain measured at the surface cannot be considered representative of the strain state at, for example, the plate's mid-plane. All neutron diffraction measurements, however, were taken with the diffraction gauge volume centred on the mid-plane of the specimen, and so did not contain any additional strain component due to the plate's residual curvature. Therefore, to compare the strain gauge measurements with the neutron diffraction measurements, it was necessary to compensate the strain gauge measurements for the effect of bending, and calculate the corresponding mid-plane strain.

Figure 22 shows a section of a plate in combined biaxial bending and in-plane loading. The strains ε_{xx} and ε_{yy} which occur at the mid-plane of the plate are independent of bending deformation, and are due to in-plane loading alone. However at the surface,

the superposition of these strains with additional strain components due to the effect of the curvature acting over the thickness of the plate, leads to measured strains ε_{mxx} and ε_{myy} [188]. Therefore, to find the strain at the mid-plane from strain data measured at the surface, it is necessary to subtract the component of the measured value which is due to curvature:

Equation 4

$$\varepsilon_{xx} = \varepsilon_{mxx} - \frac{k_{xx}t}{2} \quad \text{and} \quad \varepsilon_{yy} = \varepsilon_{myy} - \frac{k_{yy}t}{2}$$

Where k_{xx} and k_{yy} are the curvatures of the plate in the x and y directions. The curvature was found by taking sections of the interpolated surface parallel to the x and y axes, and approximating them with a 6th-order polynomial, which could be differentiated smoothly. The additional strain due to curvature could then be calculated, and was subtracted from the strains measured at the surface after unclamping.
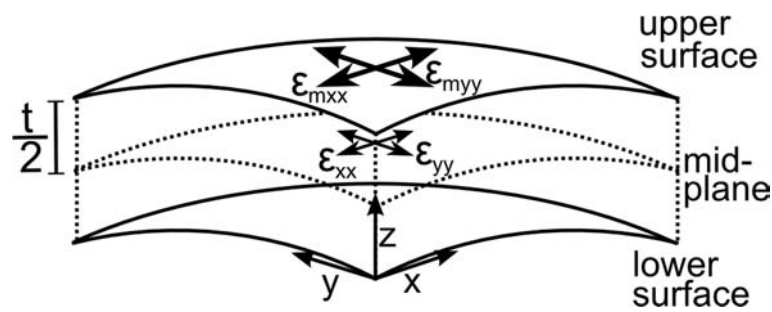
Figure 22: Strain at the surface and mid-plane of a plate in biaxial bending. Strains measured at the surface differ from the mid-plane strain by an amount proportional to the curvature of the plate in each strain direction.

Neutron diffraction measurements

Measurement of residual strains in the longitudinal, transverse and out-of-plane directions was carried out using the SALSA neutron diffractometer at the Institut Laue-Langevin, France [189]. The principle of neutron diffraction measurement of strains and stresses in polycrystalline materials is described in detail elsewhere [190]. For this experiment, the interplanar spacing of the ferrite {211} lattice plane was measured using a neutron wavelength of 1.644 Å and a cuboid gauge volume of 2x2x2 mm. The gauge volume was defined using a 2 mm primary collimator, and secondary radial collimator with 2x2 mm focus (full width at half maximum).

Since the specimens were rather thin (3 and 4 mm compared with a nominal corner-to-corner length of 2.83 mm for the gauge volume in the through-thickness direction), through-wall scans were required to accurately position the gauge volume at the mid-plane of the specimens. No additional reference measurements of the unstrained

51

lattice parameter (d_0) were taken. Instead, the assumption was made that the specimens were in a state of plane stress (and had elastically isotropic bulk properties), allowing d_0 to be calculated from the three orthogonal measured lattice spacings (d_{xx}, d_{yy}, d_{zz}) using the relation [191, 192]:

Equation 5

$$d_0 = \frac{1}{1+v}\left(vd_{xx} + vd_{yy} + (1-v)d_{zz}\right)$$

Where v is the Poisson's ratio of the material. To account for the effects of spatial variation in d_0 (due, for example to compositional and microstructural differences around the welds), it was evaluated separately for each measurement location. Since the strain was measured on only one set of *hkl* planes, i.e. {211}, it was necessary to consider the possibility of plane-specific elastic and plastic anisotropy. In body-centred cubic materials, the elastic response of the {211} plane is generally very close to that of the bulk material [193]. Therefore, it is possible to simply use plane-specific elastic constants (E = 225.5 GPa and v = 0.28) in the calculation of stress from measured lattice spacings, to get a good approximation of the bulk response. In cases of plane-specific plastic anisotropy, it is possible for the unstressed lattice spacing d_0 to vary with orientation, in which case the assumption of a single value of d_0 at each measurement point (Equation 5) would introduce error. However, the d_0 measurements presented in Figure 37 (see Chapter 6) show that while some plastic anisotropy does occur close to welds in this type of material, the effect is minor.

For the welded samples, diffraction measurements were taken at 43 points along a line perpendicular to the weld seam, and 25 mm away from the line of strain gauges (see Figure 20). Two welded specimens were measured: one butt weld and one bead-on-plate weld. Of the rolled specimens, only the plates rolled at 100 and 200 kN were measured, and measurements were carried out at a spatial resolution of 2 mm along the same transverse line as the strain gauges.

Results

Residual distortion

Table 3 shows the average out-of-plane displacement for the welded specimens, found using the method described previously in the experimental section. It can be seen that the bead-on-plate and butt welds display similar levels of distortion. Also, in both cases the sample-to-sample variation in distortion is extremely low: although not shown here, plots of the distorted plate surfaces appeared practically coincident.

Table 3: Weld-induced buckling distortion. Measurements of the average out-of-plane displacement of the surface of four bead-on-plate welds and four butt welds.

	Bead-on-plate (mm)	Butt (mm)
	8.68	8.42
	8.78	9.30
	8.98	9.28
	9.04	9.08
Mean	**8.87**	**9.02**
Std. Dev.	**0.17**	**0.41**

Residual elastic strain

During welding, von Mises stresses calculated from the strain gauge data did not exceed the yield value at any of the strain gauge locations (i.e. 20 mm or further from the weld line). Therefore, since no material plasticity had been detected at any of the strain gauge locations, the final measured strain data could be used to calculate residual stress. This also implies that all plasticity during welding was confined to within 20 mm from the weld line, which is consistent with the observation that according to the neutron diffraction data, the region of tensile longitudinal residual stress lies within ±20 mm of the weld line (see Figure 25a).

For the welded specimens, a comparison of residual strains in the longitudinal and transverse directions measured using strain gauges and neutron diffraction is shown in Figure 23. The effect of correcting for curvature in the strain gauge measurements can be clearly seen, since the correction is relatively large - in some cases over 500 µε. In the longitudinal direction, the difference between the corrected and uncorrected strain gauge measurements is almost constant across the width of the measurement region, as the longitudinal curvature is quite uniform over the transverse direction (this can also be seen in Figure 21). By contrast, the transverse curvature naturally varies significantly in the transverse direction. Good agreement is observed between the (corrected) strains gauge measurements and the diffraction measurements. Finally, it can be noted from the neutron diffraction results that both the distribution and magnitude of residual strain in the bead-on-plate and butt weld specimens are very similar.
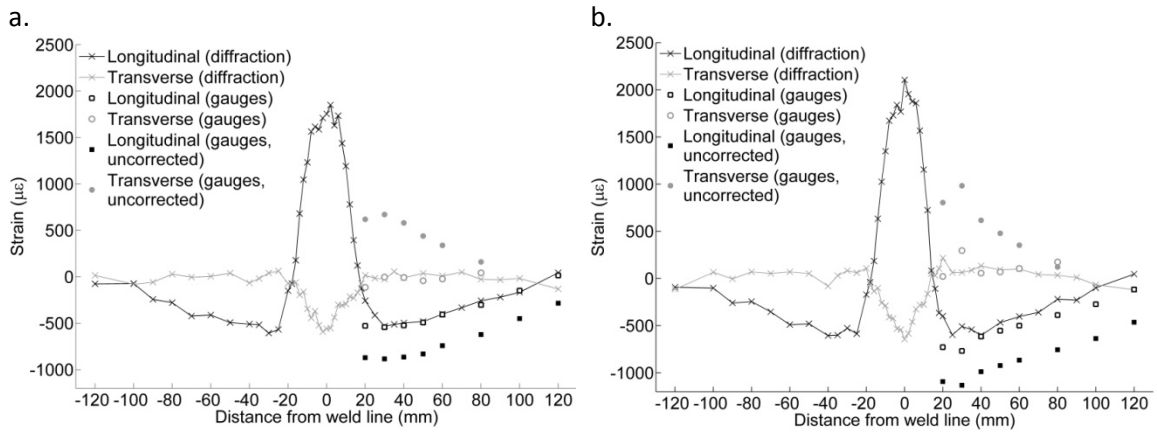
Figure 23: Comparison of residual elastic strain measured using neutron diffraction and strain gauges in (a.) bead-on-plate weld and (b.) butt weld, in 3 mm mild steel. For clarity, error bars are not plotted - the mean statistical uncertainty in the diffraction measurements is ±28 με.

Similar agreement between the neutron diffraction and strain gauge results is seen for the rolled plates in Figure 24. Here, however, the correction for bending strain applied to the strain gauge results is smaller, since the rolling process (and the fact that the rolled plates where thicker; 4 mm rather than 3 mm) resulted in lower residual curvatures. In both cases, a region of strongly negative longitudinal strain is observed directly under the roller's path.
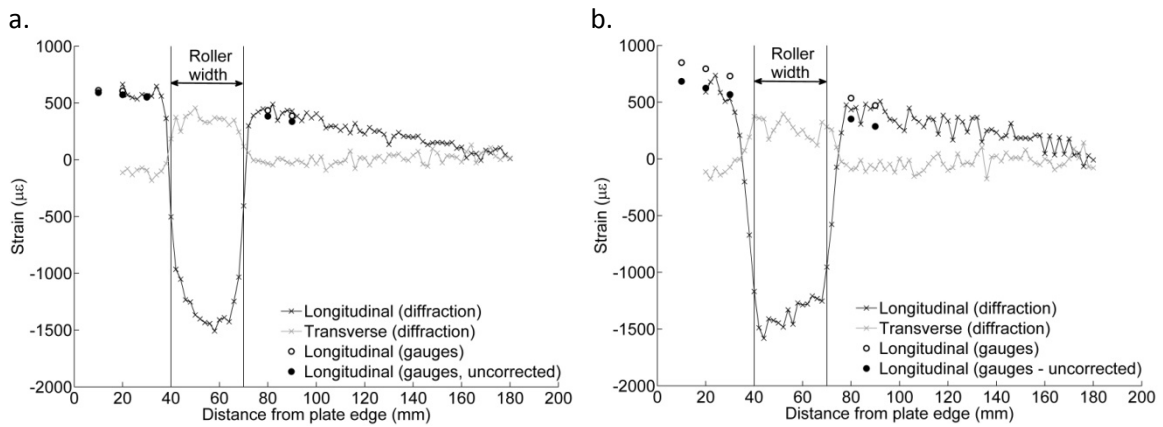
Figure 24: Comparison of residual elastic strain measured using neutron diffraction and strain gauges in locally-rolled mild steel plates: (a.) 100 kN and (b.) 200 kN roller force. For clarity, error bars are not plotted - the mean statistical uncertainty in the diffraction measurements is ±25 με.

Both Figure 23 and Figure 24 show rather low uncertainties in the residual strain measurements. However, it should be noted that this represents the uncertainty due to fitting of the diffraction peaks. Uncertainties due to other factors such as errors in spatial positioning and neutron wavelength determination, and the assumption of plane stress, have not been evaluated.

Residual stresses

The plane stress form of Hooke's law (using plane-specific elastic constants, see experimental section) was used to calculate residual stresses from the measured in-plane strains. Residual stresses in the welded and rolled specimens are shown in Figure 25. For brevity, only stresses in the bead-on-plate weld are shown in Figure 25a, since the stress distribution in the butt weld is essentially identical. In Figure 25a, good agreement is observed between stresses calculated from neutron diffraction and strain rosette measurements. This is expected, since it was also the case for the residual strains (shown in Figure 23) from which these stresses were calculated. However it is worth noting that the in-plane shear stress (τ_{xy}), found from the strain gauge measurements, is essentially zero at every point measured. This provides confirmation that the directions of the principal stresses are close to the longitudinal and transverse axes of the specimen, which is expected at these gauge locations due to the symmetry of the samples. No residual stress values were determined for the strain gauge measurements on the rolled specimens, since measurement was only carried out in a single direction (see experimental section).
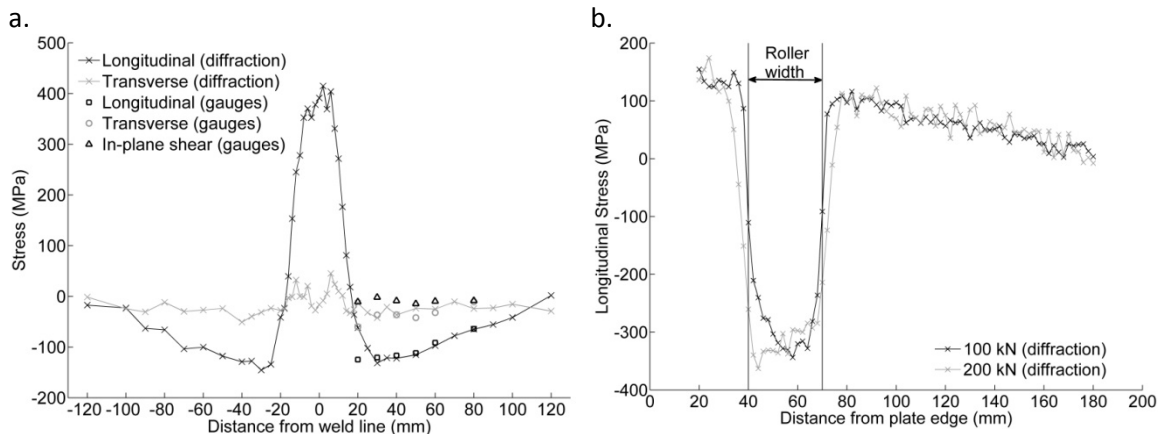
Figure 25: Residual stress measured using neutron diffraction and strain gauges in (a.) a 3mm bead-on-plate weld and (b.) locally-rolled plates (longitudinal component only). Error bars have been removed for clarity; the standard error is less than ±21 MPa for all points.

Transient strain during rolling

The development of longitudinal strain during rolling can be seen in Figure 26, and the positions of the strain measurements represented here are shown in Figure 20b. The instant at which the roller axis passes the line of strain gauges has been defined as zero seconds, and therefore the rolling operation takes place between -30 and 30 seconds. The effect of plate deflection during unclamping on the measured strain can be seen as a step change occurring between 75 and 100 seconds in each plot. Clearly, the use of higher rolling loads causes larger tensile strains to occur around the roller path during and after rolling. It can also be seen, in Figure 26c, that the strains encountered during rolling at 200 kN are significantly greater than their residual values. The nominal yield strain of this type of material is around 2000 µε and therefore, assuming an

55

approximately uniaxial stress distribution, it is unlikely that any of the material where the gauges were situated undergoes yield.
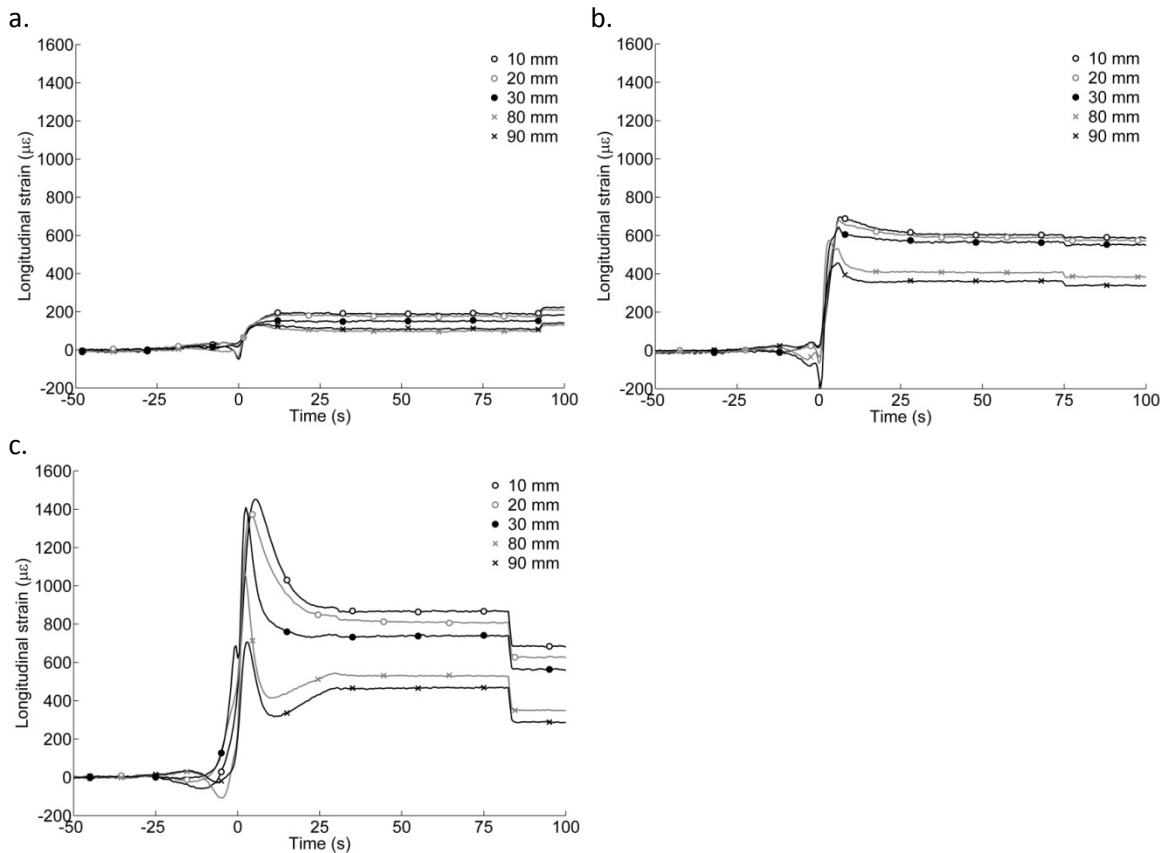
Figure 26: Longitudinal strain around the roller path during localised rolling followed by unclamping. (a.) 50 kN, (b.) 100 kN and (c.) 200 kN roller loads. The roller axis passes the line of strain gauges at 0 seconds, and unclamping occurs at 75-90 seconds.

Discussion

Strain gauge measurement

In Figure 23 and Figure 24, good agreement is observed between residual elastic strains taken from in-process strain gauge measurements and those measured using neutron diffraction. This suggests that measuring the strain difference between the start and finish of localised welding and rolling processes is a viable method for estimating stresses around the affected region. However, there are several major limitations to this technique. Firstly, the strain increment measured by a strain gauge is only proportional to the residual elastic strain when perfectly elastic material behaviour can be assumed at the measurement location. Secondly, strain gauges cannot operate close to the weld line (due to the elevated temperature), or directly in the path of the roller. For these two reasons, the central peak of longitudinal tensile strain at the weld line, and the valley of compressive strain underneath the roller path, cannot be seen in the strain gauge results. Finally, to ascertain the final state of residual stress from strain gauge measurements, the assumption must be made that

the specimen is initially completely unstressed; otherwise only the incremental addition of stress, rather than the total residual stress state is measured. Nevertheless, since the residual stress distribution in the longitudinal direction must equilibrate across the width of the object, the level of stress in the surrounding region (as may be measured using strain gauges) can be used to indicate the level of stress at the weld or rolled region.

The possibility of plastic deformation at the gauge locations during measurement means that if residual stresses are to be calculated, it is necessary to carry out continuous measurements throughout the process (rather than just at the start and finish), to check that plasticity does not occur. Furthermore, sufficient information for calculation of the stress state must be collected at every measurement point, so that an appropriate yield criterion can be applied. In these experiments, this was achieved by using 3-gauge strain rosettes and the assumption of plane stress in the specimen.

The technique presented here is largely non-destructive, although it does require cleaning and mild abrasion of the specimen's surface for strain gauge attachment. It can also be carried out with little specialised equipment, and could therefore be a useful tool for comparative studies of weld-induced residual stress. The maximum available spatial resolution depends on the size of the strain gauges used. By using alternative methods such as digital image correlation to measure the strains which occur during welding [171], rather than resistance strain gauges, the scope of this technique could be expanded to include non-contact, full-field measurement.

Coordinate measurements of the distorted surfaces of the specimens were used to quantify the curvature and eliminate the apparent strains due to bending. However, this could alternatively be achieved by measuring strains on opposing sides of the bent object and finding their shared (in-plane) and deviatory (bending) components. In these experiments, it was seen that the very large distortions encountered during the welding of thin materials can greatly redistribute residual elastic strains; both throughout the whole object and, due to bending, over the plate thickness. In Figure 23 and Figure 24, this can be seen as the difference between the strain gauge results corrected and uncorrected for distortion, and in Figure 26 it can be seen as a step change in the measured strain during unclamping.

Bead-on-plate and butt weld geometry
The low sample-to-sample variation in distortion observed for the welded specimens (see Table 3) can be attributed to a combination of the highly uniform clamping conditions applied during welding, and the low buckling strength of the relatively thin material used. Since the distortion is a direct result of the residual stresses induced in the specimens, similar magnitudes of distortion suggest that the residual stresses are

similar for all samples. Both the coordinate scans and neutron diffraction measurements show that for the weld geometry studied, there is little difference between the butt and bead-on-plate welds either in residual stress or in residual distortion. It is reasonable, therefore, to generalise between the two cases.

Effect of rolling

The residual stress distributions presented in Figure 25b show that localised rolling is capable of inducing a large compressive longitudinal residual stress along the roller path. The maximum compressive stress of around 350 MPa represents a significant fraction of the yield stress of the material (approximately 475 MPa). The distributions of stress for rolling at 100 and 200 kN are not greatly different in magnitude. However, the compressive band appears to fill out and widen at the higher value of load (see Figure 25b), suggesting that the level of residual stress is saturating at the greatest compressive stress that the material can support. This can also be seen in the plots of the longitudinal strain which occurs during rolling (Figure 26). Comparing the results for rolling at 100 and 200 kN, it is observed that while much larger transient strains occur during rolling at 200 kN, the final strain values are quite similar. Finally, Figure 27 shows that the percentage reduction in the final plate thickness along the roller path continues to increase linearly from 100 and 200 kN. The fact that this evident increase in plastic deformation is not associated with a greatly increased compressive residual stress again suggests that the compressive residual stress has a reached a saturation value. The presence, distribution and saturation of the induced residual stresses observed here is in agreement with previous work by Wang and Mote [194].
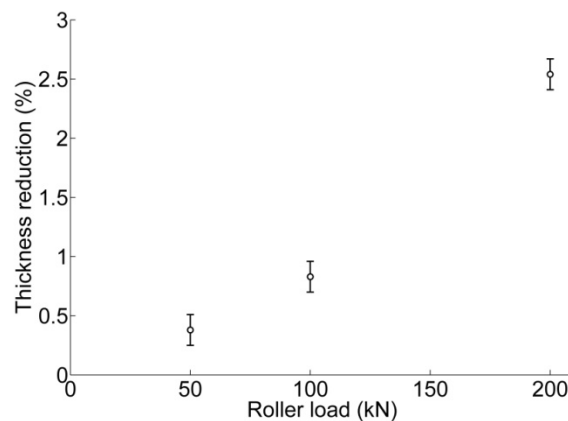
Figure 27: Average reduction in plate thickness under the roller path for different values of applied load.

It can be seen in Figure 25b that the regions of compressive stress created by rolling are well-defined by the roller width. This is especially true for rolling at 100 kN, since at the higher load of 200 kN, plastic strain is not only induced directly under the roller but also around it (see Figure 24b), which broadens the region of compressive stress. The largest gradient in longitudinal residual stress seen here is 78 MPa mm^{-1}; this occurs at

the edges of the compressive region, and results from a rolling force of 100 kN. By comparison, the largest stress gradient introduced by welding of the 3 mm plate specimens (Figure 25) is 60 MPa mm^{-1}. Therefore in theory, localised rolling of structural steel welds could produce an effect on the residual stress field of sufficient definition to almost exactly cancel residual stresses produced by welding.

One aspect of the rolling-induced stress distribution which may be relevant to the problem of welding residual stress is the ability of the process to create residual stresses close to a plate edge. It has previously been proposed that this might enable pre-tensioning methods to help reduce the formation of stresses at the weld line (see Chapter 9). The rolled specimens (shown in Figure 20) were therefore made asymmetric, with the roller closer to one of the longitudinal edges than to the other. In Figure 25b, the resulting asymmetry of the stress distribution can be seen: although no diffraction measurements were taken closer than 20 mm to the plate edge, the greatest tensile longitudinal stresses are seen on that side of the rolled region.

Finally, the presence of large positive transient strains directly adjacent to the rolled region (see Figure 26c) could also have implications for application of the rolling process to welds. Material in and around a weld seam usually contains tensile longitudinal stresses with a magnitude close to the material's yield strength. Consequently, the additional tensile strain caused by rolling adjacent to this may be enough to overload and relieve residual stress in the weld, even if it would not cause much plastic deformation adjacent to the roller in initially unstressed material. Therefore, it is likely that post-weld rolling adjacent to a weld seam (rather than directly on top of it) may also be used to relieve residual stress.

Conclusions

1. The strain change measured around the affected region during a welding or localised rolling process may be used to estimate the level of residual stress, but only in locations where elastic material behaviour may be assumed.
2. Bending due to residual distortion can cause strain measured at the surface of a weld in thin material to be unrepresentative of the mean strain through the thickness. This may be accounted for by using coordinate measurements of the distorted object to calculate and remove the portion of strain due to bending.
3. Localised high-pressure rolling of structural steel induces compressive residual stresses directly under the roller path in the direction of rolling, and tensile stresses surrounding the roller path.
4. These compressive stresses may be large – but are ultimately limited by the ability of the material to sustain them without further yielding. Saturation of the induced residual stresses occurs when rolling is carried out using a very high load.

5. The region of compressive residual stress which results from localised rolling is sharply defined, with steep stress gradients at its edges. Therefore, rolling could in principle be used to counteract the residual stress introduced by welding without also inducing additional stresses over a wider area.

Chapter 5: The effect of rolling on weld-induced residual stress

The majority of this chapter is taken from the following article:

Abstract
In this chapter, localised high-pressure rolling of gas metal arc welds to reduce residual stress has been investigated using strain gauging and neutron diffraction. Rolling was found to remove undesirable tensile stresses and even induce large compressive ones, though only when applied after, rather than during welding. Strain measurements taken during combined welding and rolling operations show that this is because material at the weld line continues to yield as it cools. This erases any beneficial effect on the stress distribution of rolling at high temperature. A method of rolling using an oscillating force is also presented, and found to be just as effective as the equivalent static-force process.

Introduction
The undesirable effects of weld-induced residual stress, discussed in Chapter 2, provide considerable motivation for designers to seek to reduce it. However, to effectively relieve or prevent the tensile stresses that form at the weld line, an expansion strain must be provided at some point in the process. Current methods that work on this principle include ultrasonic impact treatment and shot peening, which can be applied post-weld to cause localised yielding at the surface of the material (see Chapter 2). However, these are only able to cause material plasticity, and hence a beneficial change in the residual stress state, to a relatively small depth into the material - typically in the order of 1 mm for structural steels [92]. In thicker material, residual stresses induced by such methods are usually in equilibrium over the material's thickness, rather than causing the whole weld region to be stress-relieved. Therefore, while this has a beneficial effect on fatigue crack resistance at the weld surface where such treatment is applied, it is an imperfect method for distortion reduction.

High-pressure rolling of the weld line is one process that has been suggested as an alternative to peening. Applying a large compressive force in the direction normal to the welded object's surface causes a plastic expansion in the in-plane directions [3].

Rolling is able to achieve much larger strains to a much greater depth, and is simple to apply. The process may be carried out during welding - directly behind the welding heat source (here termed in situ rolling), or applied to a fully completed weld (post-weld rolling). Initial investigations into the effect of localised rolling of weld seams were carried out by Kurkin et al. in the 1980s [138, 139]. However, only recently has the process been re-examined: an experimental study by Altenkirch et al. [3] showed the dramatic effect of this method on stresses in friction-stir welds, while Wen et al. [132], Sun et al. [137] and Yang and Dong [136] demonstrated the effectiveness of the technique using finite element analysis. Altenkirch et al. and Wen et al. have indicated that post-weld rolling is far more effective at reducing residual stresses than rolling in situ [3, 132], however the reason for this is not currently known.

Rolling of the weld seam requires the application of a large force to a small area. Supporting this force means that the machine used for rolling must be of relatively heavy construction. To reduce the load on the rolling machine structure, a method of rolling using a dynamic force applied by an oscillating mass has been proposed here. In the following experiments, the effects of in situ and post-weld rolling using a constant force on residual stress formation have been assessed. Rolling using dynamic force is also demonstrated, and compared with the equivalent constant-force process.

Experimental

Welded specimens

Rectangular plates of hot-rolled S355JR structural steel, with overall dimensions 750 x 300 x 6 mm, were used for the experiments. The yield stress of this material was approximately 474 MPa (see Appendix D). For each specimen, a linear single-pass bead-on-plate weld, 600 mm long, was made using Gas Metal Arc Welding (GMAW) with the parameters shown in Table 4. This set of parameters was chosen so as to just achieve full penetration of the weld through the plate thickness. During welding, the plates were held flat by a vacuum clamping system: this applied an even suction to the entire underside of each specimen, except for a region directly underneath the weld line, 48 mm in width, where a copper backing bar was used (see Figure 28a). The clamping was maintained for 600 seconds after completion of the weld, or in the case of specimens treated with post-weld rolling, 600 seconds plus the duration of the rolling operation (approximately 72 seconds). Preliminary experiments showed that after this time, the temperature distribution in the welded specimens had fully equilibrated, and was approximately 30°C throughout the specimen.

Table 4: Welding parameters used for bead-on-plate welds in 6mm-thick S355 steel.

Process:	GMAW (Pulsed)
Mean current:	328 A
Mean voltage:	35.1 V
Welding speed:	8.33 mm s^{-1}
Filler wire feed:	250 mm s^{-1}
Filler wire:	ISO 14341-A-G 3Si1, 1.0 mm dia.
Shielding gas rate:	0.17 L s^{-1}
Shielding gas composition:	20% CO_2, 2% O_2, balance Ar

Rolling

Both in situ and post-weld rolling with a constant force, and post-weld rolling with a dynamic force, were investigated in this study. Figure 28 shows the apparatus used for weld seam rolling: this machine is capable of rolling using a constant force, or applying a time-varying force using an oscillating mass in the manner described in the section below. A hydraulic cylinder applies a vertical force through a single roller supported in a fork assembly. When rolling with a constant force, the force is set directly by changing the cylinder pressure. In dynamic-force mode, the loading cycle is a function of several parameters including the cylinder pressure, oscillating mass, and hydraulic valve timings. The applied force is monitored at a frequency of 500 Hz by a ring-type load cell installed between the end of the hydraulic cylinder shaft and the upper part of the roller fork (see Figure 28b).
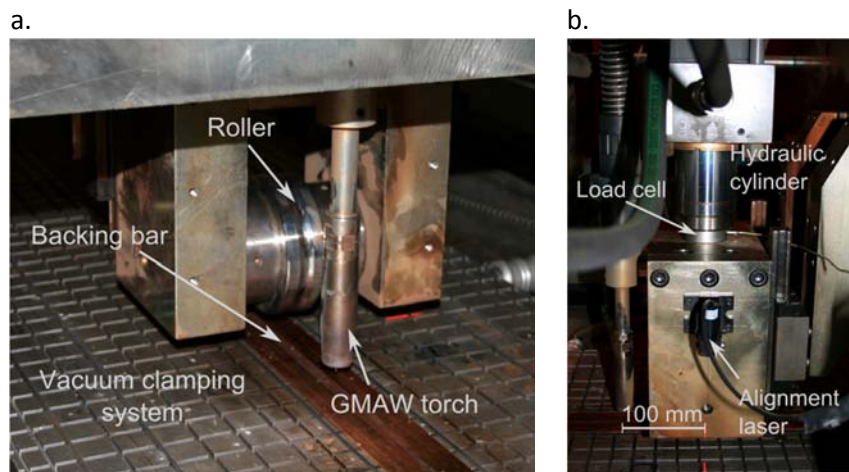
Figure 28: Apparatus for localised rolling of weld seam: (a.) front view, (b.) side view.

To carry out a welding and/or rolling operation the workpiece remains static while the crossbeam, with the roller head and welding torch attached, is translated by a linear drive system. The machine applies no torque to the roller, which is left free to rotate as it moves over the workpiece. The roller used here (see Figure 28a) was of 100 mm diameter and 30 mm axial width, and made from hardened BS4659 BH13 tool steel. A shallow groove around the circumference of the roller was used to accommodate the

weld seam. Figure 29 shows a comparison of the roller groove with the mean profile along the length of an un-rolled weld, taken from laser coordinate measurements. Visible plastic deformation of the weld seam occurs during rolling at higher loads, and the roller groove acts to contain the deforming material, producing a lower, wider weld seam. Under all rolling conditions, the roller acts only on the top of the weld seam (approximately 12 mm in width) and does not come into contact with the plate surface at either side.

Figure 29: Contoured roller to accommodate a weld seam. The initial weld profile is taken from laser coordinate measurements of an un-rolled weld.

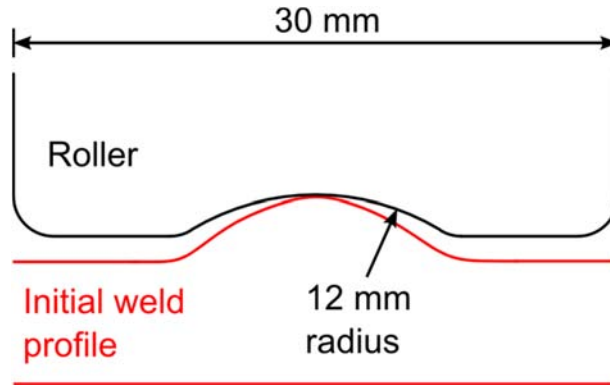Specimens were produced without rolling, with in situ rolling at static loads of 25, 50 and 100 kN, and with post-weld rolling at static loads of 25, 50, 100, and 150 kN. Post-weld rolling with a dynamic load was used to produce a single additional specimen. The parameters used for this were designed to produce a peak applied force of 50 kN, using an oscillating mass of 1500 kg and an oscillation frequency of approximately 3.8 Hz.

For in situ rolling, the GMAW torch was positioned 100 mm in front of the roller axis (as shown in Figure 28b), and rolling took place as the weld was carried out. Since the travel speed used for welding was 8.33 mm s^{-1}, the centre of the roller passed over the weld metal approximately 12 seconds after it was deposited. A finite element model of the welding process, calibrated using prior experimental temperature measurements, predicted the temperature here to be 890°C. The same travel speed (8.33 mm s^{-1}) was also used for post-weld rolling, in which case the crossbeam was returned to the start position once the weld was complete, ready to carry out the rolling operation after 600 seconds. For all specimens, only one welding and one rolling pass was used.

Application of dynamic load

A system for rolling by applying a time-varying force using an oscillating mass is shown Figure 30. The hydraulic cylinder used apply the rolling force, instead of being attached directly to the crossbeam, is coupled to a large mass which is allowed move freely in the vertical direction. With the roller in contact with the workpiece, rapidly extending

the cylinder causes the mass to accelerate upwards. This acceleration causes a peak force:

Equation 6

$$P = m(a + g)$$

where a is the maximum upwards acceleration of mass m, and g is the gravitational acceleration. As the mass approaches the top of its travel, the pressure used to extend the hydraulic cylinder is removed and the mass returns to its initial position under gravity, compressing the cylinder. Therefore in this arrangement, the crossbeam acts only to guide the roller-cylinder-mass system, and does not carry any significant vertical load. On the machine used for this experiment, the oscillating mass can either be bolted stationary to the crossbeam to enable rolling at a constant force, or left free to move vertically for the oscillating mode.
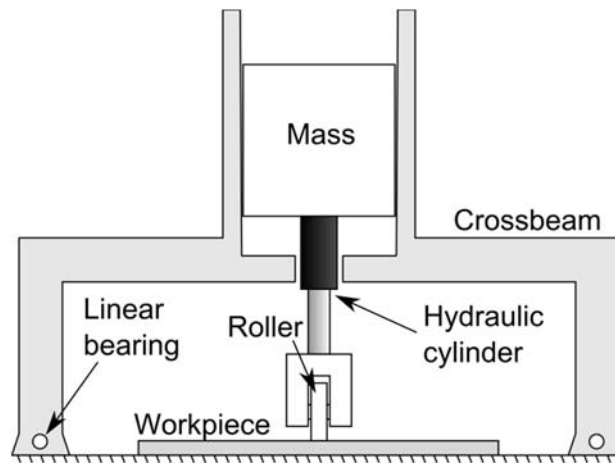
Figure 30: Dynamic-load rolling mechanism with an accelerated mass actuated by a hydraulic cylinder.

Transient strain measurement

Strain gauges were used to investigate the differences in residual stress development during post-weld and in situ rolling: a comparison was made between the two techniques operating with a static load of 50 kN. The method of transient strain measurement was similar to that described in Chapter 3, except that a slightly different strain gauge arrangement was used. The locations where strain measurements were taken are shown in Figure 31. Elevated-temperature Ni-Cr metal foil gauges (Micro Measurements WK-series) were used at 20, 30, 40 and 50 mm from the weld centre line, while standard types were used elsewhere. Rosette gauges were used to simultaneously measure strain in three in-plane directions, and hence to determine the principal strains. However, due to the limited number of measurement channels available, it was only possible to attach four rosettes and four uniaxial gauges per specimen. Consequently, two specimens were required for each of the in situ and post-weld rolling conditions: between them, each pair of specimens had a rosette

positioned at every measurement location. Individual 3-wire quarter-bridge circuits were used for each strain gauge, and the measurements were logged at a frequency of 2 Hz using a National Instruments DAQ-mx modular data acquisition unit. Thermocouples were also used to measure the temperature at each strain gauge location in Figure 31.

The total state of strain (ε) in any material may be decomposed into strain contributions due to elastic deformation (ε_e), plastic deformation (ε_p), and thermal dilation (ε_t) [165]:

Equation 7

$$\varepsilon = \varepsilon_t + \varepsilon_e + \varepsilon_p$$

Since the strain gauges used here were of a type which compensate for thermal dilation, the strain measured at each point represented only the elastic-plastic component of strain ($\varepsilon_e + \varepsilon_p$). Therefore, from the strain rosette data, the time-varying state of stress at each gauge location could be calculated using the plane-stress form of Hooke's law. The von Mises yield criterion was used to verify that no material yielding occurred at the strain gauge locations (i.e. that $\varepsilon_p = 0$), and hence that the assumption of linear elasticity inherent in the calculation of stress was valid. The techniques used here have been described in greater detail in Chapter 3 [195].
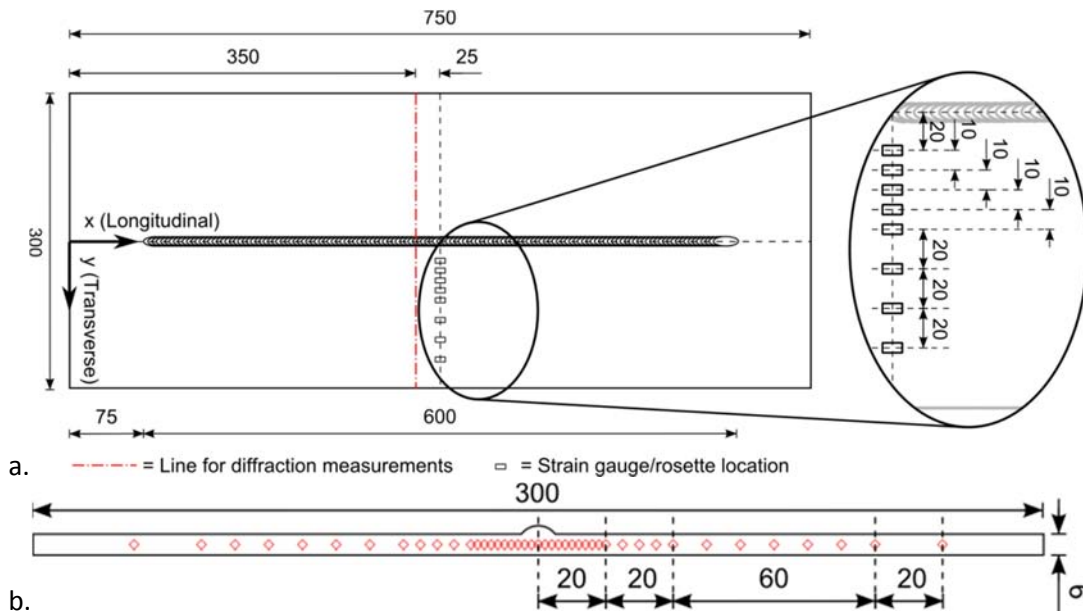
Figure 31: Measurement locations on the welded specimens. (a.) Plan view, with expanded view of strain gauge positions. (b.) Cross-section view showing gauge volumes used for neutron diffraction measurements. All dimensions in mm.

Residual strain measurement

Neutron diffraction may be used to measure inter-atomic spacings in polycrystalline materials, and from this infer residual elastic strains, from which residual stresses can

be calculated. The process of residual stress measurement using this technique is described in detail elsewhere and will not be repeated here [196, 71]. For this experiment, measurements were carried out using the SALSA monochromatic neutron strain diffractometer at the Institut Laue-Langevin, Grenoble, France [189]. Residual elastic strains were measured at 43 locations on a transverse line close to the mid-length of each specimen, as shown in Figure 31[13]. Lattice spacing in the longitudinal (x), transverse (y) and normal (z) directions was measured at each point: the ferrite {211} plane was used for all of the measurements, since this plane has a low sensitivity to intergranular strains, and is therefore well-representative of strain in the bulk material [197, 193]. Cuboid gauge volumes of 2x2x2 mm were used for measurement in the longitudinal direction, and 2x20x2 mm for the transverse and normal directions. These volumes were defined using either a 2 or 20 mm primary collimator, with a secondary collimator with a 2x2 mm focus.   A neutron wavelength of 1.644 Å was used, giving a scattering angle (2θ) close to 90°. All measurements were taken from the nominal mid-plane of the specimen (3 mm depth), and through-wall scans were used to accurately position the gauge volume in the through-thickness direction. Reference measurements of the unstressed lattice parameter (d_0) were taken from unstressed comb samples cut from nominally identical plate specimens in the manner recently discussed by Withers et al. [198] and Altenkirch et al. [192]. To account for the effect of the varying degree of plastic deformation on the single diffraction peak position used, different reference specimens were used for different rolling loads. Also, to counteract any effect of anisotropy in the unstressed lattice parameter, separate d_0 measurements were taken in the longitudinal, transverse and normal directions.

Residual stresses were determined from the strains by assuming isotropic elastic properties and a general triaxial stress state [199]:

Equation 8

$$\sigma_{xx} = \frac{\nu E}{(1 + \nu)(1 - 2\nu)}\left\{\varepsilon_{xx} + \varepsilon_{yy} + \varepsilon_{zz}\right\} + \frac{E}{1 + \nu}\varepsilon_{xx}$$

Where σ_{xx} is stress in the longitudinal (x) direction, ε_{xx}, ε_{yy} and ε_{zz} are strains measured in the longitudinal, transverse and normal directions, and E and ν are the Youngs' modulus and Poisson ratio respectively. Analogous equations hold for σ_{yy} and σ_{zz}. Kröner model predictions of the material's plane-specific elastic constants (E = 225.5 GPa, and ν = 0.28) were used in this calculation [196]. Uncertainty in the stress

---

[13] For the specimen rolled post-weld at 25kN load, measurements were instead taken every 2 mm all the way across the section to 130mm from the weld line. This can be seen in Figure 32a and c.

results was evaluated by propagation of diffraction angle uncertainties through the system of equations used for calculating the stress, in the manner described by Wimpory et al. [200, 201].

Results

Residual stress due to in situ and post-weld rolling

Longitudinal residual stress distributions resulting from rolling under various loads are shown in Figure 32a and b. For post-weld rolling (Figure 32a), a continuous decrease is observed at the weld line for increasing values of load, accompanied by a broadening of the region of induced compressive stresses. By contrast, in situ rolling (Figure 32b) has essentially no effect on the residual stress distribution, regardless of the force applied.

Transverse residual stresses after post-weld rolling are shown in Figure 32c, but do not exceed ±100 MPa anywhere on the specimens. Post-weld rolling at high loads (100 and 150 kN) gives a small region of compressive transverse stress at the weld centreline. However, the most important point to note is that the process produces no significant tensile residual stresses in the transverse direction, which could have a detrimental effect on fatigue performance. Due to the necessity of stress equilibrium, this result only represents the cross-section over which these stresses were measured: it is expected that there would be a corresponding tensile state of transverse stress elsewhere along the weld line.
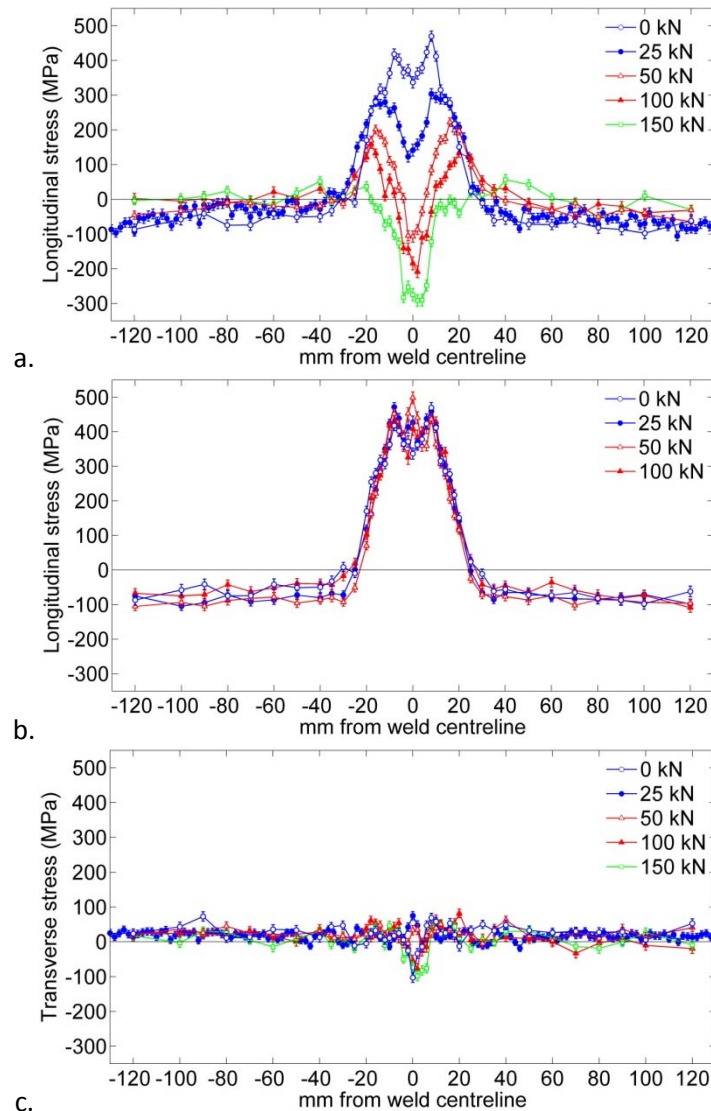
Figure 32: Comparison of residual stress distributions for different roller loads, measured using neutron diffraction. (a.) Longitudinal stress after post-weld rolling. (b.) Longitudinal stress after *in situ* rolling. (c.) Transverse stress after post-weld rolling.

Transient behaviour

Analysis of the strain gauge measurements was used to find the transient biaxial state of stress during the welding and rolling operations. The longitudinal stress component is shown in Figure 33a and b. Data is given only up to a minimum of 40 mm from the weld line, since in the case of both the in situ and post-weld rolling specimens, the strain rosettes at 20 and 30 mm from the weld line were affected by material plasticity and radiant heat from the welding arc, rendering the data invalid. The general form of the stress distribution during welding and cooling (i.e. up to around 600 seconds) is very similar regardless of whether or not in situ rolling is used. This characteristic distribution of stress is generated by the changing distribution of temperature, and the consequent pattern of thermal dilation and deformation, during the welding process. This was discussed in greater detail in a previous paper [195].

69

The effect of post-weld rolling is visible in Figure 33a at approximately 672 seconds. The modest compressive residual stresses which exist here after cooling are reduced almost to zero. For equilibrium, the distribution of longitudinal stress must sum to zero over the transverse section. Therefore, this reduction in compressive stress indicates that the corresponding tensile stresses in the weld region must also be reduced, as is also seen in the longitudinal residual stress profiles in Figure 32a. Finally, another important aspect of Figure 33a and b is that they show that the stress distribution continues to develop significantly for at least 300 seconds after the arc passes. Since the contraction of material at the weld line is more rapid than that of the surrounding area, this suggests that the weld line material yields continuously over this period.

Figure 33c shows a magnified view of the stresses at 40 and 50 mm during and immediately after welding (which takes place from -36 to +36 seconds). In situ rolling can be seen to affect the transient development of stress: the longitudinal plastic strain provided by rolling at the weld line means that thermal contraction of the material there does not cause such great stresses in the surrounding material, and so the maximum compressive stresses seen for the case of in situ rolling are slightly lower. However, during cooling the longitudinal stresses settle to roughly the same values as for unrolled specimens. By contrast, no further cooling occurs after post-weld rolling (Figure 33a), and so its effect is permanent.
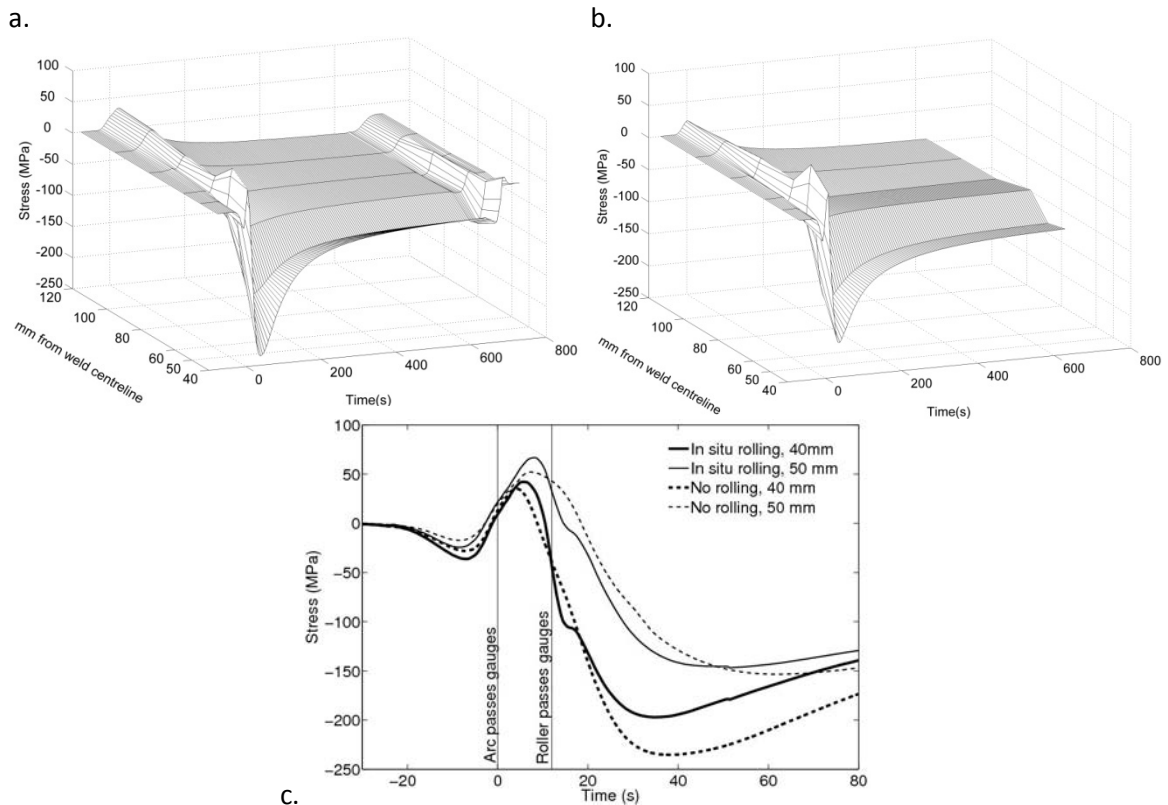
a.

b.

c.

Figure 33: Longitudinal stress calculated from strain rosette measurements during (a.) welding with post-weld rolling, and (b.) welding with in situ rolling. (c.) shows a magnified view of stresses at 40 and 50 mm from the

70

Dynamic loading

The force applied during post-weld dynamic-load rolling over a 1-second interval can be seen in Figure 34a. Although the mass oscillates at a frequency of 3.8 Hz, the figure indicates that there are additional higher-frequency variations in the applied force. These are probably related to the natural oscillation frequencies of the system which comprises of the mass and the compliance of the hydraulic cylinder and roller fork. Together, the roller travel speed (8.33 ms^{-1}) and the oscillation frequency (3.8 Hz) imply that a complete oscillation cycle occurs for every 2.2 mm of weld length. The measured residual stress distribution from this type of loading (shown in Figure 34b) is very similar in both magnitude and distribution to the one caused by rolling with a constant load of 50kN.

a.

b.
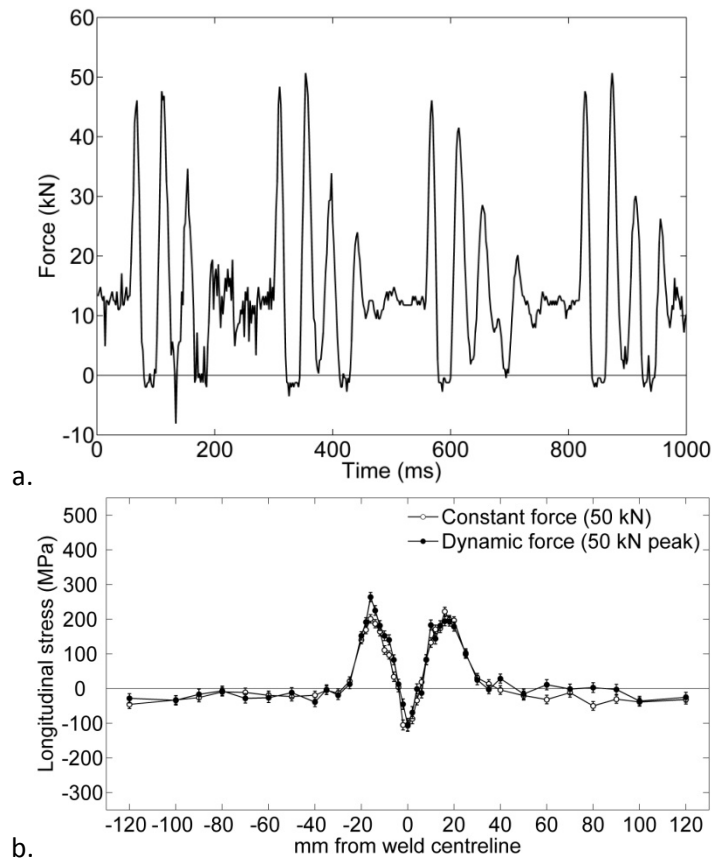
Figure 34: (a.) Time-varying force applied during dynamic-load rolling, and (b.) comparison of residual stress distributions resulting from constant and dynamic-load rolling, measured using neutron diffraction.

Discussion

Stress field development during in situ and post-weld rolling

As can be seen from Figure 32a, plastic deformation at the weld line from post-weld rolling can provide the elongation required to relieve tensile residual stresses.

Furthermore, this elongation can be sufficient to produce significant compressive residual stresses. This is in agreement with the modification of the residual stress field previously observed by Kurkin and Anufriev [139] and Altenkirch et al. [3].

While post-weld rolling can completely invert in the distribution of residual stress in the weld, in situ rolling (Figure 32b) has a negligible effect. The measurements of transient stress shown in Figure 33 suggest the reason for this: the magnitude of the thermal contraction strain which occurs in the material at the weld line during cooling is much larger than any residual elastic strain that can be supplied by in situ rolling, since the latter is limited by the yield strain of the material. Furthermore, significant thermal contraction continues for a long time (around 300 seconds), as the material cools. Therefore, any positive strain supplied by is situ rolling is irrelevant, since this would be caused anyway by yielding due to thermal contraction during cooling. On the other hand, no further cooling occurs after post-weld rolling, so no subsequent yielding of the rolled region takes place, and therefore the mechanically-induced strain remains.

A rough approximation of the contraction strain encountered during cooling can be calculated using the material's coefficient of thermal expansion (1.22 x 10^{-5} K^{-1} at ambient temperature) and the temperature during in situ rolling (890°C, from finite element predictions). Neglecting the effects of microstructural change, this indicates a thermal contraction of around -1.06 % during cooling from the in situ rolling temperature to room temperature. Since the maximum effective strain which can be provided by rolling is limited by the yield strain of the material (around 0.2 %), the effect of thermal contraction will dominate the final stress field. An important consequence of this is that any mechanical process, such as rolling or peening, which is applied exclusively at high temperature to the mechanically constrained material of a weld, will necessarily be ineffective at relieving residual stresses. Such processes instead must be applied at a temperature low enough to avoid subsequent gross plasticity.

Just as the effects of post-weld and *in situ* rolling on the residual stress state are very different, so are the effects of these processes on the weld's mechanical properties and microstructure. These aspects are discussed in Chapter 7, where it is shown that while post-weld rolling causes work-hardening of the weld, *in situ* rolling can cause grain refinement in the fusion zone. Consequently, the variation in mechanical properties of the material across the weld is defined not only by the welding process, but also by the rolling parameters.

Although post-weld rolling has been applied successfully here to structural steel and has previously been used on 2000-series aluminium alloy [3], the relatively large

deformations resulting from it might cause cracking in less ductile materials. If necessary, in situ rolling at an intermediate temperature (much lower than used here) might be used instead, but this would come at the cost of decreased stress-reduction effectiveness compared with post-weld rolling. In situ rolling also has potential applications other than residual stress control. For example, it could be used to forge the weld seam; smoothing it to remove geometric stress concentrations, or to give it a different cross-sectional profile (see Chapter 8). This might be used to improve the weld's fatigue performance or its appearance, for example.

Load requirement for residual stress relief

Larger rolling loads cause a higher degree of plastic deformation and therefore have a greater effect on the residual stress distribution, as shown in Figure 32. In addition to the greater magnitude of the induced compressive stresses, the region of compressive stress broadens with increasing roller force – an observation predicted in a recent modelling study by Wen et al. [132]. Despite being applied only to the top of the weld seam, which has a width of approximately 12 mm, rolling at higher loads causes yielding over a much wider area. Also, since the neutron diffraction measurements were taken from the nominal mid-thickness of the 6mm-thick specimen plates, and large compressive stresses are observed there after post-weld rolling, it is probable that rolling causes plasticity throughout the plate's thickness – this view is supported by the hardness measurements presented in Chapter 7 and the additional residual stress measurements in Chapter 8. However, at some point there must be a practical upper limit to the thickness of welds which can be treated in this way.

Although dynamic-load rolling was only carried out using a single value of peak force (50 kN), the residual stress distribution which resulted from this is almost identical to the corresponding distribution for static-load rolling at the same force (see Figure 34b). The process therefore seems not to be detrimentally affected by the time-varying nature of load application in dynamic-load rolling.

Conclusions

1. High-pressure post-weld rolling of weld seams can give a dramatic reduction in the tensile longitudinal residual stresses normally encountered at the weld line. By using higher values of rolling load, large compressive stresses may be created in and around the weld.

2. The region over which compressive residual stresses are induced by post-weld rolling can be much wider than the area of contact which the roller has with the weld bead surface.

3. Rolling of the weld seam at high temperature as it is welded is ineffective at reducing residual stresses, due to the subsequent yielding of material in the weld region as it cools. For the same reason, any other mechanical process

applied exclusively to the weld region at high temperature as a weld is carried out will be similarly ineffective.

4. A dynamic roller force, rather than a constant one, can be used to give the same effect on the residual stress distribution in a weld. This reduces the structural requirements of the rolling machine.

Chapter 6: Neutron diffraction analysis of complete residual stress tensors a rolled weld

The majority of this chapter is taken from the following article:

Abstract

Mitigation of residual stress in an arc weld by high-pressure rolling of the weld seam has been investigated using neutron diffraction. Rolling was found to greatly improve the residual stress distribution, causing significant compressive stresses at the weld line. A novel aspect of the data presented is that at each measurement location, normal strains in nine separate directions were evaluated, enabling calculation of the complete strain and stress tensors. It is thus confirmed that the principal stress directions generally lie close to the specimen coordinate axes (i.e. that they are well-aligned with the direction of welding and rolling), and that rolling does not cause any significant additional residual stresses which could have detrimental effects. Methods of uncertainty estimation and the applications of full-tensor residual stress measurements are also discussed.

Introduction

Rolling of welds

In the previous chapter, it was shown that post-weld localised high-pressure rolling can be used to dramatically reduce, or even reverse, tensile residual stresses at a weld seam [3, 202]. Although the longitudinal stress component typically dominates the overall residual stress state caused by welding, the other components may be significant. Especially in assessing the effectiveness for the rolling process, it is important to verify not only that the longitudinal tensile stress is reduced, but also that all other stress components remain at acceptable levels. Therefore in this study, all components of the stress tensor were evaluated at each measurement location.

Strain tensor evaluation

In the general three-dimensional case, assuming infinitesimal deformations only, stress and strain may be represented by the following 9-component Cauchy tensors:

Equation 9

$$\boldsymbol{\sigma} = \begin{bmatrix} \sigma_{xx} & \tau_{xy} & \tau_{xz} \\ \tau_{yx} & \sigma_{yy} & \tau_{yz} \\ \tau_{zx} & \tau_{zy} & \sigma_{zz} \end{bmatrix}$$

$$\boldsymbol{\varepsilon} = \begin{bmatrix} \varepsilon_{xx} & \varepsilon_{xy} & \varepsilon_{xz} \\ \varepsilon_{yx} & \varepsilon_{yy} & \varepsilon_{yz} \\ \varepsilon_{zx} & \varepsilon_{zy} & \varepsilon_{zz} \end{bmatrix}$$

It can be shown that the stress tensor is symmetric in the absence of body moments [203]. If this is the case, then in an elastically isotropic material, the strain tensor must also be symmetric. Therefore, to determine the six independent components of the stress tensor at a point, at least six (scalar) strain measurements must be made, and the elastic properties of the material known [71].

Most methods of residual stress determination are limited in terms of the strain directions they can measure. For example, in the contour method of residual stress determination, only the component of stress normal to a cutting plane is calculated [68]. Therefore, a useful characterisation of the stress state requires either of the following:

1. Appropriate assumptions to be made regarding the stress state, based on the symmetry and/or boundary conditions of the measured object. For example, in thin materials or for measurements made at the surface of an object, a state of plane stress may be assumed. In this case, three components of the stress tensor are assumed to be zero (σ_{zz}, τ_{xz} and τ_{yz}, where the z axis is perpendicular to the surface plane), which reduces the number of strain measurements required by three.
2. It is accepted that the stress tensor cannot be fully determined, but that one or more components of it may nevertheless be useful; for the purpose of comparison with a numerical model, for instance.

Neutron diffraction, however, has the notable advantage that by using different orientations of the specimen it can, in an ideal case, measure strain in any direction. The basic principles of using neutron diffraction for strain measurement are outlined elsewhere [71, 4]. Since diffraction methods work by comparing the inter-planar distances of the atomic lattice, they can only be used to measure normal strains and not shear strains. However, a normal strain measured in the arbitrary direction (ε_{lmn}) is related to the six components of the strain tensor by [204, 196]:

Equation 10

$$\varepsilon_{lmn} = \varepsilon_{xx}l^2 + \varepsilon_{yy}m^2 + \varepsilon_{zz}n^2 + 2\varepsilon_{xy}lm + 2\varepsilon_{xz}ln + 2\varepsilon_{yz}mn$$

Where l, m and n are direction cosines resulting from a rotation about the x, y and z axes respectively. Multiple measurements of normal strain in different directions therefore lead to a system of linear equations [205]:

Equation 11

$$\boldsymbol{\varepsilon}_{lmn} = \boldsymbol{A}\boldsymbol{\varepsilon}$$

Where $\boldsymbol{\varepsilon}_{lmn}$ is a vector of measured normal strains, $\boldsymbol{\varepsilon}$ is six-element vector of strain tensor components in sample coordinate system (xyz), and $\boldsymbol{A}$ is a matrix of direction cosines as per Equation 10. In the case where there are six or more measurements, and they are not all coplanar (i.e. the resulting equations are linearly independent), the system may be solved for $\boldsymbol{\varepsilon}$ [205].

Evaluation of arbitrary strain tensors in this way has been technically possible using neutron diffraction for many years: some initial experiments were made by Priesmeyer and Schroder [206] and Lorentzen and Leffers [207] in the early 1990s. Other notable studies include those of Winholtz and Krawitz [208], who investigated stress relaxation in a circumferential aerospace weld by heat treatment, and Robinson et al. [209] who used a general strain tensor measurement to confirm the principal directions of residual stress caused by water-quenching of an aluminium alloy block. However apart from these exceptions, in almost all neutron diffraction measurements involving a general three-dimensional state of stress, only strains in three mutually orthogonal directions are measured [71]. These may be used to calculate the corresponding direct stresses using the three-dimensional Hooke's law equations for an elastically isotropic material [196]:

Equation 12

$$\sigma_{ii} = \frac{E}{(1+v)}\left[\varepsilon_{ii} + \frac{v}{(1-2v)}\left(\varepsilon_{11} + \varepsilon_{22} + \varepsilon_{33}\right)\right]$$

Where E and v are the Young's modulus and Poisson ratio respectively, and $i = 1,2,3$ indicates the components of stress and strain relative to chosen axes 1,2,3. Normally, the shear components are not evaluated. Instead, either symmetry assumptions are used to show that the measured stresses are principal (option 1 above) and hence that the shear components are negligible, or finite shear components are simply ignored when knowledge of the direct stresses alone is deemed sufficient (option 2).

In the present work, complete strain tensor evaluation using neutron diffraction has been used to investigate the state of residual stress in two structural steel welds: one conventional and one treated with post-weld rolling of the weld seam. The stress

distribution resulting from post-weld rolling is discussed with reference to the 'as-welded' case, and aspects of the strain tensor calculation are reviewed.

Experimental

Specimens

Two bead-on-plate weld specimens were manufactured using 6mm-thick plates of hot-rolled S355JR structural mild steel in the configuration shown in Figure 35. The properties of the plate material are discussed in Appendix D. Single-pass pulsed gas metal arc welding was used, with the parameters given in Table 5. These parameters were designed to produce a full-penetration weld, and resulted in a weld seam width of approximately 12 mm. One of the specimens was simply welded and left to cool, but for the other specimen high-pressure localised rolling was applied after cooling in order to modify the residual stress state. During rolling, a constant 100 kN force normal to the plate surface was applied to the raised weld seam via a roller with a 100 mm diameter, and the cross-sectional profile shown in Figure 36. Throughout the process the roller only contacted the top of the weld seam; there was no contact between the roller and parent plate adjacent to the weld. The roller was moved over the weld seam once, at a speed of 8.33 mm s^{-1}. Further details of the rolling process are provided in Chapter 5, and an analysis of the mechanical properties of the welds is given in Chapter 7.
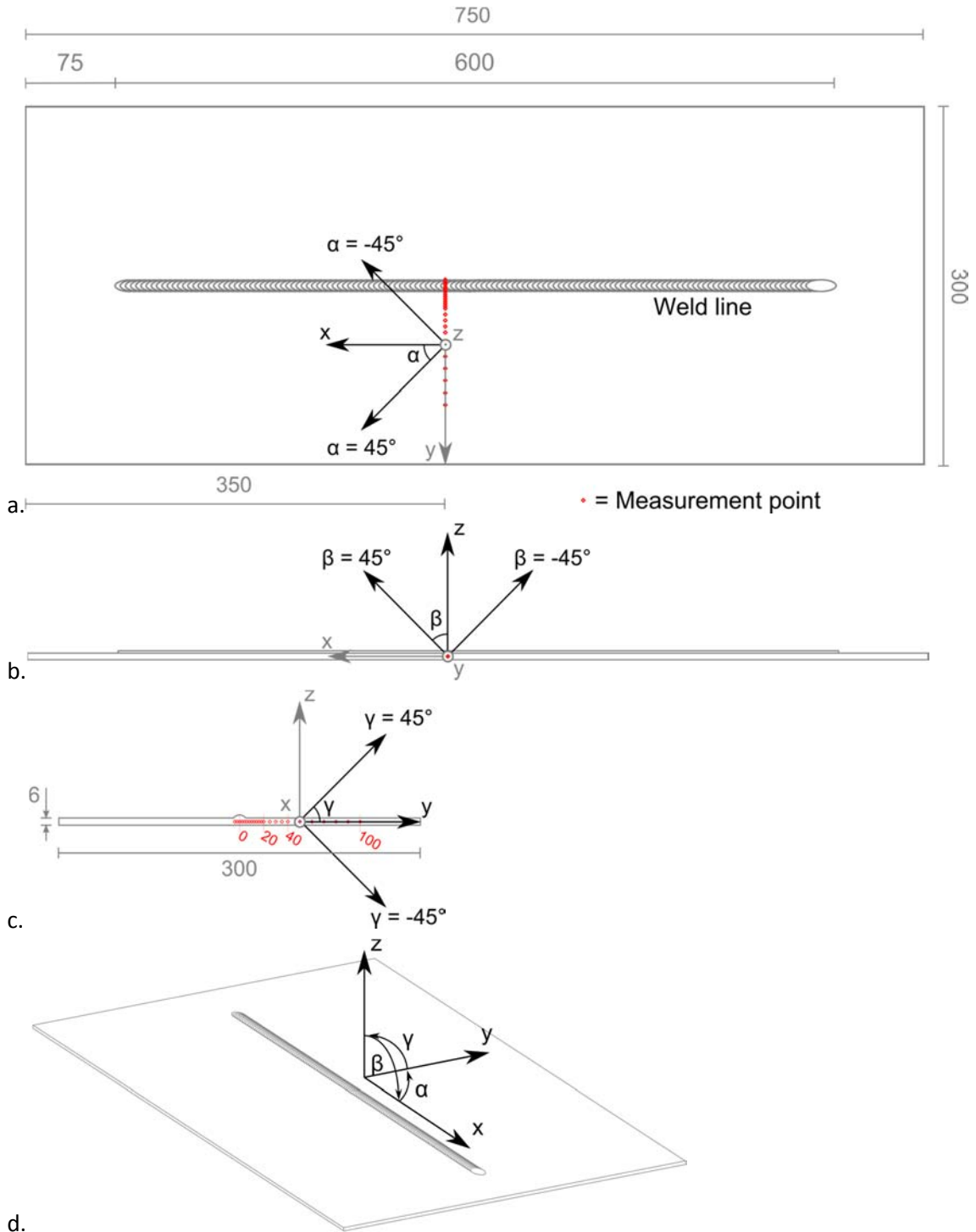
Figure 35: Plate specimen; the front, side and end views in (a-c.) each show three of the nine total measurement directions. Measurement directions are shown as black arrows, with other geometry in grey. The sample coordinate system is shown in (d.).

Table 5: Welding parameters used for both specimens.

Process:	GMAW (Pulsed)
Power supply:	Fronius TransPuls Synergic 5000
Mean current:	328 A
Mean voltage:	35.1 V
Welding speed:	8.33 mm s^{-1}
Filler wire feed:	250 mm s^{-1}
Filler wire diameter:	1 mm
Shielding gas flow rate:	166.7 ml s^{-1}
Shielding gas composition:	20% CO_2, 2% O_2, balance Ar
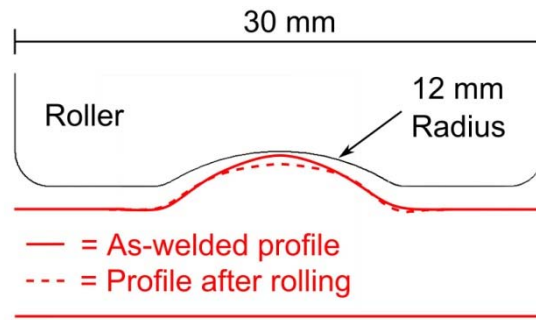
Figure 36: Roller geometry, and comparison of weld seam profiles for the two specimens (each averaged from laser coordinate measurements).

Measurement process

The SALSA neutron diffractometer at the Institut Laue Langevin, France [189] was used to measure residual elastic strain in nine directions at 23 points on each of the two specimens (shown in Figure 35). The lattice spacing (d) of the ferrite {211} plane was determined using a neutron wavelength of 1.644Å. A cuboid gauge volume 2x2x2 mm^3 in size was defined using both primary and secondary collimators. For all measurements, the gauge volume was located on mid-plane of the specimen plate; through-wall scans were used to position the gauge volume accurately in the through-thickness direction. The lattice spacing measurements were then combined with measurements of stress-free lattice spacing (d_0) to calculate strain, using the following equation.

Equation 13

$$\varepsilon_{lmn} = \frac{d_{lmn} - d_0}{d_0}$$

Position-dependant measurements of the stress-free lattice spacing were made using comb samples cut by electrical-discharge machining from nominally identical

specimens, in the manner commonly used for residual strain measurements of this type [198]. Separate reference combs were used for the as-welded and rolled cases, to eliminate the possibility of an offset in the measured Bragg angle due to diffraction peak broadening caused by the additional plasticity undergone by the rolled weld. To reduce the possibility of texture effects, separate d_0 measurements were taken in the three directions corresponding to the sample coordinate axes, and these values were interpolated to yield representative d_0 values for the six off-axis measurement directions. Such measurements were carried out at 17 locations on each unstressed sample, ranging from -4 to 40 mm in displacement from the weld centreline. For the measurements beyond 40 mm, i.e. well outside of the weld heat-affected zone, the d_0 for each orientation was assumed to be invariant and was extrapolated at a constant value (see Figure 37). Relatively little variation in unstressed lattice spacing was encountered in either weld.

a.   b.
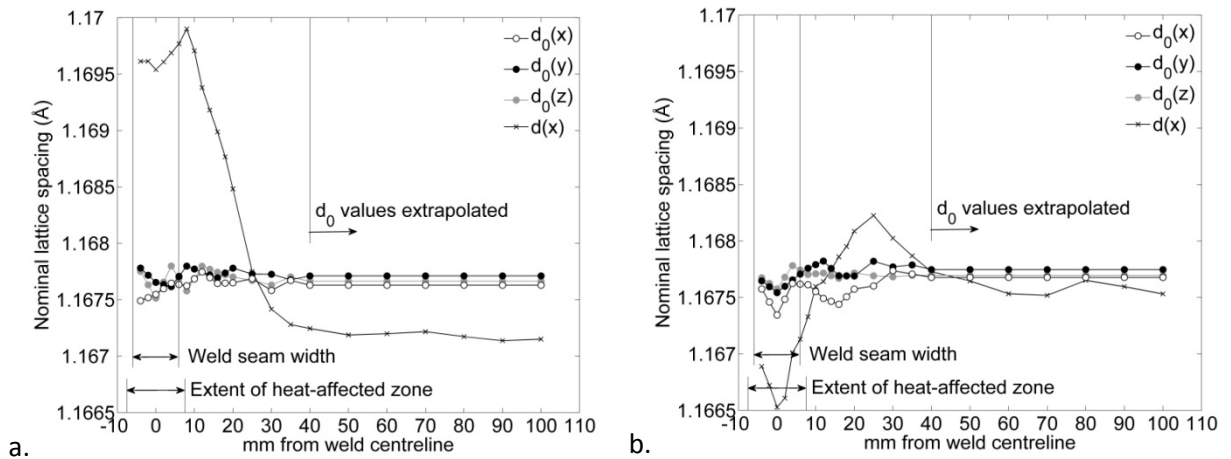
Figure 37: Variation in the unstressed αFe{211} lattice spacing d_0 measured in three orthogonal directions (see Figure 35), across (a.) normal and (b.) rolled welds. The stressed lattice spacing for the longitudinal direction $d(x)$ is also shown for comparison. Statistical uncertainty associated with diffraction peak fitting is approximately ±3.5x10^{-5} Å.

The specimen coordinate system and the nine directions in which normal strains were measured are shown in Figure 35. The measurement directions are also summarised in Table 6. It should be noted that the direction of each of the six off-axis measurements can be represented by a single rotation of ±45° about one of the axes. Approximately 13 hours of neutron counting time was required for all measurements in each plate specimen (excluding d_0 measurements) – significantly more than the approximately 3.5 hours required to scan the same points in only three directions.

81

Table 6: Measurement angles for the nine directional residual strain measurements at each measurement point (see also Figure 35).

Measurement	Rotation relative to:	α	β	γ
1	x axis	-45°	0°	0°
2	x axis	0°	0°	0°
3	x axis	45°	0°	0°
4	y axis	0°	-45°	0°
5	y axis	0°	0°	0°
6	y axis	0°	45°	0°
7	z axis	0°	0°	-45°
8	z axis	0°	0°	0°
9	z axis	0°	0°	45°

Strain tensor calculation

At each measurement location, a system of nine linear simultaneous equations (as in Equation 11) was constructed using the nine measured normal strains and corresponding angles. The rotation cosines l, m, n were found from the transformation matrices representing rotation about the x, y and z axes, which are, respectively:

Equation 14

$$R_x = \begin{bmatrix} 1 & 0 & 0 \\ 0 & \cos\gamma & -\sin\gamma \\ 0 & \sin\gamma & \cos\gamma \end{bmatrix}$$

$$R_y = \begin{bmatrix} \cos\beta & 0 & \sin\beta \\ 0 & 1 & 0 \\ -\sin\beta & 0 & \cos\beta \end{bmatrix}$$

$$R_z = \begin{bmatrix} \cos\alpha & -\sin\alpha & 0 \\ \sin\alpha & \cos\alpha & 0 \\ 0 & 0 & 1 \end{bmatrix}$$

Since each measurement direction can be represented by a single rotation of one axis about another, the corresponding direction cosines can be found straightforwardly by multiplying the unit vector of the starting axis by the appropriate rotation matrix. For example, the direction cosines (l_α, m_α, n_α) for the x-axis ($\hat{\imath}$) subjected to rotation (R_z) about the z-axis are given in the first equation below.

Equation 15

$$\begin{bmatrix} l_\alpha \\ m_\alpha \\ n_\alpha \end{bmatrix} = R_z\hat{\imath} = \begin{bmatrix} \cos\alpha \\ \sin\alpha \\ 0 \end{bmatrix}$$

82

$$\begin{bmatrix} l_\beta \\ m_\beta \\ n_\beta \end{bmatrix} = R_y \widehat{k} = \begin{bmatrix} \sin \beta \\ 0 \\ \cos \beta \end{bmatrix}$$

$$\begin{bmatrix} l_\gamma \\ m_\gamma \\ n_\gamma \end{bmatrix} = R_x \widehat{j} = \begin{bmatrix} 0 \\ \cos \gamma \\ \sin \gamma \end{bmatrix}$$

Equation 11 then becomes:

Equation 16

$$\begin{Bmatrix} \varepsilon_{\alpha_i} \\ \vdots \\ \varepsilon_{\beta_i} \\ \vdots \\ \varepsilon_{\gamma_i} \\ \vdots \end{Bmatrix} = \begin{bmatrix} \cos^2 \alpha_i & \sin^2 \alpha_i & 0 & 2\sin\alpha_i \cos\alpha_i & 0 & 0 \\ \vdots & \vdots & \vdots & \vdots & \vdots & \vdots \\ \sin^2 \beta_i & 0 & \cos^2 \beta_i & 0 & 0 & 2\sin\beta_i \cos\beta_i \\ \vdots & \vdots & \vdots & \vdots & \vdots & \vdots \\ 0 & \cos^2 \gamma_i & \sin^2 \gamma_i & 0 & 2\sin\gamma_i \cos\gamma_i & 0 \\ \vdots & \vdots & \vdots & \vdots & \vdots & \vdots \end{bmatrix} \begin{Bmatrix} \varepsilon_{xx} \\ \varepsilon_{yy} \\ \varepsilon_{zz} \\ \varepsilon_{xy} \\ \varepsilon_{yz} \\ \varepsilon_{xz} \end{Bmatrix}$$

Where angles α, β and γ are -45°, 0°, +45° for $i = 1, 2, 3$ respectively, while ε_{α_i} represents the measured normal strain at the angle α_i. This overdetermined system can be solved in a least-squares sense using Moore-Penrose inversion of the matrix of cosines [207, 209]:

Equation 17

$$\varepsilon = A^+ \varepsilon_{lmn}$$

For computational efficiency it should be noted that the matrix of direction cosines A has full rank, so the Moore-Penrose inversion is equal to the (unique) matrix left inverse in this case [210]:

Equation 18

$$A^+ = (A^T A)^{-1} A^T$$

The accuracy of the solution to Equation 17 depends on the conditioning of the matrix of direction cosines. If it is ill-conditioned, then small errors in the measured normal strains will lead to large errors in the strain tensor. To prevent this, the angles between strain measurement directions should be maximised [207]. This was the fundamental reason for the choice of measurement geometry shown in Figure 35. After the strain tensor had been determined, the corresponding stress tensor was calculated via Hooke's law. Linearly elastic and isotropic material properties were assumed, and the plane-specific elastic constants used (E = 225.5 GPa, and ν = 0.28), were Kröner model predictions [196].

Uncertainty analysis

If the distribution of error in the measured strain components is known, then the uncertainty in the calculated strain tensor components can be determined. Witte et al. [211], Winholtz and Krawitz [208] and Robinson et al. [209] used a Monte Carlo analysis for this purpose: by artificially seeding their measured strain values with errors (the distribution of which was calculated from the uncertainty in determination of the scattering angle), they found the consequent distribution of the calculated strains. In this experiment, normally-distributed pseudo-random errors with a standard deviation equal to the error in fitting the measured diffraction profiles were introduced into the measured strain data, and the strain tensor was calculated. 10^6 iterations of this procedure were performed, and the resulting distribution of strain tensor components was analysed.

This Monte Carlo analysis is in fact unnecessary because since A has full rank, each component of the strain tensor is independently calculated using a single linear equation once the matrix inverse has been calculated. While the numerical matrix inversion is subject to round-off errors, these will be in the order of the machine epsilon (the maximum relative error in rounding due to the use of floating-point arithmetic) when A is reasonably well-conditioned. This value is very small, approximately 1.1×10^{-16} for double-precision arithmetic, and may reasonably be neglected. Therefore, the standard error in each tensor component can be calculated straightforwardly using the root of the sum of squares (RSS) [212]:

Equation 19

$$\delta_i^2 = \sum_{j=1}^{n} A_{i,j}^{+2} \delta_{lmn_j}^2$$

Where $\boldsymbol{\delta}$ and $\boldsymbol{\delta_{lmn}}$ are column vectors containing the standard uncertainties in the strain tensor and measured normal strain components respectively.

After the uncertainty in the strain tensor has been established, this can be propagated through the Hooke's law calculation of the corresponding stress tensor. For normal stress components [201]:

Equation 20

$$\delta_{\sigma xx} \cong \left(\left(\frac{(1-v)E}{(1+v)(1-2v)} \right)^2 \delta_{\varepsilon xx}^2 + \left(\frac{vE}{(1+v)(1-2v)} \right)^2 \left(\delta_{\varepsilon yy}^2 + \delta_{\varepsilon zz}^2 \right) \right)^{1/2}$$

Where $\delta_{\sigma xx}$ is the absolute uncertainty in the normal stress σ_{xx}, and $\delta_{\varepsilon xx}$ etc. are the absolute uncertainties in calculated normal strain components. Similarly, for the shear stress components:

Equation 21

$$\delta_{\tau xy} = \frac{E}{(1 + v)} \delta_{\varepsilon xy}$$

In this analysis, only the effect of statistical uncertainty in the calculation of the diffraction angle has been considered. Uncertainty in the spatial orientation of the measurements (i.e. uncertainty in the angles α, β, γ) was not evaluated, and any systematic errors are assumed minimal. During the calculation of uncertainty in the stress tensor, it has been assumed that the material under investigation has perfectly isotropic elastic properties, and consequently the result should always be interpreted as the uncertainty *given* this assumption.

Results

Residual stress

The variation in residual stress across both of the plate specimens is shown in Figure 38. The familiar distribution of longitudinal residual stress (σ_{xx}) which results from welding can be seen in Figure 38a: this is strongly tensile close to the weld line, and slightly compressive further away from it. Rolling greatly modifies the residual stress distribution: in the rolled specimen (Figure 38b), the longitudinal component has been partially inverted and is strongly compressive at the weld seam.

At most locations on both of the specimens, the shear components of the stress tensor are small in comparison to the direct stresses. Only a single pair of specimens was used in this study, and therefore although the welding and rolling operations were carried out under highly controlled conditions, direct comparison of these relatively small shear stress values could be tenuous due to the possibility of sample-to-sample variation. However, rolling does seem to introduce small additional shear stresses (largely in the out-of-plane τ_{yz} and τ_{xz} directions), up to a maximum observed value of 68 MPa (see Figure 38d). The effect of this on the principal stress directions can be seen by comparing the two plots in Figure 39. For the as-welded specimen (Figure 39a), the principal stresses close to the weld are well-aligned with the coordinate axes. Further away from the weld line, the magnitude of the normal stress components is generally lower and so the small shear components have a larger effect on the principal stress directions, rotating them slightly. This is also apparent in the rolled sample (Figure 39b). However, in the rolled sample there is also significant deviation in

the principal stress direction directly around the weld, especially towards the out-of-plane direction.

a.

b.

c.

d.
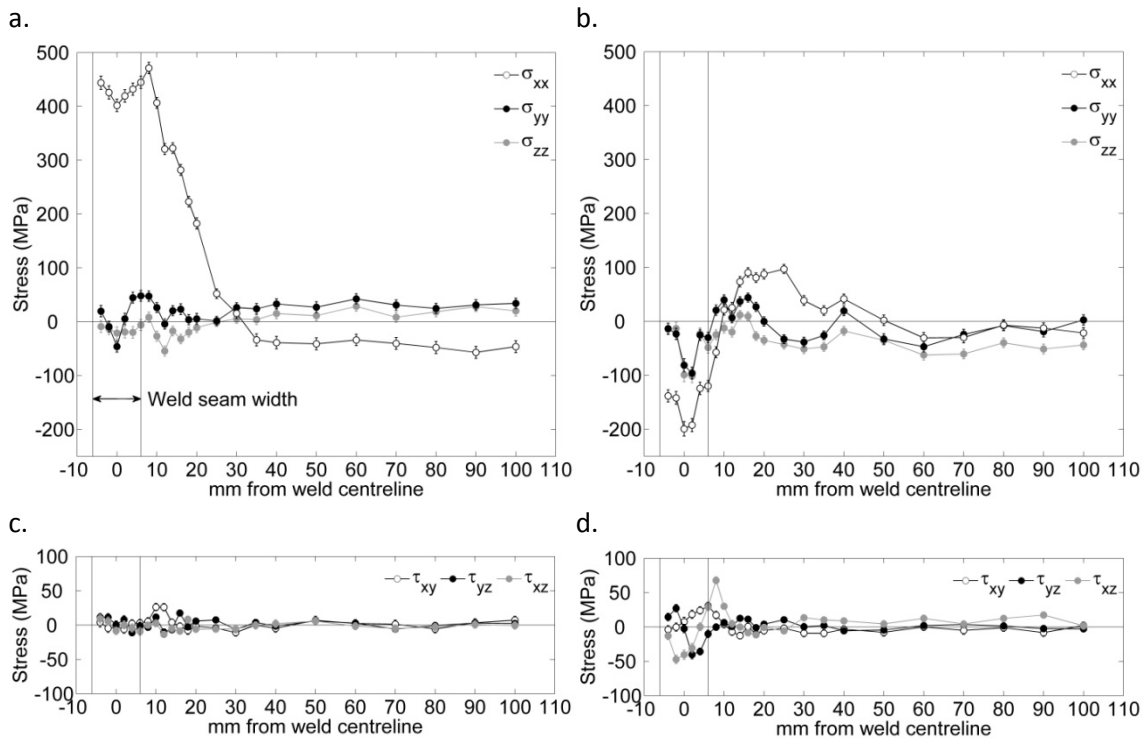
Figure 38: Components of the residual stress tensor, measured using neutron diffraction, in: (a,c.) a normal weld, (b,d.) a rolled weld.

a.

b.
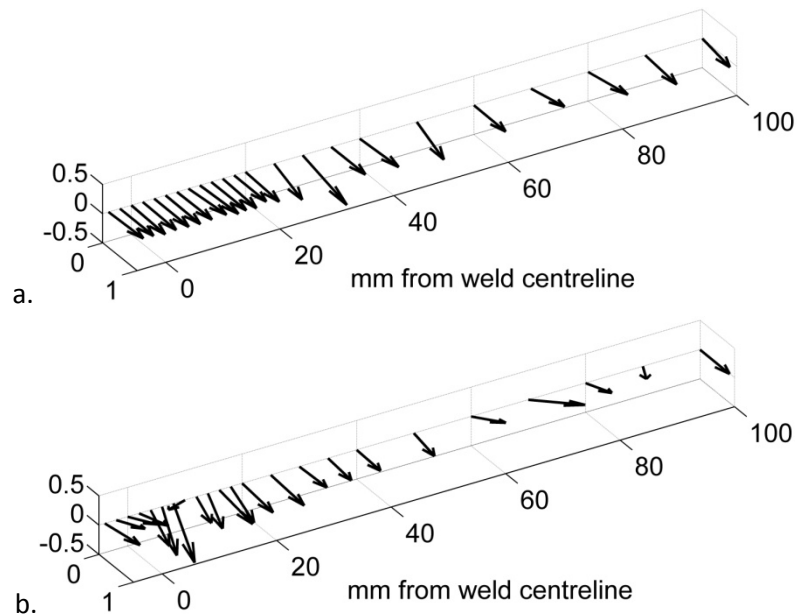
Figure 39: Unit vectors indicating the direction of the principal stress closest to the longitudinal axis at each measurement point. (a.) normal weld, (b.) rolled weld.

A comparison of residual von Mises equivalent stress in the two specimens is shown in Figure 40. Since the longitudinal component of residual stress is largest for the as-

86

welded specimen, its reduction due to post-weld rolling has a clear effect on the von Mises stress close to the weld line. The yield stress of the parent material (approximately 474 MPa) was measured before the experiment, but is not necessarily representative of the weld fusion region and the surrounding heat-affected zone. This is due to dilution of the parent material with the additional weld filler material (fusion zone only), and microstructural changes due to the thermal cycle encountered during the process. However, the von Mises stress close to the weld seam in the as-welded specimen certainly approaches the parent material's yield stress. By contrast, the maximum von Mises stress observed in the rolled specimen is only 158 MPa.
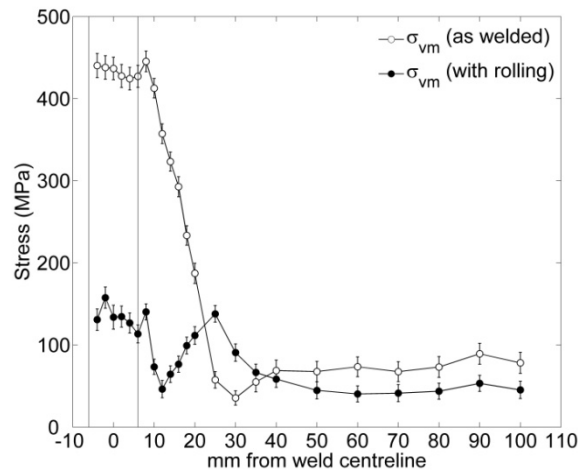
Figure 40: Distributions of residual von Mises equivalent stress in conventional and rolled welds. The vertical lines at ±6 mm indicate the approximate weld seam width.

Uncertainty

Calculated probability distributions for the magnitude of absolute error in a single strain component are given in Figure 41. The example shown is for strain in the longitudinal direction (ε_{xx}) at the weld centreline (0 mm) on the as-welded sample, however similar results apply for the error distributions of all other strain tensor components. Since there is negligible error involved in the inversion of the matrix of rotation cosines, the results for Monte Carlo and RSS calculations are identical.

Figure 41: Distribution of the magnitude of error in the longitudinal strain component at 0 mm in the as-welded sample, calculated by Monte Carlo analysis (histogram bars) and sum-of squares (solid line).

Discussion

High-pressure rolling

As can be seen from Figure 38, high-pressure rolling of the weld seam can be used to remove the central tensile peak in longitudinal residual stress. The longitudinal component of residual stress in the region of the weld instead becomes compressive. Since any stress field applie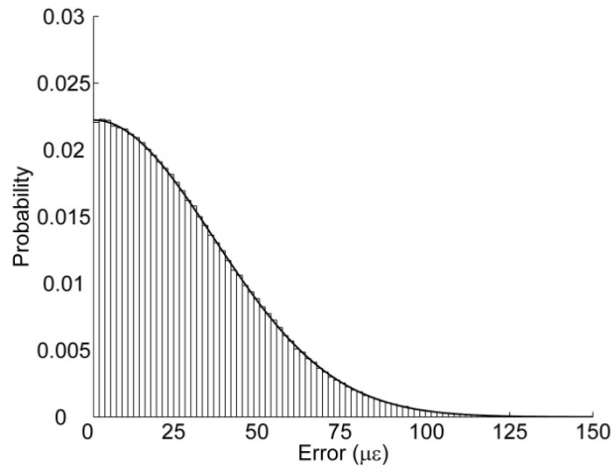d by external loading is superimposed upon the distribution of residual stress, the presence of this compressive stress component would likely inhibit crack propagation across the weld under longitudinal fatigue loading. Calculating the von Mises equivalent stress (Figure 40) from the stress tensor gives an approximation of how close the material is to yielding. Due mainly to the large longitudinal tensile component, the residual von Mises stress around the weld seam for the as-welded sample is large – close to the yield strength of the parent material. Consequently, some degree of material plasticity would be expected to occur at the weld seam given sufficient in-service loading in tension. By contrast, since the residual von Mises stress remains relatively low throughout the rolled sample, a much larger imposed stress would be needed to cause plasticity [213]. Rolled welds can therefore be expected to retain better dimensional stability under in-service loading, since less shakedown of residual stresses would occur.

The extent of the inherent strain induced by rolling corresponds to the extent of the region of compressive longitudinal stress seen in Figure 38b and to a local minimum in residual von Mises stress seen in Figure 40. Rolling must therefore cause significant plastic deformation around the weld, in a region of approximately 24 mm overall width. This is considerably wider than the region over which the roller contacts the material: during rolling the roller only contacts the top of the weld seam (see Figure 36), which is approximately 12.5 mm in width.

In most locations on both of the specimens, the principal stresses are reasonably well-aligned with the sample coordinate axes. However, there is considerable rotation of the principal stress directions close to the weld line on the rolled specimen (Figure 39b), caused by the occurrence of finite shear stress components in this region (Figure 38d) coupled with the fact that the stresses in the sample coordinate directions are relatively low compared with the as-welded case. Since the plate specimens are thin (6 mm) in one dimension, it would normally appear reasonable to assume that a state of plane stress applies. However, the presence of finite stress tensor components which violate this assumption (σ_{zz}, τ_{yz}, τ_{xz}), indicates that this is not strictly the case at the mid-plane of the plate, from which the measurements were taken.

Uncertainty estimation

For calculation of the elastic strain tensor, a relationship (based on infinitesimal strain theory) between the different measured values of strain must be assumed. Consequently, when multiple (non-orthogonal) strain measurements are related, the uncertainty in each may be reduced by reference to the others. This was the case with the calculation of the strain tensors made in this study: the uncertainty of each strain tensor component could be less than the uncertainty in any of the original measurements. This is an encouraging prospect where more accurate measurements are required, however there are two important limitations to consider. Firstly, the strain tensor can never be calculated accurately if the matrix of direction cosines (A) is not well-conditioned. Here, the choice of large angles between the different measurement directions resulted in a well-conditioned direction cosine matrix ($\kappa(A) = \sqrt{2}$). Secondly, the uncertainty in the calculated strain tensor is the uncertainty *given* the additional assumption that normal infinitesimal strain transformation rules can be applied to the measured strain values. In some circumstances this assumption may not be accurate, because strain in different orientations is measured from the lattice spacings of differently-oriented crystallites within the sample gauge volume [214].

Applications of tensor measurements

For many applications, it is not necessary to fully characterise the stress state in the measured object. For example, when comparing a numerically-determined residual stress distribution with an experimental one, it may be sufficient to compare only one component of stress in a known direction. Furthermore, in many cases where knowing the complete stress state is necessary, the principal stress directions at a measurement point are known *a priori*, or can be inferred from geometry. Such is the case in, for example, a tensile test where the stress state is known to be uniaxial.

When measuring residual stresses, it is common to use symmetry arguments to simplify the measurement process [71]. For example, the specimens used in this

experiment were linear welds in rectangular specimens, with two axes of reflective symmetry. If the same symmetry holds for the residual stress distribution, it can be assumed that on any of the specimen's mirror planes the principal stresses coincide with the specimen coordinate axes, since an in-plane shear stress existing on any of these planes would lead to asymmetry. For example, at points A and B in Figure 42 the principal stress directions must be the same as the specimen coordinate axes, however at point C they are likely to be quite different [215]. Whenever the principal stress directions are known, the measurement can be greatly simplified by measuring only the strains in these directions. Great caution should be exercised in doing this because although symmetry of the specimen might seem to indicate the principal directions, sometimes the underlying residual stress field might not share this symmetry [216]. However, in this study it has been shown that in the case of a simple linear weld, the residual stresses corresponding to the longitudinal, transverse and normal directions measured close to one of the axes of symmetry are indeed approximately principal. In the general case (as exists at point C), strains measured in any three mutually orthogonal directions can be used to calculate the stresses in these directions, but there is no guarantee that these stresses will be principal [217].
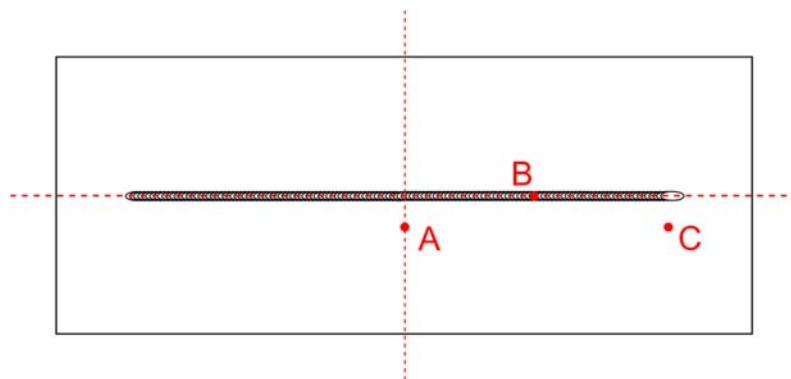
Figure 42: Welded plate specimen with two axes of reflective symmetry.

A full characterisation of the stress tensor may therefore be useful when little can be assumed about the stress state. This may occur when the specimen is geometrically complex, or (as in the example above) when measurements must be taken from a region of a stress field for which the principal stress directions are not precisely known. Furthermore, it may be required to assess (for example) how close material is to yielding, since all common yield criteria require that the values of the principal stresses be known. Therefore, applying any such criterion to an arbitrary triaxial stress state would require measurement of the full stress tensor.

The practical considerations associated with measuring strain using diffraction methods can lead to problems for specimens that are large or awkwardly-shaped. A frequent issue is that for a given measurement direction, it is not always possible to

define paths for the incoming and diffracted beams which pass through an acceptably small amount of material. This is because the measured strain direction always bisects the scattering angle, and this angle is subject to additional constraints such as the range of available wavelengths and the desired gauge volume geometry. However, using a strain tensor calculated from measurements in accessible directions could allow measurement of strain in another direction which might not be possible to measure directly. This could be especially useful for strain measurement in plane specimens by synchrotron x-ray diffraction, where the low scattering angle makes it difficult to measure strain in the direction normal to the specimen surface [218]. Similarly, it could be applied to neutron Bragg-edge transmission [219], where the measured lattice spacing lies perpendicular to the transmitted beam and so the surface-normal strain component is again difficult to measure.

Conclusions

1. Determination of complete residual strain and stress tensors from multiple neutron diffraction strain measurements has been demonstrated.

2. An assumption commonly employed to simplify residual stress measurement is that half-way along a symmetrical linear weld, the principal residual stress directions are well-aligned with the specimen coordinate axes (i.e. longitudinal, transverse and normal to the weld). This has been confirmed experimentally.

3. High-pressure rolling of mild steel gas metal arc welds drastically reduces longitudinal residual stress, causing it to become compressive around the weld seam. During rolling, plastic deformation occurs over a region significantly wider than the contacting width of the roller.

4. Rolling does not introduce additional residual stress in any other direction which could be considered particularly damaging. Some additional shear stresses were observed in this experiment, but these are relatively small, and the residual von Mises equivalent stress is significantly reduced in the weld area.

5. Full-tensor measurements of residual stress and strain can provide useful information beyond that which is gained via the usual practise of measuring in three orthogonal directions only. They could also be applied to overcome practical limitations on the strain measurement direction when using diffraction methods, or to reduce the statistical measurement uncertainty.

6. Computational rounding errors in the calculation of a strain tensor by the method used here may normally be neglected, which enables a simplified method of estimating the uncertainty in the strain tensor components.

Chapter 7: Effects of rolling on the mechanical properties and microstructure of structural steel welds

The majority of this chapter is taken from the following article:

Abstract

A variety of experimental techniques, including microhardness measurements and cross-weld tensile tests with digital image correlation, have been used to characterise the effects of rolling on the mechanical properties and microstructure of the weld material in welded structural steel specimens. It is shown that rolling applied at high temperature, as welding is carried out, promotes the formation of acicular ferrite in the weld metal. This produces a weld material with a greater yield strength and hardness, but slightly reduced impact toughness compared to un-rolled welds. Rolling of the weld metal once it has cooled instead causes work-hardening. These effects are discussed as they relate to the use of rolling for weld residual stress reduction.

Introduction

In Chapter 5, it was demonstrated that rolling is only effective for residual stress reduction when it is applied after the welding process, rather than during it. This is because if rolling is applied at too high a temperature, subsequent yielding of the material as it cools overwhelms the effective strain which may be induced by rolling. While it has less of an effect on residual stress, *in situ* rolling was shown in one study by Kondakov to influence the development of weld microstructure in austenitic stainless steel and a titanium alloy [141], however this effect has not been investigated in any modern literature.

In this chapter, the effects of rolling on the microstructure and mechanical properties of structural steel welds are investigated. Several mechanical characterisation techniques have been applied to determine the changes in material properties and microstructure which result from the rolling of low-carbon steel weld seams at different rolling temperatures and levels of roller force.

Experimental

Production of specimens

600 mm linear bead-on-plate gas metal arc welds were prepared on 750 x 300 x 6 mm rectangular plates of S355JR structural steel. These welds were treated with high-pressure rolling either during welding (*in situ*) or post-weld, with an applied force of 12.5, 25, 50 or 100 kN. Plain as-welded specimens were also produced. The welding parameters, which were identical for all of the welds carried out, are given in Table 7.

Table 7: Parameters used for all specimens (bead-on-plate welds in 6mm-thick S355 steel).

Process:	GMAW (Pulsed)
Power supply:	Fronius TransPuls Synergic 5000
Mean current:	328 A
Mean voltage:	35.1 V
Welding speed:	8.33 mm s^{-1}
Wire feed speed:	250 mm s^{-1}
Filler wire:	ISO 14341-A-G G3Si1, 1.0 mm dia.
Shielding gas flow rate:	0.17 dm^3 s^{-1}
Shielding gas composition:	20% CO_2, 2% O_2, balance Ar

Both welding and rolling operations were carried out on a purpose-built rolling machine previously described in Appendix A. During rolling, a constant force was applied using a roller actuated by a vertically-mounted hydraulic cylinder, and the roller/cylinder assembly was passed over the specimen at a constant velocity on a leadscrew-driven crossbeam. The specimens were held in place using a vacuum clamping system, which was applied to the entire underside of the specimen except for the region directly underneath the weld seam, where a copper backing bar (48 mm in width) was used. In all cases, only a single pass of rolling was applied, using the roller profile shown in Figure 43. For post-weld rolling, the specimen was welded and left to cool for 600 seconds before rolling and then release of the clamps. For *in situ* rolling, the welding torch was mounted 100 mm in front of the roller axis and the two processes were carried out simultaneously. Again, 600 seconds was allowed for cooling before the vacuum clamps were released.
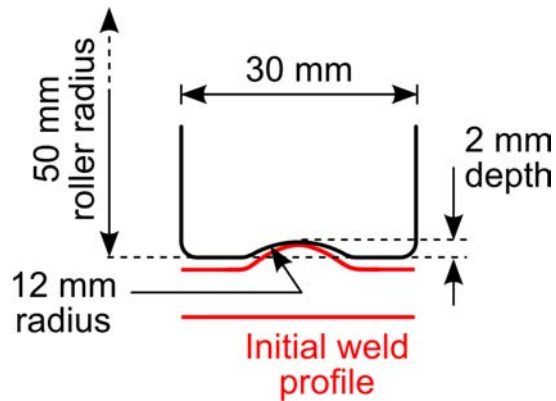
Figure 43: Schematic of the roller profile, with comparison to the profile of a weld without rolling (taken from laser coordinate measurements).

Several specimens were instrumented with K-type thermocouples on the upper surface, in 16 locations at various distances from the weld line - to a minimum of 20 mm from the centre of the weld. Data from these thermocouples was used to validate a sequentially-coupled thermo-mechanical finite element model of the process built using Abaqus/Standard v6.9-3 (Dassault Systems, France), and described in further detail elsewhere [220]. This model was, in turn, used to determine the temperature field inside the weld metal. Samples of the parent plate remote from the weld, and the weld metal inside the fusion zone were taken from a non-rolled specimen, and chemical analysis was performed via Inductively Coupled Plasma Optical Emission Spectrometry (ICP-OES) and combustion analysis. The resulting elemental compositions are given in Table 8.

Table 8: Elemental composition of the S355 parent metal and the weld fusion zone (wt. %).

	C	Si	Mn	P	S	Cr	Mo	Ni	Al	Cu	Nb
Parent	0.06	0.04	1.28	0.010	0.009	0.02	<0.01	0.02	0.03	0.02	0.03
Weld	0.06	0.27	1.02	0.011	0.007	0.03	<0.01	0.02	<0.01	0.06	<0.01

Cross-weld tensile testing

Tensile tests were carried out on specimens taken from the welded plates perpendicular to the weld line. Rectangular cross-section test pieces (see Figure 44) were produced to conform to ISO 6892-1:2009 (Annex B) [221]. The nominal cross-sectional dimensions of the parallel length were 12.5 x 2 mm, however the cross-sectional area was determined accurately for each specimen before testing using a micrometer. In all cases, the specimens were taken from the mid-thickness of the parent plate.

Two-dimensional Digital Image Correlation (DIC), was used to measure the strain variation across the frontal area of each specimen during the test, and hence investigate the localisation of strain due to the variation in mechanical properties

across the weld (see Figure 44), using the principle described by Reynolds and Duvall [222]. To carry out DIC measurement, a series of photographs are taken of the tensile specimen as it is loaded, which are then digitally compared to a reference photograph of the specimen in its undeformed state at the beginning of the test. The differences between these images are then used to calculate the displacement of points on the specimen's surface relative to their initial position, and hence infer the strain field in two dimensions [223]. A LIMESS DIC system (Correlated Solutions Inc., Columbia, SC, USA) was used for all measurements in this study. To ensure that suitable surface features are available for the image correlation process, it is normally necessary to apply a speckle pattern to the region of interest [224]. In these experiments, this was done using white spray primer (background) and black graphite spray (speckles).
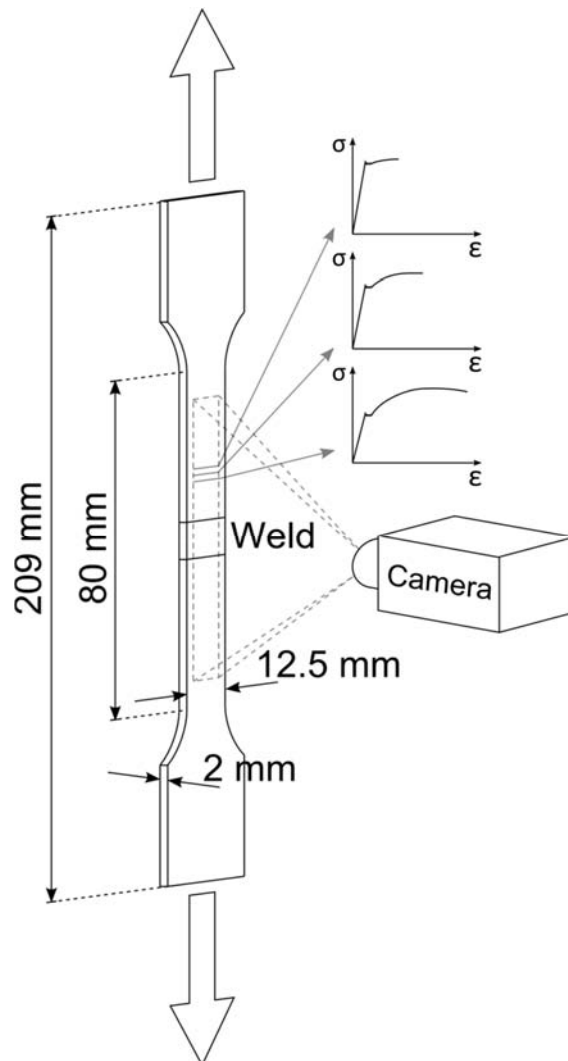

Figure 44: Cross-weld tensile test using Digital Image Correlation to observe local variations in strain. When the material properties can be assumed to vary only in the direction transverse to the weld (i.e. the direction of loading during the tensile test), the stress-strain properties of material at different transverse distances to the weld line can be found.

95

Since the weld is relatively homogenous along its length, it can be assumed that the tensile specimen's mechanical properties only vary in the loading direction, i.e. transverse to the weld. Also, it is known that all cross-sections of the tensile specimen's gauge length must carry the same tensile force. Therefore with a single tensile specimen it is possible to produce a set of stress-strain curves, spatially-resolved in the across-weld direction, in a manner similar to that described recently by Peel et al. [225] and Turski et al. [226]. This data can then be used to calculate the yield stress of the material at each point across a transverse section of the weld. A limitation of this method is that it is impossible to find the complete stress-strain curve (i.e. up to the ultimate failure strain) for all points along the tensile specimen, since the specimen will only neck and separate at one location. Consequently, only the yield/proof stress and the first part of the stress-strain curve can normally be found at most locations; it is not possible to also calculate the ultimate tensile strength and elongation at failure, except where the specimen actually fails.

In addition to the welded specimens, tensile samples consisting purely of the parent material were tested. During these tests, a conventional clip-type strain gauge was used concurrently with the DIC method. This served to both to check the accuracy of the DIC method, and verify the stress-strain properties of the parent material. All of the tensile tests were carried out at an ambient temperature of 20°C and a constant elongation rate of 5 mm/min.

Metallurgical examination, hardness, impact toughness

Cross-sectional metallurgical specimens taken from each weld were ground, polished, and etched (2% nital, 12 seconds) before optical and SEM examination. The same samples were then measured for Vickers hardness: a Zwick/Roell Intentec micro-hardness measurement machine was used to make 372 individual measurements on each sample at spatial resolution of 0.5 mm, using a mass of 500 g and an indentation time of 10 s.

Charpy impact tests were used to investigate the effect of rolling on the impact toughness of the weld metal. Transverse reduced-section Charpy V-notch specimens (5x10x55 mm) were taken from the mid-thickness of the welded plates, with the notch at the centre of the weld metal. Impact tests were then performed to ISO 148-1:2010 [227], at a range of temperatures from -100 to 20°C and using a nominal pendulum energy of 400 J.

Results

Mechanical properties

Tensile tests

Figure 45 shows a typical stress-strain curve from a uniaxial tensile test of the parent material (S355 steel). The result is essentially identical for the different methods of strain measurement used (conventional clip extensometer and DIC), confirming the accuracy of the DIC method. The result also shows that the upper yield strength of the material is approximately 475 MPa, the ultimate tensile strength is 520 MPa, and the maximum elongation is 22.2%. It should be noted that these properties are substantially different to those given for the similar material used for the experiment described in Chapter 8, since material from different sources was used for the two studies. A comparison of the basic properties of these different batches of material is given in Appendix D.
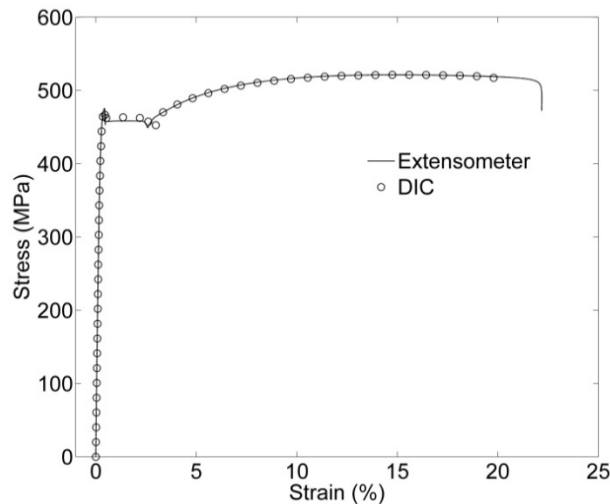

Figure 45: Stress-strain characteristics of the parent material (S355 steel), determined from a uniaxial tensile test. Two methods of strain measurement are compared: a conventional clip extensometer and Digital Image Correlation (DIC).

Plots of the local strain occurring in different weld types (i.e. with no rolling, post-weld roiling and *in situ* rolling) and at different levels of tensile stress are shown in Figure 46. In all cases, the tensile strain in the weld metal and the surrounding Heat-Affected Zone (HAZ), is lower than in the surrounding parent metal at all levels of applied load - indicating that the weld metal's yield strength is greater. Outside of the HAZ, at approximately 15-25 mm either side of the weld centreline, there are regions which initially show increased deformation compared with both the weld metal and the parent metal far remote from the weld. An example of this is marked by arrows in Figure 46c. All of the cross-weld specimens tested ultimately failed in the parent metal remote from the weld and HAZ.
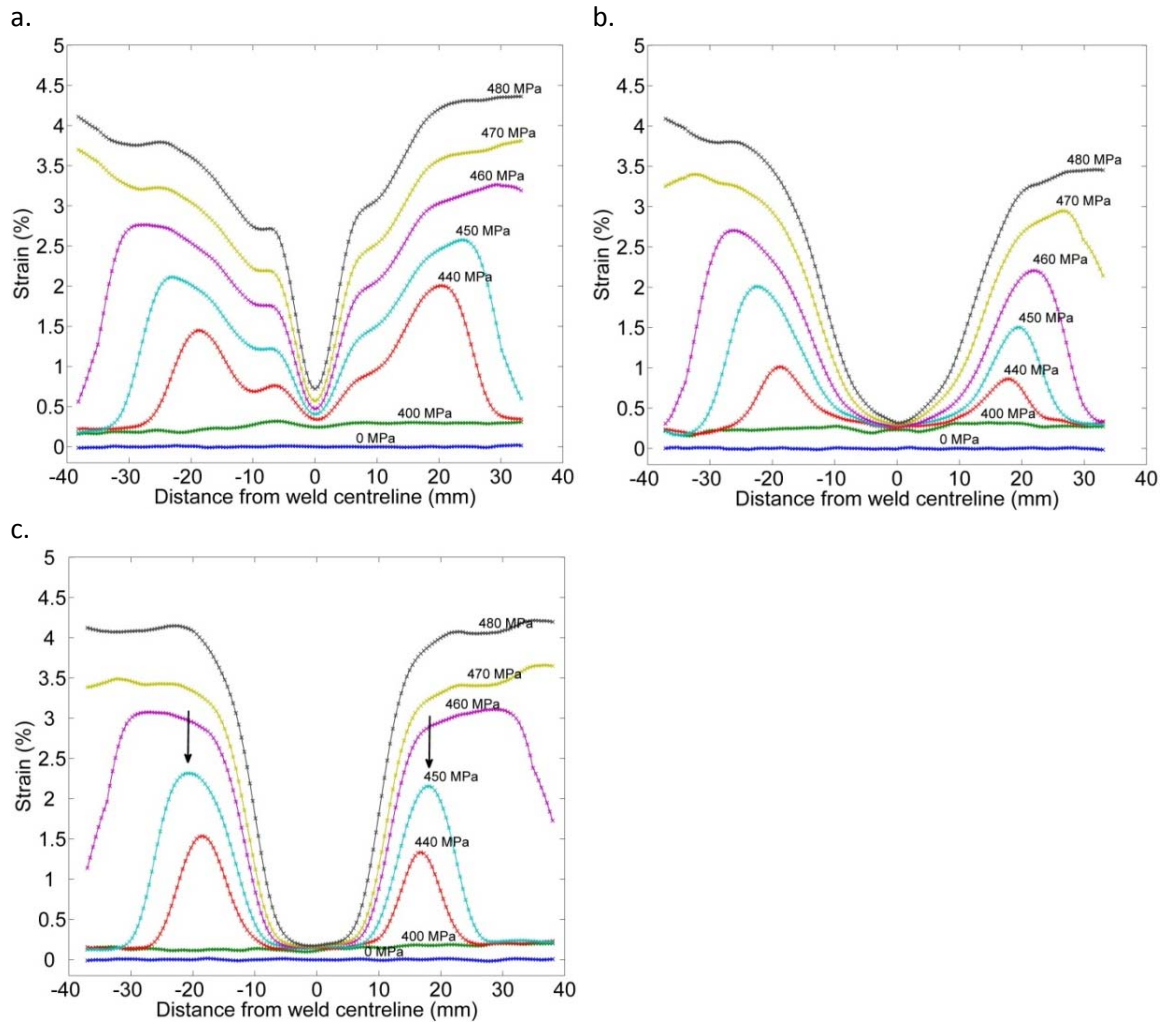
Figure 46: Tensile engineering strain as a function of position and applied stress during uniaxial tensile tests: (a.) conventional as-welded specimen, (b.) post-weld rolling with 100 kN load, (c.) *in situ* **rolling with 100 kN load.**

It is also clear from Figure 46 that both post-weld and *in situ* rolling have a dramatic effect on the stress-strain properties of the weld. Both processes harden the material close to the weld centreline, reducing the amount of deformation encountered there during the tensile test. The effect of this is perhaps best seen in the plots of offset yield stress shown in Figure 47. Rolling the weld seam either post-weld or *in situ* raises the proof stress of the weld metal and surrounding region. During either process, higher levels of roller force result in a greater degree of hardening. For both of the specimens rolled at 100 kN, the parent metal failed before part of the material in and around the weld exceeded its proof strain (0.2% offset). Consequently, for these samples it was not possible to calculate the proof stresses in a small central region; it is only known that they must be greater than for the rest of the specimen. In all samples, well-defined yield plateaus were observed in the parent material, but not in the weld metal - regardless of rolling treatment.
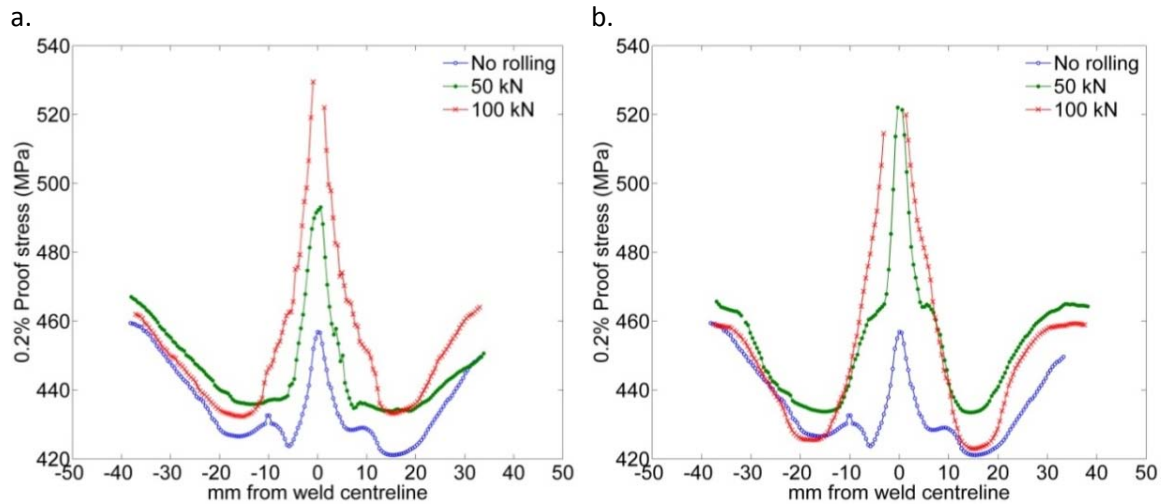
Figure 47: Variation in 0.2% offset yield strength across weld seams rolled at different levels of roller load, calculated from digital image correlation measurements. (a.) Post-weld rolling, (b.) *in situ* rolling.

Hardness

Maps of Vickers hardness across transverse sections of the weld zone are shown in Figure 48. In all cases, the fusion zone can be distinguished by a clear change in hardness corresponding to the discontinuity in composition and microstructure across the fusion boundary. In the sample which was not rolled (Figure 48b), the heat-affected zones are also visible to either side of the fusion zone; being slightly lower in hardness than either the fusion zone or the surrounding parent material. Post-weld rolling (Figure 48c-f) results in an increase in hardness with increasing rolling load, especially in the fusion zone. The same is true for *in situ* rolling (Figure 48g-j), although in this case the hardness increase is even more pronounced. The trend in weld and HAZ hardness therefore follows the trend in proof stress (Figure 47) - which is unsurprising since Vickers hardness and proof stress are related roughly linearly for most steels [228].
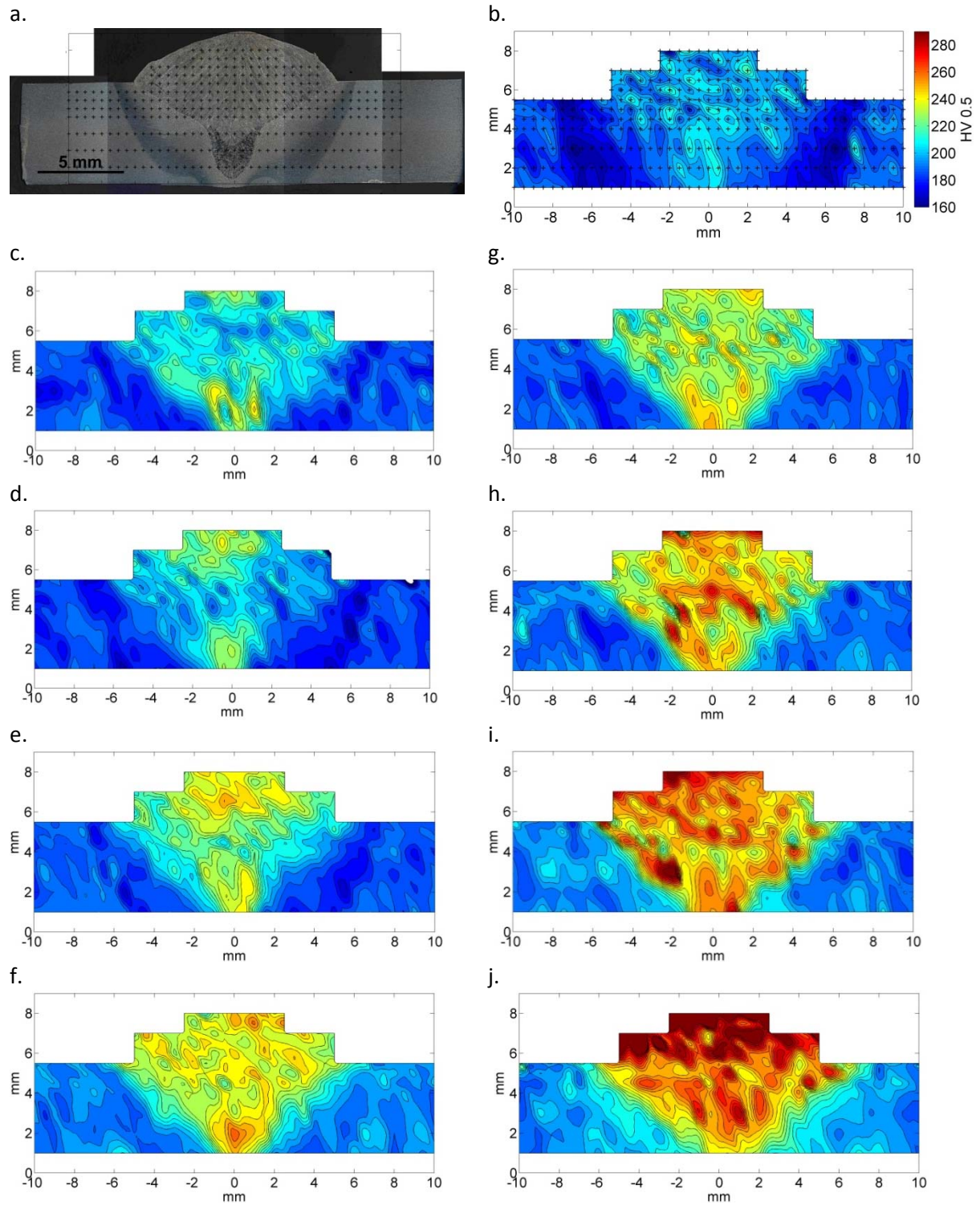
Figure 48: Cross-sectional maps of Vickers hardness (HV 0.5/10) in welded specimens. (a.) Composite macrograph of a weld without rolling, showing the measurement locations (black crosses). (b.) No rolling, also showing the measurement locations and colour scale. Plots (c-f.) show post-weld rolling at (c.) 12.5, (d.) 25, (e.) 50, and (f.) 100 kN. Plots (g-j.) show *in situ* rolling at (g.) 12.5, (h.) 25, (i.) 50, and (j.) 100 kN.

Impact toughness

Ambient-temperature measurements of the fusion zone impact toughness are shown in Figure 49a; it should be noted that reduced-section test specimens were used. The

impact toughness of specimens rolled post-weld is almost invariant with rolling load, decreasing only very slightly at higher loads. The toughness of weld metal rolled *in situ* shows a greater reduction with increasing rolling load, although even at the maximum level of roller force (100 kN), the impact energy absorbed by the weld metal is only slightly less than that of the parent metal (41.3 J compared with 44.7 J).
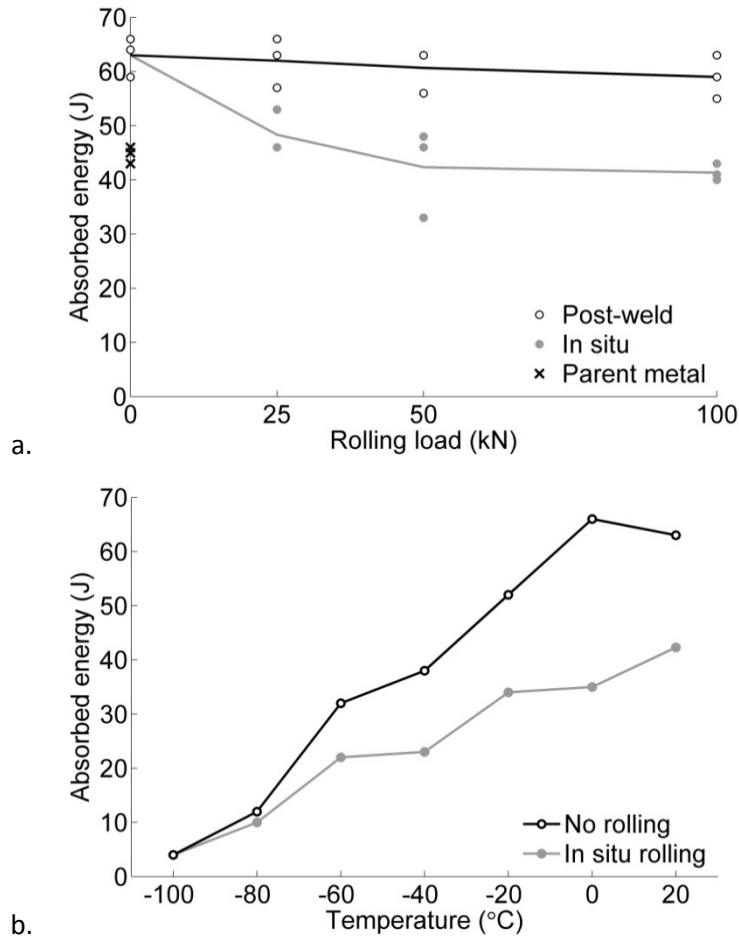
Figure 49: Absorbed impact energy for reduced-section Charpy V-notch specimens (5x10x55 mm) taken from rolled welds, with the notch at the centre of the fusion zone. (a.) Ambient-temperature impact toughness vs. rolling load for *in situ* and post weld rolling. (b.) Impact toughness vs. temperature for a weld without rolling, and one rolled *in situ* with a load of 50 kN.

The impact toughness at reduced temperature is shown in Figure 49b. Both types of weld metal (i.e. without rolling and with *in situ* rolling at 50 kN) display an almost linear reduction in impact toughness on cooling from 20°C to -100°C, with no well-defined ductile-brittle transition temperature. The weld with *in situ* rolling is less tough than the conventional weld over the whole temperature range, although the difference is small at lower temperatures.

Microstructure

The optical micrographs in Figure 50 compare the effects of post-weld and *in situ* rolling on the weld microstructure. Without rolling, the weld metal consists chiefly of a mixture of polygonal and Widmanstätten ferrite, with some acicular ferrite formations, which is typical for a low-carbon steel weld of this type. The structure is similar after post-weld rolling (Figure 50c-d), however *in situ* rolling results in the very different microstructure shown in Figure 50e-f. Fine paths of allotriomorphic and polygonal ferrite decorate the boundaries of the prior austenite grains, but otherwise the microstructure consists almost entirely of fine-grained acicular ferrite. The SEM image in Figure 51 shows this structure in greater detail: the grains have a length of 5-15 µm and a width of approximately 2 µm.
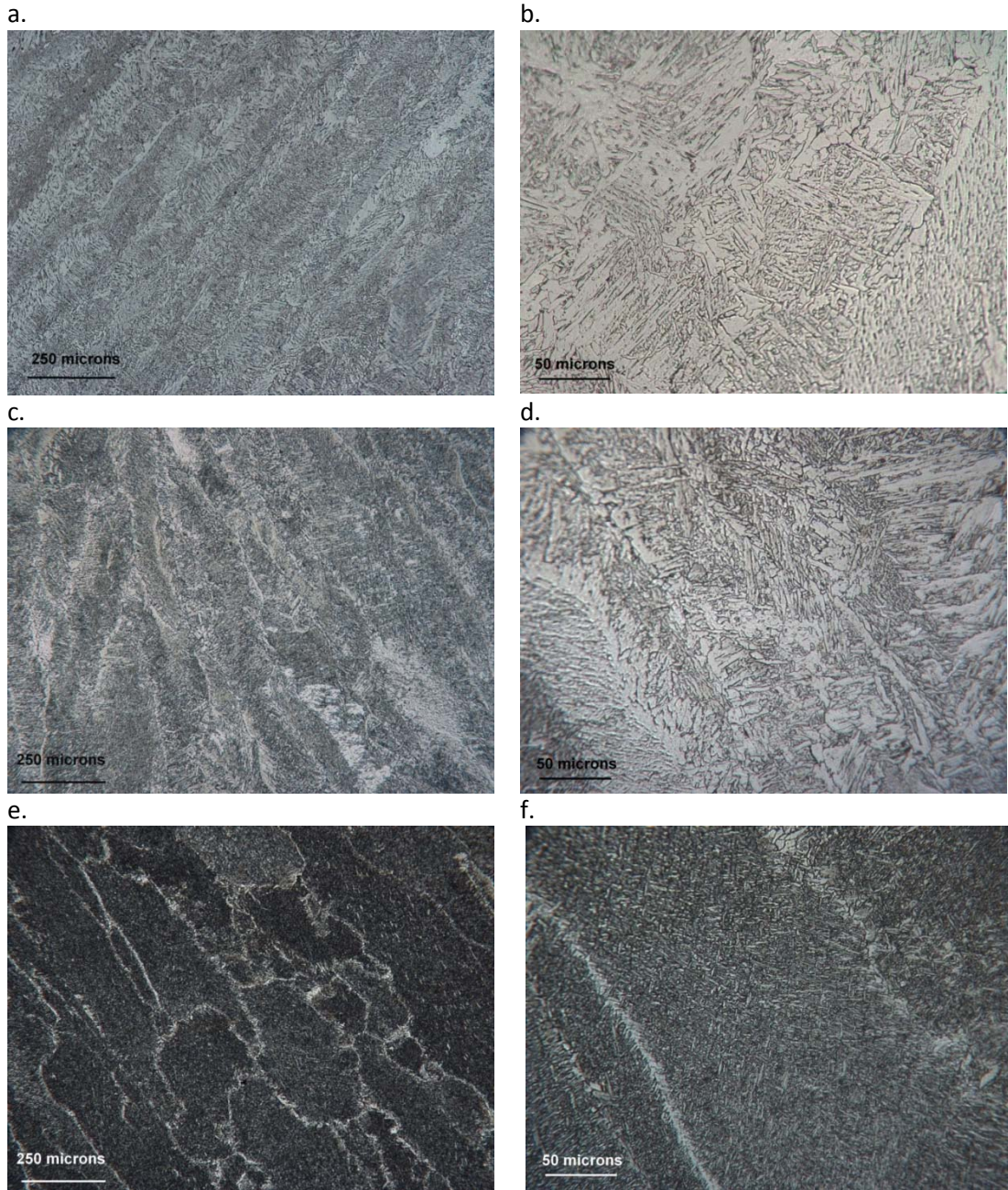
Figure 50: Optical micrographs of the fusion zone of welded steel specimens. (a, b.) No rolling, (c, d.) post-weld rolling (50 kN load), (e, f.) *in situ* rolling (50 kN load).
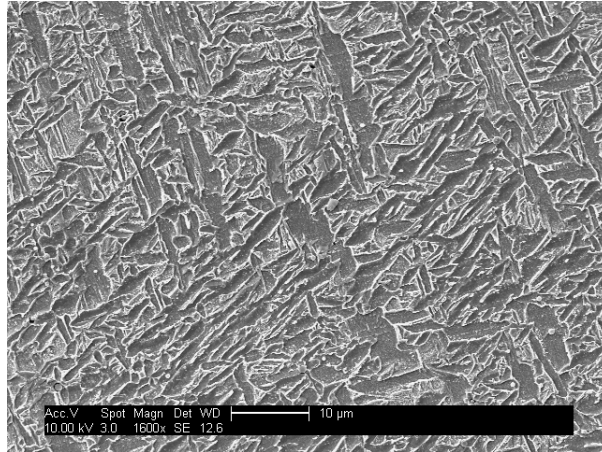
Figure 51: Acicular ferrite in the weld metal of an S355 steel weld rolled *in situ* at 50 kN (SEM image).

Within some of the prior austenite grains, the acicular ferrite laths show a significant degree of alignment (Figure 51). However, the direction of this alignment varies for different austenite grains, and there is no clear relationship between the acicular ferrite orientation and the direction of the applied rolling force.

Discussion

Weld mechanical properties

The hardness of the un-rolled welds (Figure 48b) was both relatively low and quite homogeneous across the parent metal, HAZ and fusion zone. This suggests the absence of hard martensite, and indeed no martensite is visible in the weld metal in Figure 50a and b. In all of the specimens, rolled and un-rolled, increased plastic deformation was observed in regions 15-25 mm either side of the weld during the cross-weld tensile tests (see Figure 46). Recrystallisation in the coarse-grained HAZ is known to result in a decrease in yield strength in many cases, mainly due to a reduction in grain-boundary hardening as larger grains are formed [10]. However here, the regions of increased deformation lie outside of the HAZ, the maximum extent of which was approximately ±7.5 mm. It is therefore likely that the softening of these regions is due to the recovery during welding of dislocations formed during the initial manufacture of the parent plates. This loss of work-hardening leads to increased plastic deformation in the recovered zones directly after yielding as the tensile specimen is loaded, however as larger strains are induced the material again work-hardens and becomes indistinguishable from the surrounding unaffected parent metal. It should be noted that the extent of the measurement region in the hardness maps (Figure 48) lies entirely within this annealed region, and so the hardness values at the edges of these plots are representative of the material in its annealed state, rather than indicating the hardness of the parent metal.

104

Influence of rolling on mechanical properties and microstructure

From the hardness maps shown in Figure 48 and the cross-weld tensile test results in Figure 46 and Figure 47, it is clear that both post-weld and *in situ* rolling hardens the weld metal and causes an associated rise in the proof strength. For post-weld rolling this is unsurprising, since work-hardening is an inevitable consequence of the plastic deformation induced during rolling. The lack of any significant difference in microstructure between the as-welded and post-weld-rolled specimens (Figure 50) confirms that work-hardening is the primary hardening mechanism. The hardness maps in Figure 48b-f show that during post-weld rolling, substantially more work hardening occurs in the fusion zone than in the surrounding HAZ, which is likely due to the slightly different composition of the weld metal (see Table 8). Work-hardening is seen to occur throughout the weld region, suggesting that rolling causes plastic deformation through the whole thickness of each specimen. For the welds rolled *in situ*, the temperature during rolling is too high for substantial work hardening to occur: instead of work-hardening, *in situ* rolling causes microstructural change, resulting in the acicular ferrite microstructure shown in Figure 51, which is the cause of the increased hardness. While excessive weld metal hardness is usually seen as detrimental in steel welds since it indicates the presence of brittle martensite, no significant martensite formation was detected in any of the welds studied here.

During the γ→α transformation in a ferritic steel weld fusion zone, competitive growth occurs between ferrite growing from the austenite grain boundaries (in polygonal and Widmanstätten morphologies), and intragranularly-nucleated acicular ferrite [229, 230]. Many factors, including the cooling rate, prior austenite grain size, and number density of intra-granular inclusions, influence the kinetics of this transformation [231, 232]. Additionally, stress applied during the transformation is also known to affect it when the chemical driving force is small [233]. Figure 52 shows the effect of *in situ* rolling on the thermal cycle undergone by the weld metal: an increase in thermal conduction into the roller and backing bar results in a moderate increase in cooling rate, reducing the time between 800°C and 500°C (t_{8-5}) from 11.2 to 6.6 seconds. The internal heat generation from rolling due to material visco-plasticity is negligible. Such a cooling rate increase favours the formation of acicular and Widmanstätten ferrite over polygonal ferrite, and reduces the time available for austenite grain growth. However, available continuous-cooling data for this type of material indicates that this increase in cooling rate would be insufficient to cause such a pronounced change in microstructure as seen here [234].

The weld undergoes rolling as it cools from approximately 900°C to 700°C (see Figure 52). Under equilibrium conditions, this range would lie largely within the material's intercritical region, i.e. between its Ac_3 and Ac_1 temperatures. However, since the weld

cools continuously it will still be almost fully austenitised as rolling takes place. Severe plastic deformation of the austenite grains is known to slow the growth of acicular ferrite by forming stable dislocation networks [231]. Also, such deformation can reduce the austenite grain size *via* dynamic recrystallization, increasing the availability of intergranular nucleation sites [235]. However, for the welds investigated here, the amount of plastic deformation induced by rolling is relatively small: a maximum of 13.4% principal plastic strain was observed in the simulations, and no reduction in austenite grain size was observed. Therefore it is believed that the influence of this deformation in promoting intra-granular acicular ferrite nucleation outweighs any detrimental effect on its growth: such an increase in intra-granular nucleation would explain the very fine nature of the resulting acicular structure.
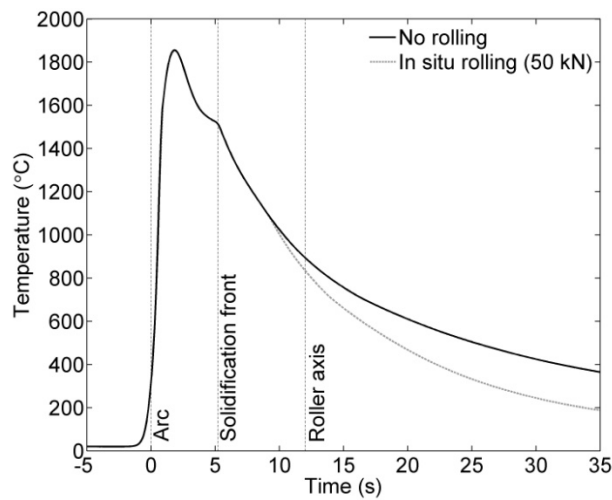
Figure 52: Thermal cycle at the weld centreline, half-way through the thickness of the specimen (modelled).

In general, acicular ferrite is a desirable component of a weld microstructure because its small and chaotically-oriented grain structure results in good toughness without any decrease in strength [230]. However in this study, the acicular ferrite weld metal of the specimens rolled *in situ* was observed to be less tough than the mixed polygonal and Widmanstätten microstructure of as-welded specimens, throughout the temperature range tested (see Figure 49b). A possible explanation for this could be dynamic strain ageing of the weld metal as it is rolled [236], however no yield point elongation effect was observed in the weld metal during tensile testing, regardless of rolling treatment. Despite being less tough than conventional weld metal, the acicular ferrite of the *in situ* rolled weld still maintains excellent impact toughness, almost equalling that of the parent material.

Applications of weld rolling

It was shown in Chapter 5 that post-weld rolling has a far greater effect on the residual stress distribution in a weld than rolling *in situ* (i.e. as welding is carried out), because

during *in situ* rolling residual stresses can re-form after the roller has passed. However, it has been shown here that in a steel weld, *in situ* rolling has an effect on the weld microstructure which would be impossible to produce once the weld has cooled. Therefore, the most desirable rolling temperature depends on the motivation for the process: residual stress control or microstructure modification. For the type of structural steel weld investigated here, it is possible that two rolling passes could be beneficially applied: one *in situ* pass to cause acicular ferrite formation, and one post-weld pass to stress-relieve. In some situations, for example with steels exhibiting an especially low transformation temperature, it may be possible to roll the weld at an intermediate temperature: high enough to promote microstructural change, but low enough to be effective for residual stress control. It is clear, however, that the effects of weld rolling would vary greatly for different alloy systems. Therefore it would be advisable to consider the material's work-hardening characteristics (and any consequences of work-hardening), its ductility at the desired rolling temperature, and the effects of deformation on any microstructural properties, if weld rolling is to be applied.

Conclusions

1. High-pressure rolling of structural steel fusion welds results in an increase in yield strength and hardness in the weld metal and heat-affected zone. This occurs regardless of whether rolling is carried out as the weld is made, or after it has cooled.

2. For post-weld rolling, the observed increase in weld metal hardness is attributable to work-hardening. However, rolling the hot material directly behind the welding tool changes the microstructure of the fusion zone, causing the widespread formation of fine acicular ferrite which also hardens the weld region.

3. The fine acicular ferrite microstructure which occurs in the fusion zone as a result of rolling during welding has a lower impact toughness than a weld without rolling. Nevertheless, its toughness is still excellent.

4. Hardness increases brought about by post-weld rolling were seen to extend throughout the 6 mm thickness of the weld, suggesting that the process can induce plastic deformation in structural steel to at least this depth.

Chapter 8: Roller geometry and its influence on the distribution of residual stress

The majority of this chapter is taken from the following article:

Abstract
Neutron diffraction has been used to map the residual stresses within low-carbon steel weld seams treated with high-pressure rolling. The effect on the residual stress distribution of using different roller types was determined, along with the influence of these different rollers on final weld seam geometry. Rolling was found to completely change the residual stress state in the weld, creating large compressive longitudinal residual stresses. It was effective for this purpose regardless of whether it was applied directly to the weld seam or to regions either side of it. The fatigue life of welded specimens was shown to be reduced by rolling, however it is suggested that this is due to geometric and metallurgical effects.

Introduction
While the effect of post-weld rolling on the general distribution of stress in a welded object is the subject of Chapters 5 & 6 of this thesis, its effect on the local residual stress state which exists in and directly adjacent to the weld metal has not so far been investigated. In many cases, material failure can be traced back to fracture initiation at geometric imperfections which exist at the weld [237, 96]. Therefore, by specifically reducing the tensile residual stresses directly around the weld, it may be possible to disproportionately affect its resistance to material failure, especially fatigue [92]. This principle is frequently cited when mechanical methods such as hammer, shot, and needle peening are applied to welds. Such methods appear to be most effective at increasing fatigue life when applied to the weld 'toes' (the longitudinal edges of the weld seam), and it is likely that the effects of both residual stress reduction and smoothing of geometric imperfections in these regions contribute to fatigue resistance.

In Chapter 7, rolling was shown to affect the microstructure and mechanical properties of a low-carbon steel weld differently depending on the applied force and rolling

temperature. In this chapter, the effects of different roller types on the distribution of residual stress close to the weld seam have been investigated. Since it was shown in Chapter 5 that rolling well after the weld has been completed has the greatest effect on the residual stress distribution in a steel weld, this study has been limited to post-weld rolling.

Experimental

Specimens

All of the specimens in this study were bead-on-plate gas metal arc welds on rectangular plates of S355JR low carbon structural steel. The overall size of the parent plates was 750 x 300 x 6 mm, and each had a single linear weld running for 600 mm longitudinally along the plate's centreline. The welding process and parameters used for the production of the specimens are shown in Table 9; they were designed to result in a steady and repeatable process, producing almost complete penetration of the weld pool through the parent plate. In preliminary uniaxial tensile tests, the yield and ultimate tensile strengths of the parent material (in the rolling direction) were determined to be 395 MPa and 520 MPa, respectively. These tensile properties are significantly different to those of the material used in Chapters 5-7, as material from different sources was used for the two experiments. A comparison of the basic properties of these different batches of material is given in Appendix D.

Table 9: Welding parameters used for all specimens.

Process:	GMAW (Pulsed)
Power supply:	Fronius TransPuls Synergic 5000
Mean current:	328 A
Mean voltage:	35.1 V
Welding speed:	8.33 mm s^{-1}
Wire feed speed:	250 mm s^{-1}
Filler wire:	G3Si1, 1.0 mm dia.
Shielding gas flow rate:	0.17 dm^3 s^{-1}
Shielding gas composition:	20% CO_2, 2% O_2, balance Ar

Four different roller profiles were used; these are shown in Figure 53. Roller profile A had a circumferential groove, shaped as a circular segment, to accommodate the raised weld seam. The dimensions of this groove were designed to conform closely to the profile of the weld, which was determined using preliminary laser coordinate measurements. Roller B had a similar groove, but this was designed to be much wider and shallower than the weld seam. Roller C was identical to Roller A except for the addition of small raised ridges (2 mm in radius and projecting 0.5 mm out from the main roller radius) on either side of the groove. Finally, in arrangement D two narrow rollers were used to roll only the edges of the weld seam and the regions to either side

of it. All of the rollers had corner radii of 2 mm at either edge of the profile (shown for Roller A in Figure 53), smoothing the transition between the axial and circumferential roller faces. It is important to note that rollers A-C were designed so that only the inside of the groove came into contact with the weld during rolling; the surfaces to either side did not touch the parent plate.
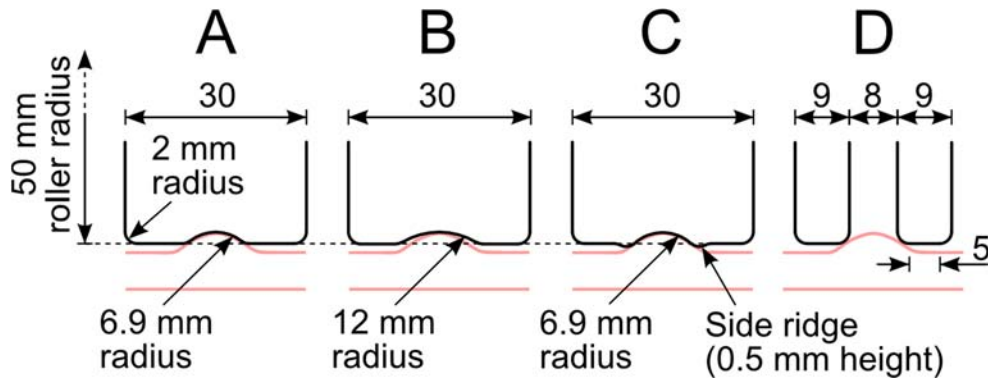

Figure 53: Different roller profiles used in the investigation. The initial weld seam profile (from laser coordinate measurements) is shown in red.

Two welded specimens were rolled using each of the roller profiles A-D, and a further two were left un-rolled. From each pair, one specimen was left intact and used for residual stress measurements, while the other was sectioned to provide metallographic specimens and samples for the determination of the stress-free lattice parameter (see section below on residual stress measurement). The cross-sectional metallographic specimens were ground, polished (using 0.05 µm silica emulsion) and etched (using 2% nitric acid in ethanol) prior to optical examination. Additional welds were carried out to produce fatigue specimens: in the as-welded condition, rolled using Roller B, and rolled using Roller D.

Rolling was carried out 600 seconds after each weld had been completed. Preliminary thermocouple measurements indicated that at this time after welding, the temperature was approximately 27°C throughout the specimen. Rolling was carried out at a constant velocity of 8.33 mm s^{-1} and using a constant force of 150 kN normal to the specimen's surface. During both the welding and rolling operations, a vacuum clamping system was used to secure the specimen to the bed of the rolling machine, and the specimens were released immediately after rolling was complete (as in Chapters 5-7). The rolling equipment used for these experiments is described further in Appendix A.

Residual stress measurement
Residual stresses were evaluated at a total of 24 locations on a transverse plane, half-way along the weld length in each sample. These points were arranged so as to produce a map of residual stress at 2 mm spatial resolution, covering the area directly

adjacent to the weld, up to 10 mm from the weld centreline. However, for arrangement D additional measurement locations were used, covering the area to 20 mm from the weld centreline (39 points in total), due to the larger width of material influenced by this roller.

The ENGIN-X time-of-flight neutron diffractometer at the ISIS neutron source, Rutherford Appleton Laboratory, UK was used for the measurements [238]. At each measurement location, residual elastic strain in three orthogonal directions (corresponding to the longitudinal, transverse and normal axes of the sample) was evaluated: Pawley refinement [239] was used to calculate the lattice parameter (a) from the measured diffraction spectra for each direction, and these values were compared with reference measurements of the stress-free lattice parameter (a_0). Spatially-resolved a_0 measurements were made using stress-free comb specimens cut from nominally identical welds, in the manner frequently used for residual strain measurements of this type [198, 192]. A sample gauge volume of 1x15x1 mm was used for measurement in the transverse and normal directions, and 1x2x1 mm for the longitudinal direction. Depending on the orientation measured, primary slits were used to define a 1x15 mm or 1x2 mm incoming beam, and 1 mm radial secondary collimators defined the third gauge volume dimension. Residual stress components in these directions were calculated using Hooke's law, assuming isotropic bulk elastic properties. For example, in the longitudinal direction:

$$\sigma_{xx} = \frac{vE}{(1+v)(1-2v)}\{\varepsilon_{xx} + \varepsilon_{yy} + \varepsilon_{zz}\} + \frac{E}{1+v}\varepsilon_{xx}$$

Where σ_{xx} is stress in the longitudinal direction, ε_{xx}, ε_{yy} and ε_{zz} are measured residual elastic strains, E is Young's modulus and v is the Poisson ratio. Bulk elastic properties (E = 202 GPa, v = 0.3) were used for this calculation.

Fatigue

The performance of the rolled welds under fatigue loading was investigated using four-point bend tests. Rectangular 300x40x6 mm fatigue samples were cut from welds rolled using Roller B and Roller D, and from un-rolled welds. These were tested using a sinusoidally-varying load with a load ratio (P_{min}/P_{max}) of 0.1 and a frequency of 2 Hz, with the test geometry shown in Figure 54. The weld seam was oriented so that the largest tensile stress produced by the applied bending moment was transverse to the weld seam, promoting fatigue fracture from the edges of the weld. The transverse stress range at the weld toes was estimated using simple beam theory [240]. Tests were carried out at a number of stress ranges to determine the S-N curve for each weld type.
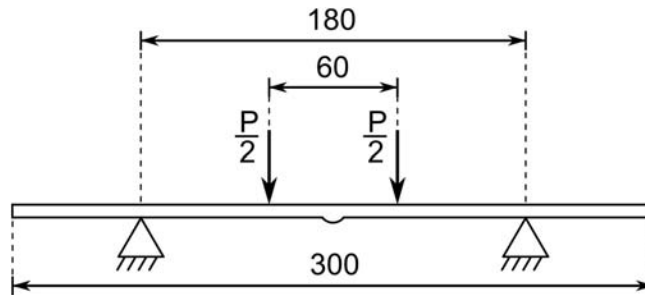
Figure 54: Four-point bend fatigue testing of welded specimens. Note that the specimen is oriented so as to produce tensile stresses transverse to the raised weld seam during the test.

Results

Weld profile

Cross-sectional macrographs of each weld are shown in Figure 55. The rolled weld seams (Figure 55b-e) have been visibly deformed during the process, assuming different profiles according to the roller type used. For rollers A and C (Figure 55b and Figure 55d, respectively), the top of the weld is only slightly deformed, since these rollers conform closely to the weld profile. However material has instead been pushed slightly outwards at the sides of the weld seam. Roller B (Figure 55c) produces a smooth, flat weld profile, with material at either side of the weld only slightly deformed. Finally, when Roller D is used (Figure 55e), the material at each weld toe is heavily deformed; this is evidenced by both the modified weld profile and the grain flow at the weld toes. The transition between the weld seam and the parent plate takes on a smooth curve (of 2 mm radius) that matches the profile applied rollers.
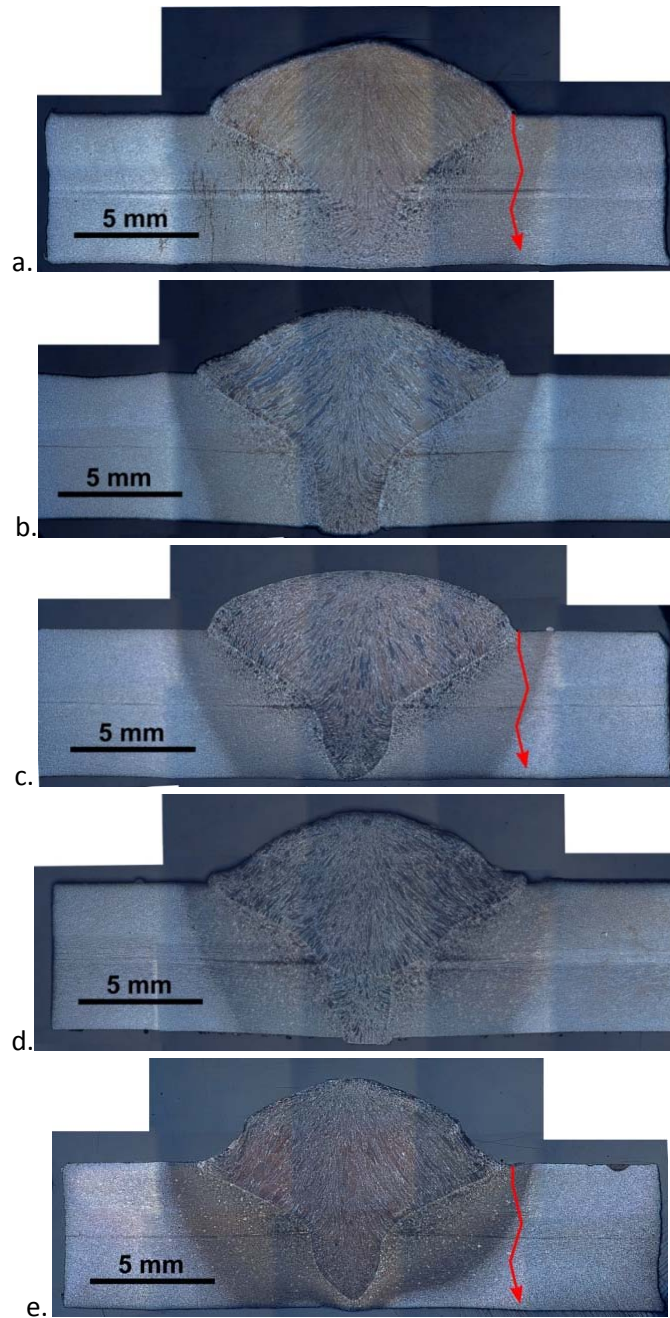
Figure 55: Composite macrographs showing a cross-section of each weld: (a.) No rolling, (b.) Roller A, (c.) Roller B, (d.) Roller C, (e.) Roller D. Red arrows show the approximate location of crack propagation during the fatigue tests.

Residual stress

The residual stress components in the directions longitudinal and transverse to the weld for the as-welded specimen are shown in Figure 56a and Figure 57a, respectively. Throughout the weld region the stress state is characterised by large tensile longitudinal stresses, which are significantly greater than the corresponding transverse stresses. Consequently, different colour scales have been used for Figure 56 and Figure 57.

113
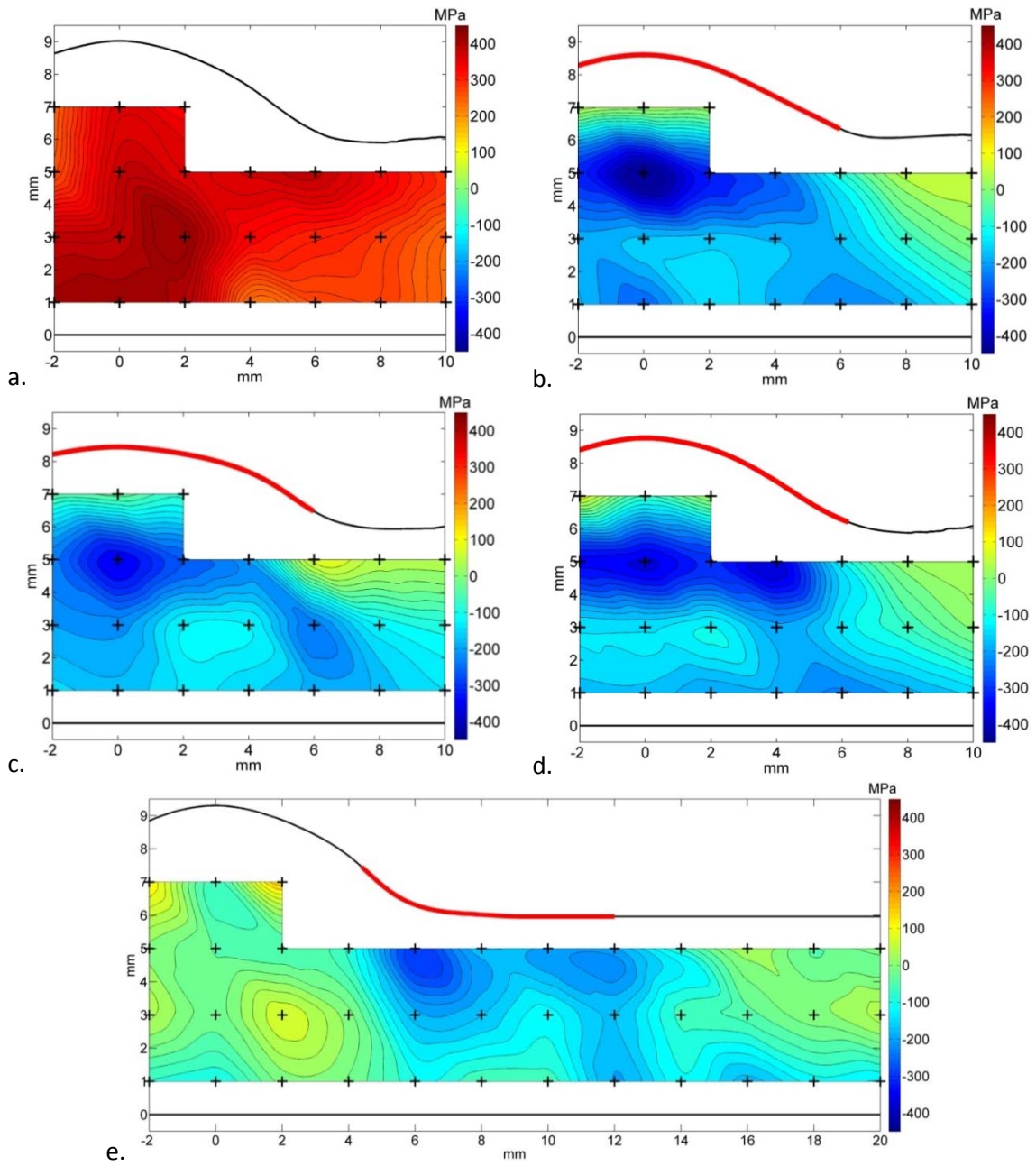
Figure 56: Longitudinal residual stress in steel weld seams: (a.) no rolling, (b.) rolled with profile A, (c.) rolled with profile B, (d.) rolled with profile C, and (e.) rolled with profile D. Measurement locations indicated with black crosses, thick red lines show the approximate roller contact area.
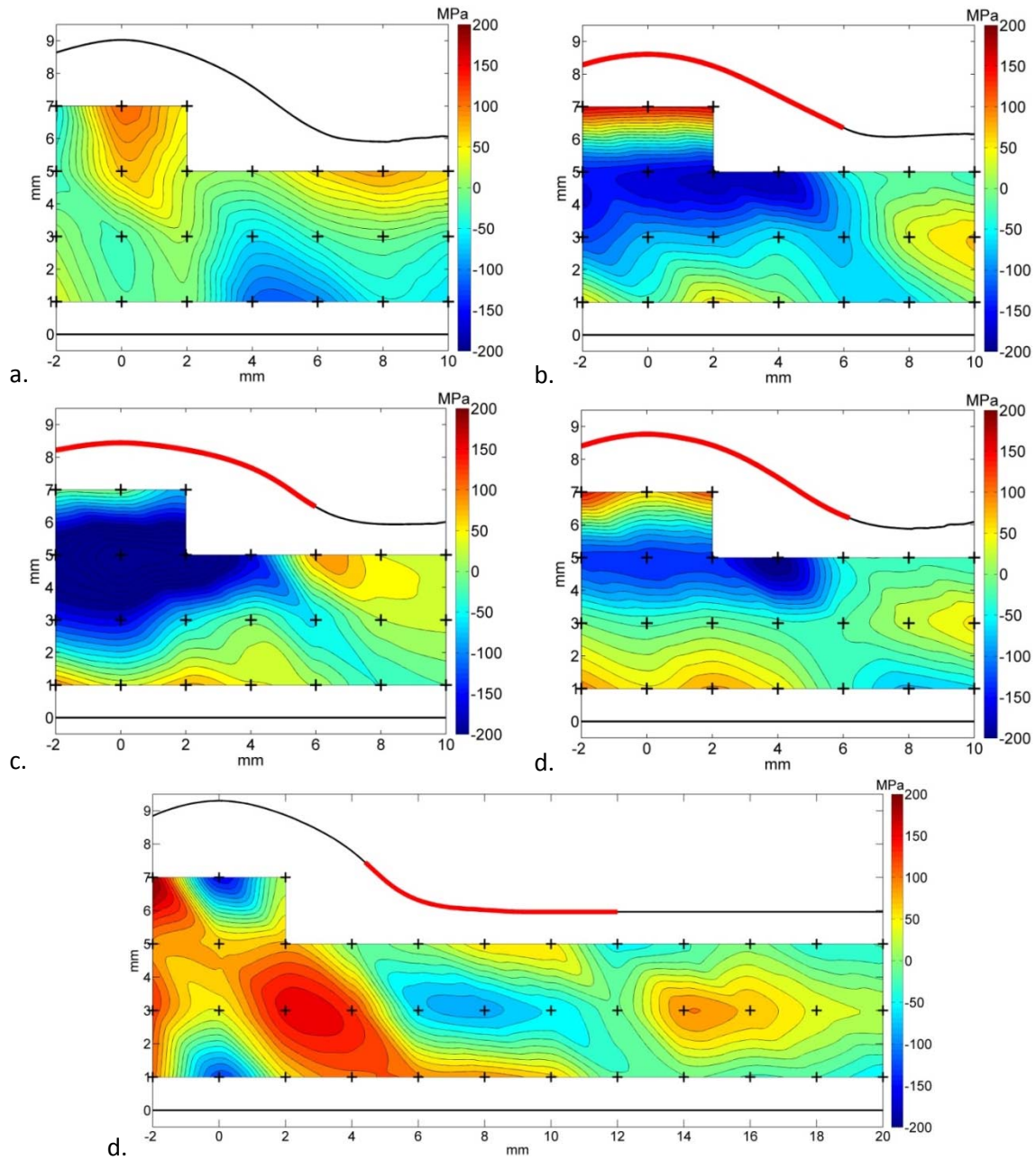
Figure 57: Transverse residual stress in steel weld seams: (a.) no rolling, (b.) rolled with profile A, (c.) rolled with profile B, (d.) rolled with profile C, and (e.) rolled with profile D. Measurement locations indicated with black crosses, thick red lines show the approximate roller contact area.

Longitudinal stress in the set of specimens rolled after welding is shown in Figure 56b-e. Over the area investigated, all of the three welds which were rolled directly on the weld seam (Rollers A-C, Figure 56b-d) are in general compression in the longitudinal direction. Likewise, the transverse residual stress component (Figure 57b-d) is similar for the three specimens, with moderate residual compression occurring towards the mid-thickness of the weld. The weld rolled at the sides of the weld seam (Figure 56e) shows only minor longitudinal residual stresses (largely in the range ±50 MPa) within the weld metal, with longitudinal compression adjacent to it beneath the roller path.

Unlike the as-welded specimen and the specimens rolled directly on top of the weld, this specimen shows significant tensile transverse stresses in the weld region (Figure 57e).

The statistical error introduced into the measurements by refinement of the diffraction pattern was estimated to be ±23 MPa, however this does not account for the possible effect of other factors such as crystallographic texture and uncertainty in gauge volume positioning.

Fatigue

Figure 58 shows the number of cycles to failure at different stress ranges for the fatigue specimens. The specimens without rolling treatment had the greatest fatigue life for any given stress range. In all cases, failure occurred due to a crack initiating at the weld toe and propagating through the thickness of the specimen (see Figure 55). None of the fatigue cracks were observed to have been deflected by microstructural interfaces in the heat-affected zone.
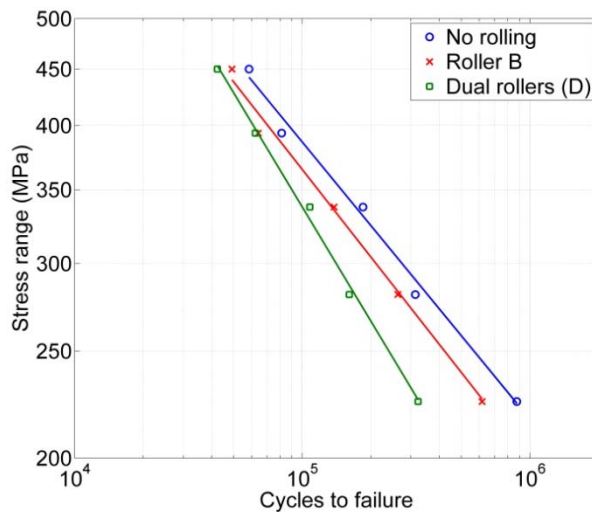
Figure 58: Endurance of rolled weld specimens under four-point bend fatigue loading.

Discussion

From Figure 56 and Figure 57, it is apparent that post-weld rolling greatly changes the residual stress state in the weld. With all roller profiles studied, this affects the entire thickness of the weld, indicating that plastic deformation induced during rolling occurs not just at the specimen's surface but also further within it. This is consistent with the observation in Chapter 7 that post-weld rolling resulted in work-hardening throughout the weld thickness.

When rolling is applied directly to the raised weld seam, the resulting distribution of residual stress is relatively insensitive to the roller geometry: all of the roller profiles which were applied directly to the weld seam (Rollers A-C, see Figure 53) had a broadly

similar effect on the final stress distribution (see Figure 56b-d). Since in all cases the longitudinal residual stress was observed to be strongly compressive, it is likely that at this level of load (150 kN), gross plasticity is induced throughout the weld. In the presence of such widespread yielding, the effect of variations in roller geometry is quite small. However, this does not preclude the possibility that the roller geometry might have more influence on the residual stress state when lower rolling loads are used, and only a small amount of localised material yielding is achieved, rather than extensive plasticity throughout the weld.

Rolling adjacent to the weld seam (see Roller D, Figure 53) as also observed to dramatically reduce tensile residual stress in the longitudinal direction (Figure 56d). It did not generate such large compressive longitudinal stresses as observed for Rollers A-C, although it should be noted that the total extent of the contacting region for Roller D was significantly greater. It has previously been shown that the magnitude of longitudinal residual stress induced by post-weld rolling varies approximately linearly with roller load [3, 202]. Therefore, it is likely that to achieve a similar level of longitudinal residual stress in the weld fusion zone, rolling at the sides of the weld seam would require a greater roller force than rolling the top of the weld directly. Furthermore, the introduction of tensile transverse stresses (see Figure 57d) during the application of this method could be detrimental to fatigue life. It should be noted however that transverse residual stresses (unlike longitudinal ones) typically vary significantly along the weld length, so the distributions shown in Figure 57 may not be representative of the entire weld.

Variation in residual stress through the specimen thickness was observed with all roller designs. For example, adjacent to the rolled region (i.e. at 6-10 mm in Figure 56b-d, and at 14-20 mm in Figure 56e), rolling appears to create a less compressive state of residual stress close to the rolled surface than it does towards the lower surface of the specimen. This is probably indicative of a distribution of longitudinal plastic deformation (induced by rolling) which varies through the weld thickness. Similarly, when the weld seam itself is rolled, the region of greatest compressive residual stress occurs at some distance within the weld (around 5 mm from the lower surface), rather than at the surface of the weld seam. Depending on the tool and workpiece geometry, there must at some point be a limit to the depth at which rolling the surface of the weld can induce plasticity, and this would limit the effectiveness of rolling for residual stress reduction in thick-section welds. However, this limit does not appear to have been reached in the relatively thin weld specimens presented here.

Specimens subjected to post-weld rolling had a lower fatigue life than as-welded samples (see Figure 58). This effect cannot immediately be attributed to the modified residual stress state, since the transverse component of residual stress in the region of

fatigue cracking (6-8 mm on the horizontal axis in Figure 57a, c and d) is approximately the same for all three cases. Furthermore, the samples used for the fatigue tests were excised from the much larger weld specimens, and it is likely that the majority of the stresses present in the original welds were relaxed during cutting [241, 242]. Indeed, the width of the fatigue test-pieces (40 mm) was approximately equal to that of the central zone of tensile longitudinal residual stress in the as-welded specimens; which is the criterion suggested by Altenkirch et al. to indicate effectively complete stress relaxation in an excised transverse sample [242]. The level of roller force used here was enough to visibly change the weld profile, essentially forging the weld seam (see Figure 55). As observed in Chapter 7, rolling also causes significant work-hardening of the weld. Therefore, while post-weld rolling was seen to reduce the fatigue life of excised specimens, this can most likely be attributed to the geometric and hardening effects of the process. However, it is clear that for any process which aims to reduce residual stress, any side-effects which may also affect fatigue properties should be carefully considered.

Conclusions

1. Gas metal arc welds in structural steel typically contain large tensile residual stresses, particularly in the direction longitudinal to the weld seam. Plastic deformation caused by post-weld rolling can effectively reduce welding-induced residual stress around the weld, or even result in large compressive residual stresses in the longitudinal direction.

2. Post-weld rolling applied either to the weld seam itself, or to the parent material directly adjacent to it, can remove tensile residual stresses in the weld. However, for the roller arrangements investigated here, rolling directly on the weld seam had the greatest effect on the residual stress distribution.

3. Post-weld rolling, using several roller geometries and a roller force of 150 kN, has been shown to induce plastic deformation throughout a 6mm-thick structural steel weld. Due to this extensive plasticity, the distribution of residual stress after directly rolling the weld seam is relatively insensitive to the precise shape of the contacting part of the roller.

4. The fatigue life of specimens from rolled welds was lower than for those without rolling. This can probably be attributed to changes in weld seam geometry and hardness, rather than to modification of the residual stress state.

Chapter 9: Pre-weld rolling

This chapter is an edited and expanded version of the following article:

Abstract

In this chapter, a method of pre-weld rolling which can be applied to components prior to fabrication has been investigated. It is demonstrated that pre-weld rolling can be used to give a moderate reduction post-weld distortion. The mechanism by which pre-rolling acts to modify the state of residual stress is discussed, and using neutron diffraction stress measurements it is shown that this form of rolling does not cause a reduction in longitudinal residual stress at the weld line. Instead, it appears that the reduction in final distortion is due to through-thickness variations in plastic deformation under the roller path.

Introduction

Localised rolling of weld seams involves the application of a large compressive force to a small area of the workpiece, which is necessary to achieve the substantial plastic strain required. Consequently the equipment required for this type of rolling may be large. The essential components which comprise this are a large, stiff structure to support the roller over the workpiece and a system, possibly hydraulic, to apply the load (see Figure 59). A means to reduce the structural requirements of a rolling system is discussed Chapter 5, but given such size constraints post-weld rolling is clearly unsuitable for use in many applications, since welded assemblies must be brought to a rolling machine which itself cannot be made portable.

If a state of residual stress could be induced in components prior to welding, such that it wholly or partially cancelled the stress produced by the weld, there would be no need to roll the assembly subsequently. Plates could be pre-rolled along the edges due to be joined, and then assembled. This pre-weld rolling technique would be easy to accomplish compared with rolling either during or after welding.

Mechanisms of stress formation and reduction
During welding, compressive plastic strain in an area surrounding the weld line is induced by a cycle of expansion, softening and constrained contraction of the parent

material under a non-uniform thermal field, resulting in a large tensile residual stress in the longitudinal direction of the weld (see Chapter 2). In-process stress reduction techniques typically work by inducing tensile plastic strain behind the welding heat source, in order to counteract the effect of thermal contraction. For example, the use of an intense cooling device trailing the heat source increases the amount of tensile plastic strain behind it, as shown by van der Aa et al. [110]. By contrast, Global Mechanical Tensioning (GMT) involves the application of a large longitudinal stretching force to the workpiece as it is welded - again, this increases tensile yielding behind the heat source [14].

The fundamental mechanism by which rolling acts is by compressive deformation of material in the direction normal to the rolled surface, which by the Poisson effect causes expansion in the in-plane directions. This has been used recently by Williams and coworkers [3, 183, 243], and previously by a number of others [139, 141, 138, 244], for both in-process and post-weld deformation of material close to the weld line. With the exception of that by Liu et al. [244], all of these experiments have used this in-plane tensile yielding to either prevent or relieve longitudinal residual stresses.

For this study, two possible mechanisms by which pre-weld rolling could reduce post-weld residual distortion in thin plate welds were proposed. Firstly, it was shown in Chapter 4 that rolling of steel plate produces a compressive longitudinal residual stress underneath the roller path. If rolling is carried out over a thin region parallel to and slightly removed from the weld line, then this compressive stress is equilibrated by a tensile one lying partly along the weld line (also see Chapter 4). This tensile stress might then have a stretching effect during welding similar to that of GMT, and the consequent reduction in residual stress would prevent or reduce the appearance of buckling deformation. Second, the roller might introduce stresses which were asymmetric about the mid-plane of the plate (as was observed in Chapter 8), causing a small amount of bending. If aligned so as to counteract the welding-induced buckling distortion this might give an overall reduction in final distortion, though not a significant reduction in residual stress.

Experimental

Rolling equipment
The rolling machine used for this work is described previously in Chapter 5, and more fully in Appendix A. The load (up to a maximum of 200 kN) is applied directly to the roller axis by a hydraulic cylinder mounted vertically and attached to the machine's crossbeam. The workpiece is attached to the machine bed using a vacuum clamping system. To roll the sample, a constant force is applied and the whole crossbeam assembly is moved in the rolling direction by a pair of motor-driven leadscrews (see

Figure 59). The compressive force is monitored using a load washer between the hydraulic cylinder and the roller head. The device also has an attachment for a welding torch, allowing rolling and welding to be carried out with the same machine.

a.

b.
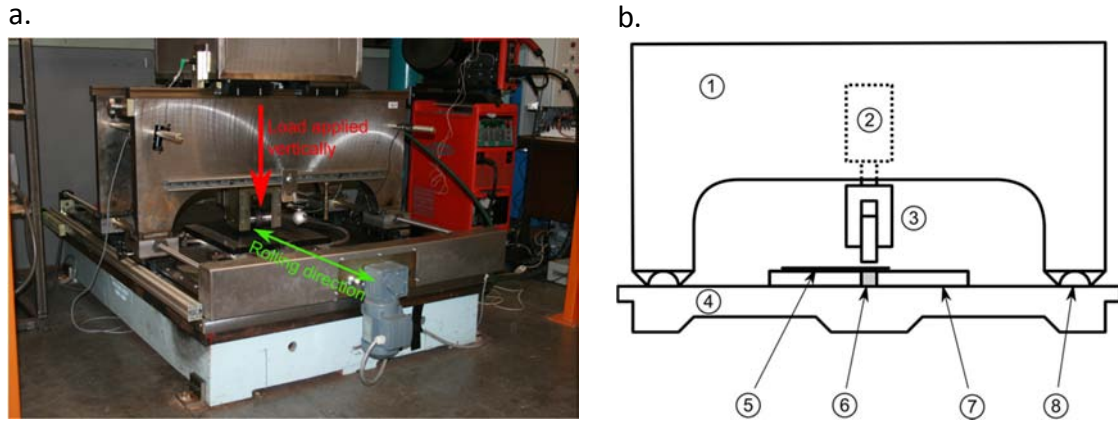
Figure 59: Experimental machine for single-sided rolling. 1. Crossbeam 2. Hydraulic cylinder 3. Roller fork 4. Bed 5. Workpiece 6. Backing bar 7. Vacuum clamps 8. Leadscrew. See Appendix A for further details.

Specimen preparation

To test the pre-weld rolling method, butt welds were made between pairs of 4mm-thick plates of S355 structural mild steel, with each individual plate measuring 500 x 200 mm. The samples were pre-rolled prior to welding using the rolling machine designed for these experiments (see Appendix A). Three basic rolling parameters were varied to assess their effect on the welded sample: the compressive force transmitted through the roller, the distance y_r from the side of the roller to the edge of the plate, and whether the roller was applied to the upper or lower surface of the plate. The upper surface of the plate was defined as the side from which the plate was welded.
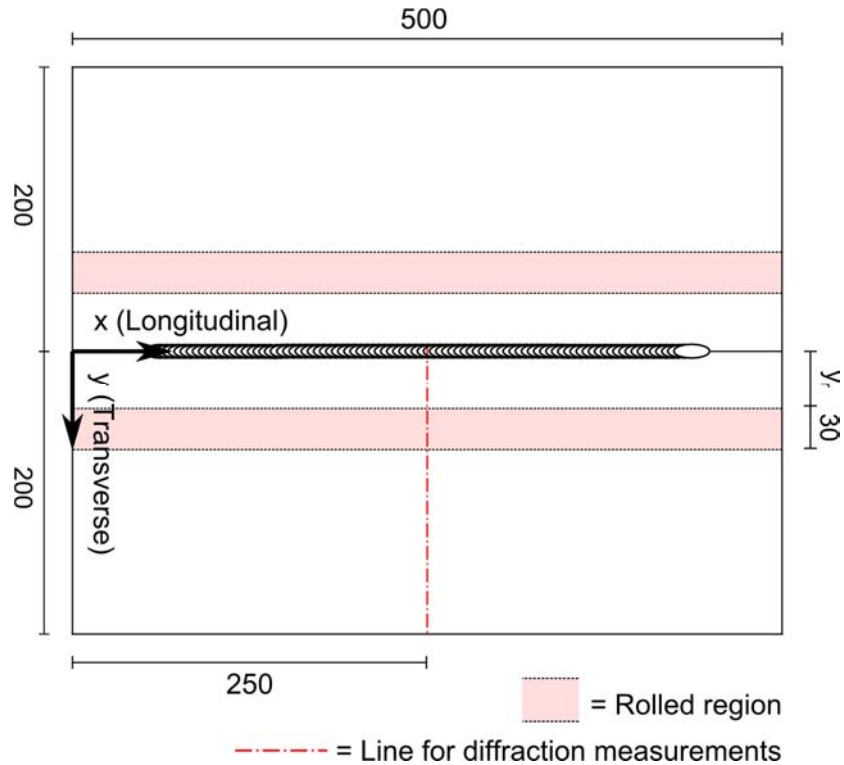
Figure 60: A completed weld comprising two individual plates rolled prior to welding at a distance y_r from the plate edge.

Two groups of specimens were manufactured using pre-weld rolling in addition to ten control samples which were welded without any rolling treatment. For the first, Set A, two pairs of plates were welded for each of the combinations of rolling parameters in Table 10, one pair each for rolling on the upper and lower sides. For Set B, rolling was carried out at a single combination of load and distance: 200 kN at 40 mm from the weld line. Five pairs of plates were rolled on the upper side and five on the lower side with these parameters.

Table 10: Rolling parameters used in Set A; for each combination of load and distance one sample was rolled on the upper side and one on the lower. *Set B contained an additional ten samples with this combination: five rolled on the upper side and five on the lower.

Distance y_r from weld line (mm)	Load (kN)			
	25	50	100	200
0	x	x	x	
10	x	x	x	
20	x	x	x	
40			x	x
60			x	x*

During rolling, each individual plate was held securely with a vacuum clamping system as the roller was passed over it. In all cases, only a single pass of rolling was used. To avoid damage to the vacuum system, the area of the plate directly underneath the path of the roller was backed with a steel backing bar, which could be replaced with a copper one for use during welding. The roller itself was 30 mm wide (see Figure 60), 100 mm in diameter and made from hardened EN24 steel; the speed at which it traversed the plate during rolling was 8.33 mm s^{-1}.

Welding parameters

After rolling, each pair of plates was tack-welded in four places to hold them together and the samples were then joined for 400 mm along their length using single-pass pulsed Gas Metal Arc Welding (GMAW). The parameters used for this process, summarised in Table 11, were designed to give full penetration of the fusion zone (where the metal had been fully melted) through the whole thickness of the plate, without using a root gap separating the plate edges.

Table 11: Welding parameters used in joining the rolled 4mm plate samples.

Process:	GMAW (pulsed)
Power supply:	Fronius TransPuls Synergic 5000
Contact tip to work distance (CTWD):	16 mm
Torch angle:	90°
Filler wire diameter:	1 mm
Filler wire feed speed:	242 mm s^{-1}
Travel speed:	10.8 mm s^{-1}
Current:	330 A
Voltage:	31.7 V
Gas composition:	5% CO_2, 2% O_2, balance Ar
Gas flow rate:	233 ml s^{-1}

Distortion measurement

To quantify the distortion present in each sample, it was placed on a flat measuring table and scans of the upper surface were taken using a laser measurement device (Romer Omega-arm and an R-Scan laser scanning head). This produced a series of measurement points which was used to fit a rectangular grid of 20 x 20 mm elements over the whole of the plate's surface; since each sample had nominal dimensions of 500 x 400 mm this resulted in a grid of 25 x 20 = 400 elements. The out-of-plane displacements of these elements were averaged to produce a single value representing the mean distortion for each plate.

123

Residual stress measurement

Neutron diffraction residual stress measurement was carried out on two specimens: one without rolling and one rolled at 200 kN, 40 mm from the plate edge on the lower surface. The general principles of neutron diffraction measurement of residual stress in polycrystalline materials are covered elsewhere [245, 196, 218], and for brevity will not be reiterated here. In this work, the SALSA strain-scanning monochromatic neutron diffractometer at the Institut Laue-Langevin, France [189] was used to measure the inter-planar spacing (d) of the material's ferrite {211} lattice plane. For each specimen, measurements were carried out at 33 points on a line running transverse to the weld, and located half-way along its length, to produce a partial transverse cross-section of the residual stress state. A neutron gauge volume of 2x2x2 mm, positioned at the mid-thickness of the specimen using through-wall scans, was used for all measurements. This gauge volume was defined using both primary and secondary radial collimators with a 2 mm focus. For the rolled specimen, lattice-spacing measurement was carried out in three orthogonal directions: in the longitudinal direction of the weld, transverse to it, and normal to the plate's surface. No additional measurements of the stress-free lattice spacing (d_0) were carried out, however using the additional assumption that stress in the normal direction was approximately zero, it was possible to calculate d_0 using [191]:

Equation 22

$$d_0 = \frac{1}{1+v}\left(vd_{xx} + vd_{yy} + (1-v)d_{zz}\right)$$

Where d_{xx}, d_{yy} and d_{zz} are the lattice spacings measured in the longitudinal, transverse and normal directions respectively, and v is the Poisson's ratio. Measures taken to ensure that the results were not affected by plane-specific material anisotropy are discussed in Chapter 4. Residual elastic strain ε in each direction was then calculated by comparing the measured lattice spacing with the calculated stress-free spacing. For example, in the longitudinal direction:

Equation 23

$$\epsilon_{xx} = \frac{d_{xx} - d_0}{d_0}$$

where ε_{xx} is the longitudinal residual elastic strain. Finally, Hooke's law was used to calculate residual stress in each direction. For example, in the longitudinal direction:

Equation 24

$$\sigma_{xx} = \frac{vE}{(1+v)(1-2v)}\left\{\varepsilon_{xx} + \varepsilon_{yy} + \varepsilon_{zz}\right\} + \frac{E}{1+v}\varepsilon_{xx}$$

Where σ_{xx} is the longitudinal residual stress. The values of the constants E and ν (the material's plane-specific Young's modulus and Poisson ratio, respectively) were Kröner model predictions [196]. For the specimen without rolling, experimental time constraints meant that it was only possible to measure the lattice spacing in the longitudinal direction (d_{xx}), and so the corresponding residual stresses could not be determined reliably.

Results and discussion

Results for Set A are shown in Figure 61, separated into plots for samples rolled on the upper and lower sides. The average out-of-plane displacement of the ten un-rolled control samples was 6.15 mm; this was used as a baseline against which distortion measurements from the rolled samples could be compared, and is included as a horizontal chain line. For samples rolled on the upper side (Figure 61a) there is a slight upward trend between distortion and roller load, indicating that rolling on this side is having a detrimental effect. However, the opposite trend is seen for samples which were rolled at higher distances from the weld line (20, 40 and 60 mm) on the lower side. In all cases, for lower roller loads (25 and 50 kN), the distortion does not deviate significantly from the mean distortion of the un-rolled samples. Hence, for this material a very large load is required to generate an observable difference in distortion post-weld.
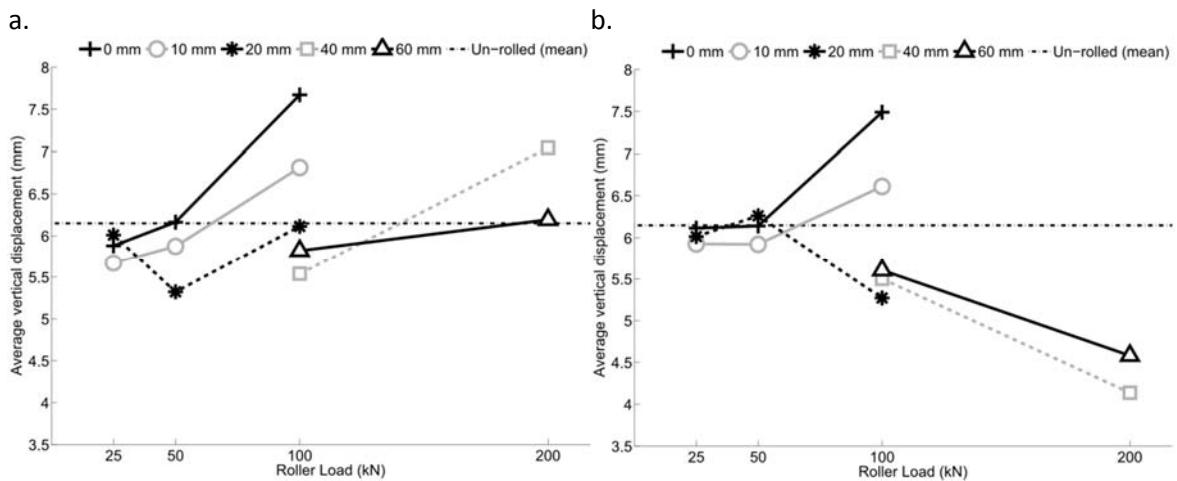

Figure 61: Average vertical displacement of rolled plates in experimental Set A. (a) Plates rolled on upper (welded) side (b) plates rolled on lower side.
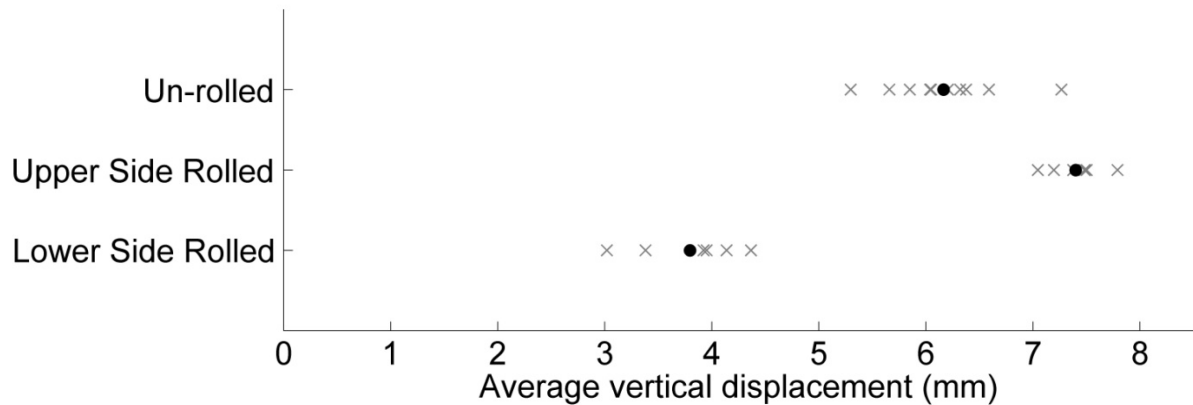
Figure 62: Mean vertical displacements for un-rolled samples, samples rolled at 200 kN and 40 mm from weld line on the upper side, and samples rolled at 200 kN and 40 mm from the weld line on the lower side. Grey crosses represent individual specimens, while black circles indicate the mean.

Sample Set B was used to further investigate a particular combination of rolling parameters with comparison to the un-rolled state, and to clarify the differences in the effect of upper and lower side rolling. The parameters were chosen based on the lowest-distortion result observed in Sample Set A: rolling at 40 mm from the plate edge, at a load of 200 kN, and on the lower side of the plate. Figure 62 compares the values average displacement for samples rolled with these parameters. The difference in residual distortion between the different cases is clear: the displacement of samples rolled on the lower side is on average 38% lower than that of un-rolled ones, while that of samples rolled on the upper side is 20% higher. Also noticeable in this figure is the moderate amount of variation in residual distortion for samples processed with identical parameters, which indicates the need for replication if measured distortion results are to be compared with computational models or used to draw strong conclusions.

Figure 63 has been used to illustrate further the differences in distortion observed in Set B; the composite surfaces have been constructed by taking the average over the sample set of the vertical displacement at each measurement point on the sample's surface. The surface representing samples rolled on the lower side is visibly flatter than both the surface for un-rolled samples and the surface for samples rolled on the upper side.
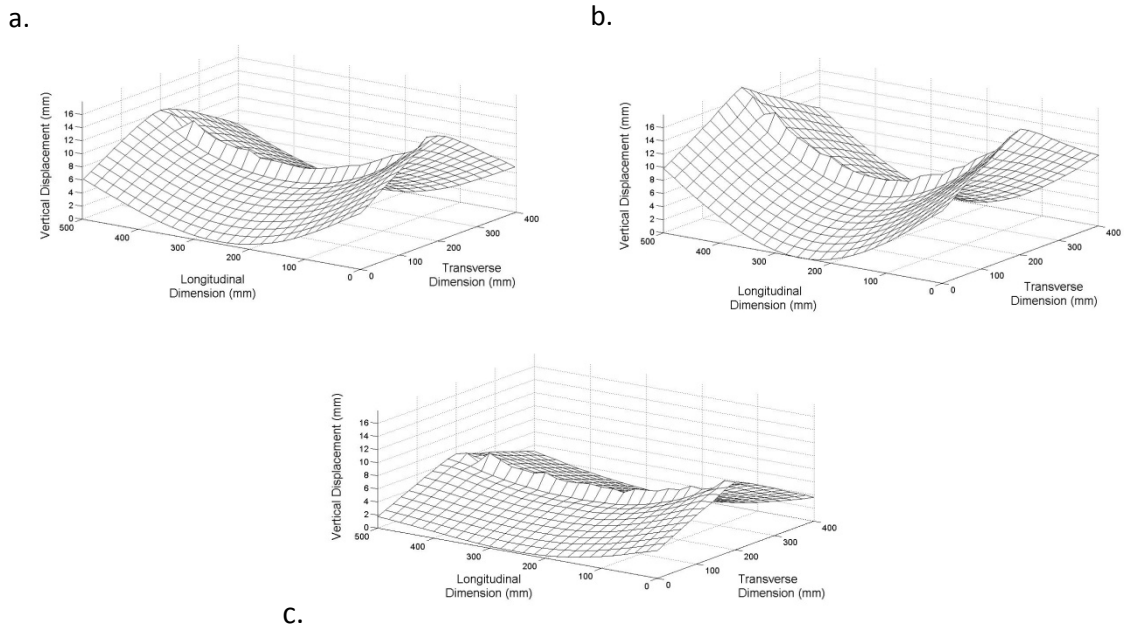
126

a.

b.

c.

Figure 63: Composite images representing the average buckling displacements of (a) plates welded without rolling (b) plates rolled on the upper side (c) plates rolled on the lower side. In all cases, rolling is at 200 kN and 40 mm from the weld line. Displacements on the vertical axis have been magnified 10x for clarity, and the welding direction is from left to right.

If the amount of plastic strain during rolling was approximately uniform over the plate thickness then the state of stress induced by rolling, and therefore the post-weld distortion, would be similar for rolling on the upper and lower sides of the plate. However, comparison of the samples rolled on opposite sides in Figure 63b and Figure 63c shows that this is not the case. A similar difference in distortion was observed by Wescott [243] in post-weld rolling of a very similar material with identical thickness. It can therefore be concluded that there is significant through-thickness variation in yielding with this roller and backing bar design during pre-weld rolling. An implication of this is that it is the bending deformation caused by this variation, rather than an overall reduction in weld-induced residual stresses, that is the primary mechanism by which post-weld distortion is modified by pre-weld rolling.

The neutron diffraction measurements described here were not designed to observe any through-thickness variation in residual stress: only stresses at the sample mid-plane were measured, and the size of the neutron scattering volume used was a significant fraction of the plate's thickness. Determining the through-thickness residual stress variation would have required a much smaller scattering volume and more measurement locations, greatly increasing the measurement time required. However, the view that the differences in average distortion brought about by pre-weld rolling is not due to a reduction in weld line residual stress is supported by the plot of residual stress across a transverse section of a weld subjected to 200 kN pre-weld rolling on the

lower surface at 40 mm from the weld line, shown in Figure 64. Although a region of significant residual longitudinal compression arises under the roller path, the residual stress state at the weld line is still strongly tensile (approximately 500 MPa) in the longitudinal direction. While the equivalent residual stress profile for a weld without rolling could not be obtained in the experimental time available, lattice spacings in the longitudinal direction for the rolled and un-rolled specimens, shown in Figure 65, can be used directly to give an approximate comparison. For the rolled specimen, the longitudinal lattice spacing at the weld centre (0 mm) is actually slightly wider than for the un-rolled weld, suggesting that the longitudinal residual compression induced by the roller adjacent to the weld may even worsen the state of longitudinal tension at the weld line.
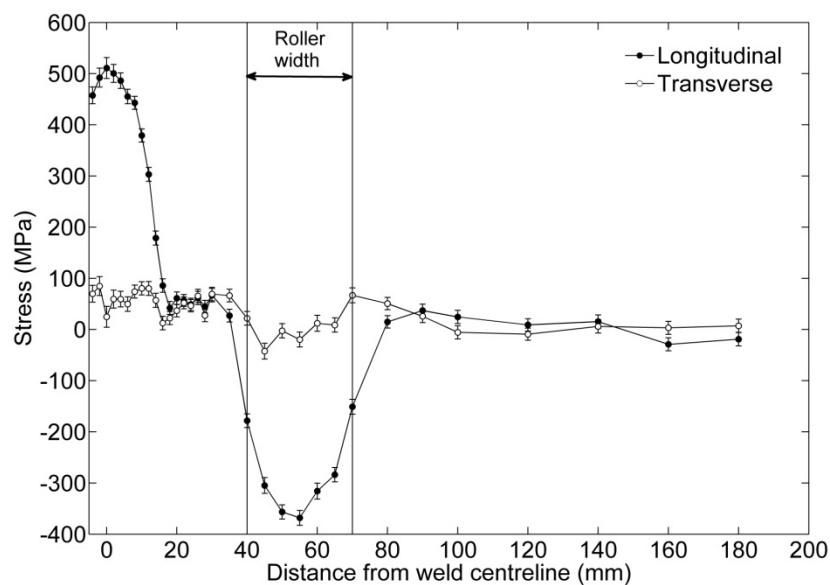

Figure 64: Residual stress in a transverse section across one side of a 4mm-thick steel plate weld treated with pre-weld rolling, measured using neutron diffraction.
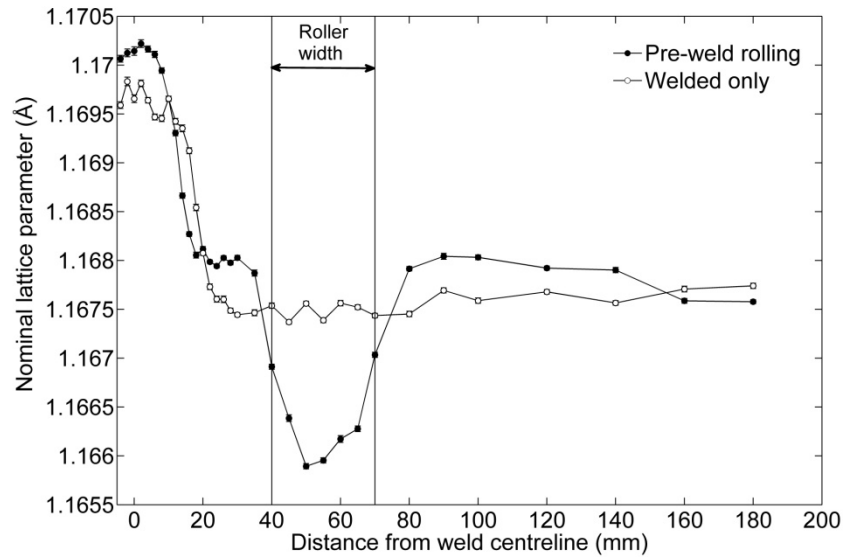
Figure 65: Nominal lattice spacing of the Fe{211} plane measured in the longitudinal direction across one side of a 4mm-thick steel plate weld specimens with and without pre-weld rolling (neutron diffraction measurements).

Conclusions

The use of pre-weld local rolling to reduce welding-induced buckling of mild steel plate has been investigated, and it has been demonstrated that out-of-plane distortion can be decreased by an average of 38% using this method. With optimisation of the rolling parameters, it may well be possible to achieve an even more pronounced reduction. A significant force (200 kN) normal to the surface of the workpiece was required to achieve the largest improvements observed during this study; for the roller geometry used here on 4 mm-thick steel samples, pre-weld rolling loads in the range 0 - 100 kN were found have relatively little influence on the final distortion.

The pre-weld rolling process described here induces a state of residual stress in the material which varies over its thickness; this was indicated by a marked difference in post-weld distortion between plates which had been rolled on opposite sides. To achieve a reduction in distortion it is necessary to roll on the side opposite to that from which the plate is subsequently welded. It is therefore proposed that for this type of pre-weld rolling, bending deformation is the primary mechanism by which the distortion is reduced: and it has been shown using neutron diffraction that there is no great reduction in longitudinal residual stress at the weld line.

A small amount of variation in the magnitude of buckling distortion for similar samples can be seen in the experimental results. Although expected due to the unstable nature of this distortion mode, it highlights the necessity of sample replication in studies involving buckling deformation under the action of residual stress.

129

Chapter 10: The application of rolling for residual stress reduction in additively-manufactured structures

Some of the results described in this chapter are also included in the following article:

Abstract

High-pressure rolling has been applied to Wire and Arc Additive Manufacturing (WAAM) – a process with which complex metal objects can be built up in layers using a welding arc to deposit molten material. The effect of rolling on residual stress and distortion are investigated using neutron diffraction and laser coordinate measurements of additively-manufactured steel test specimens. It is found that both rolling applied during metal deposition and rolling applied between deposition passes can affect the residual stress distribution, although only inter-pass rolling has a beneficial effect on the final distortion of the component. This differs from the case of a single-pass weld, where rolling during welding is ineffective for the purpose of residual stress reduction (see Chapter 5). Two different types of roller have also been tested, and found to have slightly different effects on residual stress and distortion.

Introduction

In additive manufacture, three-dimensional components are built up by the incremental addition of material, usually in discrete layers. For additive manufacture of metal components, one method of material deposition is to use an electric arc to melt filler wire, which then resolidifies on the component. This can be achieved using conventional Gas Metal Arc Welding (GMAW) or Gas Tungsten Arc Welding (GTAW) processes. While they are generally not as precise as other methods of metal deposition (such as laser powder deposition [246]), Wire and Arc Additive Manufacturing (WAAM) techniques can achieve very high material deposition rates, which allows large metal components to be constructed rapidly [247].

A problem that WAAM shares with most other methods of additive manufacture is the presence of large residual stresses in the deposited material [159, 248, 249, 250]. As is the case with all techniques which involve localised melting and resolidification, such

as fusion welding and allied processes, the presence of a varying thermal cycle means that local differences in thermal expansion and contraction cause physical incompatibility (misfit) between different areas of material [2].

Adverse distributions of residual stress in metallic materials are known to have various detrimental effects. Since tensile residual stresses across a crack tip favour crack opening, such a stress existing in a region of an object vulnerable to, for instance, fatigue or stress-corrosion cracking can accelerate failure [1, 31]. In the case of additive manufacture, as for welding, residual stresses may additionally cause problems for the manufacturing process itself. For example, physical distortion or warping of the component resulting from residual stress may unacceptably reduce its dimensional accuracy, and in some cases stress build-up can cause fracture of deposited material during the addition of subsequent layers [249].

In Chapters 5 & 6, localised high-pressure rolling of single-pass welds was shown to be highly effective at relieving tensile residual stresses at the weld seam; rolling after the weld has been carried out causes localised yielding of the weld metal, allowing residual stresses to relax. In this study, the effect of high-pressure rolling during WAAM on the residual stress state in additively-manufactured steel specimens is investigated.

Experimental

Specimen description

Rectangular substrate plates of S355 mild steel, 500 x 60 x 12 mm in overall size, were used as a base for the WAAM samples. Onto each of these, a vertical mild steel 'wall' was deposited along the specimen length in 20 linear welding passes (see Figure 66). The welding process used was controlled dip-transfer GMAW, and the parameters for this are given in Table 12. While the deposition passes were carried out, the substrate plate was kept clamped securely to a water-cooled aluminium base. After each layer was deposited, the top of the wall was allowed to cool to below 50°C before any subsequent metal deposition or inter-pass rolling was carried out.
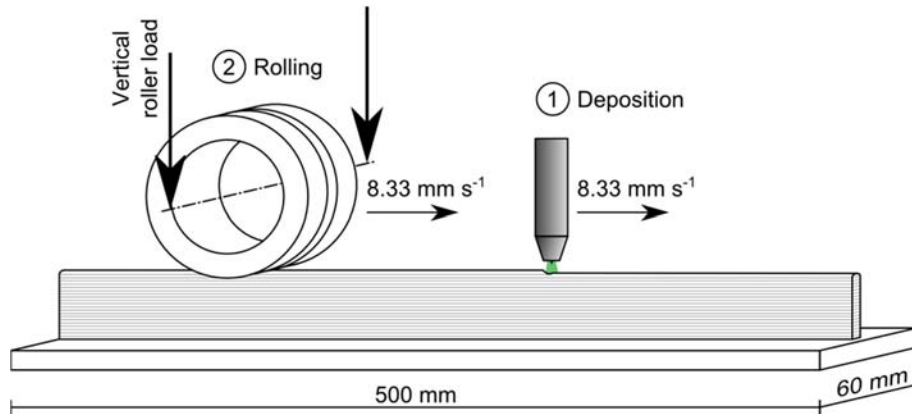
Figure 66: WAAM residual stress test specimen, showing the deposition and rolling processes. The roller is positioned 120 mm behind the arc.

Table 12: Parameters used during for the deposition of material on the WAAM specimens.

Process:	Controlled dip-transfer GMAW
Power supply:	Fronius TransPuls Synergic 5000 CMT
Mean current:	113 A
Mean voltage:	14.9 V
Welding speed:	8.33 mm s^{-1}
Filler wire feed speed:	166.7 mm s^{-1}
Filler wire type:	ISO 14341-A-G 3Si1, 0.8 mm dia.
Contact tip stand-off:	13 mm
Shielding gas rate:	0.33 dm^3 s^{-1}
Shielding gas composition:	20% CO_2, 80% Ar

Rolling process

In the case of all specimens, during rolling a constant vertical load was applied to the top of the specimen using a hardened H13 steel roller of 100 mm diameter and with a circumferential groove to accommodate the curved surface of the top of the wall. A schematic of the equipment used to apply the rolling treatment is shown in Figure 67. The roller head assembly is driven by a vertically-mounted hydraulic cylinder; applied force can be set by varying the cylinder pressure, and is monitored using a load cell. To move the roller over the specimen, the entire crossbeam is translated at a constant velocity. Rolling can be carried out either after each material deposition pass, or directly trailing the welding tool as deposition takes place.
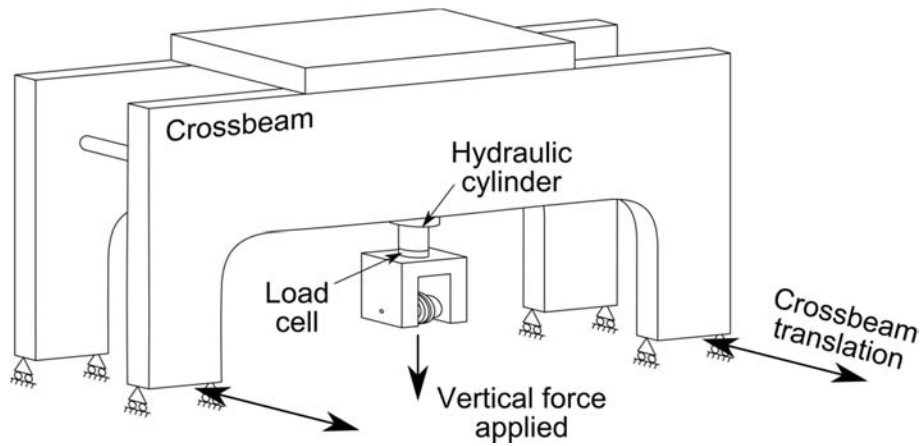
Figure 67: Schematic representation of the mechanism used to apply rolling treatment. The specimen is held stationary while the crossbeam is translated, moving the roller over it.

In addition to determining whether rolling can be used to reduce residual stresses in WAAM structures, this study aimed to investigate the effects of roller geometry, roller load, and rolling temperature on the residual stress distribution. Consequently, five pairs of specimens were produced using the rolling parameters shown in Table 13. The specimens were rolled either inter-pass (i.e. after every deposition pass, once the temperature of the deposited material had reduced to below 50 °C), or during welding with the roller axis positioned 120 mm behind the welding tool (here termed *in situ* rolling). In both cases a single rolling pass was carried out at 8.33 ms^{-1}; the same as the welding speed (see Figure 66). While most of the specimens were produced using a roller designed to contact only with the upper surface of the deposited wall (Roller A, see Figure 68), the final set used a roller profile with additional flanges designed to contain the deforming wall material (Roller B, see Figure 68). Due to the different rolling treatment applied, the overall height and thickness of the deposited walls was different for each set of specimens. For example, the specimens produced without rolling had a relatively high and thin wall, while most of the specimens rolled at 50 kN were lower and thicker (see Figure 69). In all cases the total volume of deposited material was the same.

Table 13: Rolling parameters. Two identical WAAM specimens were produced for each set of parameters shown, and the resulting mean height of the deposited wall (measured at the location used for residual stress measurement) is also indicated.

Set	When rolled	Roller	Roller force	Wall height
1	No rolling	n/a	n/a	43.0 mm
2	Inter-pass	A	25 kN	41.6 mm
3	Inter-pass	A	50 kN	33.9 mm
4	During deposition	A	50 kN	31.6 mm
5	Inter-pass	B	50 kN	38.5 mm
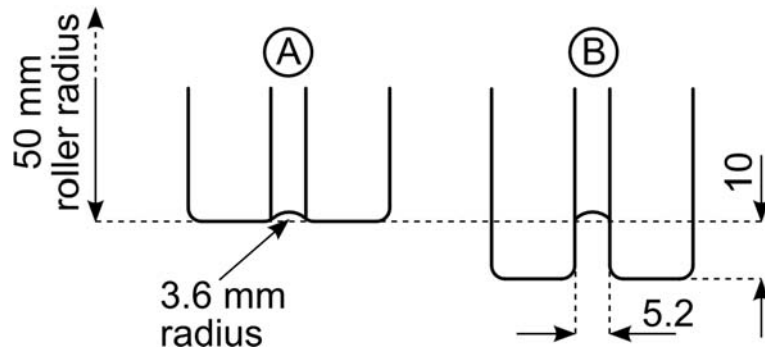
Figure 68: The two roller profiles used to produce the rolled WAAM specimens. Roller A only makes contact with the top of the specimen wall, while Roller B has additional flanges to contain the deforming wall material.

a.

b.
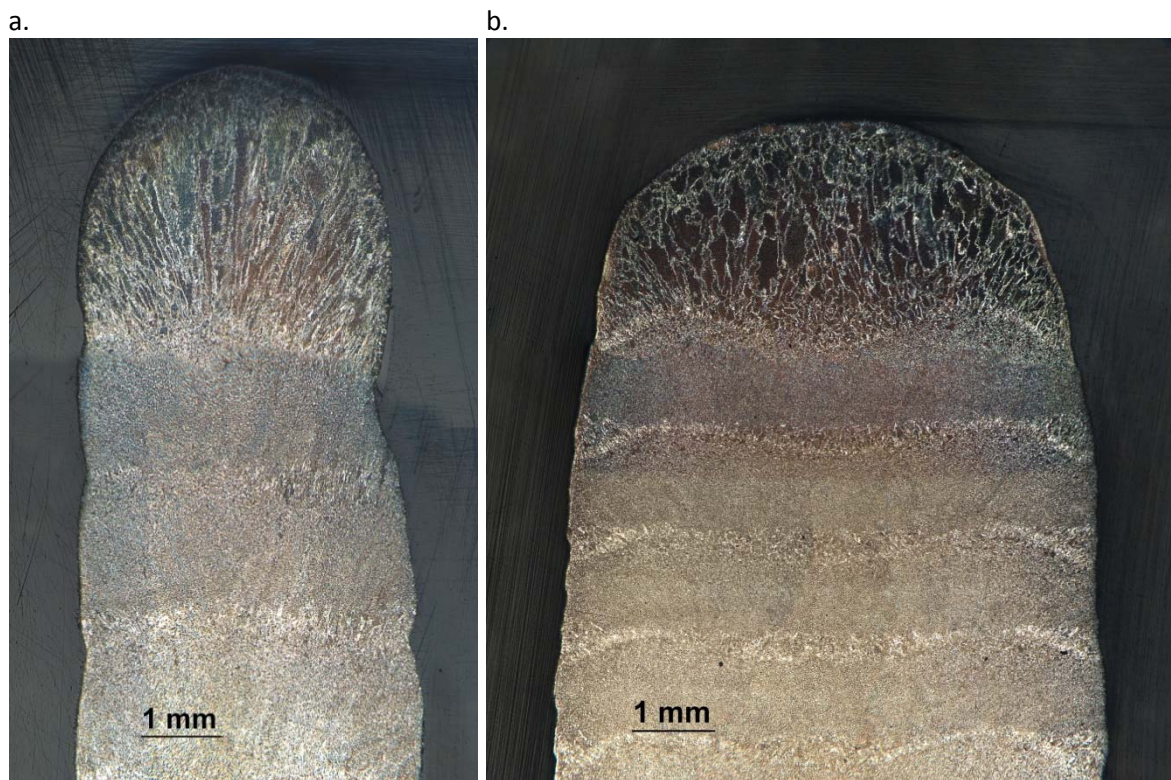
Figure 69: Cross-sectional composite macrographs of the top of two WAAM walls: (a.) without rolling, (b.) inter-pass rolling at 50kN using Roller A. Etchant: 2% nital.

Distortion measurement

After construction of each specimen was completed, it was allowed to cool to ambient temperature and then released from its clamping. In the absence of external restraint, the specimens bowed longitudinally under the action of their internal stresses. To quantify this distortion, an Omega R-Scan laser coordinate measurement machine (ROMER Inc., North Kingstown, RI, USA) was used to measure the vertical displacement of points on the upper surface of each specimen's substrate plate, on either side of the deposited wall. 10,000-15,000 scattered measurement points were

collected for each specimen. These points were then used to fit a regular surface comprising, 51 x 7 nodes (i.e. 10 mm square nodes), using the biharmonic spline interpolation method described by Sandwell [187]. The mean vertical displacement of these nodes was then used to quantify the deviation of the substrate surface from the ideal, perfectly planar, situation (see Figure 70).
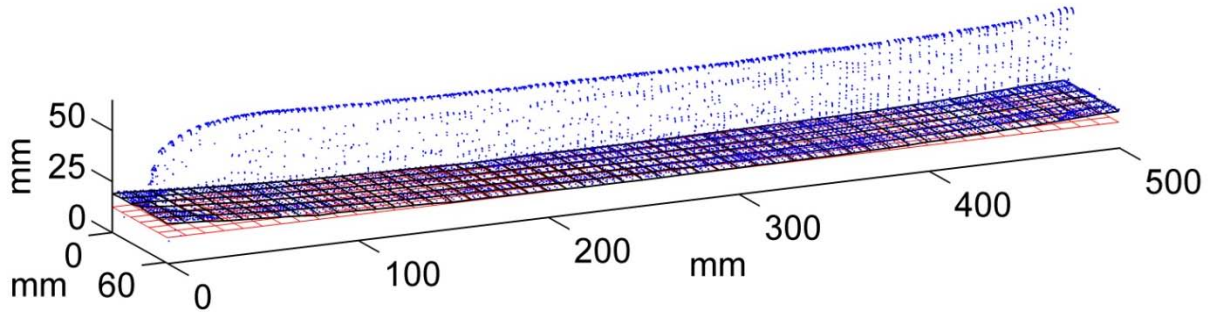
Figure 70: Distortion measurement method: raw coordinate measurements are shown as blue points, and the surface representing upper face of the substrate plate is shown in black. The mean displacement of this surface from a flat plane (red mesh) is taken. The example shown here is a specimen without rolling treatment.

Residual stress analysis

Analysis of the distribution of residual stress within the WAAM specimens was carried out using angular-dispersive neutron diffraction. The SALSA strain diffractometer at the Institut Laue-Langevin, France [189] was used to determine the inter-planar spacing (d) of the αFe {211} lattice plane in three orthogonal directions (longitudinal to deposited wall, transverse to it, and normal to the substrate plate's surface), using a neutron wavelength of 1.644Å. The residual elastic strain was then found using:

Equation 25

$$\varepsilon = \frac{d - d_0}{d_0}$$

where ε is elastic strain and d_0 is the lattice spacing of the material in its unstressed state. Two important factors affected the collection of d_0 data. Firstly, it was anticipated that the composition of each specimen would vary slightly in different parts of the measured region. Since compositional variation can affect the lattice spacing, spatially-resolved measurements of the unstressed lattice spacing were taken from stress-relieved 'comb' samples cut using electrical-discharge machining from deposited walls. Secondly, diffraction peak-broadening resulting from the different levels of plasticity undergone by each set of specimens could also cause an apparent peak-shift, affecting the determination of lattice spacing. To compensate for this effect, different d_0 comb samples were used for each set of rolling parameters. Also, to prevent any effect of plane-specific plastic anisotropy, orientation-dependent d_0 measurements were taken from the comb specimens, i.e. d_0 was measured separately

for the longitudinal, transverse and normal directions at each point. From each identical pair of WAAM specimens, one was cut to produce a d_0 sample while the other, intact, specimen was used for measurement of d itself.

All measurements were made on a cross-sectional plane half-way along the specimen's length (see Figure 71). Cuboid instrument gauge volumes were defined with dimensions of 2x20x2mm for measurements in the transverse (y) and normal (z) directions, and 2x2x2mm for the longitudinal (x) direction and d_0 specimens. Using the strain measurements in all three directions, the residual stress state at each measurement point was determined using Hooke's law. For example, in the longitudinal direction:

Equation 26

$$\sigma_{xx} = \frac{vE}{(1+v)(1-2v)}\{\varepsilon_{xx} + \varepsilon_{yy} + \varepsilon_{zz}\} + \frac{E}{1+v}\varepsilon_{xx}$$

Where σ_{xx} is residual stress in the longitudinal direction, while ε_{xx}, ε_{yy} and ε_{zz} are the residual strains. E and v are the plane-specific elastic constants; Young's modulus and the Poisson ratio, respectively. The values of the (plane-specific) elastic constants used in this calculation ($E = 225.5$ MPa and $v = 0.28$) were Kröner model predictions [196].
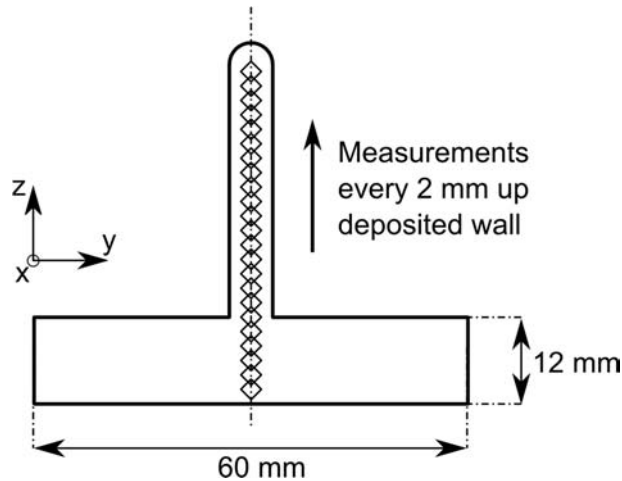
Figure 71: Cross-sectional view of a WAAM wall specimen indicating the locations used for residual stress determination.

Results

Distortion

Residual distortion of the WAAM specimens, measured using the method shown in Figure 70, is shown in Figure 72. For inter-pass rolling using Roller A (black circles), there is a gradual improvement in distortion with increasing roller force. At 50kN,

inter-pass rolling using Roller B shows an even greater distortion reduction than with Roller A. Rolling during deposition that this load, on the other hand, seems to result in even greater specimen distortion than when rolling is not applied at all.
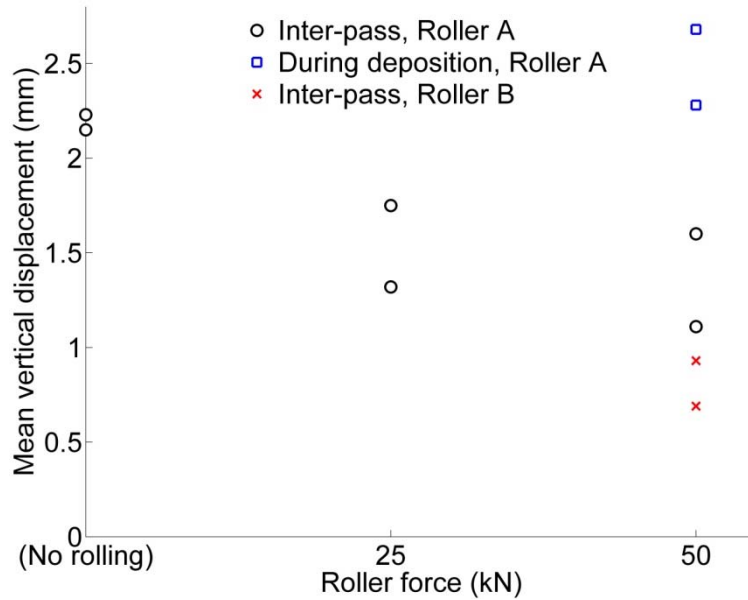
Figure 72: Mean out-of-plane displacement of the upper surface of the substrate plate for all ten WAAM specimens.

Residual stress

Figure 73a shows the variation in the longitudinal (x) component of residual stress over the height of each WAAM wall, and throughout the substrate plate directly below it. In all cases, the residual stress is most strongly tensile close to the interface between the wall and the substrate plate, while lower stresses are encountered further towards the top of the wall. For the un-rolled specimen for example, the longitudinal stress falls from a maximum at the substrate/wall interface to approximately zero at the top of the wall. Meanwhile, in the substrate plate directly below the wall, moderate tensile stresses are present. This distribution of longitudinal stress bears good resemblance to that previously found by Ding et al. [159] in similar WAAM specimens.
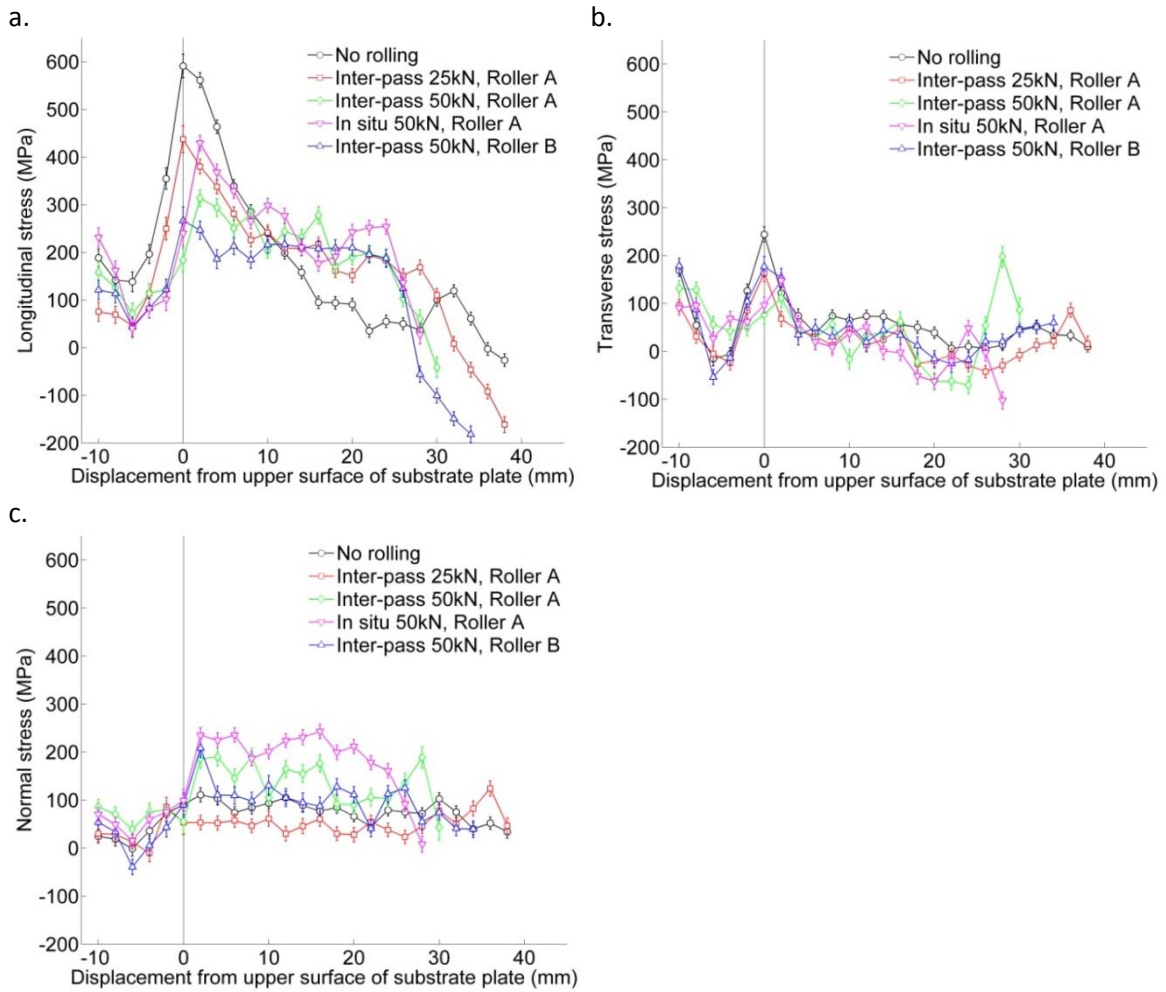
Figure 73: Residual stress in and directly below the deposited wall in WAAM specimens with different rolling parameters: (a.) longitudinal stress, (b.) transverse stress, (c.) normal stress.

All the forms of rolling investigated here seem to reduce the large tensile longitudinal stress at the substrate/wall interface, but have different effects on the state of residual stress further up the wall. For example, inter-pass rolling using Roller B (shown in blue in Figure 73a) results in an almost constant longitudinal residual stress distribution (of approximately 200 MPa) in the wall, with a distinct region close to the top of the wall where there is moderate longitudinal compression. Inter-pass rolling using the same value of roller load (50 kN) with Roller A (shown in green) gives a similar distribution of residual stress, but with a far less pronounced compressive region at the top of the wall.

It should be noted that since the specimens had different overall heights, the maximum values of displacement from the upper surface of the substrate are different. The total height of the wall at the plane of residual stress measurement for each set of rolling parameters is given in Table 13.

Discussion

In Chapter 5 of this thesis it was shown that for single-pass welds in structural steel, rolling after welding had a dramatic effect on the residual stress distribution, while rolling as welding was carried out (*in situ* rolling) was ineffective. These two rolling methods are mechanistically analogous to the two techniques used here for rolling WAAM specimens. During inter-pass rolling, the residual stress state is allowed to form completely after each deposition pass and is then acted upon by rolling, as in post-weld rolling of a single-pass weld. For rolling during WAAM deposition however, the roller acts to plastically deform the deposited metal while it cools and before the distribution of residual stress induced by the thermal process has fully formed.

Although for a single-pass weld only post-weld rolling changes the distribution of residual stress significantly (see Chapter 5), it can be seen from Figure 73 that both inter-pass and *in situ* rolling had an effect on the WAAM specimens in this study. However, the fact that inter-pass and *in situ* rolling at 50 kN using Roller A result in broadly similar residual stress distributions (Figure 73) but very different levels of distortion (Figure 72), suggests that the two processes act on the WAAM specimen in different ways. From the point of view of residual stress formation, WAAM differs significantly from a simple linear weld. The residual stress distribution is determined by many (in this case 20) thermal cycles rather than just one, with the deposition of each layer reaustenitising and partially remelting the layer before. Similarly, it is likely that rolling the top of a WAAM specimen causes plastic deformation in a number of layers. In addition to this, during WAAM the overall geometry of the built-up object changes significantly. In these experiments, the final effect of several different rolling processes has been found, but the different thermo-mechanical mechanisms by which these effects come about have not been fully investigated. To determine the exact mechanism by which rolling affects residual stress formation during WAAM would require further work including either finite element analysis or in-process strain measurement.

Roller geometry has a noticeable effect on several aspects of the completed WAAM specimens. It can be seen from Table 13 that the use of Roller B (featuring additional flanges to laterally constrain the deposited metal) rather than Roller A results in a greater wall height. The total volume of deposited material is the same in both cases, so the constraint provided by Roller B results in a taller and thinner wall. The specimens produced using Roller B also had less substrate distortion than those using Roller A with otherwise identical parameters (see Figure 72). Finally, the longitudinal residual stress in the specimens rolled inter-pass at 50 kN with Roller A and Roller B is generally similar, however in the region of material at the top of the wall rolled using Roller B it is much more compressive. While Roller B has the most beneficial effect on

distortion and residual stress, it is more difficult to apply practically. Due to the friction on the sides of the roller flanges, lubrication of the roller was required while using Roller B, which was not necessary when using Roller A. This lubrication was removed before the deposition of each new layer to remove the risk of it interfering with the welding process. While simple, straight specimens have been used in this study, the flanges on Roller B also project a short distance down the sides of the deposited wall, which would make building more complex objects difficult. For example, the rolling of curved walls and wall crossings would probably not be possible using Roller B.

Conclusions

1. High-pressure rolling can be used to reduce residual stress and distortion in metal additively-manufactured objects.

2. Rolling at low temperature between metal deposition passes and rolling at higher temperature during deposition can both be used to reduce the maximum tensile residual stress which occurs in the longitudinal direction at the interface between the substrate and deposited material. However for rolling during deposition, no beneficial effect on residual distortion was observed.

3. The shape of the roller used to apply rolling treatment affects the final distortion of, and the residual stress present in, additively-manufactured objects. Here, a roller with flanges to help contain the deposited material as it is deformed was found to be beneficial.

Chapter 11: Conclusions

Rolling for weld residual stress mitigation

The central aim of this project was to investigate high-pressure rolling for the purpose of residual stress mitigation in welds. For the practical application of rolling, the key finding of this work is that post-weld rolling can be highly effective at reducing the large tensile longitudinal residual stresses which occur in and around the weld seam. Other forms of weld rolling such as *in situ* and pre-weld rolling are, however, unsuitable for this purpose. The reasons for this have been investigated using experimental observations of residual stress formation during welding and rolling operations (outlined in Chapter 5), and can be explained in terms of the interaction between the time-varying thermal and deformation fields present. There is a fundamental thermo-mechanical reason why *in situ* rolling does not have a strong effect on the distribution of residual stress: the extent to which the plasticity induced by rolling can affect the residual stress distribution is limited by the yield strain of the rolled material. If the material is then subject to local thermal strains of a greater significantly magnitude than this as it cools, then any beneficial effect of rolling will be undone.

Aspects of the rolling process which are relevant to its practical implementation were investigated using similar lines of reasoning. For instance, it was found that while higher levels of rolling force result in more compressive residual stresses under the roller path, the level of residual stress induced is of course limited by the material's constitutive relations, and therefore the residual stress induced will 'saturate' when high rolling loads are used (see Chapter 4). Demonstrating that an oscillating roller force can be just as effective for residual stress reduction as a constant one (Chapter 5) was also important from the point of view of practical implementation: it proves that a different fundamental design of rolling apparatus is viable, which may allow the capital cost of rolling to be reduced. Finally, the buckling distortion which accompanies welding residual stress was also shown to be reduced by post-weld rolling (see Appendix C).

The basic mechanisms of residual stress modification via rolling have been investigated here, and this has led to several new questions which have not been addressed this study. The effect of rolling at intermediate temperatures is one example: it may be the case that in certain weld materials which undergo phase transformation at a relatively low temperature during cooling (some bainitic steels, for example), it would be possible to modify both the microstructure and the residual stress distribution in a single rolling operation provided it was carried out within the correct temperature range. Also, at some point there must be a ductility limit below which post-weld rolling risks cracking the material, but this has not be investigated here. While the application

of rolling to additive manufacture was studied in Chapter 10, no attempt has been made to measure or model the transient stresses and strains which occur during the process, and this will be vital to fully understanding the action of rolling in this context.

In this work, localised high-pressure rolling has been shown to be a viable and effective means of residual stress mitigation in structural steel welds. However, rolling also has inherent limitations which currently prevent its widespread use. Firstly, while rolling worked well for the simple test specimens used in this work, applying rolling to complex weld geometries would undoubtedly be more difficult. Rolling, most obviously post-weld rolling, also adds an additional step to the process of joining. In many applications where rolling would be beneficial, large seam-welds in the shipbuilding industry for instance, the cost of an additional process might be difficult to justify. However, when compared with most other methods of welding residual stress mitigation (see Chapter 2), rolling has the notable advantages of being quick and simple to apply, demonstrably effective, easily controllable, and requiring no consumable materials.

Measurement techniques

The ability to observe the emergence of residual stress using *in situ* strain measurement (Chapter 3) was important for determining the effect of rolling on a weld (Chapters 4 & 5). The methods for this described here, which are based on using sufficient data from strain gauges or digital image correlation to reconstruct the time-varying state of stress within a welded and/or rolled specimen, are simple, cheap, largely non-destructive, and can also be used to study residual stresses (Chapter 4). However, they also have the major drawback of being inherently limited in terms the measurement region which can be observed: they cannot be used to measure stress in regions which undergo plastic deformation during measurement, which are often the areas of greatest interest. Stresses in such regions must be inferred from remote measurements and suitable geometric simplifications.

Similarly, in Chapter 6 an unusual technique for determining the complete residual stress tensor using neutron diffraction was applied to study the effect of post-weld rolling. This allowed additional aspects of the residual stress distribution in a rolled weld to be studied; for example, using this data the residual von Mises stress could be calculated. It was hence shown that the shear components of residual stress induced by rolling were relatively small in magnitude, and therefore posed no additional threat for fracture or fatigue crack growth. The measurements also served to confirm that the principal residual stresses induced by welding are closely aligned with the welding direction (i.e. that the shear components are very small) at locations on the specimen's planes of symmetry - an assumption which is frequently exploited for the purposes of simplifying residual stress measurement in welds.

Effects of rolling on weld microstructure and mechanical properties

In addition to affecting the residual stress state, in Chapter 7 rolling was shown to influence other properties of structural steel welds. Post-weld rolling brings about work-hardening, while *in situ* rolling can cause greatly increased growth of acicular ferrite in the weld fusion zone, which can also increase the yield strength of the weld metal. This suggests that rolling could potentially be used for microstructural or mechanical property improvement, rather than to modify the residual stress state. While only one material (S355 structural steel) was investigated here, there are many material systems in which deformation during or after welding might have a beneficial effect. In wrought alloys, for example, work-hardening induced by post-weld rolling could be one method of returning strength to the weld zone. On the other hand, in Chapter 8 post-weld rolling was seen to reduce the fatigue lifetime of specimens excised from a steel weld. This was not thought to be primarily due to residual stress, suggesting that the cause may have been excessive work-hardening or geometric stress concentrators brought about by rolling. However, further experiments would be necessary to separate out the effects of the various consequences of rolling on the fatigue properties of rolled welds.

Although these aspects of rolling have only been dealt with briefly here, an obvious extension to this work would be to identify materials and welding techniques which might benefit from the potential effects of rolling (eg. work hardening, stress/deformation-affected phase transformation), and investigate the process on this basis.

General conclusions

Various authors (eg. [194]) have previously reported that localised rolling of metals can produce significant compressive residual stresses under the roller path. Moreover, it has recently been shown that this effect can be used to cancel-out tensile residual stresses produced by welding [3]. The results presented in this thesis strongly support these findings, and have confirmed that they are applicable to fusion welds in structural steels. However, it is clear that (for this type of material at least) rolling also increases weld hardness and can modify the weld bead geometry. As discussed in Chapter 2, the usual motivation for residual stress reduction in welds is either to improve resistance to fracture-based material failure (particularly fatigue), or to reduce stress-induced distortion. While rolling can certainly be used to control distortion (see Appendix C), the effects it has on other material properties may prevent its use for fatigue-life improvement: in Chapter 8, for example, specimens rolled post-weld were shown to have reduced fatigue life. However, other similar residual stress improvement methods which feature cold deformation (such as peening and overloading) are known to be effective at reducing fatigue crack growth rates [41, 1],

and there appears to be no fundamental reason why rolling could not have a similar effect given the right conditions. Obviously, it will also be necessary to understand better the effects of rolling on factors other than residual stress before it can be used practically.

It has been demonstrated that for single-pass welds only rolling applied post-weld, rather than prior to or during welding, can improve the residual stress distribution. This conclusion is consistent with the results of previous experiments by Kurkin et al. [138] and Altenkirch et al. [3]. Furthermore, the results presented in Chapter 5 suggest that *any* rolling or peening process applied to the weld seam before it has largely cooled will have little effect on residual stress. However, the situation is different when stress develops over repeated thermal cycles, as is the case for the additively-manufactured specimens in Chapter 10. Here, rolling at high temperature during each deposition pass, and rolling in-between passes at lower temperature both reduced residual stress, although not so completely as can be achieved in single-pass welds.

This thesis mainly concerns the effects of rolling on weld properties, but for rolling to be used practically it is also necessary to consider aspects of its implementation. There are currently two key difficulties with the practical implementation of rolling: the requirement for specialised rolling equipment, and the difficulty involved in rolling geometrically complex components without causing damage. Although the successful use of rolling with a time-varying roller force (Chapter 5), suggests that some reductions in equipment cost may be possible, the second point has not been addressed here: all of the specimens used in this research (including the additively-manufactured parts in Chapter 10) were geometrically uncomplicated, and required only simple straight-line rolling operations. Finally, while it has been shown that rolling can cause plasticity throughout the thickness of a weld in 6 mm steel (see Chapters 7 & 8), the maximum depth into material to which rolling is effective has not be established.

Reference List

[1]   P. J. Withers. Residual stress and its role in failure. *Reports on Progress in Physics*, 70(12):2211–2264, 2007.

[2]   K. Masubuchi. Residual stresses and distortion in welds. In K. H. Jürgen Buschow, R. W. Cahn, M. C. Flemings, and B. Ilschner, editors, *Encyclopedia of Materials: Science and Technology*, pages 8121–8126. Elsevier, 2001.

[3]   J. Altenkirch, A. Steuwer, P. J. Withers, S. W. Williams, M. Poad, and S. W. Wen. Residual stress engineering in friction stir welds by roller tensioning. *Science and Technology of Welding and Joining*, 14(2):185–192, 2009.

[4]   P. J. Withers. Mapping residual and internal stress in materials by neutron diffraction. *Comptes Rendus Physique*, 8(7-8):806–820, 2007.

[5]   P. J. Bouchard and P. J. Withers. The appropriateness of residual stress length scales in structural integrity. *Journal of Neutron Research*, 12(1-3):81–91, 2004.

[6]   E. C. Oliver, M. R. Daymond, and P. J. Withers. Interphase and intergranular stress generation in carbon steels. *Acta Materialia*, 52(7):1937–1951, 2004.

[7]   P. J. Withers and H.K.D.H. Bhadeshia. Residual stress: Part 1 - Measurement techniques. *Materials Science and Technology*, 17(4):355–365, 2001.

[8]   Y. F. Kudryavtsev. Residual stress. In W. N. Sharpe, editor, *Springer Handbook of Experimental Solid Mechanics*, pages 371–387. Springer, 2008.

[9]   R. W. Messler. *Joining of Advanced Materials*. Butterworth Heinemann, 1993.

[10]   S. Kou. *Welding Metallurgy*, pages 122–141. Wiley, 2003.

[11]   R. H. Leggatt. Residual stresses in welded structures. *International Journal of Pressure Vessels and Piping*, 85(3):144–151, 2008.

[12]   P. Colegrove, C. Ikeagu, A. Thistlethwaite, S. W. Williams, T. Nagy, W. Suder, A. Steuwer, and T. Pirling. Welding process impact on residual stress and distortion. *Science and Technology of Welding and Joining*, 14(8):717–725, 2009.

[13]   H.K.D.H. Bhadeshia. Residual stress: Material factors. In G. Totten, M. Howes, and T. Inoue, editors, *Handbook of Residual Stress and Deformation of Steel*, pages 3–10. ASM International, 2002.

[14]   D. G. Richards, P. B. Prangnell, S. W. Williams, and P. J. Withers. Global mechanical tensioning for the management of residual stresses in welds. *Materials Science and Engineering A*, 489(1-2):351–362, 2008.

[15]   D. Radaj. *Welding Residual Stress and Distortion: Calculation and Measurement*. DVS Verlag, 2003.

[16]   H. Lombard, D. G. Hattingh, A. Steuwer, and M. N. James. Effect of process parameters on the residual stresses in AA5083-H321 friction stir welds. *Materials Science and Engineering A*, 501(1-2):119–124, 2009.

[17]   S. Ganguly, V. Stelmukh, L. Edwards, and M. E. Fitzpatrick. Analysis of residual stress in metal-inert-gas-welded Al-2024 using neutron and synchrotron x-ray diffraction. *Materials Science and Engineering A*, 491(1-2):248–257, 2008.

[18]   L.-E. Lindgren. Finite element modeling and simulation of welding Part 1: Increased complexity. *Journal of Thermal Stresses*, 24(2):141–192, 2001.

[19]   L.-E. Lindgren. Numerical modelling of welding. *Computer Methods in Applied Mechanics and Engineering*, 195(48-49):6710–6736, 2006.

[20]   L. Zhang, P. Michaleris, and P. Marugabandhu. Evaluation of applied plastic strain methods for welding distortion prediction. *Journal of Manufacturing Science and Engineering*, 129(6):1000 − 1010, 2007.

[21]   P. Michaleris. Modelling welding residual stress and distortion: Current and future research trends. *Science and Technology of Welding and Joining*, 16(4):363–368, 2011.

[22]   J. H. Hattel. Integrated modelling in materials and process technology. *Materials Science and Technology*, 24(2):137–148, 2008.

[23]   L.-E. Lindgren. *Computational Welding Mechanics*. Woodhead Publishing, 2007.

[24]   J. A. Goldak and M. Akhlaghi. *Computational Welding Mechanics*. Springer, 2005.

[25]   K. Masubuchi. *Analysis of Welded Structures*. Pergamon Press, Oxford, 1980.

[26]   D. Radaj. *Heat Effects of Welding*. Springer-Verlag, 1992.

[27]   T. Nitschke-Pagel and H. Wohlfahrt. Residual stresses in welded joints - Sources and consequences. *Materials Science Forum*, 404-407:215–226, 2002.

[28]   K. Hellan. *Introduction to Fracture Mechanics*. McGraw-Hill, 1985.

[29]   D. M. Finch and F. M. Burdekin. Effects of welding residual stresses on significance of defects in various types of welded joint. *Engineering Fracture Mechanics*, 41(5):721–735, 1992.

[30]   K. H. Chang and C. H. Lee. Residual stresses and fracture mechanics analysis of a crack in welds of high strength steels. *Engineering Fracture Mechanics*, 74(6):980–994, 2007.

[31]   A. H. Mahmoudi, C. E. Truman, and D. J. Smith. Using local out-of-plane compression (LOPC) to study the effects of residual stress on apparent fracture toughness. *Engineering Fracture Mechanics*, 75(13):1516–1534, 2008.

[32]   M. N. James, D. J. Hughes, Z. Chen, H. Lombard, D. G. Hattingh, D. Asquith, J. R. Yates, and P. J. Webster. Residual stresses and fatigue performance. *Engineering Failure Analysis*, 14(2):384–395, 2007.

[33]   R. A. Ainsworth, J. K. Sharples, and S. D. Smith. Effects of residual stresses on fracture behaviour - experimental results and assessment methods. *Journal of Strain Analysis for Engineering Design*, 35(4):307–316, 2000.

[34]   T. L. Anderson. *Fracture Mechanics: Fundamentals and Applications*. CRC Press, 2005.

[35]   U. Zerbst, M. Heinimann, C. D. Donne, and D. Steglich. Fracture and damage mechanics modelling of thin-walled structures - An overview. *Engineering Fracture Mechanics*, 76(1):5–43, 2009.

[36]   X. B. Ren, Z. L. Zhang, and B. Nyhus. Effect of residual stresses on ductile crack growth resistance. *Engineering Fracture Mechanics*, 77(8):1325–1337, 2010.

[37]   R. C. McClung. A literature survey on the stability and significance of residual stresses during fatigue. *Fatigue and Fracture of Engineering Materials and Structures*, 30(3):173–205, 2007.

[38]   S. Wang, Y. Li, M. Yao, and R. Wang. Compressive residual stress introduced by shot peening. *Journal of Materials Processing Technology*, 73(1-3):64–73, 1998.

[39]   P. Dong. Length scale of secondary stresses in fracture and fatigue. *International Journal of Pressure Vessels and Piping*, 85(3):128–143, 2008.

[40]   D. Radaj. Review of fatigue strength assessment of non-welded and welded structures based on local parameters. *International Journal of Fatigue*, 18(3):153–170, 1996.

[41]   G. A. Webster and A. N. Ezeilo. Residual stress distributions and their influence on fatigue lifetimes. *International Journal of Fatigue*, 23(SUPPL. 1):S375–S383, 2001.

[42]   S. J. Maddox. *Fatigue Strength of Welded Structures*. Abington Publishing, Cambridge, UK, 2nd edition, 1991.

[43]   K. V. Jata, K. K. Sankaran, and J. J. Ruschau. Friction-stir welding effects on microstructure and fatigue of aluminum alloy 7050-T7451. *Metallurgical and Materials Transactions A: Physical Metallurgy and Materials Science*, 31(9):2181–2192, 2000.

[44]   N. T. Nguyen and M. A. Wahab. The effect of undercut and residual stresses on fatigue behaviour of misaligned butt joints. *Engineering Fracture Mechanics*, 55(3):453–469, 1996.

[45]   M. Farajian, T. Nitschke-Pagel, and K. Dilger. Stability and relaxation of welding residual stresses. *Materials Science Forum*, 681:55–60, 2011.

[46]   R. H. Jones. Mechanisms of stress-corrosion cracking. In R. H. Jones and R. E. Ricker, editors, *Stress-Corrosion Cracking*. ASM International, 1992.

[47]   J. A. Francis, H. K. D. H. Bhadeshia, and P. J. Withers. Welding residual stresses in ferritic power plant steels. *Materials Science and Technology*, 23(9):1009–1020, 2007.

[48]   S. Fricke, E. Keim, and J. Schmidt. Numerical weld modeling - A method for calculating weld-induced residual stresses. *Nuclear Engineering and Design*, 206(2-3):139–150, 2001.

[49]   R. M. Horn, G. M. Gordon, F. P. Ford, and R. L. Cowan. Experience and assessment of stress corrosion cracking in l-grade stainless steel BWR internals. *Nuclear Engineering and Design*, 174(3):313–325, 1997.

[50]   B. N. Leis and R. N. Parkins. Mechanics and material aspects in predicting serviceability limited by stress-corrosion cracking. *Fatigue and Fracture of Engineering Materials and Structures*, 21(5):583–601, 1998.

[51]   T. Mura. *Micromechanics of Defects in Solids*. Springer, 1987.

[52]   A. M. Korsunsky, G. M. Regino, and D. A. Nowell. Variational eigenstrain analysis of residual stresses in a welded plate. *International Journal of Solids and Structures*, 44(13):4574–4591, 2007.

[53]   P. Dong. Residual stresses and distortions in welded structures: a perspective for engineering applications. *Science and Technology of Welding and Joining*, 10:389–398(10), 2005.

[54]   T. D. Huang, P. Dong, L. DeCan, D. Harwig, and R. Kumar. Fabrication and engineering technology for lightweight ship structures, Part 1: Distortions and residual stresses in panel fabrication. *Journal of Ship Production*, 20(1):43–59, 2004.

[55]   N. A. McPherson. Correcting thin-plate distortion in shipbuilding. *Welding Journal*, 89(1):30–34, 2010.

[56]   K. J. R. Rasmussen and G. J. Hancock. Deformations and residual stresses induced in channel section columns by presetting and welding. *Journal of Constructional Steel Research*, 11(3):175–204, 1988.

[57]   K. Masubuchi. Prediction and control of residual stresses and distortion in welded structures. *Welding Research Abroad*, 43(6-7):2–16, 1996.

[58]   T. Schenk, I. M. Richardson, M. Kraska, and S. Ohnimus. Influence of clamping on distortion of welded S355 T-joints. *Science and Technology of Welding and Joining*, 14(4):369–375, 2009.

[59]   A. K. Dhingra and C. L. Murphy. Numerical simulation of welding-induced distortion in thin-walled structures. *Science and Technology of Welding and Joining*, 10(5):528–536, 2005.

[60]   T.-L. Teng, P.-H. Chang, and W.-C Tseng. Effect of welding sequences on residual stresses. *Computers and Structures*, 81(5):273–286, 2003.

[61]   D. Deng, H. Serizawa, and H. Murakawa. Theoretical prediction of welding distortion considering positioning and the gap between parts. *Transactions of the JWRI*, 30(2):89–96, 2001.

[62]   C. Conrardy and R. Dull. Control of distortion in thin ship panels. *Journal of Ship Production*, 13(2):83–92, 1997.

[63]   T. Schenk, I.M. Richardson, M. Kraska, and S. Ohnimus. A study on the influence of clamping on welding distortion. *Computational Materials Science*, 45(4):999 – 1005, 2009.

[64]   N. S. Rossini, M. Dassisti, K. Y. Benyounis, and A. G. Olabi. Methods of measuring residual stresses in components. *Materials and Design*, 35(1):572–588, 2012.

[65]   P. J. Withers, M. Turski, L. Edwards, P. J. Bouchard, and D. J. Buttle. Recent advances in residual stress measurement. *International Journal of Pressure Vessels and Piping*, 85(3):118–127, 2008.

[66]   G. S. Schajer. Hole-drilling residual stress measurements at 75: Origins, advances, opportunities. *Experimental Mechanics*, 50:245–253, 2010.

[67]   G. S. Schajer. Advances in hole-drilling residual stress measurements. *Experimental Mechanics*, 50:59–168, 2010.

[68]   M. B. Prime. Cross-sectional mapping of residual stresses by measuring the surface contour after a cut. *Journal of Engineering Materials and Technology, Transactions of the ASME*, 123(2):162–168, 2001.

[69]   G. S. Schajer. Relaxation methods for measuring residual stresses: Techniques and opportunities. *Experimental Mechanics*, 50:1117–1127, 2010.

[70]   J. Gauthier, T. W. Krause, and D. L. Atherton. Measurement of residual stress in steel using the magnetic Barkhausen noise technique. *NDT and E International*, 31(1):23–31, 1998.

[71]   A. D. Krawitz. Neutron strain measurement. *Materials Science and Technology*, 27(3):589–603, 2011.

[72]   W. Reimers, M. Broda, G. Brusch, D. Dantz, K. D. Liss, A. Pyzalla, T. Schmackers, and T. Tschentscher. Evaluation of residual stresses in the bulk of materials by high energy synchrotron diffraction. *Journal of Nondestructive Evaluation*, 17(3):129–140, 1998.

[73]   J. D. Almer and R. A. Winholtz. X-ray stress analysis. In W. N. Sharpe, editor, *Springer Handbook of Experimental Solid Mechanics*, pages 801–820. Springer, 2008.

[74]   Z. Feng. *Processes and Mechanisms of Welding Residual Stress and Distortion*. Woodhead Publishing, 2005.

[75]   S. W. Williams and A. Steuwer. Residual stresses in friction stir welding. In D. Lohwasser and Z. Chen, editors, *Friction Stir Welding: from Basics to Applications.* Woodhead Publishing, 2010.

[76]   J. Altenkirch. *Stress Engineering of Friction Stir Welding: Measurement and Control of Welding Residual Stresses*. PhD thesis, School of Materials, University of Manchester, 2009.

[77]   V. I. Pavlovsky and K. Masubuchi. Research in the U.S.S.R. on residual stresses and distortion in welded structures. Bulletin 388, Welding Research Council, 1994.

[78]   A. Joseph, P. Palanichamy, S. K. Rai, T. Jayakumar, and B. Raj. Non-destructive measurement of residual stresses in carbon steel weld joints. *Science and Technology of Welding and Joining*, 3(6):267–271, 1998.

[79]   J.-I. Jang, D. Son, Y.-H Lee, Y. Choi, and D. Kwon. Assessing welding residual stress in A335 P12 steel welds before and after stress-relaxation annealing through instrumented indentation technique. *Scripta Materialia*, 48(6):743–748, 2003.

[80]   J. R. Cho, B. Y. Lee, Y. H. Moon, and C. J. Van Tyne. Investigation of residual stress and post weld heat treatment of multi-pass welds by finite element method and experiments. *Journal of Materials Processing Technology*, 155-156(1-3):1690–1695, 2004.

[81]   J. X. Zhang, Y. Xue, and S. L. Gong. Residual welding stresses in laser beam and tungsten inert gas weldments of titanium alloy. *Science and Technology of Welding and Joining*, 10(6):643–646, 2005.

[82]   A.M. Paradowska, J.W.H. Price, B. Kerezsi, P. Dayawansa, and X.-L. Zhao. Stress relieving and its effect on life of welded tubular joints. *Engineering Failure Analysis*, 17(1):320 – 327, 2010.

[83]   D. N. Croft. *Heat Treatment of Welded Steel Structures*. Abington Publishing, 1996.

[84]   W. Bleck. *Material Science of Steel, Textbook for RWTH Students*. Verlag Mainz, 2007.

[85]   I. Hrivnák. A review of the metallurgy of heat treatment of welded joints. *International Journal of Pressure Vessels and Piping*, 20(3):223 – 237, 1985.

[86]   P. Sedek, J. Brozda, L. Wang, and P. J. Withers. Residual stress relief in MAG welded joints of dissimilar steels. *International Journal of Pressure Vessels and Piping*, 80(10):705–713, 2003.

[87]   A. Dhooge and A. Vinckier. Reheat cracking - A review of recent studies. *International Journal of Pressure Vessels and Piping*, 27(4):239–269, 1987.

[88]   D. Gery, H. Long, and P. Maropoulos. Effects of welding speed, energy input and heat source distribution on temperature variations in butt joint welding. *Journal of Materials Processing Technology*, 167(2-3):393–401, 2005.

[89]   N. Yurioka and H. Suzuki. Hydrogen assisted cracking in C-Mn and low alloy steel weldments. *International Materials Reviews*, 35(33):217–249, 1990.

[90]   Y. C. Lin and K. H. Lee. Effect of preheating on the residual stress in type 304 stainless steel weldment. *Journal of Materials Processing Technology*, 63(1-3):797–801, 1997.

[91]   C. S. Montross, T. Wei, L. Ye, G. Clark, and Y.-W. Mai. Laser shock processing and its effects on microstructure and properties of metal alloys: A review. *International Journal of Fatigue*, 24:1021–1036, 2002.

[92]   X. Cheng, J. W. Fisher, H. J. Prask, T. Gnäupel-Herold, B. T. Yen, and S. Roy. Residual stress modification by post-weld treatment and its beneficial effect on fatigue strength of welded structures. *International Journal of Fatigue*, 25(9-11):1259–1269, 2003.

[93]   Y. Ochi, K. Masaki, T. Matsumura, and T. Sekino. Effect of shot-peening treatment on high cycle fatigue property of ductile cast iron. *International Journal of Fatigue*, 23(5):441–448, 2001.

[94]   L. Bertini, V. Fontanari, and G. Straffelini. Influence of post weld treatments on the fatigue behaviour of Al-alloy welded joints. *International Journal of Fatigue*, 20(10):749–755, 1998.

[95]   E. R. de los Rios, A. Walley, M. T. Milan, and G. Hammersley. Fatigue crack initiation and propagation on shot-peened surfaces in A316 stainless steel. *International Journal of Fatigue*, 17(7):493–499, 1995.

[96]   K. J. Kirkhope, R. Bell, L. Caron, R. I. Basu, and K.-T. Ma. Weld detail fatigue life improvement techniques. Part 1: Review. *Marine Structures*, 12(6):447–474, 1999.

[97]   Th. Nitschke-Pagel and K. Dilger. Residual stresses and near-surface material condition of welded high strength steels after different mechanical post-weld treatments. In *20th International Offshore and Polar Engineering Conference, ISOPE-2010*, pages 269–274, 2010.

[98]   R. T. McGoldrick and H. E. Saunders. Experiments in stress relieving castings and welded structures by vibration. *Journal of the American Society of Naval Engineers*, 55(4):589–609, 1943.

[99]   G. Gnirss. Vibration and vibratory stress relief: Historical development, theory and practical application. *Welding in the World*, 26(11-12):284–291, 1988.

[100]   C. M. Sonsino, F. Müller, J. De Back, and A. M. Gresnigt. Influence of stress relieving by vibration on the fatigue behaviour of welded joints in comparison to post-weld heat treatment. *Fatigue and Fracture of Engineering Materials and Structures*, 19(6):703–708, 1996.

[101]   C. A. Walker, A. J. Waddell, and D. J. Johnston. Vibratory stress relief - An investigation of the underlying processes. *Proceedings of the Institution of Mechanical Engineers, Part E: Journal of Process Mechanical Engineering*, 209(E1):51–58, 1995.

[102]   C. Walker. A theoretical review of the operation of vibratory stress relief with particular reference to the stabilization of large-scale fabrications. *Proceedings of the Institution of Mechanical Engineers, Part L: Journal of Materials: Design and Applications*, 225(3):195–204, 2011.

[103]   R. Dawson and D.G. D. G. Moffat. Vibratory stress relief: A fundamental study of its effectiveness. *Journal of Engineering Materials and Technology, Transactions of the ASME*, 102(1):169–176, 1980.

[104]   S. Kwofie. Plasticity model for simulation, description and evaluation of vibratory stress relief. *Materials Science and Engineering: A*, 516(1-2):154–161, 2009.

[105]   Y. P. Yang. Understanding of vibration stress relief with computation modeling. *Journal of Materials Engineering and Performance*, 18(7):856–862, 2009.

[106]   D. Q. Cole. Development of techniques for controlling warpage and residual stresses in welded structures. Technical Report CR-61235, NASA, 1968.

[107]   Y. P. Yang, P. Dong, J. Zhang, and X. Tian. Hot-cracking mitigation technique for welding high-strength aluminum alloy. *Welding Journal*, 79(1), 2000.

[108]   J. Li, Q. Guan, Y. W. Shi, and D. L. Guo. Stress and distortion mitigation technique for welding titanium alloy thin sheet. *Science and Technology of Welding and Joining*, 9(5):451–458, 2004.

[109]   F. A. Soul and Y.-H. Zhang. Numerical study on stress induced cambering distortion and its mitigation in welded titanium alloy sheet. *Science and Technology of Welding and Joining*, 11(6):688–693, 2006.

[110]   E. M. van der Aa, M. J. M. Hermans, and I. M. Richardson. Conceptual model for stress and strain development during welding with trailing heat sink. *Science and Technology of Welding and Joining*, 11(4):488–495, 2006.

[111]   D. G. Richards, P. B. Prangnell, P. J. Withers, S. W. Williams, T. Nagy, and S. Morgan. Efficacy of active cooling for controlling residual stresses in friction stir welds. *Science and Technology of Welding and Joining*, 15(2):156–165, 2010.

[112]   Q. Guan, D. L. Guo, C. Q. Li, and R. H. Leggatt. Low stress non-distortion (LSND) welding - a new technique for thin materials. *Welding in the World*, 33(4):160–167, 1994.

[113]   R. Saraswat. Low stress no distortion (LSND) modelling of aluminium alloy welds. Technical Report 902/2008, TWI, Abington, UK, 2008.

[114]   F. Soul, M. Ateeg, S. Beshay, and M. Senfier. Residual stress correlation in two different mitigation techniques using FEA. *Advanced Materials Research*, 83-86:1254–1261, 2010.

[115]   P. Staron, M. Kocak, and S. W. Williams. Residual stresses in friction stir welded Al sheets. *Applied Physics A: Materials Science and Processing*, 74(SUPPL.II):S1161–S1162, 2002.

[116]   N. Bagshaw. Low stress no distortion (LSND) welding in 304 stainless steel: improved numerical simulation and experimental validation. Technical Report 813/2004, TWI, Abington, UK, 2004.

[117]   E. M. van der Aa. *Local Cooling During Welding: Prediction and Control of Residual Stresses and Distortion*. PhD thesis, Delft University of Technology, 2007.

[118]   J. Li. Localized thermal tensioning technique to prevent buckling distortion. *Welding in the World*, 49(11-12):4–14, 2005.

[119]   N. Bagshaw, E. Olden, and D. Bertaso. Numerical simulation and experimental validation of low stress no distortion (LSND) welding in 304 stainless steel. Technical Report 780/2003, TWI, Abington, UK, 2003.

[120]   D. Richards. *Control of Residual Stresses in Welding Al Aerospace Alloys by Mechanical/ Thermal Tensioning*. PhD thesis, University of Manchester, 2009.

[121]   R. V. Preston, H. R. Shercliff, P. J. Withers, and S. D. Smith. Finite element modelling of tungsten inert gas welding of aluminium alloy 2024. *Science and Technology of Welding and Joining*, 8(1):10–18, 2003.

[122]   M. V. Deo and P. Michaleris. Elimination of bowing distortion in welded stiffeners. *Journal of Ship Production*, 19(2):76–83, 2003.

[123]   Y. C. Lin and C. P. Chou. A new technique for reducing the residual stress induced by welding in type 304 stainless steel. *Journal of Materials Processing Technology*, 48(1-4):693–698, 1995.

[124]   P. Michaleris and X. Sun. Finite element analysis of thermal tensioning techniques mitigating weld buckling distortion. *Welding Journal*, 76(12):451s–457s, 1997.

[125]   P. Michaleris, J. Dantzig, and D. Tortorelli. Minimization of welding residual stress and distortion in large structures. *Welding Journal*, 78(11):361s–366s, 1999.

[126]   T. W. Greene and A. A. Holzbaur. Controlled low-temperature stress relieving. *Welding Journal*, 25(11):171s–185s, 1946.

[127]   M. V. Deo and P. Michaleris. Mitigation of welding induced buckling distortion using transient thermal tensioning. *Science and Technology of Welding and Joining*, 8(1):49–54, 2003.

[128]   J. U. Park, S. C. Park, and C. H. Lee. Control of longitudinal bending distortion of built-up beams by high-frequency induction heating. *Welding Journal*, 88(2):29s–34s, 2009.

[129]   M. V. Deo, P. Michaleris, and J. Sun. Prediction of buckling distortion of welded structures. *Science and Technology of Welding and Joining*, 8(1):55–61, 2003.

[130]   S. A. Kurkin and G. Tsyao. The relief of welding residual stresses in titanium alloy sheet structures. *Welding Production*, 10:1–5, 1962.

[131]   V. A. Vinokurov. *Welding Stresses and Distortion: Determination and Elimination*. Wetherby, 1977.

[132]   S. W. Wen, P. Colegrove, S. W. Williams, S. A. Morgan, A. Wescott, and M. Poad. Rolling to control residual stress and distortion in friction stir welds. *Science and Technology of Welding and Joining*, 15(6):440–447, 2010.

[133]   Y. P. Yang, P. Dong, X. Tian, and Z. Zhang. Prevention of hot cracking of high strength aluminum alloy by mechanical rolling. In *Proceedings of the 5th International Conference on Trends in Welding Research*, pages 700–705, 1998.

[134]   Q. Guan. A survey of development in welding stress and distortion controlling in aerospace manufacturing engineering in China. *Welding in the World*, 43(1):64–74, 1999.

[135]   Y. Sun, Y. Zang, and Y.-Q. Shi. High precision modeling of welding and post welding cold rolling continuous process in numerical simulation. In *Proceedings of the 2nd International Conference on Modelling and Simulation, ICMS2009*, volume 7, pages 312–318, 2009.

[136]   Y. P. Yang and P. Dong. Buckling distortions and mitigation techniques for thin-section structures. *Journal of Materials Engineering and Performance*, 21(2):153–160, 2011.

[137]   Y.-J. Sun, Y. Zang, and Q.-Y. Shi. Numerical simulations of friction stir welding process and subsequent post weld cold rolling process. *Key Engineering Materials*, 419-420:433–436, 2010.

[138]   S. A. Kurkin, V. I. Anufriev, and E. S. Milekhin. Improving the mechanical properties of welded joints in the AMg6 alloy by plastic deformation during arc welding. *Welding Production*, 27(3):20–24, 1980.

[139]   S. A. Kurkin and V. I. Anufriev. Preventing distortion of welded thin-walled members of AMg6 and 1201 aluminum alloys by rolling the weld with a roller behind the welding arc. *Welding Production*, 31(10):52–55, 1984.

[140]   G. F. Kondakov and A. N. Martynov. Effect of methods of local deformation on residual stresses and properties of welded joints. *Welding Production*, 30(5):28–30, 1986.

[141]   G. F. Kondakov. High temperature rolling in welding butt joints. *Welding International*, 2(2):172–175, 1988.

[142]   J. W. Anderson and R. E. Holt. Prestressing for warpage control of welded steel sheet. *Welding Journal*, 53(7):430–437, 1974.

[143]   A. P. Chakravarti, L. M. Malik, and J. A. Goldak. Distortion control in simulated one-pass panel bead welds. *Marine Structures*, 3(1):3–24, 1990.

[144]   P. Staron, M. Koçak, S. W. Williams, and A. Wescott. Residual stress in friction stir-welded Al sheets. *Physica B: Condensed Matter*, 350(1-3 SUPPL. 1):e491–e493, 2004.

[145]   D. A. Price, S. W. Williams, A. Wescott, C. J. C. Harrison, A. Rezai, A. Steuwer, M. Peel, P. Staron, and M. Kocak. Distortion control in welding by mechanical tensioning. *Science and Technology of Welding and Joining*, 12(7):620–633, 2007.

[146]   J. Altenkirch, A. Steuwer, M. J. Peel, D. G. Richards, and P. J. Withers. The effect of tensioning and sectioning on residual stresses in aluminium AA7749 friction stir welds. *Materials Science and Engineering A*, 488(1-2):16–24, 2007.

[147]   J. Altenkirch, A. Steuwer, M. Peel, P. J. Withers, S. W. Williams, and M. Poad. Mechanical tensioning of high-strength aluminum alloy friction stir welds. *Metallurgical and Materials Transactions: A Physical Metallurgy and Materials Science*, 39(13):3246–3259, 2008.

[148]   B. Taljat, B. Radhakrishnan, and T. Zacharia. Numerical analysis of GTA welding process with emphasis on post-solidification phase transformation effects on residual stresses. *Materials Science and Engineering A*, 246(1-2):45–54, 1998.

[149]   S.-H. Cho and J.-W. Kim. Analysis of residual stress in carbon steel weldment incorporating phase transformations. *Science and Technology of Welding and Joining*, 7(4):212–216, 2002.

[150]   H. K. D. H. Bhadeshia. Possible effects of stress on steel weld microstructures. In H. Cerjak and H. K. D. H. Bhadeshia, editors, *Mathematical Modelling of Weld Phenomena*, pages 71–118, 1995.

[151]   K. Satoh. Transient thermal stresses of weld heat-affected zone by both-ends-fixed bar analogy. *Kovove Materialy*, 8(6):569–587, 1970.

[152]   W. K. C. Jones and P. J. Alberry. A model for stress accumulation in steels during welding. In R. W. Nichols, editor, *Residual Stresses in Welded Construction and Their Effects*, pages 15–26, Abington, UK, 1977. The Welding Institute.

[153]   A. A. Shirzadi, H. K. D. H. Bhadeshia, L. Karlsson, and P. J. Withers. Stainless steel weld metal designed to mitigate residual stresses. *Science and Technology of Welding and Joining*, 14(6):559–565, 2009.

[154]   R. J. Moat, H. J. Stone, A. A. Shirzadi, J. A. Francis, S. Kundu, A. F. Mark, H. K. D. H. Bhadeshia, L. Karlsson, and P. J. Withers. Design of weld fillers for mitigation of residual stresses in ferritic and austenitic steel welds. *Science and Technology of Welding and Joining*, 16(3):279–284, 2011.

[155]   W. Wang, L. Huo, Y. Zhang, D. Wang, and H. Jing. New developed welding electrode for improving the fatigue strength of welded joints. *Journal of Materials Science and Technology*, 18(6):527–531, 2002.

[156]   H. Dai, J. A. Francis, H. J. Stone, H. K. D. H. Bhadeshia, and P. J. Withers. Characterizing phase transformations and their effects on ferritic weld residual

stresses with x-rays and neutrons. *Metallurgical and Materials Transactions A: Physical Metallurgy and Materials Science*, 39(13):3070–3078, 2008.

[157]   J. Altenkirch, J. Gibmeier, A. Kromm, Th. Kannengiesser, Th. Nitschke-Pagel, and M. Hofmann. In situ study of structural integrity of low transformation temperature (LTT) welds. *Materials Science and Engineering A*, 528(16-17):5566–5575, 2011.

[158]   A. M. Korsunsky. Eigenstrain analysis of residual strains and stresses. *Journal of Strain Analysis for Engineering Design*, 44(1):29–43, 2009.

[159]   J. Ding, P. Colegrove, J. Mehnen, S. Ganguly, P.M. Sequeira Almeida, F. Wang, and S. W. Williams. Thermo-mechanical analysis of wire and arc additive layer manufacturing process on large multi-layer parts. *Computational Materials Science*, 50(12):3315–3322, 2011.

[160]   J. W. Elmer and T. A. Palmer. In-situ phase mapping and direct observations of phase tranformations during arc welding of 1045 steel. *Metallurgical and Materials Transactions A: Physical Metallurgy and Materials Science*, 37(7):2171–2182, 2006.

[161]   J. Altenkirch, J. Gibmeier, V. Kostov, A. Kromm, Th. Kannengiesser, S. Doyle, and A. Wanner. Time-and temperature-resolved synchrotron x-ray diffraction: Observation of phase transformation and strain evolution in novel low temperature transformation weld filler materials. *Journal of Strain Analysis for Engineering Design*, 46(7):563–579, 2011.

[162]   Y. Ueda and T. Yamakawa. Analysis of thermal elastic-plastic stress and strain during welding by finite element method. *Transactions for the Japan Welding Society*, 2(2):90–100, 1971.

[163]   T. Muraki, J. J. Bryan, and K. Masubuchi. Analysis of thermal stresses and metal movement during welding - 1. Analytical study. *Journal of Engineering Materials and Technology, Transactions of the ASME*, 97 Ser H(1):81–84, 1975.

[164]   F. M. Pattee. Buckling distortion of thin aluminium plates during welding. Master's thesis, Massachusetts Institute of Technology, 1975.

[165]   V. J. Papazoglou and K. Masubuchi. Analysis and control of distortion in welded aluminum structures. *Welding Journal*, 57(9):251s–262s, 1978.

[166]   M. Jonsson and B. L. Josefson. Experimentally determined transient and residual stresses in a butt-welded pipe. *The Journal of Strain Analysis for Engineering Design*, 23(1):25–31, 1988.

[167]   P. Tekriwal and J. Mazumder. Transient and residual thermal strain-stress analysis of GMAW. *Journal of Engineering Materials and Technology, Transactions of the ASME*, 113(3):336–343, 1991.

[168]   S. E. Chidiac and F. A. Mirza. Thermal stress analysis due to welding processes by the finite element method. *Computers and Structures*, 46(3):407–412, 1993.

[169]   J. C. Suárez, B. Remartinez, J. M. Menéndez, A. Güemes, and F. Molleda. Optical fibre sensors for monitoring of welding residual stresses. *Journal of Materials Processing Technology*, 143-144(1):316–320, 2003.

[170]   V. Richter-Trummer, S. O. Silva, D. F. C. Peixoto, O. Frazao, P. M. G. P. Moreira, J. L. Santos, and P. M. S. T. De Castro. Fibre Bragg grating sensors for monitoring the metal inert gas and friction stir welding processes. *Measurement Science and Technology*, 21(8), 2010.

[171]   M. De Strycker, P. Lava, W. van Paepegem, L. Schueremans, and D. Debruyne. Measuring welding deformations with the digital image correlation technique. *Welding Journal*, 90:107s–112s, 2011.

[172]   W. Woo, Z. Feng, X.-L. Wang, K. An, C. R. Hubbard, S. A. David, and H. Choo. In situ neutron diffraction measurement of transient temperature and stress fields in a thin plate. *Applied Physics Letters*, 88(26), 2006.

[173]   M. A. Gharghouri, M. J. Watson, D. Dye, and R. B. Rogge. In-situ neutron diffraction study of gas tungsten arc welding of a 1018 plain carbon steel. *Materials Research Society Symposium Proceedings*, 1027:58–62, 2008.

[174]   M. S. Davoud. Temperature and strain history measurement during an arc welding process. In *2005 ASME International Mechanical Engineering Congress and Exposition*, pages 435–443, 2005.

[175]   Strain gage thermal output and gage factor variation with temperature. Technical Report TN-504-1, Vishay Precision Group, 2010.

[176]   R. C. Juvinall and K. M. Marshek. *Fundamentals of Machine Component Design*. John Wiley & Sons, 2nd edition, 1991.

[177]   Z. Zhou, Y. Lam, P. F. Thomson, and D. D. W. Yuen. Numerical analysis of the flatness of thin, rolled steel strip on the runout table. *Proceedings of the Institution of Mechanical Engineers, Part B: Journal of Engineering Manufacture*, 221(2):241–254, 2007.

[178]   J. Outinen and P. Mäkeläinen. Mechanical properties of structural steel at elevated temperatures and after cooling down. *Fire and Materials*, 28:237 – 251, 2004.

[179]   J. Y. Shanghvi and P. Michaleris. Thermo-elasto-plastic finite element analysis of quasi-state processes in Eulerian reference frames. *International Journal for Numerical Methods in Engineering*, 53(7):1533–1556, 2002.

[180]   N. S. Al-Huniti, M. A. Al-Nimr, and M. A. Da'as. Transient variations of thermal stresses and the resulting residual stresses within a thin plate during welding processes. *Journal of Thermal Stresses*, 27(8):671–689, 2004.

[181]   P. Michaleris and A. DeBiccari. Prediction of welding distortion. *Welding Journal*, 76(12):172–s, 1997.

[182]   Y. Ueda, K. Fukuda, K. Nakacho, and S. Endo. A new measuring method of residual stresses with the aid of finite element method and reliability of estimated values. *Transactions of the JWRI*, 4(2):123–131, 1975.

[183]   S. W. Wen, S. W. Williams, S. A. Morgan, A. Wescott, M. Poad, and G. Moore. Rolling of friction stir welds for residual stress and distortion control. In H. Cerjak and N. Enzinger, editors, *proc. 9th International Seminar on Numerical Analysis of Weldability*, pages 579–610, 2009.

[184]   L. D. Cozzolino, H. E. Coules, P. Colegrove, and S. W. Wen. Modelling distortion reduction on pre- and post-weld rolled gas metal arc welded plates. In F. Vollertsen, editor, *Proceedings of the IWOTE'11*, pages 169–179, Bremen, Germany, 2011.

[185]   N. Tebedge, G. Alpsten, and L. Tall. Residual stress measurement by the sectioning method. *Experimental Mechanics*, 13:88–96, 1973.

[186]   D. A. Hills. The connection between the elastic and plastic components of residual strain and residual stress. *Journal of Strain Analysis for Engineering Design*, 37(4):371–372, 2002.

[187]   D. T. Sandwell. Biharmonic spline interpolation of GEOS-3 and SEASAT altimeter data. *Geophysical Research Letters*, 14(2):139–142, 1987.

[188]   S. Timoshenko and S. Woinowsky-Krieger. *Theory of Plates and Shells*. McGraw-Hill, 2nd edition, 1959.

[189]   T. Pirling, G. Bruno, and P. J. Withers. SALSA - A new instrument for strain imaging in engineering materials and components. *Materials Science and Engineering: A*, 437(1):139 – 144, 2006.

[190]   M. E. Fitzpatrick and A. Lodini. *Analysis of residual stress by diffraction using neutron and synchrotron radiation*. Taylor and Francis, 2003.

[191]   G. Albertini, G. Bruno, B. D. Dunn, F. Fiori, W. Reimers, and J. S. Wright. Comparative neutron and X-ray residual stress measurements on Al-2219 welded plate. *Materials Science and Engineering A*, 224(1-2):157–165, 1997.

[192]   J. Altenkirch, M. J. Peel, A. Steuwer, and P. J. Withers. Comparison of methods to determine variations in unstrained unit cell parameter across welds. *Journal of Strain Analysis for Engineering Design*, 46(7):651–662, 2011.

[193]   ISO. 21432:2005 - Non-destructive testing: Standard test method for determining residual stresses by neutron diffraction, 2005.

[194]   J. Wang and C. D. Mote. Analysis of roller-induced residual stresses in bandsaw plates. *Journal of Sound and Vibration*, 175(5):647–659, 1994.

[195]   H. E. Coules, P. Colegrove, L. D. Cozzolino, and S. W. Wen. Experimental measurement of biaxial thermal stress fields caused by arc welding. *Journal of Materials Processing Technology*, 212(4):962–968, 2012.

[196]   M. T. Hutchings, P. J. Withers, T. M. Holden, and T. Lorentzen. *Introduction to the characterization of residual stress by neutron diffraction*. Taylor and Francis, 2005.

[197]   J. W. L. Pang, T. M. Holden, and T. E. Mason. The development of intergranular strains in a high-strength steel. *Journal of Strain Analysis for Engineering Design*, 33(5):373–383, 1998.

[198]   P. J. Withers, M. Preuss, A. Steuwer, and J. W. L. Pang. Methods for obtaining the strain-free lattice parameter when using diffraction to determine residual stress. *Journal of Applied Crystallography*, 40(5):891–904, 2007.

[199]   W. C. Young and R. G. Budynas. *Roark's formulas for stress and strain*. McGraw-Hill, 7th edition, 2002.

[200]   R. C. Wimpory, C. Ohms, M. Hofmann, R. Schneider, and A. G. Youtsos. Statistical analysis of residual stress determinations using neutron diffraction. *International Journal of Pressure Vessels and Piping*, 86(1):48–62, 2009.

[201]   R. C. Wimpory, C. Ohms, M. Hofmann, R. Schneider, and A. G. Youtsos. Corrigendum to "Statistical analysis of residual stress determinations using neutron diffraction". *International Journal of Pressure Vessels and Piping*, 86(10):721, 2009.

[202]   H. E. Coules, P. Colegrove, L. D. Cozzolino, S. W. Wen, S. Ganguly, and T. Pirling. Effect of high pressure rolling on weld-induced residual stresses. *Science and Technology of Welding and Joining*, 17(5):394–401, 2012.

[203]   R. G. Budynas. *Advanced strength and applied stress analysis*. McGraw-Hill, 1977.

[204]   S. P. Timoshenko and J. N. Goodier. *Theory of elasticity*. McGraw-Hill, 1970.

[205]   T. Lorentzen and J. Christoffersen. Limitations on the strain tensor determination by neutron diffraction using a position-sensitive detector. *NDT International*, 23(2):107–109, 1990.

[206]   H. G. Priesmeyer and J. Schroder. Strain tensor determination using neutron diffraction. In J. S. Eckersey and J. Champaigne, editors, *Shot peening - Theory and application*, pages 95–100. IITT-International, 1991.

[207]   T. Lorentzen and T. Leffers. Strain tensor measurements by neutron diffraction. In M. T. Hutchings and A. D. Krawitz, editors, *Measurement of residual and applied stress using neutron diffraction*, volume 216 of *NATO ANSI Series E*, page 253, 1992.

[208]   R. A. Winholtz and A. D. Krawitz. The relaxation of residual stresses with postweld heat treatment in a high-performance weld measured with neutron diffraction. *Metallurgical and Materials Transactions A*, 26(5):1287–1295, 1995.

[209]   J. S. Robinson, D. J. Hughes, and C. E. Truman. Confirmation of principal residual stress directions in rectilinear components by neutron diffraction. *Strain*, 47(Suppl. 2):36–42, 2011.

[210]   S. L. Campbell and C. D. Meyer. *Generalized inverses of linear transformations*. Society for Industrial and Applied Mathematics, 2009.

[211]   D.A. Witte, R.A. Winholtz, and S.P. Neal. Counting statistical errors in principal stresses and directions determined by diffraction. *Advances in X-ray Analysis*, 37:265–278, 1994.

[212]   R. S. Figliola and D. E. Beasley. *Theory and design for mechanical measurements*. Wiley, 2011.

[213]   M. Farajian, R. C. Wimpory, and T. Nitschke-Pagel. Relaxation and stability of welding residual stresses in high strength steel under mechanical loading. *Steel Research International*, 81(12):1137–1143, 2010.

[214]   T. M. Holden. A Canadian perspective on engineering strain measurements by neutron diffraction. *Canadian Journal of Physics*, 88(10):799–808, 2010.

[215]   S. Spooner. Neutron residual stress measurement in welds. In M. E. Fitzpatrick and A. Lodini, editors, *Analysis of residual stress by diffraction using neutron and synchrotron radiation*, pages 296–318. Taylor and Francis, 2003.

[216]   D. Balzar, N. C. Popa, and S. Vogel. Strain and stress tensors of rolled uranium plate by Rietveld refinement of TOF neutron-diffraction data. *Materials Science and Engineering: A*, 528(1):122–126, 2010.

[217]   R. A. Winholtz and A. D. Krawitz. The effect of assuming the principal directions in neutron diffraction measurement of stress tensors. *Materials Science and Engineering: A*, 205(1-2):257–258, 1996.

[218]   P. J. Withers and P. J. Webster. Neutron and synchrotron X-ray strain scanning. *Strain*, 37(1):19–33, 2001.

[219]   J. R. Santisteban, L. Edwards, M. E. Fizpatrick, A. Steuwer, and P. J. Withers. Engineering applications of Bragg-edge neutron transmission. *Applied Physics A: Materials Science and Processing*, 74(SUPPL.II):S1433–S1436, 2002.

[220]   L. D. Cozzolino. PhD thesis, Cranfield University. In preparation.

[221]   ISO. 6892-1:2009 Metallic materials - Tensile testing - Part 1: Method of test at ambient temperature, 2009.

[222]   A. P. Reynolds and F. Duvall. Digital image correlation for determination of weld and base metal constitutive behavior. *Welding Journal (Miami, Fla)*, 78(10):355–s, 1999.

[223]   B. Pan, K. Qian, H. Xie, and A. Asundi. Two-dimensional digital image correlation for in-plane displacement and strain measurement: A review. *Measurement Science and Technology*, 20(6), 2009.

[224]   B. Pan. Recent progress in digital image correlation. *Experimental Mechanics*, 51(7):1223–1235, 2011.

[225]   M. J. Peel, A. Steuwer, M. Preuss, and P. J. Withers. Microstructure, mechanical properties and residual stresses as a function of welding speed in aluminium AA5083 friction stir welds. *Acta Materialia*, 51(16):4791–4801, 2003.

[226]   M. Turski, M. C. Smith, P. J. Bouchard, L. Edwards, and P. J. Withers. Spatially resolved materials property data from a uniaxial cross-weld tensile test. *Journal of*

Pressure Vessel Technology, Transactions of the ASME, 131(6):0614061–0614067, 2009.

[227] ISO. Metallic materials - Charpy pendulum impact test - Part : Test method, 2010.

[228] E. J. Pavlina and C. J. Van Tyne. Correlation of yield strength and tensile strength with hardness for steels. *Journal of Materials Engineering and Performance*, 17(6):888–893, 2008.

[229] S. J. Jones and H. K. D. H. Bhadeshia. Competitive formation of inter- and intragranularly nucleated ferrite. *Metallurgical and Materials Transactions A: Physical Metallurgy and Materials Science*, 28(10):2005–2013, 1997.

[230] H. K. D. H. Bhadeshia. *Bainite in Steels*. IOM Communications Ltd., 2nd edition, 2001.

[231] C. H. Lee, H. K. D. H. Bhadeshia, and H.-C. Lee. Effect of plastic deformation on the formation of acicular ferrite. *Materials Science and Engineering A*, 360(1-2):249–257, 2003.

[232] S. S. Babu. The mechanism of acicular ferrite in weld deposits. *Current Opinion in Solid State and Materials Science*, 8(3-4):267–278, 2004.

[233] P. H. Shipway and H. K. D. H. Bhadeshia. The effect of small stresses on the kinetics of the bainite transformation. *Materials Science and Engineering A*, 201(1-2):143–149, 1995.

[234] P. Seyffarth, B. Meyer, and A. Scharff. *Großer Atlas Schweiß-ZTU-Schaubilder*. DVS Verlag, 1992.

[235] J.-H. Shim, J.-S. Byun, Y. W. Cho, Y.-J. Oh, J.-D. Shim, and D. N. Lee. Hot deformation and acicular ferrite microstructure in C-Mn steel containing Ti_2O_3 inclusions. *ISIJ International*, 40(8):819–823, 2000.

[236] M. R. Barnett and J. J. Jonas. Distinctive aspects of the physical metallurgy of warm rolling. *ISIJ International*, 39(9):856–873, 1999.

[237] N. T. Nguyen and M. A. Wahab. The effect of undercut, misalignment and residual stresses on the fatigue behaviour of butt welded joints. *Fatigue & Fracture of Engineering Materials & Structures*, 19(6):769 – 778, 1996.

[238] J. R. Santisteban, M. R. Daymond, J. A. James, and L. Edwards. ENGIN-X: A third-generation neutron strain scanner. *Journal of Applied Crystallography*, 39(6):812–825, 2006.

[239] G. S. Pawley. Unit-cell refinement from powder diffraction scans. *Journal of Applied Crystallography*, 14(6):357–361, 1981.

[240] F. I. Baratta and W. T. Matthews. Errors associated with flexure testing of brittle materials. Technical Report MTL TR 87-35, U. S. Army Materials Technology Laboratory, 1987.

[241] M. Law, O. Kirstein, and V. Luzin. An assessment of the effect of cutting welded samples on residual stress measurements by chill modelling. *Journal of Strain Analysis for Engineering Design*, 45(8):567–573, 2010.

[242] J. Altenkirch, A. Steuwer, M. J. Peel, and P. J. Withers. The extent of relaxation of weld residual stresses on cutting out cross-weld test-pieces. *Powder Diffraction*, 24(SUPPL. 1):S31–S36, 2009.

[243] A. Wescott. Residual stress and distortion control of weldments by applying local mechanical tensioning methods. Master's thesis, Cranfield University, 2009.

[244] W. Liu, X. Tian, and X. Zhang. Preventing weld hot cracking by synchronous rolling during welding. *Welding Journal*, 75(9):297–s, 1996.

[245] G. A. Webster and A. N. Ezeilo. Neutron scattering in engineering applications. *Physica B: Condensed Matter*, 234-236:949–955, 1997.

[246] L. Costa and R. Vilar. Laser powder deposition. *Rapid Prototyping Journal*, 15(4):264–279, 2009.

[247] B. Baufeld, O. V. D. Biest, and R. Gault. Additive manufacturing of Ti-6Al-4V components by shaped metal deposition: Microstructure and mechanical properties. *Materials and Design*, 31(SUPPL. 1):S106–S111, 2010.

[248] M. F. Zaeh and G. Branner. Investigations on residual stresses and deformations in selective laser melting. *Production Engineering*, 4(1):35–45, 2010.

[249] P. Mercelis and J.-P. Kruth. Residual stresses in selective laser sintering and selective laser melting. *Rapid Prototyping Journal*, 12(5):254–265, 2006.

[250] R. K. Chin, K. L. Beuth, and C. H. Amon. Successive deposition of metals in solid freeform fabrication processes, part 2: Thermomechanical models of adjacent

droplets. *Journal of Manufacturing Science and Engineering, Transactions of the ASME*, 123(4):632–638, 2001.

[251]   S. P. Timoshenko and J. M. Gere. *Theory of Elastic Stability*. McGraw-Hill, 1961.

[252]   R. Szilard. *Theories and applications of plate analysis*. Wiley, 2004.

[253]   Y. J. Chao. Measuring welding-induced distortion. In Z. Zeng, editor, *Processes and mechanisms of welding residual stress and distortion*, chapter 6, pages 209–224. Woodhead Publishing in Materials, 1st edition, 2005.

[254]   ISO. BS EN 10025-1:2004 - Hot rolled products of structural steels - Part 1, General technical delivery conditions, 2004.

[255]   ISO. BS EN 10025-2:2004 - Hot rolled products of structural steels - Part 2, Technical delivery conditions for non-alloy structural steels, 2004.

[256]   Y. C. Fung. What principle governs the stress distribution in living organs? In E. Fukada Y. C. Fung and J. J. Wang, editors, *Biomechanics in China, Japan, and USA: Proceedings of an International Conference held in Wuhan, China in May 1983*, pages 1–13. Science Press, Beijing, China, 1983.

[257]   E. Assuncao, S. Williams, and D. Yapp. Interaction time and beam diameter effects on the conduction mode limit. *Optics and Lasers in Engineering*, 50(6):823–828, 2012.

[258]   Q. Guan, R. H. Leggatt, and K. W. Brown. Low stress non-distortion (LSND) TIG welding of thin-walled structural elements. Technical Report 374/1988, TWI, Abington, UK, 1988.

[259]   H. K. D. H. Bhadeshia. Developments in martensitic and bainitic steels: Role of the shape deformation. *Materials Science and Engineering A*, 378(1-2 SPEC. ISS.):34–39, 2004.

[260]   A. Matsuzaki, H. K. D. H. Bhadeshia, and H. Harada. Stress affected bainitic transformation in a Fe-C-Si-Mn alloy. *Acta Metallurgica Et Materialia*, 42(4):1081–1090, 1994.

[261]   C. Shiga, H. Y. Yasuda, K. Hiraoka, and H. Suzuki. Effect of M_s temperature on residual stress in welded joints of high-strength steels. *Welding in the World*, 54(3-4):R71–R79, 2010.

Appendix A: Description of rolling machine

Throughout the work described in this thesis, all rolling operations were carried out using a purpose-built machine. While aspects of rolling machine design are briefly discussed in Chapter 5, and several other chapters mention the rolling equipment used, a broader description of the rolling machine is given below. The general design and construction of the rolling machine was carried out by Peter Wright Associates (High Wycombe, Bucks., UK).

Overview and general description

The major components of the rolling system are shown in Figure 74. To carry out a rolling operation, the specimen is placed on the bed of the machine and held securely. Most of the experiments described in this thesis used the vacuum clamping system shown in Figure 74 for this purpose. The roller fork assembly is then lowered by the hydraulic cylinder and translated by moving the entire crossbeam. The crossbeam has only one axis of movement (i.e. the rolling direction); however the assembly comprising the roller fork, hydraulic cylinder and oscillating mass can be manually positioned along the crossbeam prior to rolling. All functions of the rolling machine are normally controlled manually using the control console shown to the right in Figure 74. Welding can be carried out on the same machine by attaching the welding torch to the crossbeam in front of the roller.
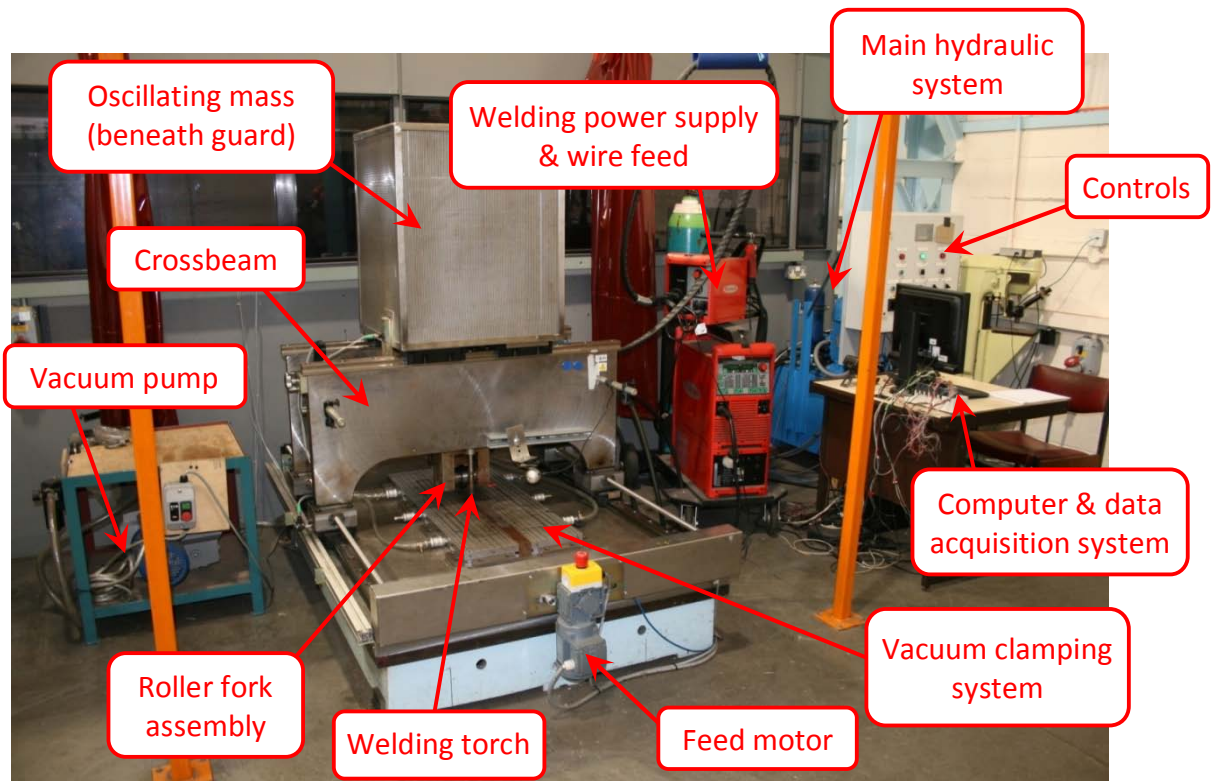
Figure 74: Overview of the rolling system. The hydraulic cylinder which actuates the roller fork is mounted vertically inside the crossbeam.

Force application

Figure 75 shows a side view inside the crossbeam. The lower end of the piston rod connects to the roller fork via a load cell which, is used to monitor the applied force. The top of the cylinder barrel is attached to the underside of the oscillating mass. The machine can operate two modes: either producing a constant force or a dynamic force. In constant-force mode the oscillating mass is bolted to the crossbeam plate, allowing the top of the cylinder to push against the crossbeam. The force applied by the cylinder is then entirely determined by the cylinder pressure which is kept constant by the hydraulic system. The maximum force which can be safely applied in constant-force mode is 200 kN, and the magnitude of the force applied in this way is repeatable always to within ±2%. A plot of roller load versus cylinder pressure for the machine in constant-force mode is shown in Figure 76.
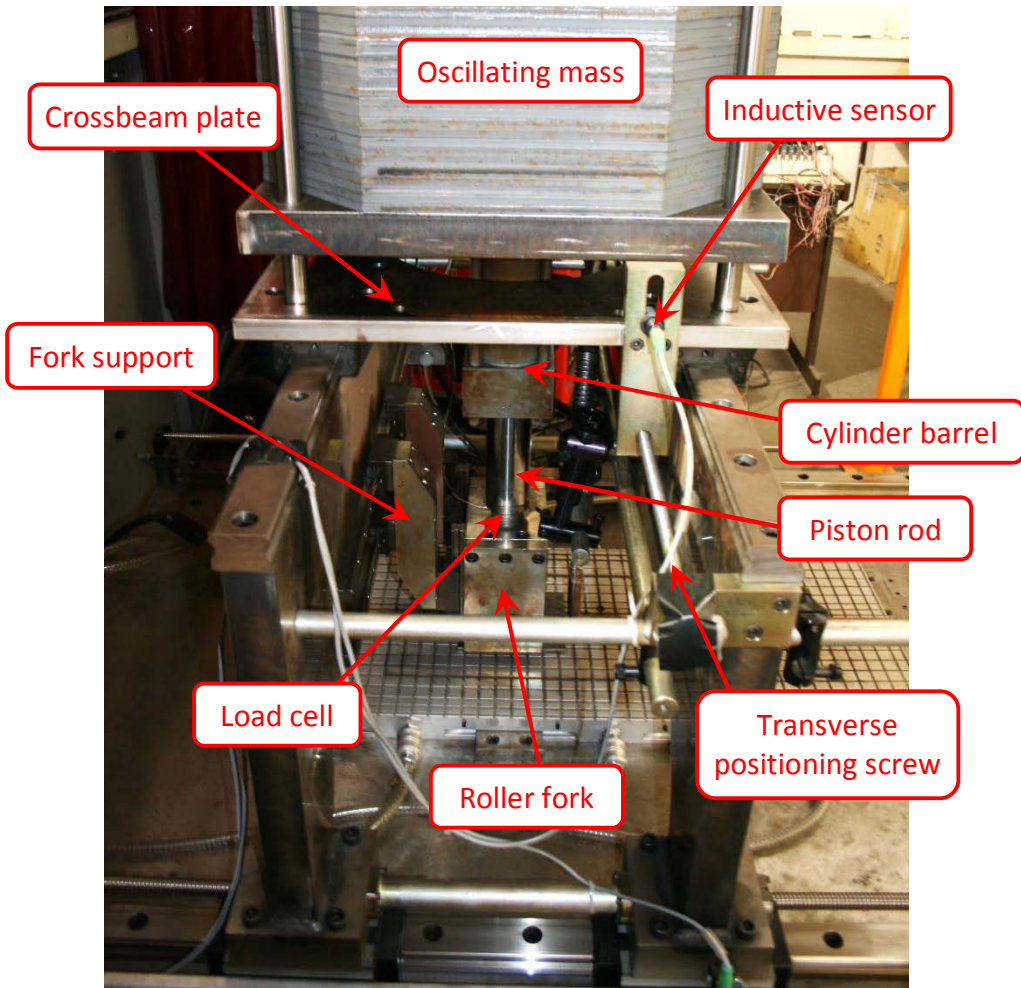
Figure 75: View inside the crossbeam. In this image the oscillating mass has been detached from the crossbeam and raised by extending the cylinder. The mass guard has been removed showing how the mass now is free to move in the vertical direction.
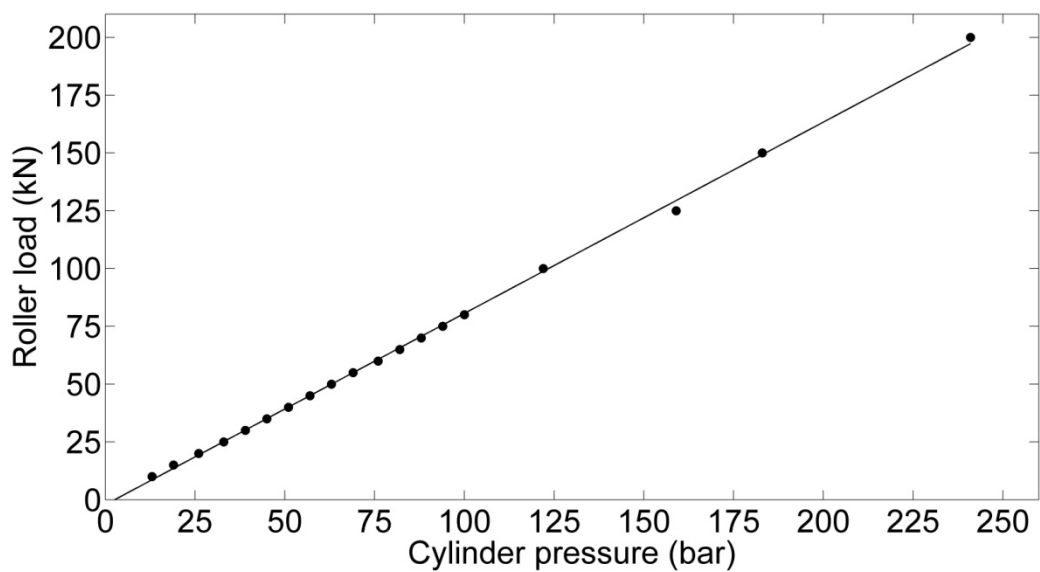

Figure 76: Roller load versus cylinder pressure for the rolling machine in constant-force mode.

In the dynamic-force mode the oscillating mass is unbolted from the crossbeam plate, allowing it to move freely in the vertical direction (as demonstrated in Figure 75). The cylinder is then controlled by an inductive sensor: when the sensor detects that the mass has lowered it switches a high-speed valve which allows high-pressure oil to flow into the top of the cylinder, pushing the mass up (see Figure 77). When the sensor does not detect the mass (i.e. when the mass has been raised), it switches the high-speed valve to another hydraulic line which allows oil to be forced out of the cylinder by the weight of the mass and flow into the unpressurised oil reservoir. The timing of the high-speed valve relative to the signal from the sensor can also be adjusted if necessary. The mass itself can be varied between 300 kg and 1500 kg by adding or removing some of the steel plates that comprise it. While the oscillation frequency cannot be controlled directly, it depends upon the cylinder pressure, mass, and position of the inductive sensor: all of which can be set by the user. For the experiment described in Chapter 5 in which the oscillating mode is used, preliminary trials were used to find the combination of these parameters which produced the desired peak load.
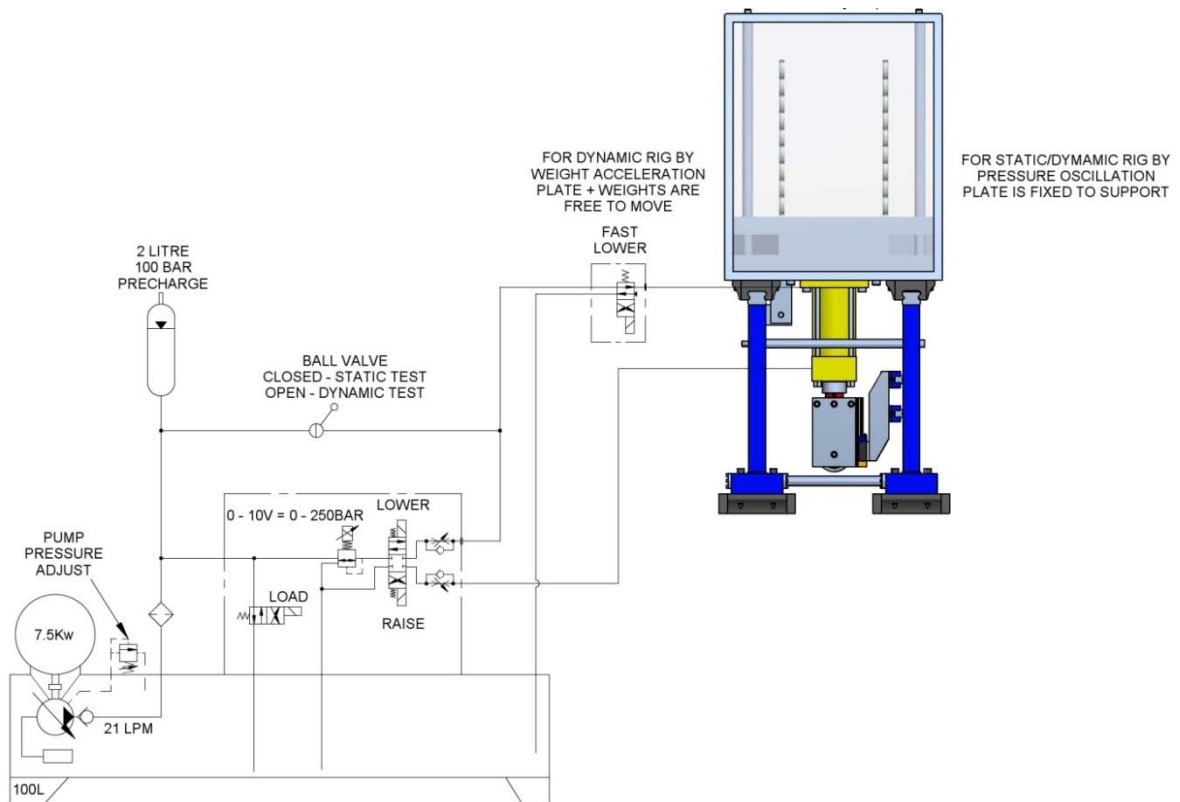

Figure 77: Rolling machine hydraulic circuit. The high-speed valve (marked FAST LOWER) is used for the dynamic-force mode.

Crossbeam movement

The crossbeam is moved by a pair of leadscrews driven by the induction motor indicated in Figure 74, allowing a maximum crossbeam speed of 25 mm s^{-1}. Setting a travel speed using the rolling machine's main control panel only determines AC frequency supplied to the motor: on this machine there is no closed-loop feedback for maintaining the crossbeam velocity. However, the true speed is measured separately by an inductive sensor on the leadscrew drive gear, and this can be used to calibrate the motor's speed/current curve for a given situation via the motor controller. Even without such calibration, in most situations the additional resistance caused by rolling of a weld would only result in quite small deviations from the desired velocity.

Roller fork

The roller fork is attached to the lower end of the piston rod, and may be disassembled to allow changing of the roller. To prevent an excessive moment from being exerted on the cylinder during rolling, the roller fork is supported from behind by the fork supports which are visible in Figure 75. The fork can hold either a single axle (Figure 78a) or two separate short axles with separate rollers (Figure 78b). The ability to hold two separate axles allows the rolling machine to accommodate the stiffener during the rolling of fillet (T-joint) welds. Figure 79 shows the different parts which comprise the axle and roller assembly: the holder is designed to allow quick changing of the roller ring, and the complete holder/roller ring assembly rotates on the axle. Machine can take roller rings between 100 mm and 200 mm diameter, and up to 30 mm maximum axial width. The roller rings themselves are turned from hollow bar sections of BS4659 BH13 tool steel, and heat treated to achieve a surface hardness of approximately 540 HV. An alignment laser is attached to one side of the roller fork and indicates the position of the roller in the rolling direction, allowing the operator to start and stop the roller accurately.
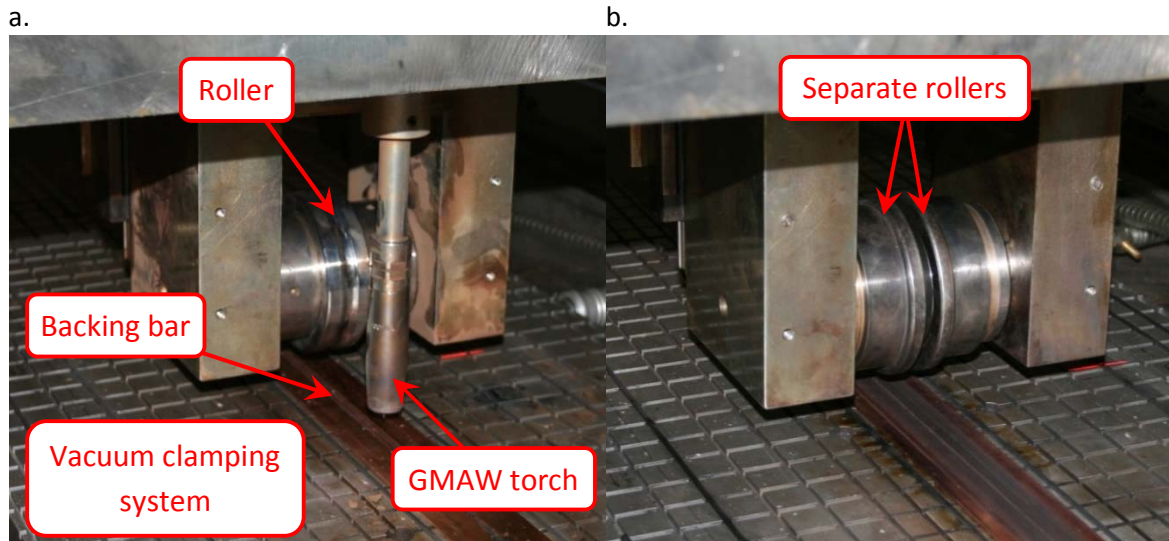
Figure 78: Front views of the roller fork with: (a.) single roller with a circumferential groove to accommodate a weld seam, and a GMAW torch positioned in front the roller for *in situ* rolling, (b.) the torch removed and a pair of rollers (these designed for rolling the weld toes only), mounted on separate short axles.

Figure 79: Roller assembly. The roller holder, roller, and end ring rotate together on the axle.

The load cell which sits between the end of the piston rod and the roller fork is a ring-type piezoelectric Kistler 9106A (Kistler Group A.G., Winterthur, Switzerland). This is connected to a charge amplifier to produce an analogue voltage which can be read by a data acquisition unit (see Figure 74) at an appropriate sampling rate: 500 Hz was used during all of the experiments described in this thesis.

Control

All functions of the rolling machine can be controlled manually using the control panel shown in Figure 80. Additionally, it is possible to switch the feed motor and hydraulic cylinder using an external control signal. The control system uses a programmable logic controller which controls the display, feed motor frequency inverter and hydraulic valves. This includes the analogue valve shown in Figure 77 (marked 0-10V – 0-250BAR) which controls the cylinder pressure, however before any test the pressure of the high-pressure reservoir must be set to a value greater than the cylinder pressure using the manual valve marked PUMP PRESSURE ADJUST. This allows the pump

pressure to be reduced when only a low cylinder pressure will be used, which reduces the load on the pump motor. The machine also has automatic feed motor and pump motor overload cut-out switches (see indicator lights, Figure 80a), and an inductive sensor mounted on the crossbeam which can be used to trigger a welding power supply (or other equipment) based on the crossbeam position.
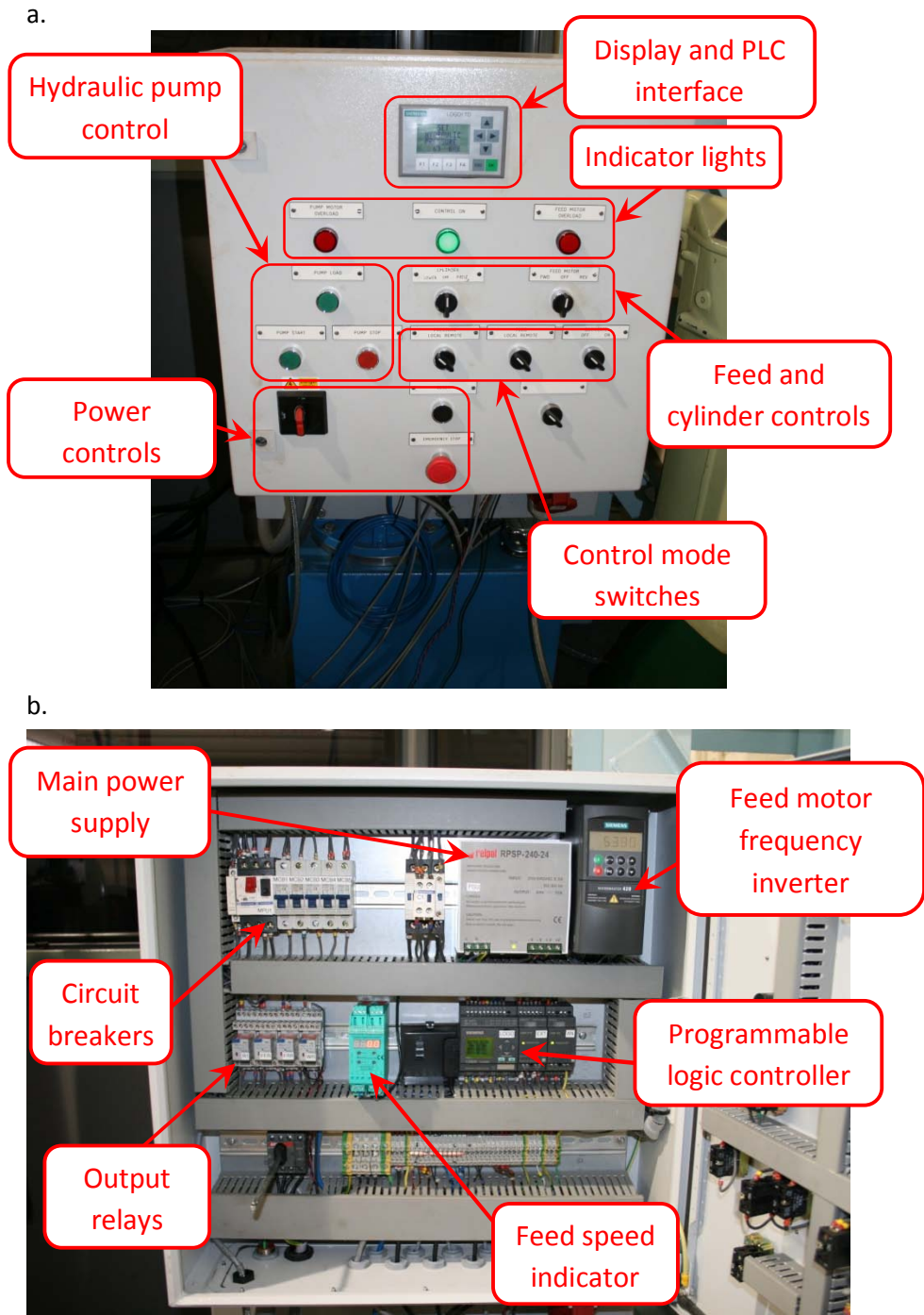
a.

b.

Figure 80: Rolling machine control unit. (a.) Front panel, (b.) internal view.

Appendix B: Selection of plate specimen geometry – buckling analysis

Introduction

Many of the experiments described in this thesis used standardised rectangular steel plate specimens with an aspect ratio: 750 x 300 mm. This type of specimen is used with 3mm-thick material in Chapters 3 and 4, and with 6 mm-thick material in Chapters 5-7. This specimen geometry was chosen with the intention that the plates would consistently display a single type of distortion, with a distortion magnitude roughly proportional to the longitudinal residual stress. The aspect ratio selection was informed by calculations based on small-displacement plate buckling theory: an aspect ratio was sought for which the critical level of residual stress necessary to cause mode 1 buckling (in which the longitudinal profile of the distorted surface approximates a single half-sine wave) was significantly lower than the critical stress necessary to cause any other buckling mode. The calculations used for this are given below.

Classical plate theory

The buckling of thin elastic plates can be analysed using energy methods. In theory, a perfectly elastic plate will buckle when the energy expended by external forces in causing buckling exceeds that stored internally in the elastically-buckled plate. The internal energy U in an elastically-deformed plate is given by [251]:

Equation 27

$$U = \frac{D}{2} \int_{-\frac{a}{2}}^{\frac{a}{2}} \int_{-\frac{b}{2}}^{\frac{b}{2}} \left(\frac{\partial^2 w}{\partial x^2}\right)^2 + \left(\frac{\partial^2 w}{\partial y^2}\right)^2 + 2v \frac{\partial^2 w}{\partial x^2}\frac{\partial^2 w}{\partial y^2} + 2(1-v)\left(\frac{\partial^2 w}{\partial x \partial y}\right)^2 dx\, dy$$

Where a is the plate length in longitudinal direction x, b is the plate width in transverse direction y, v is the Poisson's ratio, and D is the plate's flexural rigidity. The function $w(x, y)$ describes the (small) deflection of the plate in the out-of-plane direction z (see Figure 81) when it is at the point of incipient buckling. D is given by the equation:

Equation 28

$$D = \frac{Et^3}{12(1-v^2)}$$

Where E is Young's modulus and t is the plate's thickness (it is assumed that $t \ll a, b$).
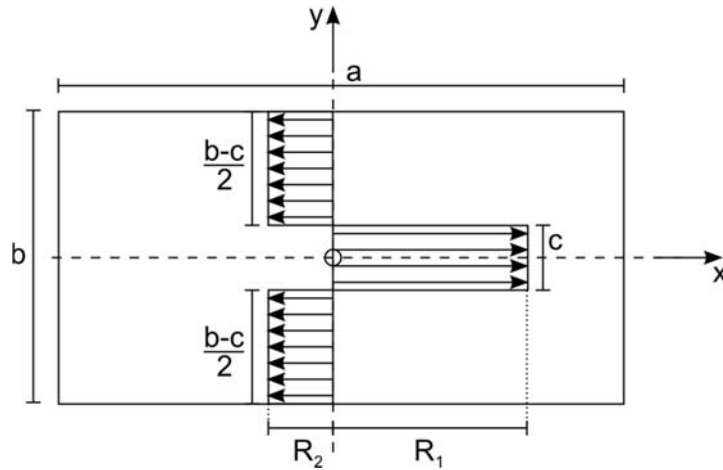
Figure 81: Simplified load distribution to simulate the action of residual stress in a rectangular welded plate.

For the case of buckling under the action of residual stress there are no external forces, although internal stresses may make buckling energetically favourable. However, Masubuchi and co-workers used externally-applied force distributions of an assumed form to simulate the action of residual stress [164, 165, 25]. For a set of externally applied forces $N_x(y)$ acting along the longitudinal ends of the plate in the x direction only, the work (T) done by external forces is [251]:

Equation 29

$$T = -\frac{1}{2} \int_{-\frac{a}{2}}^{\frac{a}{2}} \int_{-\frac{b}{2}}^{\frac{b}{2}} N_x \left(\frac{\partial w}{\partial x} \right)^2 dx \, dy$$

To solve $U = T$, both an assumed form of the deflection function $w(x, y)$ and a force distribution $N_x(y)$ are required. However, the appropriate deflection function is dependent on the external load distribution and the mechanical boundary conditions at each plate edge.

Representative load distribution

The load distribution assumed by Masubuchi and co-workers is shown in Figure 81 [25]. This simple piecewise distribution has a central region of tensile stress at the plate's central longitudinal axes, representing the tensile residual stress typically found at the weld line. Elsewhere, the force is compressive, so that it equilibrates over the section. This is described by the equations:

Equation 30

$$N_x = R_2 \quad for \quad -\frac{b}{2} \leq y < -\frac{c}{2}$$

$$N_x = R_1 \quad for \quad -\frac{c}{2} \leq y \leq \frac{c}{2}$$

$$N_x = R_2 \quad for \quad \frac{c}{2} < y \leq \frac{b}{2}$$

$$R_2(b - c) = -R_1 c$$

Where R_1 is the central tensile force per unit width, R_2 is the compressive force per unit width. The ratio $c/_b$ describes the width of the tensile region of the force distribution relative to the overall plate width. This is only a crude approximation of the state of residual stress in a real welded plate. Firstly, it does not satisfy the boundary condition that any point at the edge of the plate (at $x = -\frac{a}{2}, \frac{a}{2}$ and $y = -\frac{b}{2}, \frac{b}{2}$) must be free of stress. However, this is necessary to simplify the calculation of external work, allowing Equation 29 to be used. Secondly, the assumption of a piecewise constant load distribution is clearly unrealistic.

Boundary conditions

All edges simply-supported (SSSS)

The most straightforward set of mechanical boundary conditions for the plate is where it is simply supported on all four edges (SSSS). Other sets of boundary conditions frequently make it difficult to obtain a realistic function for w, and hence to obtain a buckling solution [252]. For the plate shown in Figure 81, SSSS boundary conditions are defined by:

Equation 31

$$w = 0 \quad , \quad \frac{\partial^2 w}{\partial x^2} + v \frac{\partial^2 w}{\partial y^2} = 0 \quad for \quad x = -\frac{a}{2}, \frac{a}{2}$$

$$w = 0 \quad , \quad \frac{\partial^2 w}{\partial y^2} + v \frac{\partial^2 w}{\partial x^2} = 0 \quad for \quad y = -\frac{b}{2}, \frac{b}{2}$$

This simplifies the analysis required to generate an expression for the critical buckling stress because a deflection function $w(x, y)$ which satisfies these conditions can be easily expressed as [25]:

Equation 32

$$w_{SSSS} = A \cos\left(\frac{m\pi x}{a}\right) \cos\left(\frac{n\pi y}{b}\right)$$

Where A is the (arbitrary) deflection amplitude, and m and n are integers. Now, solving $U = T$ using the boundary conditions in Equation 31 gives [117]:

Equation 33

$$\sigma_{cr} = \left(\frac{E\pi^2}{12(1-v^2)}\right)\left(\frac{t}{b}\right)^2\left(\frac{a}{bm} + \frac{bm}{a}\right)^2\left(\frac{\pi c/b}{\sin(\pi c/b)}\right)$$

Where σ_{cr} is the critical stress in the two regions to either side of the weld (see Figure 81), i.e. $\sigma_{cr} = \frac{R_2}{t}$, required for incipient buckling. It should be noted that the critical

stress depends on the integer m which represents the number of half sine waves in the x direction in the deflection function, i.e. different buckling modes have different critical stresses. While the SSSS condition is possible to solve it is not particularly realistic: in a real plate specimen containing residual stress, no restraint is provided at the edges.

Ends simply supported, sides free (SFSF)

A slightly more realistic set of boundary conditions than SSSS is where the longitudinal ends of the plate (the right and left edges in Figure 81) are simply-supported but the other two edges are free (SFSF), defined by [188]:

Equation 34

$$w = 0 \quad , \quad \frac{\partial^2 w}{\partial x^2} + v\frac{\partial^2 w}{\partial y^2} = 0 \quad for \quad x = -\frac{a}{2}, \frac{a}{2}$$

$$\frac{\partial^3 w}{\partial y^3} + (2-v)\frac{\partial^3 w}{\partial x^2 \partial y} \quad , \quad \frac{\partial^2 w}{\partial y^2} + v\frac{\partial^2 w}{\partial x^2} = 0 \quad for \quad y = -\frac{b}{2}, \frac{b}{2}$$

For this set of boundary conditions, van der Aa used a deflection function based on the results of a finite element analysis [117]:

Equation 35

$$w_{SFSF} = A\sin\left(\frac{\pi x}{a}\right)\left(\left(1 + (1-v)\left(\frac{a}{b}\right)^2\right) - \sin\left(\frac{\pi y}{b}\right)\right)$$

Which yields:

Equation 36

$$\sigma_{cr} = \left(\frac{E\pi^2}{12(1-v^2)}\right)\left(\frac{t}{b}\right)^2 \left(\frac{8cva^2b^2p + 8cb^4p - 2ca^2b^2\pi - 2cb^4p^2\pi - ca^4\pi - cb^4\pi}{-8a^2b^2cp + 8a^2b^3p\sin\left(\frac{\pi c}{2b}\right) - a^2b^3\sin\left(\frac{\pi c}{b}\right)}\right)$$

Where $p = 1 + (1-v)\left(\frac{a}{b}\right)^2$. While this does not satisfy the condition, given in Equation 34, that bending moments should be zero at the free edges (i.e. $\frac{\partial^2 w}{\partial y^2} + v\frac{\partial^2 w}{\partial x^2} = 0$ when $= -\frac{b}{2}, \frac{b}{2}$), it is a useful approximation, and was used to find a solution roughly approximating the FFFF (all sides free) case of a real plate specimen.

Results and conclusion

Surfaces representing the critical buckling stress over a range of normalised plate aspect ratios (a/b) and central stress region widths (c/b), for the first six buckling modes ($m = 1 : 6$), are shown in Figure 82. The calculation of these functions was based on material constants E = 210 GPa and v = 0.3 (approximately those of structural steel), and a plate thickness-to-width ratio (t/b) of 0.01.
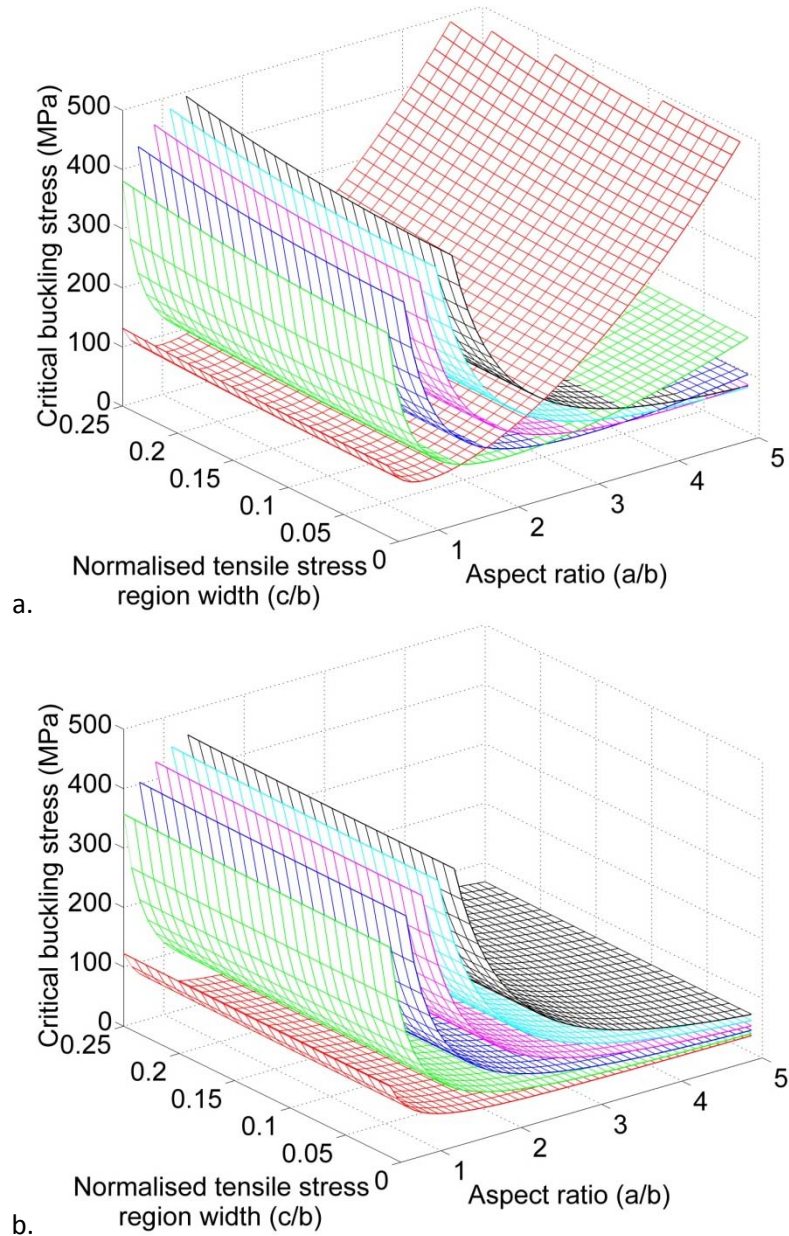
Figure 82: Surfaces indicating the variation of critical buckling stress with plate aspect ratio and tensile stress region width for (a.) SSSS and (b.) SFSF boundary conditions. The first six buckling modes are shown, with the red surface indicating mode 1.

In both cases, the critical buckling load is only slightly sensitive to the width of the central tensile region; there is a much stronger dependence on the plate aspect ratio. For the SSSS boundary condition (Figure 82a) it is clear that at low plate aspect ratios, mode 1 buckling is most likely to occur, since this requires the lowest critical buckling stress. Other buckling modes are slightly more energetically favourable at higher aspect ratios $(a/b > \sqrt{2})$. However, for the SFSF boundary condition (Figure 82b), mode 1 buckling has a lower critical buckling stress over the whole range of aspect ratios shown, although at higher aspect ratios the difference between the critical stress required for mode 1 and for higher modes is greatly reduced. Assuming that the

179

SFSF condition is most closely representative of the real case of an unrestrained welded plate, this means that the occurrence of higher buckling modes is unlikely, although it would still be prudent to avoid very high aspect ratios where the relatively small difference in critical buckling energy between different modes might not be enough to guarantee that buckling will not occur in a higher mode. Likewise, it would be sensible to avoid very low aspect ratios where torsional buckling modes, which have not been included in this analysis, may occur. Consequently, an aspect ratio of 2.5 was selected for the experiments reported in Chapters 3-8. Overall specimen dimensions of 300 x 750 mm were used, since this was a suitable size for the rolling machine (described in Appendix A), and material thicknesses of 3 and 6 mm were used for different purposes at various points in the work. Throughout all of the experiments, specimens with this aspect ratio only displayed buckling in mode 1. Therefore, it can be said that while the analysis given above is based on several unrealistic assumptions, provides a useful first approximation for predicting the buckling mode in unrestrained rectangular plate welds.

Appendix C: Distortion measurement method and distortion of welded 6mm plate specimens

Introduction, measurement method

Throughout most of the experimental work described in this thesis, the focus has been on measurement of residual stress rather than the distortion which it causes. In this section, measurements of the residual distortion of a number of 6mm-thick steel plate specimens are presented. These specimens include those used for the experiments described in Chapters 5, 6 and 7, plus additional duplications and specimens rolled with different parameters.

A method for quantifying the distortion of plate specimens was developed, and was used in the experiments described in Chapters 4, 8 and 9. Most studies of residual distortion use simple metrics such as the peak displacement of a buckled plate edge or the total shrinkage of a defined part of the specimen [253]. This has the advantage of making the distortion measurement process simple: most measurements can be carried out to a reasonable degree of accuracy using rulers and dial gauges. However, it does not promote easy comparison of results between different experiments, and can result in misleading measurements when different modes of distortion are present. The basic method of measurement is outlined in Chapter 4. Briefly, laser coordinate scanning was used to locate a large number of scattered points on the specimen's upper surface, and interpolation of these data to a regular rectangular mesh of 10 x 10 mm square elements was carried out using the algorithm described by Sandwell [187]. The mean out-of-plane displacement of the elements of this grid (minus the plate thickness) was then calculated. This method is more representative of the entire specimen than measurements at single points, but it requires time and more complicated equipment. However, collecting data from the entire upper surface of the specimen means that its shape can be analysed or plotted in three dimensions. A subroutine was also developed to find the different distortion components, such as the longitudinal bow, mean angular distortion, longitudinal twist etc.

Results

The effect of post-weld rolling at different levels of roller load on weld distortion is shown in Figure 83a. It is apparent that a large decrease in overall distortion is possible even at relatively small roller loads. The application of larger rolling loads (eg. 100 or 150 kN) causes only an insignificant additional improvement in distortion, despite having a pronounced effect on the residual stress distribution (see Chapter 5). The reason for this is unclear, but is likely to be because either the small change in residual stress induced by rolling at a low load disproportionately reduces the buckling propensity of the plate, or because of through-thickness variations in stress which

reduce distortion even at low rolling loads. It can also be seen in this figure that the distribution of distortion values for rolled plates is noticeably lower than for the un-rolled welds (0 kN). Although fewer measurements are presented for the case of *in situ* rolling (Figure 83b), those which are available indicate that this form of rolling reduces distortion much less effectively. This is compatible with the residual stress results presented in Chapter 5, which show that rolling is also far less effective at modifying the residual stress state.
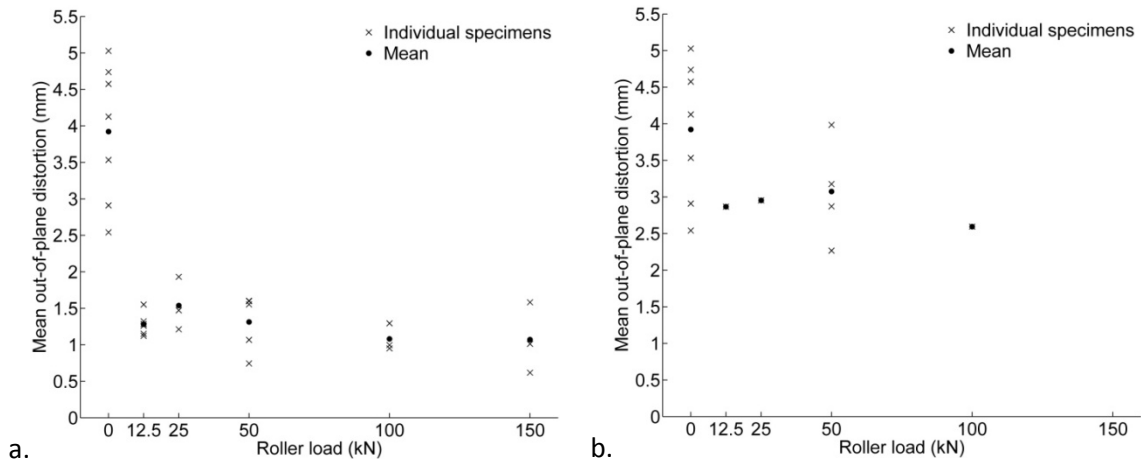

Figure 83: Mean out-of-plane distortion for 6mm bead-on-plate weld specimens rolled (a.) post-weld, (b.) *in situ***. The roller profile used is described in Chapter 5 and 6, and the rolling speed is 8.33 mm s^{-1}.**

Appendix D: Parent material properties

All of welds in this thesis use S355 structural steel (specified in European standard EN 100025:2004 [254]) as the parent material. However, within this standard there is scope for variation in composition and mechanical properties. For instance, minimum yield strength is specified (355 MPa for products of ≤16 mm thickness), but there is no direct constraint on maximum yield strength [255]. Ultimate Tensile Strength (UTS) must be in the range 470 - 630 MPa (for material thicknesses of $3 \leq t \leq 100$ mm). Since plate material of various thicknesses is used at different points in the work, a comparison of the basic properties of this material is given here.

A summary of the different materials used is given in Table 14. All of the material was hot-rolled coil supplied by Tata Steel Europe ltd (formerly Corus Group plc). Table 15 shows the chemical composition of each batch. In the case of the 3 mm, 4 mm, and 6 mm Batch 2 material, the composition was determined by the supplier. For the 6 mm Batch 1 material, chemical analysis was carried out by Exova (UK) ltd.

Table 14: Summary of the four batches of S355 structural steel used for bead-on-plate and butt welds in the experiments.

Material thickness	Used in Chapters	Yield (MPa)	UTS (MPa)
3 mm	3, 4	490	555
4 mm	4, 9	475	535
6 mm (Batch 1)	5, 6, 7	474	520
6 mm (Batch 2)	8	395	520

Table 15: Chemical composition of different material batches (wt. %).

Material	C	Si	Mn	P	S	Cr	Mo	Ni	Al	Cu	Nb
3 mm	0.063	0.013	1.29	0.009	0.007	0.016	0.003	0.022	0.030	0.021	0.034
4 mm	0.062	0.016	1.28	0.010	0.004	0.011	0.002	0.022	0.035	0.009	0.033
6 mm (Batch 1)	0.06	0.04	1.28	0.010	0.009	0.02	<0.01	0.02	0.03	0.02	0.03
6 mm (Batch 2)	0.158	0.010	1.41	0.013	0.006	-	-	-	0.022	0.009	-

Tensile tests on all of the material, to ISO 6892-1:2009 [221], were carried out at Cranfield using an Instron 5500 load frame. All tests were at ambient temperature on samples cut in the rolling direction, and at a constant elongation rate of 5mm/min. Typical stress-strain curves for each batch of material are shown in Figure 84. All of the yield and UTS values (see Table 14) are well within the S355 specification, however there is some variation between different material batches. Notably, the two batches of 6 mm material have quite different yield strengths: the second batch (used in Chapter 8) yields at a lower stress but hardens more, resulting in a UTS identical (within the measurement accuracy) to that of Batch 1.
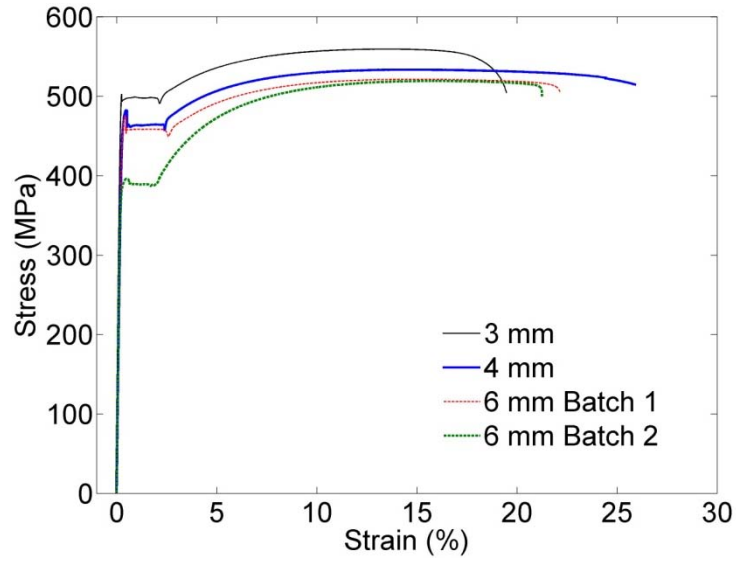
Figure 84: Ambient-temperature tensile stress-strain curves for the four different batches of S355 steel of different thicknesses (rolling direction). Note that 'engineering' stress (load/initial cross-section) rather than 'true' stress is given.